Title

Leveraging the Primary and Secondary Coordination Sphere of Molecular Catalysts Towards Electrocatalytic and Photocatalytic Carbon Dioxide Reduction

Author

De La Torre, Patricia L

Publication Date

2023

Leveraging the Primary and Secondary Coordination Sphere of Molecular Catalysts Towards Electrocatalytic and Photocatalytic Carbon Dioxide Reduction

By

Patricia L. De La Torre

A dissertation submitted in partial satisfaction of the

requirements for the degree of

Doctor of Philosophy

in

Chemistry

in the

Graduate Division

of the

University of California, Berkeley

Committee in charge:

Professor Christopher J. Chang, Chair
Professor John Arnold
Professor Jeffrey Reimer

Spring 2023

Spring 2023

Leveraging the Primary and Secondary Coordination Sphere of Molecular Catalysts Towards Electrocatalytic and Photocatalytic Carbon Dioxide Reduction

by Patricia L. De La Torre

Abstract

Leveraging the Primary and Secondary Coordination Sphere of Molecular Catalysts Towards Electrocatalytic and Photocatalytic Carbon Dioxide Reduction

by

Patricia L. De La Torre

Doctor of Philosophy in Chemistry

University of California, Berkeley

Professor Christopher J. Chang, Chair

Industrialization and urbanization have encouraged rapid population increases, improved standards of living, access to education, and advanced technological development in large economies across the globe. Simultaneously, these events have strained our natural resources, which over time has drawn attention to their scarcity as well as the secondary environmental consequences of their exploitation. In particular, the combustion of fossil fuels, a non-renewable source of energy, is directly correlated to increased concentrations of atmospheric greenhouse gases such as carbon dioxide (CO_2). Since the beginning of industrialization, we have monitored rising anthropogenic carbon dioxide and the resulting effects of increased global surface temperatures, including stronger and more frequent heat waves, droughts, wildfires, and hurricanes. Changes to the Earth's climate disproportionately affect marginalized communities such as people of color, non-European immigrants, people with disabilities, and low-income groups— as well as populations outside of the Western purview, such as the Philippines, Madagascar, and India. In light of this, scientists are propelled to develop alternatives to petroleum-based energy sources, especially those with carbon-neutral footprints. The capture of atmospheric CO_2 and its conversion to chemicals currently derived from petroleum is under investigation as an approach to remove CO_2 pollution while providing a net-zero carbon source. The goal of this thesis is to study the use of artificial photosynthesis, specifically, molecular photocatalysis and electrocatalysis, to study the CO_2 reduction reaction (CO_2RR) as a method of transforming CO_2 into useful chemical feedstocks using sustainable energy inputs such as electricity, which can be derived from wind or solar power. To understand and optimize molecular systems with atomic-level tunability in their activity towards CO_2RR, our work involves the investigation of primary and secondary coordination sphere modifications to molecular catalysts based on transition metal complexes of polypyridine and supramolecular porphyrin ligands. The ability to modulate both the primary and secondary coordination sphere of molecular species provides insight into the fundamental properties that are important in optimizing selectivity and rates in electro- and photocatalysts for CO_2RR. We hope this work highlights the value of molecular chemistry in the future development of large-scale CO_2 capture and conversion for sustainable and renewable energy.

~~

Para mis abuelitos, Josefina Rivera y Manuel De La Torre

~~

Table of Contents

Agradecimientos / Acknowledgements iii

Chapter 1: Porosity as a Design Element for Developing Catalytic Molecular Materials for Electrochemical and Photochemical Carbon Dioxide Reduction 1

Chapter 2: Exchange Coupling Determines Metal-Dependent Efficiency for Iron- and Cobalt-Catalyzed Photochemical CO_2 Reduction 35

Chapter 3: Synergistic Porosity and Charge Effects in a Supramolecular Porphyrin Cage Promote Efficient Photocatalytic CO_2 Reduction 79

Appendix A: A Ruthenium Polypyridyl Complex for CO_2 Reduction Beyond Two Electrons...168

Appendix B: Experimental Procedures for the Evaluation of Homogeneous Photocatalysts .176

Agradecimientos / Acknowledgements

Siento mucho amor y gratitud al reconocer a todos los que me apoyaron en el viaje de convertirme en científica que comenzó cuando tenía 17 años. Es increíble reflexionar sobre cuánto he crecido en los últimos 9 años y cada uno de ustedes ha sido parte, especialmente al recordarme que soy capaz y amada sin importar mi camino ni las barreras que encuentre.

Estoy agradecida por mi asesor, el Prof. Chris Chang, quien ha sido paciente y comprensivo durante los momentos difíciles y me ha apoyado durante mis triunfos y el desarrollo de mi carrera. Aprendí mucho al estar en su equipo y aprecio el ambiente de rigor académico equilibrado con la compasión que trata de cultivar. También me gustaría agradecer a mis comités de disertación y examen de calificación por su apoyo a mis estudios de posgrado: los profesores Don Tilley, Kenneth Raymond, Jeffrey Reimer y John Arnold.

A mis colegas de Berkeley: Dr. Peter Smith, Dr. Marco Messina, Dra. Audrey Reeves, Dr. Lun An, Dr. Mina Narouz, Abigail Hinojosa, Angel Gonzalez-Valero, Aila Rothweiler y Luke Elissiry, gracias por todo lo que me enseñaron, por las cosas que aprendimos juntos y por su amabilidad.

Perseguir la investigación científica y crecer en el asombro de la química provino de mis maravillosas experiencias como estudiante universitaria en la Universidad Estatal de Sonoma. Estoy increíblemente agradecida con la Dra. Carmen Bustos-Works, quien enseñó mi primera clase de química y fue mi primera asesora de investigación. Su inteligencia y tutoría me inspiraron más y más cada año y me empujaron a dar lo mejor de mí y realmente sacarme de mi zona de confort en la búsqueda de esta carrera. A mis colegas en Sonoma: Blaine Baker, Faven Berhane, Amir Arshi, Liridona Leti, Lilia Ortiz, Annie Nelson, Bernardo Guerrero, Brandon Jolly, Valentino Perez y Annalise Thompson, gracias por su increíble amistad y todos los buenos momentos en el laboratorio de nerds.

A mis padres: Patricia Gómez y Fernando De La Torre. ¿Cómo pongo en palabras todo lo que les agradezco? Gracias por quedarse hasta tarde ayudándome con mi tarea. Gracias por toda la comida increíble que hacen y por enseñarme a cocinar. Gracias por enseñarme a ser valiente y defenderme. Gracias por apoyar este camino educativo extremadamente largo, ninguno de nosotros esperaba que aquí es donde estaríamos, pero siempre me han inculcado un impulso para perseguir cosas que parecen estar fuera de mi alcance. ¡Lo hicimos! Llevo todo su arduo trabajo y sacrificios conmigo como motivación para nunca rendirme. ¡Los quiero mucho!

A mis hermanitas y a mi perra (sobrina): Leslie, Aurora, Marifer y Koko. Gracias a todas por ser tan cariñosas, tan divertidas, tan inteligentes y tan dulces, estoy muy orgullosa de ustedes. Leslie, todo lo que eres es tan hermoso e inspirador para mí desde que éramos niñes. Trabajas muy duro y siempre te mantienes fiel a ti misme, gracias por ser mi brújula moral y por animarme cuando estoy deprimida. Aurora, eres la persona más valiente y resistente que conozco, he aprendido mucho de ti en los últimos años y me siento afortunada de crecer a tu lado. Gracias por vivir conmigo este año, tú y Koko han hecho la vida dulce y divertida. Koko, gracias por ser mala y por apoyarnos emocionalmente a Aurora ya mí. Marifer, eres tan creativa y encantadora. Gracias por jugar a las muñecas, hornear y hacer arte conmigo, y por toda la suerte que me das cuando la necesito. Las quiero mucho.

Finalmente, a mi amado prometido Blaine Baker (otra vez). Tu humor, compasión, inteligencia y amor me hacen seguir adelante. Gracias por pasar tus fines de semana en la biblioteca conmigo, por escucharme practicar presentaciones y por todo el descanso, la relajación y las aventuras que compartimos después del trabajo. Soy muy afortunada de tenerte en mi vida y estoy emocionada de reunirnos pronto. Juntos somos imparables y no tengo ninguna duda de que todos nuestros sueños se harán realidad. Te amo mi amor.

I feel so much love and gratitude as I acknowledge everyone who supported me through the journey of becoming a scientist that started when I was 17 years old. It is incredible to reflect on how much I have grown over the past 9 years and everyone one of you has played a part, especially in reminding me that I am capable and loved no matter my path and the barriers I come across.

I am thankful for my advisor, Prof. Chris Chang, who has been patient and understanding throughout the difficult moments and supportive during my triumphs and career development. I learned a lot from being on his research team and I appreciate the environment of academic rigor balanced with compassion he tries to cultivate. I would also like to thank my Dissertation and Qualifying Exam Committees for their support of my graduate studies: Professors Don Tilley, Kenneth Raymond, Jeffrey Reimer, and John Arnold.

To my colleagues at the College of Chemistry: Dr. Peter Smith, Dr. Marco Messina, Dr. Audrey Reeves, Dr. Lun An, Dr. Mina Narouz, Abigail Hinojosa, Angel Gonzalez-Valero, Aila Rothweiler, and Luke Elissiry, thank you for all you taught me, for the things we learned together, and for your kindness.

Pursuing scientific research and growing in awe of chemistry came from my wonderful experiences as an undergraduate at Sonoma State University. I am incredibly grateful for Dr. Carmen Bustos-Works, who taught my first college chemistry class and was my first research advisor. Her intelligence and mentorship inspired me more and more each year and pushed me to do my best and really put myself out of my comfort zone in pursuit of this career. To my colleagues at Sonoma State: Blaine Baker, Faven Berhane, Amir Arshi, Liridona Leti, Lilia Ortiz, Annie Nelson, Bernardo Guerrero, Brandon Jolly, Valentino Perez, and Annalise Thompson, thank you for your amazing friendship and all the good times in the Nerd Lab.

To my parents: Patricia Gomez and Fernando De La Torre. How do I put in words all that I am grateful to you? Thank you for staying up late helping me with my homework. Thanks for all the amazing food you feed me, and for teaching me to cook. Thank you for teaching me to be brave and stand up for myself. Thank you for being supportive of this extremely long educational path, neither of us expected that this is where we would be, but you have always instilled in me a drive for pursuing things that seem to be out of reach. We did it! I carry all of your hard work and sacrifices with me as motivation to never give up. I love you!

To my baby sisters and dog (niece): Leslie, Aurora, Marifer, and Koko. Thank you all for being so loving, so funny, so smart, and so sweet, I am very proud of you. Leslie, all that you are is so beautiful and inspiring for me since we were kids. You work so hard and always stay true to yourself, thank you for being my moral compass and for hyping me up when I'm down. Aurora, you are the bravest and most resilient person I know, I have learned so much from you in the past few years and I feel lucky to grow alongside you. Thank you for living with me this year, you and Koko have made life so sweet and fun. Koko, thank you for being bad, and for emotionally supporting Aurora and I. Marifer, you are so creative and lovely. Thank you for playing dolls, baking, and making art with me, and for all the luck you give me when I need it. Love you all.

Finally, to my beloved fiancé Blaine Baker (again). Your humor, compassion, intelligence, and love keep me going. Thank you for spending your weekends in the library with me, for listening to me practice presentations, and for all the rest, relaxation, and adventures we share after work. I am so lucky to have you in my life and am excited to be reunited soon. Together we are unstoppable, and I have no doubt all of our dreams will come true. I love you dearly.

Chapter 1: Porosity as a Design Element for Developing Catalytic Molecular Materials for Electrochemical and Photochemical Carbon Dioxide Reduction

This review article was accepted with minor revisions and is pending final publication in the following scientific journal:

Patricia De La Torre, Lun An, and Christopher J. Chang, Porosity as a Design Element for Developing Catalytic Molecular Materials for Electrochemical and Photochemical Carbon Dioxide Reduction. *Advanced Materials*, **2023**

Abstract:

The catalytic reduction of carbon dioxide (CO_2) using sustainable energy inputs is a promising strategy for upcycling of atmospheric carbon into value-added chemical products. This goal has inspired the development of catalysts for selective and efficient CO_2 conversion using electrochemical and photochemical methods. Among the diverse array of catalyst systems designed for this purpose, two- and three-dimensional platforms that feature porosity offer the potential to combine carbon capture and conversion. Included are covalent organic frameworks (COFs), metal-organic frameworks (MOFs), porous molecular cages, and other hybrid molecular materials developed to increase active site exposure, stability, and water compatibility while maintaining precise molecular tunability. This mini-review showcases catalysts for the CO_2 reduction reaction (CO_2RR) that incorporate well-defined molecular elements integrated into porous materials structures. Selected examples provide insights into how different approaches to this overall design strategy can augment their electrocatalytic and/or photocatalytic CO_2 reduction activity.

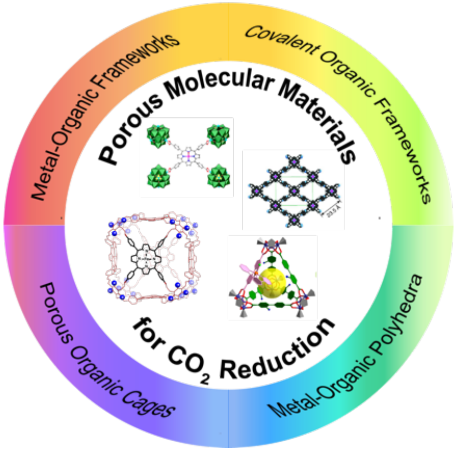

1. Introduction

The world population's dependence on finite natural resources for energy storage and generation can be mitigated by replacement with renewable and sustainable sources such as electricity from wind, solar, and hydropower.[1-4] Efforts to decarbonize our current and future energy infrastructure are critical to addressing detrimental effects of petroleum combustion manifesting as rising global temperatures, ocean acidification, and increased frequency of extreme weather events.[5, 6] Many of these phenomena can be attributed to rising concentrations of atmospheric CO_2, now peaking at 421 ppm in 2022; this situation demands restoration of the carbon cycle to its natural balance as an important step in a zero-emissions future.[7, 8] One approach under current investigation is the direct air capture of CO_2 and its subsequent transformation into value-added products via the CO_2 reduction reaction (CO_2RR). CO_2 reduction via multi-electron, multi-proton transfer reaction processes can effectively store sustainable energy in the form of chemical bonds.[6, 9-15]

Although CO_2RR is a promising strategy to store energy derived from clean and renewable sources and simultaneously mitigate climate change, it is thermodynamically costly to activate the linear and symmetric CO_2 molecule by a single electron transfer due to the large reorganization energy associated with producing the bent radical anion (–1.9 V vs NHE).[16] With the inclusion of multiple protons and electrons, CO_2 reduction can be achieved at more moderate potentials. However, this multielectron, multiproton chemistry comes at the cost of product selectivity; within a relatively narrow potential window (–0.24 to –0.61 V), a variety of carbon products such as CO, HCOOH, HCHO, CH_3OH, and CH_4 can theoretically be formed, but in most cases the reduction of protons to hydrogen in the hydrogen evolution reaction (HER) is facile (0 V) and dominant over carbon-based product formation. As such, developing catalyst platforms capable of efficient and selective CO_2RR presents one attractive avenue in solving these challenges. Moreover, applying electrochemistry and/or photochemistry as sustainable energy inputs that drive the electron transfer processes for CO_2RR can guide the optimization of these platforms.[9] In terms of efficiency, CO_2RR electrocatalysts require close energy matching between their onset potential and the thermodynamic potential required for the desired CO_2 transformation in order to minimize the excess energy required to drive the reaction (i.e., overpotential). Performance metrics such as Faradaic efficiency (FE) and current density further describe the catalyst activity relative to the electron transfer productivity and stability from electrode to catalyst. In photocatalytic CO_2RR systems, efficiency is in turn affected by photosensitization, which can be achieved by the catalyst itself if it has productive light absorption, or by a separate photosensitizer with a matched excited state energy (analogous to overpotential).[17] Additionally, sacrificial electron donors are needed to regenerate the active photosensitizer. Performance metrics such as the turnover number (TON) and the quantum yield (QY) for product formation quantify the photocatalyst activity in terms of stability and productive photon absorption (analogous to FE). Along these lines, achieving the delicate balance between low overpotentials, high turnover frequencies (TOF), FE,QY, and the suppression of the HER in the presence of aqueous media is essential for effective catalyst performance.

Against this backdrop, the development of homogeneous catalysts offers a valuable starting point towards fundamental understanding of CO_2 activation and reduction mechanisms, where molecular complexes bearing precise chemical structures can be tuned via metal substitutions, ligand variations, and secondary coordination sphere modifications.[9, 16, 18-26] In contrast, heterogeneous materials present greater challenges in defining active sites and reaction intermediates, but are often more water compatible and achieve higher activities and longer life cycles compared to homogenous congeners.[12, 13, 27-33] As such, bridging the interface between molecularly precise homogeneous catalysts and polymorphous yet robust heterogeneous material catalysts, in an area termed molecular materials, offers the possibility to draw from the best attributes of both worlds.[24, 26, 34-37] Indeed, molecular materials designed to mirror aspects of both homogeneous and heterogeneous catalysts can produce highly stable, crystalline systems with molecular modularity.

In this context, a unifying feature of an important class of molecular materials, which span covalent organic frameworks (COFs), metal-organic frameworks (MOFs), and porous molecular cages, is the construction of porosity from precise geometric connection of molecular building blocks (Figure 1.1). In terms of biology-to-chemistry concept transfer for designing CO_2RR catalysts, porous molecular materials can serve as functional synthetic models for biological enzyme-substrate dynamics by providing a confined space microenvironment to target increased CO_2 substrate diffusion and activation for efficient conversion into value-added chemical products.[14] In this mini-review, we highlight major classes of porous molecular materials structures for electrochemical and/or photochemical CO_2RR, including MOFs, COFs, porous molecular cages, and hybrid molecular materials. Rather than provide a comprehensive compilation of structures, we focus on select examples to showcase key design elements to achieving stable and active CO_2RR catalysis, including **mass transport, charge transfer, light absorption, activating groups, and electrode construction** (Figure 1.1).

2. Key Design Features to Achieving Effective CO_2 Reduction Catalyzed by Porous Molecular Materials

Effective catalysts for CO_2RR using porous molecular materials must meet several criteria, including high selectivity for reduction of the CO_2 substrate over competing proton substrate to avoid the off-target hydrogen evolution reaction (HER), particularly in water, as well as suitable turnover frequencies to match electron and/or solar flux of the sustainable energy input and long-term stability. Porous structures provide a host of key design features that can be used to augment CO_2RR reactivity. First and foremost is **mass transport**, as porous structures enable higher surface areas for diffusion and capture of substrate and/or release of products relative to non-porous analogs. Porosity also benefits **charge transfer**, particularly in electrochemical CO_2RR platforms where site isolation can increase the percentage of electrochemically active sites available for catalysis by alleviating steric blocking between electrode materials and molecular redox units and between molecular units themselves, as well as extending charge transfer beyond the molecule into an extended materials structure in two or three dimensions. **Light absorption** is another element that can be improved by porosity, particularly in two main ways. The first benefit is in site isolation of chromophores, enabling the properties of molecular light-harvesting entities to be translated more directly into materials frameworks. Second, porosity also enables precise placements of donor-acceptor pairs in defined electron-transfer pathways, without direct contact between these components. The confined space environments also provide a modular approach for introduction of **activating groups** to increase CO_2 capture and orient substrate binding and activation, stabilize CO_2RR intermediates, and/or release value-added products through careful tuning of the secondary coordination sphere. Finally, in terms of electrochemical or photoelectrochemical CO_2RR, porosity can enhance **electrode construction**, where higher surface areas give more sites in the same three-dimensional volume. We now provide a select set of examples of porous molecular materials, grouped by type, that showcase these design features to augment electrochemical and/or photochemical CO_2RR chemistry. As such, a wide range of other design concepts and strategies to constructing selective and efficient CO_2RR catalysts have been reviewed previously and should be explored for a more extensive understanding of this field.[35, 37-45].

3. Covalent Organic Frameworks (COFs)

Reticular chemistry transforms discrete molecular building blocks into extended material scaffolds by linking them in deliberate spatial orientations that result in predictable periodic structures;[46-49] such reticular materials can retain permanent porosity with molecular-level control of structure. Covalent organic frameworks (COFs) represent one important family of reticular crystalline solids whose molecular units are composed of functional organic ligands.[34, 46, 50] Such molecular materials have been developed for applications spanning gas storage and separation, optoelectronics, drug delivery and catalysis.[34, 51-56] The COF examples for CO_2RR highlighted in this section outline how the principles of homogeneous molecular catalyst design, such as electronic conjugation, inner and outer-sphere activating groups, merge with porosity and electrode construction in an attempt to create robust CO_2RR materials with tunable reactivity.

3.1. Porphyrin-based COFs

Privileged molecular scaffolds such as porphyrin and phthalocyanine metal complexes have been studied extensively for electrochemical and photochemical catalytic CO_2 reduction.[17, 19, 23, 57-71] An atomic level understanding of how these catalysts operate makes them ideal candidates for incorporation into COF structures,[56, 72] thus permitting the exploration of molecular properties extrinsic to the CO_2 binding and activation site.

Our laboratory, in collaboration with Yaghi group, reported the first examples of electrochemical CO_2RR in porous structures using COF catalysts as a prototype reticular molecular material.[73] We selected metalloporphyrins as functional COF building units and constructed COF-366-M and COF-367-M (M= Co, Cu) catalysts from the condensation of amine functionalized metalloporphyrin nodes with aldehyde-functionalized phenyl linker struts (Figure 1.2a). The sizes of the porous cavities were predictably modified by using either mono or biphenyl linkers between the cobalt porphyrin catalytic units, resulting in a 3 Å difference between COF-366-Co and COF-367-Co. With its larger pore size, COF-367-Co achieved a 2-fold and 5-fold enhancement in catalytic efficiency for conversion of CO_2 to CO relative to its COF-366-Co and Co-TAP monomer counterparts, respectively (Figure 1.2b), which was attributed to higher *s* and an increase in accessible electrochemically active centers from 4 to 8%. Faradaic efficiencies (FEs) for selective CO production reached 91%, even in neutral pH aqueous solvent. Beyond these molecular-level modifications, complementary materials modifications could synergistically improve the performance of these COF platforms as CO_2RR catalysts. In one key advance, the relatively low percentage of observed electroactive centers in first-generation COF CO_2RR catalysts inspired the **electrode construction** that could achieve better electrical contact with the catalytic COF material. For example, moving from deposition of the COF powder to growing oriented thin films of the COF directly onto the electrode surface resulted in improved current density for CO_2-to-CO conversion from 5 to 45 mA/mg and turnover frequencies (TOFs) rising from 98 to 665 h^{-1} for COF-366-Co, with total turnover numbers (TONs) reaching 3,542. The same electrode construction was utilized in a follow-up study, where electron withdrawing groups incorporated at the phenyl linkers established reticular tuning as a design principle for improving CO_2 reduction activity.[74] Indeed, substituting the phenyl linkers in a COF-366-Co platform with the **activating groups** –$(OMe)_2$, –F, and –$(F)_4$ resulted in molecularly precise tuning of reduction potentials and current densities in the functional heterogeneous material (Figure 1.2a, c).

3.2. Enhancing Charge Transfer in Porphyrin-Based COF CO_2RR Catalysts

Porphyrin molecules are intrinsically highly conjugated compounds. When integrated into a COF structure, this molecular conjugation can extend in multiple dimensions, giving rise to unique electron transfer properties in the resulting materials that can be exploited for electrocatalysis. For example, the use of tetrathiafulvalene (TTF) as a linker in metalloporphyrin-based COFs establishes a catalyst framework with high **charge transfer** mobility. This approach offers a design strategy to improve traditional COF electrodes, which often possess limited conductivity. Indeed, Lan and co-workers reported that in Co-TTCOF, the TTF linkers enable rapid charge transfer from the electrode to catalytic Co centers,[75] and Co-TTCOF converts CO_2 into CO with a FE of 91.3% at −0.7 V vs RHE at a rate of 1.28 s^{-1}. Moreover, exfoliation of this COF leads to the formation of Co-TTCOF nanosheets (~5 nm in thickness) with an improved FE of 99.7% at −0.8 V, which is attributed to its higher surface area and more accessible active sites from this new **electrode construction.** Exfoliation was also applied as a method to enhance CO_2-to-CH_4 activity in another porphyrin-based COF electrocatalyst.[76]

3.3. Increasing Accessible Active Sites by Expanding COFs from 2D to 3D Materials

The COF-366-Co and Co-TTCOF examples showcase the importance of **electrode construction** in optimizing active site utilization in 2D COF structures for CO_2RR. A complementary approach is to change the materials dimension of the catalyst itself. In this context, although more difficult to design and synthesize compared to their 2D counterparts, 3D COFs offer an attractive family of alternative platform materials for creating frameworks with intrinsic porosity that can achieve larger surface areas and pore diameters for improved CO_2 uptake via **mass transport**.[77, 78] In one example of CO_2RR using a 3D COF, 3D-Por(Co/H)-COF,[78] demonstrated a FE of 92% for CO production, compared to 82% for COF-366-Co under similar conditions, where both electrodes were constructed from deposition of a COF catalyst ink onto a carbon electrode. The observed improvement in FE for CO_2RR was attributed to a higher number of exposed active sites in the 3D porous COF relative to its 2D congener. In a recent study, Fang and coworkers reported the 3D photocatalyst series, JUC-640-M (M= H, Ni, Co).[79] This unique stp-topologized COF combined triptycene and porphyrin building units resulting in a low-density, ultra-porous structure achieving efficient **mass transport**. This was reflected in the Co derivative, JUC-640-Co, which showed unprecedented CO_2-to-CO production rates of 15 mmol $g^{-1}h^{-1}$ in conjunction with $[Ru(bpy)_3]^{2+}$ as a photosensitizer and BIH as a sacrificial electron donor.

3.4. Secondary Coordination Sphere Modifications of COF Structures to Improve CO_2RR Performance

In addition to augmenting charge transfer and dimensionality of molecular materials, secondary coordination sphere approaches can be employed to improve catalytic performance of COF systems for CO_2RR. For example, the use of pendant amines as **activating groups** that can form adducts with CO_2 can improve substrate capture for subsequent substrate conversion. Indeed, amines are commonly used as additives in CO_2 capture and conversion, forming carbamate structures.[80-85] Not only can amines within a COF structure help capture CO_2, but they can also impart high stability for such adducts under harsh catalytic conditions. Specifically, post-synthetic solid-state reduction of a 3D COF (COF-300) or 2D COF (COF-366-M) bearing imine linkages can form the amine-linked analogs COF-300-AR and COF-366-M-AR, respectively.[86] These frameworks persist even after immersion in 6 M HCl and NaOH aqueous solutions for over 12 hours. Further, the addition of COF-300-AR material showed improved FE for CO_2 reduction to CO over a bare Ag electrode (43 vs 83% at –0.85 V vs RHE) under similar conditions. Enhancement in CO_2 uptake and subsequent improvement in reactivity was observed *in situ* in other COF systems, which may be attributed to the reduction of imine linkages by H_2 generated at the start of the photolysis.[87] Finally, the introduction of charged functionalities as **activating groups** has also proven successful in enhancing CO_2RR activity in COF structures. In a recent example, Co-iBFBim-COF-X (X=F^-, Cl^-, Br^-, and I^-),[88] incorporates charged imidazolium groups with variable anions to enhance the stabilization of CO_2 reduction intermediates through hydrogen bonding (Figure 1.2d). Compared to a neutral analog, Co-iBFBim-COF-I^- displayed 3.5-fold increase in turnover frequency for the production of CO.

3.5. Phthalocyanine based COFs

Cobalt phthalocyanine (CoPc) is another privileged molecular catalyst complex amenable to incorporation into COFs for CO_2RR.[89-91] Similar to porphyrin analogs, CoPc-based COFs target improved **charge transfer** from electrodes via conjugation of the linkers with its structure. In one example, connecting CoPC in both x and y directions with phenazine linkages creates a highly conjugated 2D COF with tetragonal topology (Figure 1.2e).[89] The metal phthalocyanine units have pore channels created by 2.2 nm distance between CoPc units. High chemical stability of CoPc-PDQ-COF was recorded under various organic solvents as well as highly acidic/basic aqueous electrolytes between 25 to 100 ºC. Additionally, CoPc-PDQ-COF was stable over a wide range of applied potentials (−0.32 to −0.66 V). In comparison to the CoPc molecular analog, the PDQ-COF material displayed a 32-fold higher TOF at a 560 mV overpotential. More recently, CoPc-derived COFs were used to compare catalytic activities of 2D versus 3D frameworks. A 3D CoPc polyimide COF with tetraaminophenyl adamantine linkers (Figure 1.2f), CoPc-PI-COF-3,[91] possesses 33% electroactive sites compared to only 5% for its 2D analog.[90] This improvement in electroactive sites and **mass transport** resulted in a 1.5-fold higher current density for CO_2-to-CO conversion (Figure 1.2g).

3.6. COFs Bearing Metal-Bipyridine Catalytic Units

In addition to porphyrin-based and phthalocyanine-based COFs, another type of privileged catalytic unit for COF-mediated CO_2RR is based on metal-bipyridine complexes, where active sites are incorporated onto a bipyridine-based ligand strut. In this regard, rhenium tricarbonyl complexes of the type [Re(bpy)$(CO)_3$Cl] are canonical examples of molecular CO_2RR catalysts. Interestingly, these molecular complexes are known to suffer from catalyst degradation pathways involving dimerization of individual Re units to form inactive dimers.[92, 93] Indeed, efforts to address this deactivation pathway in homogeneous solution include the introduction of large alkyl groups proximal to the metal center to sterically encumber the open coordination site under catalytic conditions to prevent the deactivation pathway.[94-96] A complementary materials approach to prevent this type of deactivation is to immobilize [Re(bpy)$(CO)_3$Cl] within a COF structure for site isolation. Despite the reasonable nature of this approach, [Re(bpy)$(CO)_3$Cl] COFs reported to date show only low electrocatalytic[97] and photocatalytic[98, 99] performance for CO_2RR. In one example, a conjugated triazine COF containing $[Re(bpy)(CO)_3Cl]$ active sites (denoted Re-COF) was designed for self-sensitized CO_2RR using visible light irradiation in organic solvent, showing how **light absorption** can be optimized .[98] After a 20-hour reaction period, Re-COF exhibits a total turnover number (TON) of only 48, and a TOF of 750 μmol g^{-1} h^{-1} . Under similar reaction conditions, Re-bpy-sp^2c-COF,[99] composed of olefin linked pyrene and bipyridine units (Figure 2h), gave a TOF of 1040 μmol g^{-1} h^{-1} (TON = 18). In these studies, the $[Re(bpy)(CO)_3Cl]$-incorporated COFs have a longer duration of catalytic activity compared to the molecular analog but only marginally higher TONs. These results suggest that Re catalyst immobilization within a COF matrix may slow or prevent unwanted dimerization deactivation pathways, but also hinders catalytic reactivity. Similar trends are observed in MOF analogs.[100, 101] Examples of Ni, Mn, and Rh as CO_2RR active sites on bpy-linked COFs have also been reported and warrant further investigation.[102-104]

4. Metal-Organic Frameworks

Metal-organic frameworks (MOFs) are another class of extended crystalline solids that incorporate modular organic linkers, but in contrast utilize metal ions or clusters as secondary building units.[105-113] The similarity between these reticular materials and COFs leads to analogous MOF designs for CO_2RR applications, where the area is largely dominated by structures based on the heterogenization of porphyrin and phthalocyanine catalytic units.[72, 100, 111, 114-124]

4.1. Porphyrin-based MOFs

One of the first examples of photocatalytic CO_2 reduction using a porphyrin-based MOF was reported by Jiang et al, termed PCN-222.[125] The MOF formulated as $Zr_6(\mu_3\text{-}OH)_8(OH)_8(TCPP)_2$ contains metal-free porphyrin linkers and Zr_6 cluster nodes. It was observed that incorporating TCPP into a MOF structure resulted in broad visible light absorption with higher molar absorptivity compared to H_2TCPP. Indeed, this allowed self-sensitized photochemical CO_2RR selective for formate, resulting in 30 μL of product after 10 h of irradiation. Transient absorption studies suggest that long-lived **charge transfer** states in PCN-222 prevented fast electron-hole recombination, boosting CO_2RR activity. An early example of MOFs applied to electrochemical CO_2RR was reported by Yang, Yaghi, and our laboratory. $[Al_2(OH)_2TCPP\text{-}Co]$,[114] incorporating cobalt porphyrin molecular units linked with aluminum oxide rods in a 3D MOF structure, was fabricated into thin films of varying thickness as an integrated electrode material. MOF thickness values between 30 and 70 nm resulted in optimal conditions for CO_2-to-CO conversion with a maximum TOF of 200 h^{-1} and a stable current density over 7 h. The emphasis in examining **electrode construction** is presented as a balance between reactant diffusion and charge transport and was executed with the use of atomic layer deposition. This concept was expanded upon by the Wang laboratory using MOFs constructed from $Cu_2(COO)_4$ paddle wheels linked by Cu porphyrins (Figure 1.3a) .[123] The 2D MOF was utilized as either a monolayer or a bilayer of 0.28 and 0.7 nm thickness, respectively, and demonstrated distinct product selectivity under photocoupled electrocatalysis of CO_2 reduction. Interestingly, the monolayer version favored the formation of C-C coupled products, while the bilayer generates only C-1 products (CO, CH_4, and formate). However, upon electrolysis, the authors found that within the monolayer, more active sites are accessible to the electrode, and the generation of Cu clusters is observed. Catalyst restructuring occurs at the Cu-O sites, irreversibly changing them to Cu-Cu sites that can subsequently form multi-carbon products from CO_2. Furthermore, the Faradaic efficiency (FE) of

C-C product formation from the monolayer showed light dependence (Figure 1.3b, c), where neither structural instability nor enhancement by irradiation is observed in the bilayer.

Returning to the discussion of **charge transfer** as a design concept for efficient CO_2RR catalysis, the use of metal clusters in MOFs is advantageous. Reductive polyoxometalates such as Z-e-Keggin cluster, $\varepsilon\text{-}PMo_8^{V}Mo_4^{VI}O_{40}Zn_4$, are electron rich aggregates that can facilitate electron transfer from the electrode to a porphyrin active site (Figure 1.3d). Lan and colleagues reported that the cobalt porphyrin-linked polyoxometalate MOF, Co-PMOF, shows excellent catalytic performance, with 99% FE for CO_2 to CO and a TOF of 1656 h^{-1}.[118] The design of this CO_2RR catalyst system mirrors that of Co-TTCOF, further supporting the idea that efficient, directional **charge transfer** can be designed into molecular materials.

4.2. Zinc Imidazolate Frameworks

In related family of molecular materials, Zinc Imidazolate Frameworks (ZIFs) can enable CO_2 reduction in MOF-type materials without the need to immobilize known molecular CO_2RR catalysts. [120, 126-129] ZIFs are class of MOFs based on zeolite topologies, and contain Zn clusters and imidazolate ligands as building units of the framework. Specifically, the ZIF-8 congener (Figure 3e) possesses high CO_2 adsorption properties, and the tuning of peripheral components, such as electrolyte anions and ligand doping, has been studied in the context of CO_2RR. Indeed, work by Kang and colleagues on ZIF-8 generated from Zn(II) sources containing different anions (SO_4^{2-}, NO_3^{-}, and acetate) showed that the SO_4^{2-} derived MOF showed the highest current density for CO formation (Figure 1.3f), with 66% FE and catalytic stability for at least 4 hours.[129] Additionally, varying the electrolyte anions between Cl^{-}, ClO_4^{-}, and HCO_3^{-} showed that use of a NaCl electrolyte achieved the highest FE for CO production, credited to more facile anion exchange within the MOF cavity. Another approach taken by Wang and co-workers towards enhancing ZIF-8 CO_2RR reactivity was ligand doping with 1,10-phenanthroline.[120] An increase in the FE and current density (Figure 1.3g) for CO production from 50 to 75% was observed with phenanthroline doping, which appears to be a function of charge transfer boosting into the imidazolate sp^2 carbons responsible for the generation of the CO_2 reduction intermediate, *COOH. We note that the studies highlighted here do not resolve the open question of whether the Zn nodes or the imidazole ligands within these catalytic ZIF cavities are the major active sites for electrochemical CO_2 reduction.

5. Porous Molecular Cages and Related Hybrid Molecular-Materials Cages

Taking extended heterogeneous molecular materials a step closer towards homogeneous molecules, porous molecular cages provide a distinct class of crystalline, microporous materials that resemble discrete analogs of MOFs and COFs. Unlike extended frameworks, porous molecular cages offer intrinsic permanent porosity in homogeneous molecular form, in which each discrete supramolecular unit can be utilized for photo- and electrocatalysis across a variety of formulations. Included are heterogeneous electrodes, particle suspensions of varying sizes, and homogeneous molecules in solution.

5.1. Porous Organic Cages

Porphyrin boxes (PB) are a prominent class of porous organic cages[130-134] assembled from six porphyrin face units connected by eight triamine linkers, creating a hollow box-like structure with a defined permanent inner cavity per discrete molecular unit.[135-140] Work from our laboratory in collaboration with Kim's group has established the use of Fe- and Co-metalated PBs for electrochemical and photochemical activation of various small molecule substrates, including oxygen,[141] nitrate,[142] and water.[143] Together we reported the first application of porous organic cages for CO_2RR activity. Specifically, the porous cage Fe-PB was formulated as a water-compatible heterogeneous electrode catalyst for direct comparison with the mononuclear analog, Fe-TPP.[26, 144] In particular, we reasoned that creating a heterogeneous electrode material with Fe-TPP would result in stacking of flat 2D porphyrin molecules parallel to the electrode, thus limiting substrate accessibility and charge transport (Figure 1.4a). In contrast, owing to their permanent porosity, the porphyrin boxes would exhibit higher CO_2 substrate accessibility and **charge transport** from the electrode relative to the porphyrin monomer. Indeed, the permanent porosity and increased surface area of the 3D porphyrin box supramolecule relative to the 2D porphyrin molecule enhanced the percentage of accessible electroactive Fe centers for the former (54% in Fe-PB, 38% in Fe-TPP). Under electrochemical CO_2RR conditions in neutral pH aqueous media, Fe-PB generated 2-fold more CO product than Fe-TPP, reaching 100% FE and achieving TOF values of 0.64 s^{-1} while maintaining electrochemical activity for at least 24 hours.

Building upon these results, we were successful in attempts to solubilize Fe-PB-like structures for homogeneous CO_2RR catalysis by the incorporation of 24 cationic trimethylammonium groups to furnish Fe-PB-2(P); we then evaluated this porous cage under photocatalytic CO_2RR conditions (Figure 1.4b).[145] The highly cationic, soluble porphyrin box platform, featuring dual second-sphere additions of porosity and charge as **activating groups**, led to synergistic improvements in selective and efficient CO_2-to-CO conversion in homogeneous solution. Fe-PB-2(P) exhibited a maximum TON of 1,168 for CO production with 97% selectivity within a one-hour photolysis experiment using $Ir(ppy)_3$ as a photosensitizer. The direct comparison of Fe-PB-2(P), featuring both porosity and charge, to the porosity-only porphyrin box Fe-PB-3(N), the charged-only mononuclear porphyrin Fe-*p*-TMA, and the parent Fe-TPP analog showed that Fe-PB-2(P) exhibited a 41-fold higher activity over Fe-TPP (Figure 1.4c) with a maximum TON of ca. 500, with the neutral porous FePB-3(N) and charged mononuclear Fe-*p*-TMA catalysts displaying similar levels of activity under these conditions, with 4-fold (TON = 50) and 6-fold (TON= 70) higher CO_2RR activities compared to Fe-TPP, respectively. Taken together, these results established that integrating dual porosity and electrostatic interactions as **activating groups** onto a single platform can work in tandem to enhance photocatalytic CO_2RR activity in synergistic manner beyond introduction of a single porosity or electrostatic design element alone. Finally, the Fe-PB-2(P) catalyst also enabled photochemical CO_2RR activity under low CO_2 concentrations. Indeed, in the presence of as little as 2% CO_2 in acetonitrile solution, Fe-PB-2(P) retained up to 78% of its original activity compared to CO_2-saturated conditions, suggesting that the porous organic cage platforms can promote both carbon capture and conversion.

5.2. Metal-Organic Cages/Metal-Organic Polyhedra

Metal-organic cages (MOC), otherwise known as metal-organic polyhedra (MOP), are reticular structures featuring connections between organic linkers and inorganic joints, and can be thought of as discrete molecular analogs of MOFs.[111, 146-156] Like porous organic cages, MOCs/MOPs feature intrinsic permanent porosity and can be used to make heterogeneous analogs of molecular catalysts.[157-159] For example, efficient CO_2RR catalysis from heterogenized Re-bpy catalysts can be achieved under photocatalytic conditions. Choi and colleagues designed a MOP structure using the Zr cluster ($[Cp_3Zr_3O(OH)_3(CO_2)_3]^+$) linked with biphenyldicarboxylate

(BPDC) struts; one BPDC unit was substituted with a carboxylate functionalized version of $[Re(CO)_3(bpy)(Cl)]$, forming 1.8 nm particles of ReTC-MOP.[157] The self-sensitized photocatalyst ReTC-MOP with molecular-like **light absorption** properties displayed a TON of 12,847 for CO production over a 24-hour photolysis experiment in acetonitrile solution. The observed high activity far surpassed the molecular analog, as well as nano (400 nm) and micro-scaled (400 μm) ReTC MOF particles constructed for comparison to ReTC-MOP. The authors speculated that the reaction microenvironment of MOP particles dispersed in solution could permit better access of CO_2 to the active site. Further dilution of MOP/MOC particles to single cages by Su and colleagues was shown to increase utilization efficiency in Ir^{III}-MOC-NH_2.[158] The MOC in this case comprises four $Cp_3Zr_3\mu_3$-$O(\mu_2$-$OH)_3$ nodes linked by an Ir(III) polypyridyl complex and amino-functionalized BPDC (Figure 1.5a). Photocatalytic assays showed a 3.4-fold improvement in TOF for a single-cage MOC unit versus bulk Ir^{III}-MOC-NH_2 (Figure 1.5b). DFT analysis of possible mechanistic pathways suggested that the free amines in the cage can enhance CO_2 reduction by acting as **activating groups** for increased CO_2 capture, akin to what was proposed for COF-300-AR.[86]

5.3. Molecular-Materials Cages

A final series of porous molecular materials to highlight for CO_2 reduction chemistry are hybrid combinations of discrete molecules or cages with materials surfaces. Such systems are comprised of molecules that can directly interact with a CO_2RR-active electrode to provide systems that exhibit permanent porosity and electrochemical activity, improving both **mass transport** and **charge transfer**.[26, 133, 160, 161] In one study, our laboratory developed hybrid molecular-materials porphyrin molecular cages that were formed between α,α,α,α-atropisomers of thioacetate-functionalized porphyrins and a metal foil electrode. The thiols on the legs of the table-shaped porphyrin molecule bind the electrode surface, fixing the porphyrins parallel to the electrode surface at synthetically modular distances (Figure 1.6a).[160] Using copper foil electrodes, we evaluated the reduction of CO to value-added two-carbon products formed from C-C coupling (e.g., ethylene, ethanol, acetate) using these hybrid materials. Both bare copper and porphyrin-functionalized hybrids produced ethylene, ethanol, and acetate upon electrochemical CO reduction, but the addition of porosity created by the supramolecular porphyrin cage structures led to a marked increase in FE for the latter two C-C oxygenated products. Molecular optimization of linker length (1-4 carbon chains) showed that the C2 linker produced optimal Faradaic efficiencies to maximize two-carbon product formation (Figure 1.6b). We then used the C2-spaced porphyrin cap to probe multimetallic catalysis by inserting Fe, Ni, or Zn into the center of the porphyrin cap. Insertion of Fe as a secondary **activating group** resulted in an increased ethanol selectivity, reaching 52% FE (Figure 1.6c). Various control experiments using porphyrin isomers without the proper electrode capping configuration, or porphyrins without the coordinating thiol caps, were evaluated to corroborate the importance of porous cage formation for the observed results. In related work by Reisner, Scherman, and Han, among others, porous organic cages and cucurbit[n]urils have been used as additives to enhance CO_2 diffusion at the surfaces of Cu and Au electrodes, respectively. Interestingly, only the CC3[133] porous organic cage resulted in more efficient CO_2RR catalysis, whereas cucurbit[6]uril[161] caused a decrease in current density.

6. Summary and Perspectives

Molecular materials are emerging as valuable class of CO_2 reduction catalysts that can be driven by sustainable electrical or solar input. Indeed, these systems merge two of the most important aspects in the development of functional catalysts: modularity and durability. In particular, the development of functional molecular materials catalysts that exhibit permanent porosity, including COFs, MOFs, and porous molecular cages, have led to advances in design principles that exploit both the molecular precision afforded in homogeneous systems and the durability of heterogenous counterparts. In the context of CO_2RR, a key property in the molecular materials space is porosity, which can enhance the diffusion and/or capture of CO_2 substrate and funnel it towards the active site of the catalyst. Furthermore, examples highlighted in this mini-review leverage the molecular modularity of these porous materials systems via implementation of directional charge transfer, second-sphere cationic interactions, CO_2 capture and activating groups, pore size manipulation, and dimensionality.

Against this backdrop, many exciting opportunities merit further investigation to achieve significant advances in molecular materials for CO_2RR chemistry and related small-molecule transformations of energy consequence. First and foremost is the development of systems that can go beyond two-electron reduction, as the vast majority of molecular materials for catalytic CO_2RR are limited to producing CO, akin to their pure molecular counterparts. Indeed, the immobilization of a relatively small subset of well-established molecular catalysts as active sites in these materials has been studied extensively, therefore future efforts in the field should seek to heterogenize the rapidly emerging body of new state-of-the-art molecular catalysts into porous structures. Another common challenge arising in these molecularly-designed materials is how to optimize the construction of electrodes in order to increase conductivity of the material and electroactivity of catalytic sites. Additionally, as has been repeatedly observed in porous molecular cages, devoting more attention to contributions of the secondary coordination sphere and leveraging these confined space microenvironments is an important new development in enhancing CO_2RR reactivity. In this context, inspiration from recently generated molecular coordination complexes that append hydrogen bonding and/or electrostatic moieties that aid CO_2 reduction offers a molecular-to-materials roadmap for developing next-generation catalysts for combined carbon capture and fixation. These and other avenues of basic and translation energy research will bring us closer to the larger goal of decarbonizing our global energy infrastructure, of which CO_2RR catalysis is but one part of the puzzle.

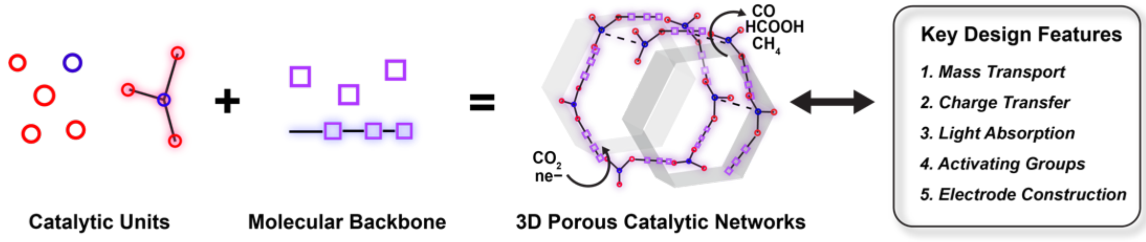

Figure 1.1. Conceptual design schematic of porous molecular materials catalysts for the carbon dioxide reduction reaction (CO_2RR), comprised of discrete molecular units combining to form functional porous materials with higher-order dimensions.

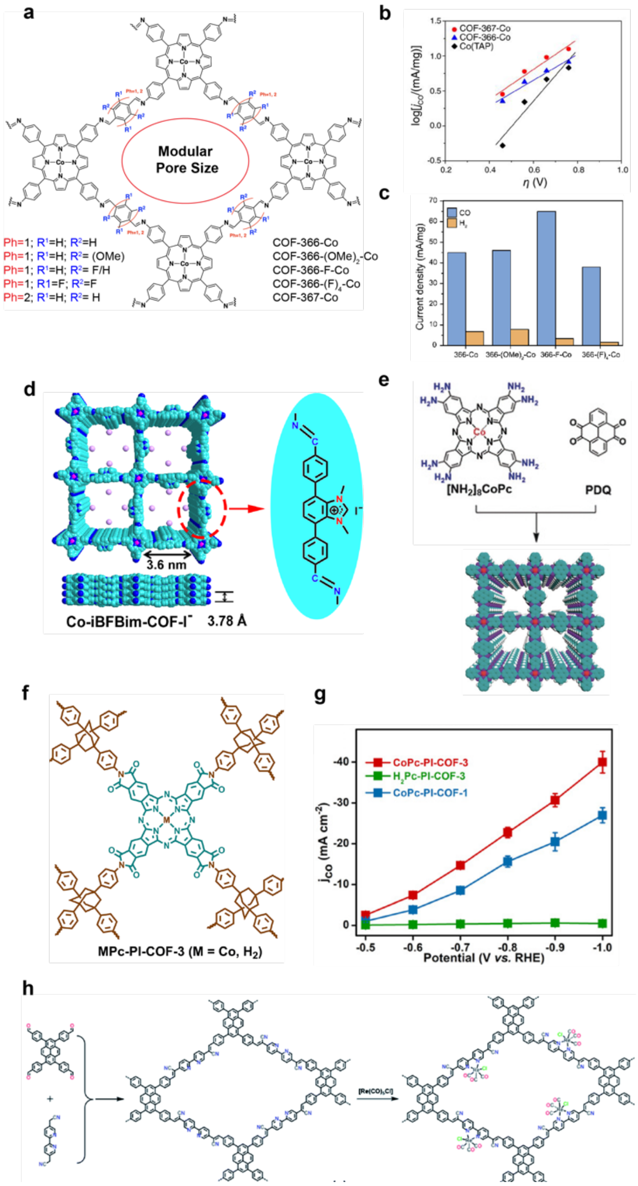

Figure 1.2. Representative covalent organic framework (COFs) catalysts for carbon dioxide reduction reaction (CO_2RR). (a) Chemical structures of Co complexes of COF-366, COF-367, and synthetically tuned analogs. (b) Tafel plots comparing electrochemical CO_2RR activity of COF-366-Co, COF-367-Co, and a molecular analog Co(TAP). (c) Current density comparison for COF-366-Co with reticular tuning of struts with –H, –(OMe)$_2$, –F, and –(F)$_4$ substituents. (d) Crystal structure representation of Co-iBFBim-COF-I^-. (e) Structure of phenazine-linked phthalocyanine COF, CoPc-PDQ-COF. (f) Chemical structure of CoPc-PI-COF-3 and (f) current density plot comparing the 2D, 3D, and Co-free analogs of CoPc-PI-COF. Adapted with permission from (a, c) ref 17, © American Chemical Society 2018; (b) ref 16, © 2015 American Association for the Advancement of Science; (d) ref 25, © 2022 Wiley-VCH; (e) ref 26a, ©Wiley-VCH; (f, g) ref 26 c, © 2022 Wiley-VCH; (h) ref 30b, © 2020 Royal Society of Chemistry.

Table 1.1. Catalytic CO$_2$RR Activity of Selected COF Catalysts

Catalyst	Product (Selectivity %)	TON	TOF	Energy Input*	FE (%)	QY (%)	Current Density
COF-366-Co	CO	1,352	98 h^{-1}	η= 550 mV	90	–	5 mAmg^{-1}
COF-366-Co oriented thin film	CO	3,542	665 h^{-1}	η= 550 mV	86	–	45 mAmg^{-1}
COF-367-Co	CO	3,901	165 h^{-1}	η= 550 mV	91	–	13 mAmg^{-1}
Co-TTCOF	CO	141,479	1.28 s^{-1}	η= 790 mV	91.3	–	1.84 mAcm^{-2}
Co-TTCOF NSs	CO	–	–	–0.8 V vs RHE	99.7	–	–
3D-Por(Co/H)-COF	CO	–	4610 h^{-1}	–1.1 V vs RHE	92.4	–	15.5 mAcm^{-2}
JUC-640-Co	CO	–	15.1 mmol g^{-1}h^{-1}	Ru(bpy)$_3$Cl$_2$·6H$_2$O at 450 nm	94.4	1.48	–
COF-300-AR	CO	–	–	–0.85 V vs RHE	83	–	2 mAcm^{-2}
Co-iBFBim-COF-I$^-$	CO (100)	–	3018 h^{-1}	2.4 V full cell voltage	99	–	52 mAcm^{-2}
CoPc-PDQ-COF	CO (96)	320,000	11412 h^{-1}	η= 560 mV	96	–	762 mAmg^{-1}
CoPc-PI-COF-3	CO	35,500	0.6 s^{-1}	–1.0 V vs RHE	96	–	31.7 mAcm^{-2}
Re-COF	CO (98)	48	750 μmol g^{-1}h^{-1}	Self-sensitized >420 nm	–	–	–
Re-bpy-sp^{2}c-COF	CO (81)	18.7	1040 μmol g^{-1}h^{-1}	Self-sensitized >420 nm	–	0.5	–

*Overpotential (η), applied potential (V vs RHE), or photosensitizer/irradiation wavelength provided

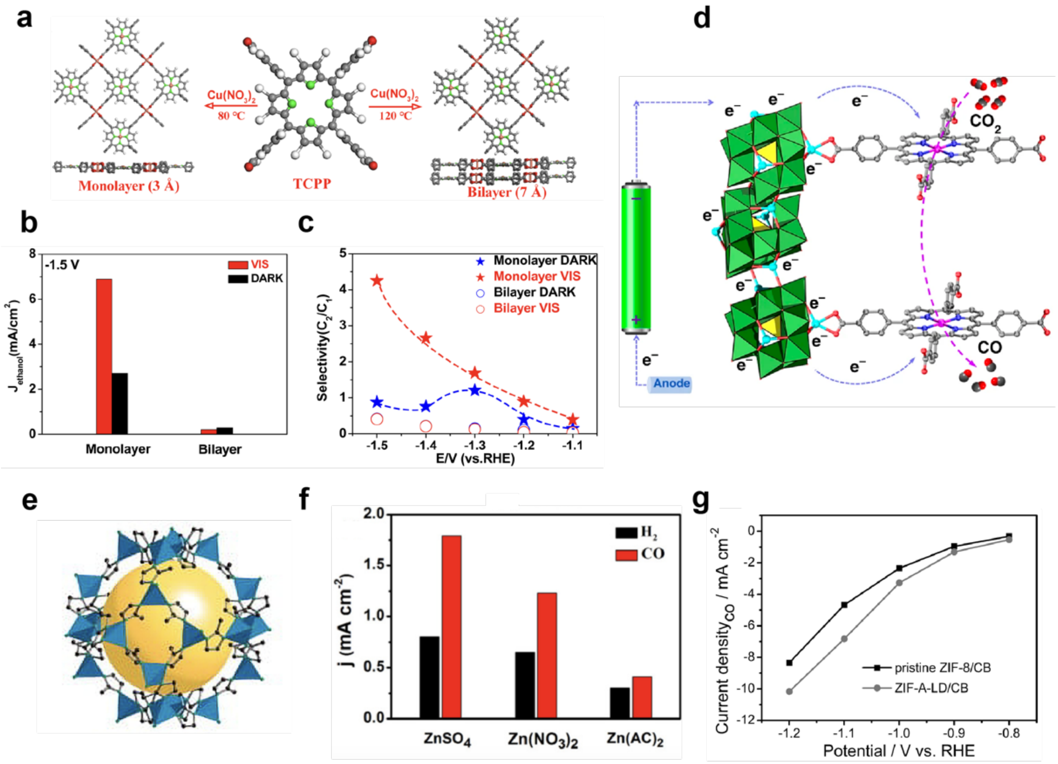

Figure 1.3. Representative metal organic framework catalysts for CO$_2$RR. (a) Monolayer and bilayer representations of Cu-porphyrin MOFs with data comparing (b) light dependent ethanol production and (c) light dependent C2/C1 selectivity ratios between the two catalyst compositions. (d) Depiction of electron transmission from an electrode through Co-PMOF. (e) Crystal structure representation of the first reported ZIF-8 and current density plots for electrochemical CO$_2$RR with (f) ZIF-8 synthesized from different Zn starting material and (g) phenanthroline ligand doped (ZIF-A-LD/CB) doped versus pristine (ZIF-8/CB). Adapted with permission from (a-c) ref 34k, © 2022 Wiley-VCH; (d) ref 34e, © 2018 Springer Nature; (e) ref 36a, © 2006 National Academy of Sciences; (f) ref 36d, © 2017 Wiley-VCH (g) ref 34g, © 2019 Wiley-VCH

Table 1.2. Catalytic CO_2RR Activity of Selected MOF Catalysts

Catalyst	**Product (Selectivity %)**	**TON**	**TOF**	**Energy Input**	**FE (%)**	**QY (%)**	**Current Density**
PCN-222	$HCOO^{-}$ (100)	–	3 μmol h^{-1}	Self-sensitized >420 nm	–	–	–
$[Al_2(OH)_2TCPP$-Co]	CO	1400	200 h^{-1}	–0.7 V vs RHE	76	–	1.8 $mAcm^{-2}$
Cu monolayer	ethanol(25.9), ethene(12)	–	–	–1.4 V vs RHE >420 nm	41.1	–	6.89 $mAcm^{-2}$ (ethanol)
Cu bilayer	CO, HCOO-	–	–	–1.3 V vs RHE >420 nm	78.6	–	0.29 $mAcm^{-2}$
Co-PMOF	CO	53,433	1656 h^{-1}	–0.8 V vs RHE	98.7	–	18.08 $mAcm^{-2}$
ZIF-8 (SO_4^{2-})	CO	–	–	–1.8 V vs SCE	65.5	–	1.55 $mAcm^{-2}$
ZIF-8 (NO_3^{-})	CO	–	–	–1.8 V vs SCE	69.8	–	1.25 $mAcm^{-2}$
ZIF-8 (Acetate)	CO	–	–	–1.8 V vs SCE	57.7	–	0.5 $mAcm^{-2}$
ZIF-8 (doped)	CO	–	–	–1.1 V vs RHE	90.6	–	10 $mAcm^{-2}$

*Overpotential (η), applied potential (V vs RHE), or photosensitizer/irradiation wavelength provided

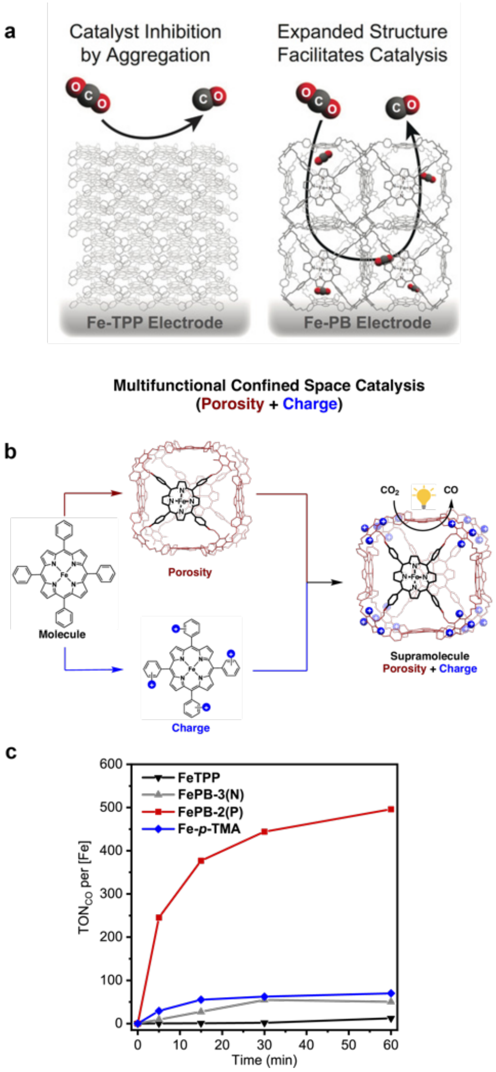

Figure 1.4. A representative porous molecular cage architecture to improve CO$_2$RR activity over monomeric molecular counterparts. (a) Proposed orientation adopted by planar Fe-TPP porphyrins compared with porous supramolecular Fe-PB on an electrode, where the 3D structure facilitates mass transport (b) Schematic representation of the planar molecular catalyst Fe-TPP transformed by porosity only (Fe-PB) or porosity and charge (Fe-PB-2(P)). (b). Photocatalytic CO$_2$RR results comparing activities of Fe-TPP, Fe-PB-3(N), Fe-PB-2(P), and Fe-p-TMA under a CO$_2$-saturated atmosphere. Adapted with permission from (a) ref 42, © 2018 Wiley-VCH; ref 43, © 2023 Wiley-VCH.

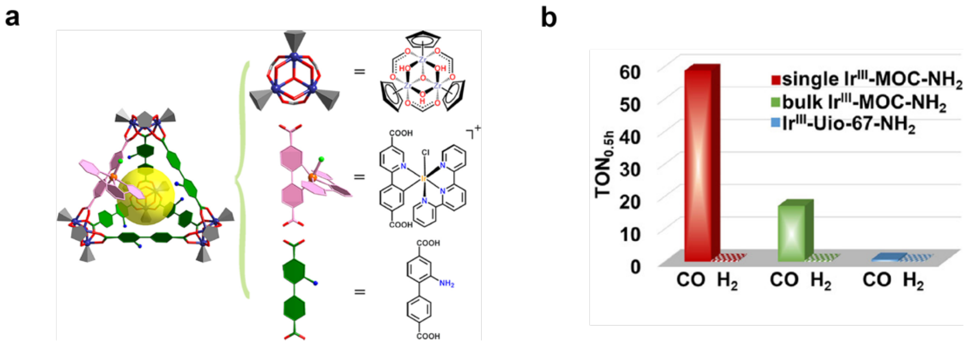

Figure 1.5. Representative Metal-Organic Cages for CO_2RR. (a) Structure representations of Ir^{III}-MOC-NH_2 and (b) photocatalytic CO_2RR data comparing the activity of single versus bulk Ir^{III}-MOC-NH_2, and a known MOF analog. Adapted with permission from ref 45b, © 2021 American Chemical Society.

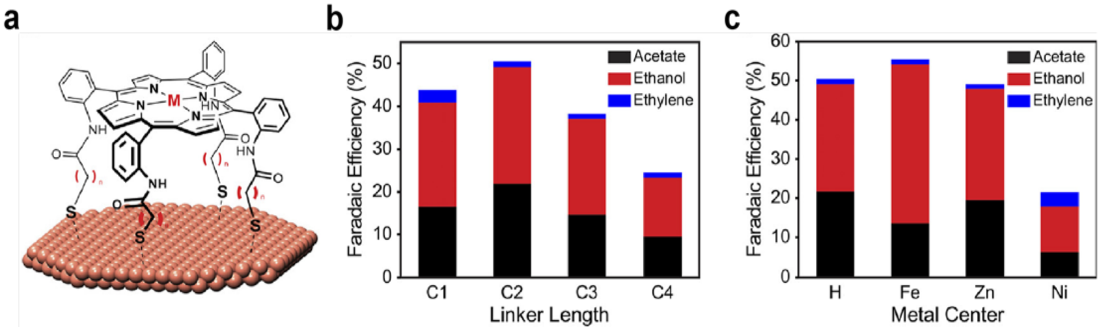

Figure 1.6. (a) Schematic of a hybrid molecular material exhibiting permanent porosity generated by supramolecular self-assembly between a table-shaped porphyrin molecule and an electroactive metal electrode surface. The Faradaic efficiency (FE) for value-added two-carbon products generated by C-C product formation from electrochemical CO reduction (e.g., ethylene, ethanol, acetate) is dependent on (b) molecular tuning of porphyrin linker length and (c) identity of porphyrin metal center. Reproduced with permission from ref 7b, © 2020 American Chemical Society.

Table 1.3. Catalytic CO$_2$RR Activity of Selected Porous Molecular Cages and Hybrid Materials

Catalyst	**Product (Selectivity %)**	**TON**	**TOF**	**Energy Input***	**FE (%)**	**QY (%)**	**Current Density**
Fe-PB	CO	55,250	0.64 s^{-1}	η =510 mV	100		0.4 mAcm^{-2}
Fe-PB-2P	CO (97)	1,168	164 min^{-1}	Ir(ppy)$_3$ at 450 nm	–	5.75	–
Fe-PB-3N	CO (88)	50	1.9 min^{-1}	Ir(ppy)$_3$ at 450 nm	–	–	–
ReTC-MOP	CO	12,847	660 h^{-1}	Self-sensitized >420 nm	–	–	–
ReTC MOF$_{\text{nano}}$	CO	654	36 h^{-1}	Self-sensitized >420 nm	–	–	–
ReTC MOF$_{\text{micro}}$	CO	438	24 h^{-1}	Self-sensitized >420 nm	–	–	–
Ir$^{\text{III}}$-MOC-NH$_2$ $_{\text{single}}$	CO (99)	59	120 h^{-1}	Self-sensitized 420 nm		6.71	
Ir$^{\text{III}}$-MOC-NH$_2$ $_{\text{bulk}}$	CO (96)	20	–	Self-sensitized 420 nm	–	–	–
Fe Cap, C2 linker	Ethanol (53)** Acetate (24)**	–	–	–0.40 V vs RHE	83	–	1.34 mAcm^{-2}

*Overpotential (η), applied potential (V vs RHE), or photosensitizer/irradiation wavelength provided

** refers to the Faradaic efficiency (FE) values

References:

(1) Chu, S.; Cui, Y.; Liu, N. The path towards sustainable energy. *Nat. Mater.* **2017**, *16* (1), 16-22.

(2) Zhao, N.; You, F. Can renewable generation, energy storage and energy efficient technologies enable carbon neutral energy transition? *Appl. Energy* **2020**, *279*, 115889.

(3) Kabeyi, M. J. B.; Olanrewaju, O. A. Sustainable Energy Transition for Renewable and Low Carbon Grid Electricity Generation and Supply. *Front. Energy Res* **2022**, *9*.

(4) De La Peña, L.; Guo, R.; Cao, X.; Ni, X.; Zhang, W. Accelerating the energy transition to achieve carbon neutrality. *Resources, Conservation and Recycling* **2022**, *177*, 105957.

(5) Majumdar, A.; Deutch, J. Research Opportunities for CO_2 Utilization and Negative Emissions at the Gigatonne Scale. *Joule* **2018**, *2* (5), 805-809.

(6) De Luna, P.; Hahn, C.; Higgins, D.; Jaffer Shaffiq, A.; Jaramillo Thomas, F.; Sargent Edward, H. What would it take for renewably powered electrosynthesis to displace petrochemical processes? *Science* **2019**, *364* (6438), eaav3506.

(7) Mac Dowell, N.; Fennell, P. S.; Shah, N.; Maitland, G. C. The role of CO_2 capture and utilization in mitigating climate change. *Nat. Clim. Change* **2017**, *7* (4), 243-249.

(8) Gabrielli, P.; Gazzani, M.; Mazzotti, M. The Role of Carbon Capture and Utilization, Carbon Capture and Storage, and Biomass to Enable a Net-Zero-CO_2 Emissions Chemical Industry. *Ind. Eng. Chem. Res.* **2020**, *59* (15), 7033-7045.

(9) Benson, E. E.; Kubiak, C. P.; Sathrum, A. J.; Smieja, J. M. Electrocatalytic and homogeneous approaches to conversion of CO_2 to liquid fuels. *Chemical Society Reviews* **2009**, *38* (1), 89-99.

(10) Appel, A. M.; Bercaw, J. E.; Bocarsly, A. B.; Dobbek, H.; DuBois, D. L.; Dupuis, M.; Ferry, J. G.; Fujita, E.; Hille, R.; Kenis, P. J. A.; et al. Frontiers, Opportunities, and Challenges in Biochemical and Chemical Catalysis of CO_2 Fixation. *Chem. Rev.* **2013**, *113* (8), 6621-6658.

(11) Costentin, C.; Robert, M.; Savéant, J.-M. Catalysis of the electrochemical reduction of carbon dioxide. *Chem. Soc. Rev.* **2013**, *42* (6), 2423-2436.

(12) Nitopi, S.; Bertheussen, E.; Scott, S. B.; Liu, X.; Engstfeld, A. K.; Horch, S.; Seger, B.; Stephens, I. E. L.; Chan, K.; Hahn, C.; et al. Progress and Perspectives of Electrochemical CO_2 Reduction on Copper in Aqueous Electrolyte. *Chem. Rev.* **2019**, *119* (12), 7610-7672.

(13) Proppe, A. H.; Li, Y. C.; Aspuru-Guzik, A.; Berlinguette, C. P.; Chang, C. J.; Cogdell, R.; Doyle, A. G.; Flick, J.; Gabor, N. M.; van Grondelle, R.; et al. Bioinspiration in light harvesting and catalysis. *Nat. Rev. Mat.* **2020**, *5* (11), 828-846.

(14) Shafaat, H. S.; Yang, J. Y. Uniting biological and chemical strategies for selective CO_2 reduction. *Nat. Catal.* **2021**, *4* (11), 928-933.

(15) Lees, E. W.; Mowbray, B. A. W.; Parlane, F. G. L.; Berlinguette, C. P. Gas diffusion electrodes and membranes for CO2 reduction electrolysers. *Nat. Rev. Mat.* **2022**, *7* (1), 55-64.

(16) Saha, P.; Amanullah, S.; Dey, A. Selectivity in Electrochemical CO_2 Reduction. *Acc. Chem. Res.* **2022**, *55* (2), 134-144.

(17) Takeda, H.; Cometto, C.; Ishitani, O.; Robert, M. Electrons, Photons, Protons and Earth-Abundant Metal Complexes for Molecular Catalysis of CO_2 Reduction. *ACS Catal.* **2017**, *7* (1), 70-88.

(18) Taheri, A.; Berben, L. A. Tailoring Electrocatalysts for Selective CO_2 or H+ Reduction: Iron Carbonyl Clusters as a Case Study. *Inorg. Chem.* **2016**, *55* (2), 378-385.

(19) Azcarate, I.; Costentin, C.; Robert, M.; Savéant, J.-M. Through-Space Charge Interaction Substituent Effects in Molecular Catalysis Leading to the Design of the Most Efficient Catalyst of CO_2-to-CO Electrochemical Conversion. *J. Am. Chem. Soc.* **2016**, *138* (51), 16639-16644.

(20) Francke, R.; Schille, B.; Roemelt, M. Homogeneously Catalyzed Electroreduction of Carbon Dioxide—Methods, Mechanisms, and Catalysts. *Chem. Rev.* **2018**, *118* (9), 4631-4701.

(21) Nichols, A. W.; Machan, C. W. Secondary-Sphere Effects in Molecular Electrocatalytic CO_2 Reduction. *Front. Chem.* **2019**, *7*.

(22) Barlow, J. M.; Yang, J. Y. Thermodynamic Considerations for Optimizing Selective CO_2 Reduction by Molecular Catalysts. *ACS Cent. Sci* **2019**, *5* (4), 580-588.

(23) Margarit, C. G.; Schnedermann, C.; Asimow, N. G.; Nocera, D. G. Carbon Dioxide Reduction by Iron Hangman Porphyrins. *Organometallics* **2019**, *38* (6), 1219-1223.

(24) Boutin, E.; Merakeb, L.; Ma, B.; Boudy, B.; Wang, M.; Bonin, J.; Anxolabéhère-Mallart, E.; Robert, M. Molecular catalysis of CO_2 reduction: recent advances and perspectives in electrochemical and light-driven processes with selected Fe, Ni and Co aza macrocyclic and polypyridine complexes. *Chem. Soc. Rev.* **2020**, *49* (16), 5772-5809.

(25) Gotico, P.; Halime, Z.; Aukauloo, A. Recent advances in metalloporphyrin-based catalyst design towards carbon dioxide reduction: from bio-inspired second coordination sphere modifications to hierarchical architectures. *J. Chem. Soc., Dalton Trans.* **2020**, *49* (8), 2381-2396.

(26) Smith, P. T.; Nichols, E. M.; Cao, Z.; Chang, C. J. Hybrid Catalysts for Artificial Photosynthesis: Merging Approaches from Molecular, Materials, and Biological Catalysis. *Acc. Chem. Res.* **2020**, *53* (3), 575-587.

(27) Hori, Y. Electrochemical CO_2 Reduction on Metal Electrodes. In *Modern Aspects of Electrochemistry*, Vayenas, C. G., White, R. E., Gamboa-Aldeco, M. E. Eds.; Springer New York, 2008; pp 89-189.

(28) Zhu, D. D.; Liu, J. L.; Qiao, S. Z. Recent Advances in Inorganic Heterogeneous Electrocatalysts for Reduction of Carbon Dioxide. *Adv. Mater.* **2016**, *28* (18), 3423-3452.

(29) Zhang, L.; Zhao, Z.-J.; Gong, J. Nanostructured Materials for Heterogeneous Electrocatalytic CO_2 Reduction and their Related Reaction Mechanisms. *Angew. Chem. Int. Ed.* **2017**, *56* (38), 11326-11353.

(30) Jiang, K.; Sandberg, R. B.; Akey, A. J.; Liu, X.; Bell, D. C.; Nørskov, J. K.; Chan, K.; Wang, H. Metal ion cycling of Cu foil for selective C–C coupling in electrochemical CO_2 reduction. *Nat. Catal.* **2018**, *1* (2), 111-119.

(31) Zhao, S.; Jin, R.; Jin, R. Opportunities and Challenges in CO_2 Reduction by Gold- and Silver-Based Electrocatalysts: From Bulk Metals to Nanoparticles and Atomically Precise Nanoclusters. *ACS Energy Lett.* **2018**, *3* (2), 452-462.

(32) Li, M.; Wang, H.; Luo, W.; Sherrell, P. C.; Chen, J.; Yang, J. Heterogeneous Single-Atom Catalysts for Electrochemical CO_2 Reduction Reaction. *Adv. Mater.* **2020**, *32* (34), 2001848.

(33) Huang, J. E.; Li, F.; Ozden, A.; Sedighian Rasouli, A.; García de Arquer, F. P.; Liu, S.; Zhang, S.; Luo, M.; Wang, X.; Lum, Y.; et al. CO_2 electrolysis to multicarbon products in strong acid. *Science* **2021**, *372* (6546), 1074-1078.

(34) Diercks, C. S.; Liu, Y.; Cordova, K. E.; Yaghi, O. M. The role of reticular chemistry in the design of CO_2 reduction catalysts. *Nat. Mater.* **2018**, *17* (4), 301-307.

(35) Wagner, A.; Sahm, C. D.; Reisner, E. Towards molecular understanding of local chemical environment effects in electro- and photocatalytic CO_2 reduction. *Nat. Catal.* **2020**, *3* (10), 775-786.

(36) Zhang, S.; Fan, Q.; Xia, R.; Meyer, T. J. CO_2 Reduction: From Homogeneous to Heterogeneous Electrocatalysis. *Acc. Chem. Res.* **2020**, *53* (1), 255-264.

(37) Nam, D.-H.; De Luna, P.; Rosas-Hernández, A.; Thevenon, A.; Li, F.; Agapie, T.; Peters, J. C.; Shekhah, O.; Eddaoudi, M.; Sargent, E. H. Molecular enhancement of heterogeneous CO_2 reduction. *Nat. Mater.* **2020**, *19* (3), 266-276.

(38) Gao, D.; Arán-Ais, R. M.; Jeon, H. S.; Roldan Cuenya, B. Rational catalyst and electrolyte design for CO_2 electroreduction towards multicarbon products. *Nat. Catal.* **2019**, *2* (3), 198-210.

(39) Zhang, X.; Guo, S.-X.; Gandionco, K. A.; Bond, A. M.; Zhang, J. Electrocatalytic carbon dioxide reduction: from fundamental principles to catalyst design. *Materials Today Advances* **2020**, *7*, 100074.

(40) Fan, L.; Xia, C.; Yang, F.; Wang, J.; Wang, H.; Lu, Y. Strategies in catalysts and electrolyzer design for electrochemical CO_2 reduction toward C_{2+} products. *Science Advances* **2020**, *6* (8), eaay3111.

(41) Xue, Y.; Guo, Y.; Cui, H.; Zhou, Z. Catalyst Design for Electrochemical Reduction of CO_2 to Multicarbon Products. *Small Methods* **2021**, *5* (10), 2100736.

(42) Xiong, H.; Dong, Y.; Liu, D.; Long, R.; Kong, T.; Xiong, Y. Recent Advances in Porous Materials for Photocatalytic CO_2 Reduction. *J. Phys. Chem. Lett* **2022**, *13* (5), 1272-1282.

(43) Wang, J.; Shi, Y.; Wang, Y.; Li, Z. Rational Design of Metal Halide Perovskite Nanocrystals for Photocatalytic CO_2 Reduction: Recent Advances, Challenges, and Prospects. *ACS Energy Lett.* **2022**, *7* (6), 2043-2059.

(44) Bagchi, D.; Roy, S.; Sarma, S. C.; C. Peter, S. Toward Unifying the Mechanistic Concepts in Electrochemical CO_2 Reduction from an Integrated Material Design and Catalytic Perspective. *Adv. Funct. Mater.* **2022**, *32* (51), 2209023.

(45) Banerjee, S.; Gerke, C. S.; Thoi, V. S. Guiding CO_2RR Selectivity by Compositional Tuning in the Electrochemical Double Layer. *Acc. Chem. Res.* **2022**, *55* (4), 504-515.

(46) Diercks, C. S.; Yaghi, O. M. The atom, the molecule, and the covalent organic framework. *Science* **2017**, *355* (6328), eaal1585.

(47) Yaghi, O. M. Reticular Chemistry in All Dimensions. *ACS Cent. Sci* **2019**, *5* (8), 1295-1300.

(48) Gropp, C.; Canossa, S.; Wuttke, S.; Gándara, F.; Li, Q.; Gagliardi, L.; Yaghi, O. M. Standard Practices of Reticular Chemistry. *ACS Cent. Sci* **2020**, *6* (8), 1255-1273.

(49) Freund, R.; Canossa, S.; Cohen, S. M.; Yan, W.; Deng, H.; Guillerm, V.; Eddaoudi, M.; Madden, D. G.; Fairen-Jimenez, D.; Lyu, H.; et al. 25 Years of Reticular Chemistry. *Angew. Chem. Int. Ed.* **2021**, *60* (45), 23946-23974.

(50) Côté, A. P.; Benin, A. I.; Ockwig, N. W.; O'Keeffe, M.; Matzger, A. J.; Yaghi, O. M. Porous, Crystalline, Covalent Organic Frameworks. *Science* **2005**, *310* (5751), 1166-1170.

(51) Colson, J. W.; Woll, A. R.; Mukherjee, A.; Levendorf, M. P.; Spitler, E. L.; Shields, V. B.; Spencer, M. G.; Park, J.; Dichtel, W. R. Oriented 2D Covalent Organic Framework Thin Films on Single-Layer Graphene. *Science* **2011**, *332* (6026), 228-231.

(52) DeBlase, C. R.; Silberstein, K. E.; Truong, T.-T.; Abruña, H. D.; Dichtel, W. R. β-Ketoenamine-Linked Covalent Organic Frameworks Capable of Pseudocapacitive Energy Storage. *J. Am. Chem. Soc.* **2013**, *135* (45), 16821-16824.

(53) Dalapati, S.; Jin, E.; Addicoat, M.; Heine, T.; Jiang, D. Highly Emissive Covalent Organic Frameworks. *J. Am. Chem. Soc.* **2016**, *138* (18), 5797-5800.

(54) Guan, X.; Chen, F.; Fang, Q.; Qiu, S. Design and applications of three dimensional covalent organic frameworks. *Chem. Soc. Rev.* **2020**, *49* (5), 1357-1384.

(55) Geng, K.; He, T.; Liu, R.; Dalapati, S.; Tan, K. T.; Li, Z.; Tao, S.; Gong, Y.; Jiang, Q.; Jiang, D. Covalent Organic Frameworks: Design, Synthesis, and Functions. *Chem. Rev.* **2020**, *120* (16), 8814-8933.

(56) Lu, M.; Zhang, M.; Liu, J.; Chen, Y.; Liao, J.-P.; Yang, M.-Y.; Cai, Y.-P.; Li, S.-L.; Lan, Y.-Q. Covalent Organic Framework Based Functional Materials: Important Catalysts for Efficient CO_2 Utilization. *Angew. Chem. Int. Ed.* **2022**, *61* (15), e202200003.

(57) Behar, D.; Dhanasekaran, T.; Neta, P.; Hosten, C. M.; Ejeh, D.; Hambright, P.; Fujita, E. Cobalt Porphyrin Catalyzed Reduction of CO_2. Radiation Chemical, Photochemical, and Electrochemical Studies. *J. Phys. Chem. A* **1998**, *102* (17), 2870-2877.

(58) Costentin, C.; Drouet, S.; Robert, M.; Savéant, J.-M. A Local Proton Source Enhances CO_2 Electroreduction to CO by a Molecular Fe Catalyst. *Science* **2012**, *338* (6103), 90-94.

(59) Costentin, C.; Passard, G.; Robert, M.; Savéant, J.-M. Ultraefficient homogeneous catalyst for the CO_2-to-CO electrochemical conversion. *Proc. Natl. Acad. Sci.* **2014**, *111* (42), 14990-14994.

(60) Manbeck, G. F.; Fujita, E. A review of iron and cobalt porphyrins, phthalocyanines and related complexes for electrochemical and photochemical reduction of carbon dioxide. *J. Porphyr. Phthalocyanines* **2015**, *19* (01-03), 45-64.

(61) Costentin, C.; Robert, M.; Savéant, J.-M.; Tatin, A. Efficient and selective molecular catalyst for the CO_2-to-CO electrochemical conversion in water. *Proc. Natl. Acad. Sci.* **2015**, *112* (22), 6882-6886.

(62) Morlanés, N.; Takanabe, K.; Rodionov, V. Simultaneous Reduction of CO_2 and Splitting of H_2O by a Single Immobilized Cobalt Phthalocyanine Electrocatalyst. *ACS Catal.* **2016**, *6* (5), 3092-3095.

(63) Rao, H.; Schmidt, L. C.; Bonin, J.; Robert, M. Visible-light-driven methane formation from CO_2 with a molecular iron catalyst. *Nature* **2017**, *548* (7665), 74-77.

(64) Zhang, X.; Wu, Z.; Zhang, X.; Li, L.; Li, Y.; Xu, H.; Li, X.; Yu, X.; Zhang, Z.; Liang, Y.; et al. Highly selective and active CO_2 reduction electrocatalysts based on cobalt phthalocyanine/carbon nanotube hybrid structures. *Nat. Commun.* **2017**, *8* (1), 14675.

(65) Nichols, E. M.; Derrick, J. S.; Nistanaki, S. K.; Smith, P. T.; Chang, C. J. Positional effects of second-sphere amide pendants on electrochemical CO_2 reduction catalyzed by iron porphyrins. *Chem. Sci* **2018**, *9* (11), 2952-2960.

(66) Wang, M.; Torbensen, K.; Salvatore, D.; Ren, S.; Joulié, D.; Dumoulin, F.; Mendoza, D.; Lassalle-Kaiser, B.; Işci, U.; Berlinguette, C. P.; et al. CO_2 electrochemical catalytic reduction with a highly active cobalt phthalocyanine. *Nat. Commun.* **2019**, *10* (1), 3602.

(67) Gotico, P.; Boitrel, B.; Guillot, R.; Sircoglou, M.; Quaranta, A.; Halime, Z.; Leibl, W.; Aukauloo, A. Second-Sphere Biomimetic Multipoint Hydrogen-Bonding Patterns to Boost CO_2 Reduction of Iron Porphyrins. *Angew. Chem. Int. Ed.* **2019**, *58* (14), 4504-4509.

(68) Gotico, P.; Roupnel, L.; Guillot, R.; Sircoglou, M.; Leibl, W.; Halime, Z.; Aukauloo, A. Atropisomeric Hydrogen Bonding Control for CO_2 Binding and Enhancement of Electrocatalytic Reduction at Iron Porphyrins. *Angew. Chem. Int. Ed.* **2020**, *59* (50), 22451-22455.

(69) Amanullah, S.; Saha, P.; Dey, A. Activating the Fe(I) State of Iron Porphyrinoid with Second-Sphere Proton Transfer Residues for Selective Reduction of CO_2 to HCOOH via Fe(III/II)–COOH Intermediate(s). *J. Am. Chem. Soc.* **2021**, *143* (34), 13579-13592.

(70) Derrick, J. S.; Loipersberger, M.; Nistanaki, S. K.; Rothweiler, A. V.; Head-Gordon, M.; Nichols, E. M.; Chang, C. J. Templating Bicarbonate in the Second Coordination Sphere Enhances Electrochemical CO_2 Reduction Catalyzed by Iron Porphyrins. *J. Am. Chem. Soc.* **2022**, *144* (26), 11656-11663.

(71) Narouz, M. R.; De La Torre, P.; An, L.; Chang, C. J. Multifunctional Charge and Hydrogen-Bond Effects of Second-Sphere Imidazolium Pendants Promote Capture and Electrochemical Reduction of CO_2 in Water Catalyzed by Iron Porphyrins**. *Angew. Chem. Int. Ed.* **2022**, *61* (37), e202207666.

(72) Liang, Z.; Wang, H.-Y.; Zheng, H.; Zhang, W.; Cao, R. Porphyrin-based frameworks for oxygen electrocatalysis and catalytic reduction of carbon dioxide. *Chem. Soc. Rev.* **2021**, *50* (4), 2540-2581.

(73) Lin, S.; Diercks, C. S.; Zhang, Y.-B.; Kornienko, N.; Nichols, E. M.; Zhao, Y.; Paris, A. R.; Kim, D.; Yang, P.; Yaghi, O. M.; et al. Covalent organic frameworks comprising cobalt porphyrins for catalytic CO_2 reduction in water. *Science* **2015**, *349* (6253), 1208-1213.

(74) Diercks, C. S.; Lin, S.; Kornienko, N.; Kapustin, E. A.; Nichols, E. M.; Zhu, C.; Zhao, Y.; Chang, C. J.; Yaghi, O. M. Reticular Electronic Tuning of Porphyrin Active Sites in Covalent Organic Frameworks for Electrocatalytic Carbon Dioxide Reduction. *J. Am. Chem. Soc.* **2018**, *140* (3), 1116-1122.

(75) Zhu, H.-J.; Lu, M.; Wang, Y.-R.; Yao, S.-J.; Zhang, M.; Kan, Y.-H.; Liu, J.; Chen, Y.; Li, S.-L.; Lan, Y.-Q. Efficient electron transmission in covalent organic framework nanosheets for highly active electrocatalytic carbon dioxide reduction. *Nat. Commun.* **2020**, *11* (1), 497.

(76) Wang, Y.-R.; Ding, H.-M.; Ma, X.-Y.; Liu, M.; Yang, Y.-L.; Chen, Y.; Li, S.-L.; Lan, Y.-Q. Imparting CO_2 Electroreduction Auxiliary for Integrated Morphology Tuning and Performance Boosting in a Porphyrin-based Covalent Organic Framework. *Angew. Chem. Int. Ed.* **2022**, *61* (5), e202114648.

(77) Lin, G.; Ding, H.; Chen, R.; Peng, Z.; Wang, B.; Wang, C. 3D Porphyrin-Based Covalent Organic Frameworks. *J. Am. Chem. Soc.* **2017**, *139* (25), 8705-8709.

(78) Chi, S.-Y.; Chen, Q.; Zhao, S.-S.; Si, D.-H.; Wu, Q.-J.; Huang, Y.-B.; Cao, R. Three-dimensional porphyrinic covalent organic frameworks for highly efficient electroreduction of carbon dioxide. *J. Mater. Chem. A* **2022**, *10* (9), 4653-4659.

(79) Ding, J.; Guan, X.; Lv, J.; Chen, X.; Zhang, Y.; Li, H.; Zhang, D.; Qiu, S.; Jiang, H.-L.; Fang, Q. Three-Dimensional Covalent Organic Frameworks with Ultra-Large Pores for Highly Efficient Photocatalysis. *J. Am. Chem. Soc.* **2023**, *145* (5), 3248-3254.

(80) D'Alessandro, D. M.; Smit, B.; Long, J. R. Carbon Dioxide Capture: Prospects for New Materials. *Angew. Chem. Int. Ed.* **2010**, *49* (35), 6058-6082.

(81) McDonald, T. M.; Lee, W. R.; Mason, J. A.; Wiers, B. M.; Hong, C. S.; Long, J. R. Capture of Carbon Dioxide from Air and Flue Gas in the Alkylamine-Appended Metal–Organic Framework mmen-Mg2(dobpdc). *J. Am. Chem. Soc.* **2012**, *134* (16), 7056-7065.

(82) Kenarsari, S. D.; Yang, D.; Jiang, G.; Zhang, S.; Wang, J.; Russell, A. G.; Wei, Q.; Fan, M. Review of recent advances in carbon dioxide separation and capture. *RSC Advances* **2013**, *3* (45), 22739-22773.

(83) Dutcher, B.; Fan, M.; Russell, A. G. Amine-Based CO_2 Capture Technology Development from the Beginning of 2013—A Review. *ACS Applied Materials & Interfaces* **2015**, *7* (4), 2137-2148.

(84) McDonald, T. M.; Mason, J. A.; Kong, X.; Bloch, E. D.; Gygi, D.; Dani, A.; Crocellà, V.; Giordanino, F.; Odoh, S. O.; Drisdell, W. S.; et al. Cooperative insertion of CO_2 in diamine-appended metal-organic frameworks. *Nature* **2015**, *519* (7543), 303-308.

(85) Sanz-Pérez, E. S.; Murdock, C. R.; Didas, S. A.; Jones, C. W. Direct Capture of CO_2 from Ambient Air. *Chem. Rev.* **2016**, *116* (19), 11840-11876.

(86) Liu, H.; Chu, J.; Yin, Z.; Cai, X.; Zhuang, L.; Deng, H. Covalent Organic Frameworks Linked by Amine Bonding for Concerted Electrochemical Reduction of CO_2. *Chem* **2018**, *4* (7), 1696-1709.

(87) Gong, Y.-N.; Zhong, W.; Li, Y.; Qiu, Y.; Zheng, L.; Jiang, J.; Jiang, H.-L. Regulating Photocatalysis by Spin-State Manipulation of Cobalt in Covalent Organic Frameworks. *J. Am. Chem. Soc.* **2020**, *142* (39), 16723-16731.

(88) Wu, Q.-J.; Si, D.-H.; Wu, Q.; Dong, Y.-L.; Cao, R.; Huang, Y.-B. Boosting Electroreduction of CO_2 over Cationic Covalent Organic Frameworks: Hydrogen Bonding Effects of Halogen Ions. *Angew. Chem. Int. Ed.* **2023**, *62* (7), e202215687.

(89) Huang, N.; Lee, K. H.; Yue, Y.; Xu, X.; Irle, S.; Jiang, Q.; Jiang, D. A Stable and Conductive Metallophthalocyanine Framework for Electrocatalytic Carbon Dioxide Reduction in Water. *Angew. Chem. Int. Ed.* **2020**, *59* (38), 16587-16593.

(90) Han, B.; Ding, X.; Yu, B.; Wu, H.; Zhou, W.; Liu, W.; Wei, C.; Chen, B.; Qi, D.; Wang, H.; et al. Two-Dimensional Covalent Organic Frameworks with Cobalt(II)-Phthalocyanine Sites for Efficient Electrocatalytic Carbon Dioxide Reduction. *J. Am. Chem. Soc.* **2021**, *143* (18), 7104-7113.

(91) Han, B.; Jin, Y.; Chen, B.; Zhou, W.; Yu, B.; Wei, C.; Wang, H.; Wang, K.; Chen, Y.; Chen, B.; et al. Maximizing Electroactive Sites in a Three-Dimensional Covalent Organic Framework for Significantly Improved Carbon Dioxide Reduction Electrocatalysis. *Angew. Chem. Int. Ed.* **2022**, *61* (1), e202114244.

(92) Hawecker, J.; Lehn, J.-M.; Ziessel, R. Electrocatalytic reduction of carbon dioxide mediated by Re(bipy)$(CO)_3Cl$ (bipy = 2,2′-bipyridine). *J. Chem. Soc., Chem. Commun.* **1984**, (6), 328-330.

(93) Barrett, J. A.; Miller, C. J.; Kubiak, C. P. Electrochemical Reduction of CO_2 Using Group VII Metal Catalysts. *Trends in Chemistry* **2021**, *3* (3), 176-187.

(94) Benson, E. E.; Kubiak, C. P. Structural investigations into the deactivation pathway of the CO_2 reduction electrocatalyst Re(bpy)$(CO)_3Cl$. *Chem. Commun.* **2012**, *48* (59), 7374-7376.

(95) Sampson, M. D.; Nguyen, A. D.; Grice, K. A.; Moore, C. E.; Rheingold, A. L.; Kubiak, C. P. Manganese Catalysts with Bulky Bipyridine Ligands for the Electrocatalytic Reduction of Carbon Dioxide: Eliminating Dimerization and Altering Catalysis. *J. Am. Chem. Soc.* **2014**, *136* (14), 5460-5471.

(96) Shipp, J. D.; Carson, H.; Spall, S. J. P.; Parker, S. C.; Chekulaev, D.; Jones, N.; Mel'nikov, M. Y.; Robertson, C. C.; Meijer, A. J. H. M.; Weinstein, J. A. Sterically hindered Re- and Mn-CO_2 reduction catalysts for solar energy conversion. *J. Chem. Soc., Dalton Trans.* **2020**, *49* (14), 4230-4243.

(97) Popov, D. A.; Luna, J. M.; Orchanian, N. M.; Haiges, R.; Downes, C. A.; Marinescu, S. C. A 2,2′-bipyridine-containing covalent organic framework bearing rhenium(i) tricarbonyl moieties for CO_2 reduction. *J. Chem. Soc., Dalton Trans.* **2018**, *47* (48), 17450-17460.

(98) Yang, S.; Hu, W.; Zhang, X.; He, P.; Pattengale, B.; Liu, C.; Cendejas, M.; Hermans, I.; Zhang, X.; Zhang, J.; et al. 2D Covalent Organic Frameworks as Intrinsic Photocatalysts for Visible Light-Driven CO_2 Reduction. *J. Am. Chem. Soc.* **2018**, *140* (44), 14614-14618.

(99) Fu, Z.; Wang, X.; Gardner, A. M.; Wang, X.; Chong, S. Y.; Neri, G.; Cowan, A. J.; Liu, L.; Li, X.; Vogel, A.; et al. A stable covalent organic framework for photocatalytic carbon dioxide reduction. *Chem. Sci* **2020**, *11* (2), 543-550.

(100) Choi, K. M.; Kim, D.; Rungtaweevoranit, B.; Trickett, C. A.; Barmanbek, J. T. D.; Alshammari, A. S.; Yang, P.; Yaghi, O. M. Plasmon-Enhanced Photocatalytic CO_2 Conversion within Metal–Organic Frameworks under Visible Light. *J. Am. Chem. Soc.* **2017**, *139* (1), 356-362.

(101) Stanley, P. M.; Thomas, C.; Thyrhaug, E.; Urstoeger, A.; Schuster, M.; Hauer, J.; Rieger, B.; Warnan, J.; Fischer, R. A. Entrapped Molecular Photocatalyst and Photosensitizer in Metal–Organic Framework Nanoreactors for Enhanced Solar CO_2 Reduction. *ACS Catal.* **2021**, *11* (2), 871-882.

(102) Zhong, W.; Sa, R.; Li, L.; He, Y.; Li, L.; Bi, J.; Zhuang, Z.; Yu, Y.; Zou, Z. A Covalent Organic Framework Bearing Single Ni Sites as a Synergistic Photocatalyst for Selective Photoreduction of CO_2 to CO. *J. Am. Chem. Soc.* **2019**, *141* (18), 7615-7621.

(103) Dubed Bandomo, G. C.; Mondal, S. S.; Franco, F.; Bucci, A.; Martin-Diaconescu, V.; Ortuño, M. A.; van Langevelde, P. H.; Shafir, A.; López, N.; Lloret-Fillol, J. Mechanically Constrained Catalytic $Mn(CO)_3Br$ Single Sites in a Two-Dimensional Covalent Organic Framework for CO_2 Electroreduction in H_2O. *ACS Catal.* **2021**, *11* (12), 7210-7222.

(104) Zhao, Z.; Zheng, D.; Guo, M.; Yu, J.; Zhang, S.; Zhang, Z.; Chen, Y. Engineering Olefin-Linked Covalent Organic Frameworks for Photoenzymatic Reduction of CO_2. *Angew. Chem. Int. Ed.* **2022**, *61* (12), e202200261.

(105) Hoskins, B. F.; Robson, R. Design and construction of a new class of scaffolding-like materials comprising infinite polymeric frameworks of 3D-linked molecular rods. A reappraisal of the zinc cyanide and cadmium cyanide structures and the synthesis and structure of the diamond-related frameworks [N(CH3)4][CuIZnII(CN)4] and CuI[4,4',4",4"'-tetracyanotetraphenylmethane]BF4.xC6H5NO2. *J. Am. Chem. Soc.* **1990**, *112* (4), 1546-1554.

(106) Li, H.; Eddaoudi, M.; O'Keeffe, M.; Yaghi, O. M. Design and synthesis of an exceptionally stable and highly porous metal-organic framework. *Nature* **1999**, *402* (6759), 276-279.

(107) Yaghi, O. M.; Li, H. Hydrothermal Synthesis of a Metal-Organic Framework Containing Large Rectangular Channels. *J. Am. Chem. Soc.* **1995**, *117* (41), 10401-10402.

(108) Horcajada, P.; Chalati, T.; Serre, C.; Gillet, B.; Sebrie, C.; Baati, T.; Eubank, J. F.; Heurtaux, D.; Clayette, P.; Kreuz, C.; et al. Porous metal–organic-framework nanoscale carriers as a potential platform for drug delivery and imaging. *Nat. Mater.* **2010**, *9* (2), 172-178.

(109) Furukawa, H.; Ko, N.; Go, Y. B.; Aratani, N.; Choi, S. B.; Choi, E.; Yazaydin, A. Ö.; Snurr, R. Q.; O'Keeffe, M.; Kim, J.; et al. Ultrahigh Porosity in Metal-Organic Frameworks. *Science* **2010**, *329* (5990), 424-428.

(110) Zhou, H.-C.; Long, J. R.; Yaghi, O. M. Introduction to Metal–Organic Frameworks. *Chem. Rev.* **2012**, *112* (2), 673-674.

(111) Cook, T. R.; Zheng, Y.-R.; Stang, P. J. Metal–Organic Frameworks and Self-Assembled Supramolecular Coordination Complexes: Comparing and Contrasting the Design, Synthesis, and Functionality of Metal–Organic Materials. *Chem. Rev.* **2013**, *113* (1), 734-777.

(112) Zhou, H.-C. J.; Kitagawa, S. Metal–Organic Frameworks (MOFs). *Chem. Soc. Rev.* **2014**, *43* (16), 5415-5418.

(113) Baumann, A. E.; Burns, D. A.; Liu, B.; Thoi, V. S. Metal-organic framework functionalization and design strategies for advanced electrochemical energy storage devices. *Commun. Chem* **2019**, *2* (1), 86.

(114) Kornienko, N.; Zhao, Y.; Kley, C. S.; Zhu, C.; Kim, D.; Lin, S.; Chang, C. J.; Yaghi, O. M.; Yang, P. Metal–Organic Frameworks for Electrocatalytic Reduction of Carbon Dioxide. *J. Am. Chem. Soc.* **2015**, *137* (44), 14129-14135.

(115) Trickett, C. A.; Helal, A.; Al-Maythalony, B. A.; Yamani, Z. H.; Cordova, K. E.; Yaghi, O. M. The chemistry of metal–organic frameworks for CO_2 capture, regeneration and conversion. *Nat. Rev. Mat.* **2017**, *2* (8), 17045.

(116) Majewski, M. B.; Peters, A. W.; Wasielewski, M. R.; Hupp, J. T.; Farha, O. K. Metal–Organic Frameworks as Platform Materials for Solar Fuels Catalysis. *ACS Energy Lett.* **2018**, *3* (3), 598-611.

(117) Dong, B.-X.; Qian, S.-L.; Bu, F.-Y.; Wu, Y.-C.; Feng, L.-G.; Teng, Y.-L.; Liu, W.-L.; Li, Z.-W. Electrochemical Reduction of CO_2 to CO by a Heterogeneous Catalyst of Fe–Porphyrin-Based Metal–Organic Framework. *ACS Applied Energy Materials* **2018**, *1* (9), 4662-4669.

(118) Wang, Y.-R.; Huang, Q.; He, C.-T.; Chen, Y.; Liu, J.; Shen, F.-C.; Lan, Y.-Q. Oriented electron transmission in polyoxometalate-metalloporphyrin organic framework for highly selective electroreduction of CO_2. *Nat. Commun.* **2018**, *9* (1), 4466.

(119) Matheu, R.; Gutierrez-Puebla, E.; Monge, M. Á.; Diercks, C. S.; Kang, J.; Prévot, M. S.; Pei, X.; Hanikel, N.; Zhang, B.; Yang, P.; et al. Three-Dimensional Phthalocyanine Metal-Catecholates for High Electrochemical Carbon Dioxide Reduction. *J. Am. Chem. Soc.* **2019**, *141* (43), 17081-17085.

(120) Dou, S.; Song, J.; Xi, S.; Du, Y.; Wang, J.; Huang, Z.-F.; Xu, Z. J.; Wang, X. Boosting Electrochemical CO_2 Reduction on Metal–Organic Frameworks via Ligand Doping. *Angew. Chem. Int. Ed.* **2019**, *58* (12), 4041-4045.

(121) Zhong, H.; Ghorbani-Asl, M.; Ly, K. H.; Zhang, J.; Ge, J.; Wang, M.; Liao, Z.; Makarov, D.; Zschech, E.; Brunner, E.; et al. Synergistic electroreduction of carbon dioxide to carbon monoxide on bimetallic layered conjugated metal-organic frameworks. *Nat. Commun.* **2020**, *11* (1), 1409.

(122) Shah, S. S. A.; Najam, T.; Wen, M.; Zang, S.-Q.; Waseem, A.; Jiang, H.-L. Metal–Organic Framework-Based Electrocatalysts for CO_2 Reduction. *Small Structures* **2022**, *3* (5), 2100090.

(123) Yang, D.; Zuo, S.; Yang, H.; Zhou, Y.; Lu, Q.; Wang, X. Tailoring Layer Number of 2D Porphyrin-Based MOFs Towards Photocoupled Electroreduction of CO_2. *Adv. Mater.* **2022**, *34* (7), 2107293.

(124) Di, Z.; Qi, Y.; Yu, X.; Hu, F. The Progress of Metal-Organic Framework for Boosting CO_2 Conversion. *Catalysts* **2022**, *12* (12), 1582.

(125) Xu, H.-Q.; Hu, J.; Wang, D.; Li, Z.; Zhang, Q.; Luo, Y.; Yu, S.-H.; Jiang, H.-L. Visible-Light Photoreduction of CO_2 in a Metal–Organic Framework: Boosting Electron–Hole Separation via Electron Trap States. *J. Am. Chem. Soc.* **2015**, *137* (42), 13440-13443.

(126) Park, K. S.; Ni, Z.; Côté, A. P.; Choi, J. Y.; Huang, R.; Uribe-Romo, F. J.; Chae, H. K.; O'Keeffe, M.; Yaghi, O. M. Exceptional chemical and thermal stability of zeolitic imidazolate frameworks. *Proc. Natl. Acad. Sci.* **2006**, *103* (27), 10186-10191.

(127) Hayashi, H.; Côté, A. P.; Furukawa, H.; O'Keeffe, M.; Yaghi, O. M. Zeolite A imidazolate frameworks. *Nat. Mater.* **2007**, *6* (7), 501-506.

(128) Banerjee, R.; Phan, A.; Wang, B.; Knobler, C.; Furukawa, H.; O'Keeffe, M.; Yaghi, O. M. High-Throughput Synthesis of Zeolitic Imidazolate Frameworks and Application to CO_2 Capture. *Science* **2008**, *319* (5865), 939-943.

(129) Wang, Y.; Hou, P.; Wang, Z.; Kang, P. Zinc Imidazolate Metal–Organic Frameworks (ZIF-8) for Electrochemical Reduction of CO_2 to CO. *ChemPhysChem* **2017**, *18* (22), 3142-3147.

(130) Evans, J. D.; Sumby, C. J.; Doonan, C. J. Synthesis and Applications of Porous Organic Cages. *Chem. Lett.* **2015**, *44* (5), 582-588.

(131) Hasell, T.; Cooper, A. I. Porous organic cages: soluble, modular and molecular pores. *Nat. Rev. Mat.* **2016**, *1* (9), 16053.

(132) Huang, H. H.; Šolomek, T. Photochemistry Meets Porous Organic Cages. *Chimia (Aarau)* **2021**, *75* (4), 285-290.

(133) Chen, C.; Yan, X.; Wu, Y.; Liu, S.; Zhang, X.; Sun, X.; Zhu, Q.; Wu, H.; Han, B. Boosting the Productivity of Electrochemical CO_2 Reduction to Multi-Carbon Products by Enhancing CO_2 Diffusion through a Porous Organic Cage. *Angew. Chem. Int. Ed.* **2022**, *61* (23), e202202607.

(134) Zhang, G.; Mastalerz, M. Organic cage compounds – from shape-persistency to function. *Chem. Soc. Rev.* **2014**, *43* (6), 1934-1947.

(135) Hong, S.; Rohman, M. R.; Jia, J.; Kim, Y.; Moon, D.; Kim, Y.; Ko, Y. H.; Lee, E.; Kim, K. Porphyrin Boxes: Rationally Designed Porous Organic Cages. *Angew. Chem. Int. Ed.* **2015**, *54* (45), 13241-13244.

(136) Benke, B. P.; Aich, P.; Kim, Y.; Kim, K. L.; Rohman, M. R.; Hong, S.; Hwang, I.-C.; Lee, E. H.; Roh, J. H.; Kim, K. Iodide-Selective Synthetic Ion Channels Based on Shape-Persistent Organic Cages. *J. Am. Chem. Soc.* **2017**, *139* (22), 7432-7435.

(137) Mukhopadhyay, R. D.; Kim, Y.; Koo, J.; Kim, K. Porphyrin Boxes. *Acc. Chem. Res.* **2018**, *51* (11), 2730-2738.

(138) Kim, Y.; Koo, J.; Hwang, I.-C.; Mukhopadhyay, R. D.; Hong, S.; Yoo, J.; Dar, A. A.; Kim, I.; Moon, D.; Shin, T. J.; et al. Rational Design and Construction of Hierarchical Superstructures Using Shape-Persistent Organic Cages: Porphyrin Box-Based Metallosupramolecular Assemblies. *J. Am. Chem. Soc.* **2018**, *140* (44), 14547-14551.

(139) Yu, X.; Wang, B.; Kim, Y.; Park, J.; Ghosh, S.; Dhara, B.; Mukhopadhyay, R. D.; Koo, J.; Kim, I.; Kim, S.; et al. Supramolecular Fullerene Tetramers Concocted with Porphyrin Boxes

Enable Efficient Charge Separation and Delocalization. *J. Am. Chem. Soc.* **2020**, *142* (29), 12596-12601.

(140) Koo, J.; Kim, I.; Kim, Y.; Cho, D.; Hwang, I.-C.; Mukhopadhyay, R. D.; Song, H.; Ko, Y. H.; Dhamija, A.; Lee, H.; et al. Gigantic Porphyrinic Cages. *Chem* **2020**, *6* (12), 3374-3384.

(141) Smith, P. T.; Kim, Y.; Benke, B. P.; Kim, K.; Chang, C. J. Supramolecular Tuning Enables Selective Oxygen Reduction Catalyzed by Cobalt Porphyrins for Direct Electrosynthesis of Hydrogen Peroxide. *Angew. Chem. Int. Ed.* **2020**, *59* (12), 4902-4907.

(142) An, L.; Narouz, M. R.; Smith, P. T.; De La Torre, P.; Chang, C. J. Supramolecular Enhancement of Electrochemical Nitrate Reduction Catalyzed by Cobalt Porphyrin Organic Cages for Ammonia Electrosynthesis in Water. *ChemRxiv* **2022**.

(143) Smith, P. T.; Benke, B. P.; An, L.; Kim, Y.; Kim, K.; Chang, C. J. A Supramolecular Porous Organic Cage Platform Promotes Electrochemical Hydrogen Evolution from Water Catalyzed by Cobalt Porphyrins. *ChemElectroChem* **2021**, *8* (9), 1653-1657.

(144) Smith, P. T.; Benke, B. P.; Cao, Z.; Kim, Y.; Nichols, E. M.; Kim, K.; Chang, C. J. Iron Porphyrins Embedded into a Supramolecular Porous Organic Cage for Electrochemical CO_2 Reduction in Water. *Angew. Chem. Int. Ed.* **2018**, *57* (31), 9684-9688.

(145) An, L.; De La Torre, P.; Smith, P. T.; Narouz, M. R.; Chang, C. J. Synergistic Porosity and Charge Effects in a Supramolecular Porphyrin Cage Promote Efficient Photocatalytic CO_2 Reduction**. *Angew. Chem. Int. Ed.* **2023**, *62* (5), e202209396.

(146) Yoshizawa, M.; Tamura, M.; Fujita, M. Diels-Alder in Aqueous Molecular Hosts: Unusual Regioselectivity and Efficient Catalysis. *Science* **2006**, *312* (5771), 251-254.

(147) Tranchemontagne, D. J.; Ni, Z.; O'Keeffe, M.; Yaghi, O. M. Reticular Chemistry of Metal–Organic Polyhedra. *Angew. Chem. Int. Ed.* **2008**, *47* (28), 5136-5147.

(148) Lu, Z.; Knobler, C. B.; Furukawa, H.; Wang, B.; Liu, G.; Yaghi, O. M. Synthesis and Structure of Chemically Stable Metal−Organic Polyhedra. *J. Am. Chem. Soc.* **2009**, *131* (35), 12532-12533.

(149) Yoshizawa, M.; Klosterman, J. K.; Fujita, M. Functional Molecular Flasks: New Properties and Reactions within Discrete, Self-Assembled Hosts. *Angew. Chem. Int. Ed.* **2009**, *48* (19), 3418-3438.

(150) Inokuma, Y.; Kawano, M.; Fujita, M. Crystalline molecular flasks. *Nature Chemistry* **2011**, *3* (5), 349-358.

(151) Chakrabarty, R.; Mukherjee, P. S.; Stang, P. J. Supramolecular Coordination: Self-Assembly of Finite Two- and Three-Dimensional Ensembles. *Chem. Rev.* **2011**, *111* (11), 6810-6918.

(152) Cook, T. R.; Stang, P. J. Recent Developments in the Preparation and Chemistry of Metallacycles and Metallacages via Coordination. *Chem. Rev.* **2015**, *115* (15), 7001-7045.

(153) Gosselin, A. J.; Rowland, C. A.; Bloch, E. D. Permanently Microporous Metal–Organic Polyhedra. *Chem. Rev.* **2020**, *120* (16), 8987-9014.

(154) Hauke, C. E.; Cook, T. R. 1.27 - Self-Assembly Processes for the Construction of Supramolecular Coordination Compounds. In *Comprehensive Coordination Chemistry III*, Constable, E. C., Parkin, G., Que Jr, L. Eds.; Elsevier, 2021; pp 1074-1085.

(155) McTernan, C. T.; Davies, J. A.; Nitschke, J. R. Beyond Platonic: How to Build Metal–Organic Polyhedra Capable of Binding Low-Symmetry, Information-Rich Molecular Cargoes. *Chem. Rev.* **2022**, *122* (11), 10393-10437.

(156) Liu, J.; Wang, Z.; Cheng, P.; Zaworotko, M. J.; Chen, Y.; Zhang, Z. Post-synthetic modifications of metal–organic cages. *Nat. Rev. Chem.* **2022**, *6* (5), 339-356.

(157) Lee, H. S.; Jee, S.; Kim, R.; Bui, H.-T.; Kim, B.; Kim, J.-K.; Park, K. S.; Choi, W.; Kim, W.; Choi, K. M. A highly active, robust photocatalyst heterogenized in discrete cages of metal–organic polyhedra for CO_2 reduction. *Energy & Environmental Science* **2020**, *13* (2), 519-526.

(158) Qi, X.; Zhong, R.; Chen, M.; Sun, C.; You, S.; Gu, J.; Shan, G.; Cui, D.; Wang, X.; Su, Z. Single Metal–Organic Cage Decorated with an Ir(III) Complex for CO_2 Photoreduction. *ACS Catal.* **2021**, *11* (12), 7241-7248.

(159) Ghosh, A. C.; Legrand, A.; Rajapaksha, R.; Craig, G. A.; Sassoye, C.; Balázs, G.; Farrusseng, D.; Furukawa, S.; Canivet, J.; Wisser, F. M. Rhodium-Based Metal–Organic Polyhedra Assemblies for Selective CO_2 Photoreduction. *J. Am. Chem. Soc.* **2022**, *144* (8), 3626-3636.

(160) Gong, M.; Cao, Z.; Liu, W.; Nichols, E. M.; Smith, P. T.; Derrick, J. S.; Liu, Y.-S.; Liu, J.; Wen, X.; Chang, C. J. Supramolecular Porphyrin Cages Assembled at Molecular–Materials Interfaces for Electrocatalytic CO Reduction. *ACS Cent. Sci* **2017**, *3* (9), 1032-1040.

(161) Wagner, A.; Ly, K. H.; Heidary, N.; Szabó, I.; Földes, T.; Assaf, K. I.; Barrow, S. J.; Sokołowski, K.; Al-Hada, M.; Kornienko, N.; et al. Host–Guest Chemistry Meets Electrocatalysis: Cucurbit[6]uril on a Au Surface as a Hybrid System in CO_2 Reduction. *ACS Catal.* **2020**, *10* (1), 751-761.

Chapter 2: Exchange Coupling Determines Metal-Dependent Efficiency for Iron- and Cobalt-Catalyzed Photochemical CO_2 Reduction

This work was published in the following scientific journal:

Patricia De La Torre, Jeffrey S. Derrick, Andrew Snider, Peter T. Smith, Matthias Loipersberger, Martin Head-Gordon, and Christopher J. Chang. Exchange Coupling Determines Metal-Dependent Efficiency for Iron- and Cobalt-Catalyzed Photochemical CO_2 Reduction. *ACS Catalysis* **2022** *12* (14), 8484-8493.

Abstract:

Catalysts promoting multielectron charge delocalization offer selectivity for the CO_2 reduction reaction (CO_2RR) over the competing hydrogen evolution reaction (HER). Here, we show metal-ligand exchange coupling as an example of charge delocalization that can determine efficiency for photocatalytic CO_2RR. A comparative evaluation of iron and cobalt complexes supported by the redox-active ligand tpyPY2Me establishes that the two-electron reduction of [Co(tpyPY2Me)]$^{2+}$ (**[Co]**$^{\mathbf{2+}}$) occurs at potentials 770 mV more negative than the [Fe(tpyPY2Me)]$^{2+}$ (**[Fe]**$^{\mathbf{2+}}$) analog by maximizing exchange coupling in the latter compound. The positive shift in reduction potential promoted by metal-ligand exchange coupling drives **[Fe]**$^{\mathbf{2+}}$ to be among the most active and selective molecular catalysts for photochemical CO_2RR reported to date, maintaining up to 99% CO product selectivity with total turnover numbers (TON) and initial turnover frequencies (TOF) exceeding 30,000 and 900 min^{-1}, respectively. In contrast, **[Co]**$^{\mathbf{2+}}$ shows much lower CO_2RR activity, reaching only ca. 600 TON at 83% CO product selectivity under similar conditions accompanied by rapid catalyst decomposition. Spin density plots of the two-electron reduced **[Co]**$^{\mathbf{0}}$ complex implicate a paramagnetic open-shell doublet ground state compared to the diamagnetic open-shell singlet ground state of reduced **[Fe]**$^{\mathbf{0}}$, rationalizing the observed negative shift in two-electron reduction potentials from the **[M]**$^{\mathbf{2+}}$ species and lowered CO_2RR efficiency for the cobalt complex relative to its iron congener. This work emphasizes the contributions of multielectron metal-ligand exchange coupling in promoting effective CO_2RR and provides a starting point for the broader incorporation of this strategy in catalyst design.

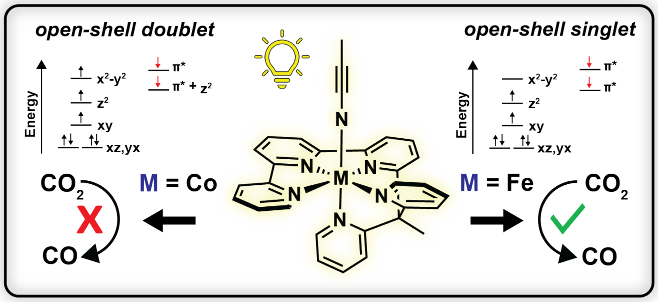

1. Introduction

The selective and efficient transformation of carbon dioxide into value-added products offers a sustainable approach to generate fuels, foods, materials, and medicines from renewable feedstocks.[1-4] Artificial photosynthesis is a potentially powerful strategy towards achieving this goal,[5-15] where concept transfer from natural photosynthesis can be incorporated into synthetic systems capable of reducing CO_2 through light-initiated proton- and electron-transfer reactions. In this context, homogeneous artificial photosynthesis platforms offer the capacity to tune system performance using well-defined components, including the molecular catalyst, photosensitizer with an energy-matched reduction potential, and sacrificial electron donor with maximum quenching efficiency.[11, 16-22] Indeed, recent advances in molecular photocatalysis for the carbon dioxide reduction reaction (CO_2RR) include metal-dependent enhancement of organic photosensitizers,[20, 23]the use of hydrogen bonding,[24] electrostatic,[14,25, 26] or covalent[27] interactions between photosensitizer and catalyst to improve electron transfer, and additives to increase CO_2 solubility.[28-32]

In terms of new catalyst design, first-row transition metal complexes supported by polypyridyl ligand frameworks[30, 32-52] have emerged as privileged scaffolds for CO_2RR. For example, we recently found that strong metal-ligand exchange coupling between an iron center and pentadentate polypyridyl ligand (tpyPY2Me) promotes its facile two-electron reduction to yield a reduced diamagnetic complex, [Fe(tpyPY2Me)] (**[Fe]^0**), which we assigned to an open-shell singlet ground state that is composed of an intermediate-spin Fe^{2+} center antiferromagnetically coupled to a doubly-reduced triplet tpyPY2Me ligand.[44] The metal-ligand cooperativity in this Fe^{2+} complex leads to a 640 mV positive shift in the first two ligand-centered reductions relative to the Zn^{2+} analog. This feature enables catalysis of electrochemical CO_2RR at low overpotentials with high selectivity by delocalizing electron density beyond the primary metal center. Moreover, the analogous nickel tpyPY2Me complex, $[Ni(tpyPY2Me)]^{2+}$ (**[Ni]$^{2+}$**), has found application as an efficient redox mediator for controlling radical pathways by ligand-centered redox reactivity.[53]

Against this backdrop, we sought to expand the reactivity of metal tpyPY2Me complexes to photochemical CO_2RR. Considering the precedent for cobalt-based CO_2RR catalysts,[11, 18, 23, 39, 54-58] we now report a comparative study between iron and cobalt tpyPY2Me complexes for photochemical CO_2RR, including synthesis and characterization of the novel cobalt tpyPY2Me complex, $[Co(tpyPY2Me)]^{2+}$ (**[Co]$^{2+}$**). We find that electron count makes a substantial contribution to metal-ligand cooperativity and redox behavior in these transition metal tpyPY2Me complexes. In contrast to the **[Fe]$^{2+}$** complex, where the first two single-electron, ligand-based reduction waves are virtually superimposable, electrochemical characterization of **[Co]$^{2+}$** shows a 1.39 V separation between the first and second redox processes where two-electron reduction potential of **[Co]$^{2+}$** is shifted negatively by 770 mV compared to **[Fe]$^{2+}$**. This marked difference in multielectron redox behavior correlates with observed photocatalytic CO_2RR reactivity. Indeed, the **[Fe]$^{2+}$** complex is compatible with photosensitizers spanning reduction potentials over a range of 1 V and can promote efficient light-driven CO_2 reduction with high activity and selectivity, achieving up to 99% CO product selectivity with total TON and initial TOF exceeding 30,000 and 900 min^{-1}, respectively, whereas the **[Co]$^{2+}$** complex shows much lower CO_2RR activity under similar conditions (ca. 600 TON, 83% CO product selectivity). Density functional theory (DFT) calculations support these experimental findings by suggesting that the first reduction of **[Co]$^{2+}$** to **[Co]$^+$** is metal-centered, and that the second reduction to **[Co]^0** is accompanied by a significant rearrangement of electrons that enforces exchange coupling between a formal Co^{2+} center and a two-electron reduced ligand, resulting in a paramagnetic open-shell doublet. This electronic structure differs from the two-electron reduction of **[Fe]$^{2+}$**, resulting in a diamagnetic, open-shell singlet **[Fe]^{0}** complex between a formal Fe^{2+} center and a two-electron reduced ligand. As such, we attribute the superior catalytic performance of the iron system over the cobalt congener to the more stable electronic configuration for reduced **[Fe]^{0}** vs **[Co]^{0}** driven by this metal-ligand exchange coupling. Taken together, these data highlight the importance of metal-ligand redox cooperativity in developing efficient CO$_2$RR catalysts, which can be carried forward as a design principle for a broader range of multielectron redox transformations of interest.

2. Results and Discussion

2.1. Synthesis and Structural Characterization of the [Co(tpyPY2Me)]$^{2+}$ Complex.

The [Co(tpyPY2Me)]$^{2+}$ complex ([Co]$^{2+}$) was obtained in nearly quantitative yield by stirring the ligand tpyPY2Me with an equimolar amount of the cobalt precursor [Co(OTf)$_2$(CH$_3$CN)$_2$] in dry CH$_3$CN at room temperature for 12 hours (Figure **2.**1a). Diffraction quality crystals for [Co]$^{2+}$ were obtained by slow vapor diffusion of diethyl ether into a saturated CH$_3$CN solution. The crystal structure of [Co]$^{2+}$ (Figure **2.**1b) shows its connectivity as a five-coordinate square pyramidal complex, analogous to the previously reported [Zn(tpyPY2Me)]$^{2+}$ analog.**[44]** Co–N$_{tpy}$ bond lengths range from 1.8975(17) to 1.9610(18) Å, consistent with a low-spin Co^{2+} configuration, exhibiting shorter bond lengths compared to high-spin Co d^{7} complexes with a similar coordination environment.**[59, 60]** Analysis of the two C$_{py}$–C$_{py}$ bonds within the terpyridine moiety and the C–N bonds of the terpyridine chelate rings (with average bond lengths of 1.471 and 1.356 Å, respectively) suggest that the ground state of [Co]$^{2+}$ bears a neutral tpyPY2Me ligand and a Co^{2+} metal center**[61]**; this assignment was supported by an effective magnetic moment of 1.8 μB determined by the Evans' method (Figure **2.**1b, **2.**9).

2.2. Electrochemical Characterization Reveals Differences in Redox Behavior, Catalytic Efficiency, and Reductive Stability Between [Co(tpyPY2Me)]$^{2+}$ and [Fe(tpyPY2Me)]$^{2+}$ for CO$_2$RR.

As a starting point to compare the redox properties of the **[Co]$^{2+}$** and **[Fe]$^{2+}$** complexes, we measured the cyclic voltammogram (CV) of **[Co]$^{2+}$** under an argon atmosphere. The CV shows a quasi-reversible wave at $E_{1/2}$ = +0.023 V vs Fc$^{+/0}$ and three reversible waves at $E_{1/2}$ = –0.81, –2.20, –2.34 V vs Fc$^{+/0}$ (Figure 2.2). Currents for all redox waves vary linearly with the square root of the scan rate, indicative of diffusion-controlled processes (Figure 2.8). The first wave at $E_{1/2}$ = +0.02 V vs Fc$^{+/0}$ is assigned to a Co$^{2+/3+}$ oxidation, as its quasi-reversible nature is characteristic for cobalt complexes exhibiting low/high spin transitions coupled to a redox process.[62-65] The second wave is assigned to a Co$^{2+/+}$ reduction process, which is positively shifted by +0.39 V compared to the Co^{2+} complex of bpy2PYMe, and consistent with an observed pattern of stabilization with increasing conjugation in pyridine-based redox active ligands.[65] We assign the latter two waves at $E_{1/2}$ = –2.20 and –2.34 V vs Fc$^{+/0}$ as ligand-centered reductions by comparison to the [Zn(tpyPY2Me)]$^{2+}$ analog bearing a redox-silent Zn^{2+} center, whose first two ligand-centered redox processes lie between –1.56 and –2.41 V vs Fc$^{+/0}$.[44] This electrochemical behavior contrasts with the two closely-spaced ligand-dependent reductions in [Fe]$^{2+}$ centered at –1.43 V vs Fc$^{+/0}$ [44] (Figure 2.2). As such, the change from iron to cobalt shifts the first two reductions in a negative direction by 770 mV, indicating a significant difference in the thermodynamic stability of metal-ligand electronic coupling in the reduced cobalt complex compared to its iron congener.

We next moved on to screen **[Co]$^{2+}$** for electrochemical CO_2RR reactivity. Upon addition of CO_2, we observe a current enhancement, which increases further upon the addition of 0.1 M phenol as an acid source (Figure 2.3a). Under an Ar atmosphere, the addition of 0.1 M phenol results in a larger relative current enhancement, indicative of HER reactivity (Figure 2.3b). We then measured product selectivity and long-term catalyst stability via controlled potential electrolysis (CPE) experiments conducted at various applied potentials. Initially, we used glassy carbon (GC) as a working electrode for CPE experiments; however, the current density asymptotically decays within the first 50 seconds at the selected potentials (Figure 2.10a). CVs recorded before and immediately after electrolysis show a total loss in current response; upon polishing the GC electrode after electrolysis and resubmerging in the same electrolysis cell, the voltammograms show recovery of the same pre-electrolysis wave (Figure 2.10c). This behavior is indicative of catalyst deposition onto the working electrode, resulting in an inactive film that limits charge transfer during the electrolysis experiment. To limit this deposition, we turned to the use of reticulated vitreous carbon (RVC) foam as a carbon-based electrode with higher surface area for further electrolysis experiments. Use of RVC foam led to a modest enhancement in the stability and enabled more charge to be passed during the electrolysis experiment (Figure 2.10d, e). At an applied potential of –2.09 vs $Fc^{+/0}$ under a CO_2 atmosphere in the presence of 0.1 M phenol, **[Co]$^{2+}$** achieved 64% faradaic efficiency for CO formation (Table 2.2). During CPE experiments with the RVC working electrode, we observed a color change in the electrolyte that was not observed when the GC working electrode was used, where the pale orange-colored solution characteristic of **[Co]$^{2+}$** converted to a dark red purple-colored solution. We speculate that this species is most likely the two-electron reduced species, **[Co]^0**, based on a similar color change observed for the chemical reduction of **[Fe]$^{2+}$** to **[Fe]^0** using decamethylcobaltocene.[44] We have not yet been successful in isolating the reduced cobalt species owing to its redox instability, but its appearance in bulk solution suggests that it contributes to the lower Faradaic efficiency and electrochemical stability observed for the cobalt catalyst relative to the iron analog.

2.3. Evaluation of [Co(tpyPY2Me)]$^{2+}$ as a Catalyst for Photochemical CO_2RR.

Building upon these electrochemical results, we reasoned that moving to photochemical CO_2RR would enable lower catalyst loading (1 mM for electrolysis to 2 μM for photolysis, *vide infra*) to mitigate unproductive [Co]^0 accumulation by dispersing it in solution as opposed to concentrating the reduced species at the electrode double layer. Indeed, in a photocatalytic system, electron transfer operates via the bimolecular reaction of the catalyst with a photosensitizer; thus, we expected improved catalyst stability relative to the electrolysis experiments. As a starting point, we evaluated [Co]$^{2+}$ as a catalyst for photochemical CO_2RR. In a typical experiment, 2 μM [Co]$^{2+}$ was added to a CO_2-saturated CH_3CN solution containing 200 μM photosensitizer, 50 mM triethylamine (TEA) as a sacrificial electron donor, and 1 M phenol as a proton source. Reactions were irradiated in 1-hour intervals using a blue LED light source. Multiple photosensitizers were chosen for screening owing to their close energy match to reduction waves of [Co]$^{2+}$, including $[Ru(bpy)_3]^{2+}$ (RuPS, E^0= –1.71 V vs $Fc^{+/0}$), as well as the iridium complexes $[Ir(dFCF_3ppy)_2(dtbbpy)]^+$ (IrPS-1, E^0 = –2.39 V vs $Fc^{+/0}$) and $Ir(ppy)_3$ (IrPS-2, E^0= –2.61 V vs $Fc^{+/0}$) (Figure **2**.4a). Results of photochemical CO_2RR screening studies show some improvements and similarities in activity trends compared to electrochemical CO_2RR experiments (Figure 2.11, Table 2.3). The average activity of the IrPS-1 system over a 15-hour period shows that in the first hour, CO_2 reduction is 93% selective for CO with an average TON of 120. Data collected at subsequent timepoints show a marked drop in activity as well as a loss of CO_2RR selectivity down to 50-57% CO product due to increased HER. We hypothesized that the modest observed CO_2RR activity may be a consequence of inefficiencies in photocatalytic system design, in particular the requirement for a high concentration of acid that may participate in hydrogen bonding with the basic TEA sacrificial electron donor, which can possibly lower its quenching efficiency. We turned to 1,3-dimethyl-2-phenyl-2,3-dihydro-1H-benzo[d]imidazole (BIH) as a replacement for TEA, which has literature precedent as an excellent quencher for photocatalytic CO_2 reduction using organic, ruthenium- and iridium-based photosensitizers.**[20, 39, 45, 66, 67]** With 100 mM BIH, $[Co]^{2+}$ exhibits a switch in selectivity from CO_2RR to HER using either RuPS or IrPS-1 as a photosensitizer, with an average H_2 TON of 488 achieved in one hour. Lowering the BIH concentration to 50 mM improves the selectivity to 67-83% CO, with IrPS-1 giving the highest TON of 647 in one hour of photolysis. Despite observed gains in activity and selectivity with lower BIH loading, reactions still show a loss in CO_2RR selectivity beyond the first hour, analogous to results obtained with TEA, indicating that lowering BIH loading only slowed off-pathway H_2 evolution and deactivation pathways rather than eliminating them. Indeed, dynamic light scattering experiments confirm that within 15-30 min of irradiation, $[Co]^{2+}$ decomposes into a particulate species with sizes in the range of 100 to 1000 nm under catalytic conditions (Figure 2.12a), showing that photochemical CO_2RR reactivity is ultimately limited by the stability of the catalyst under reductive conditions.

2.4. $[Fe(tpyPY2Me)]^{2+}$ Shows Superior Catalytic Activity to the $[Co(tpyPY2Me)]^{2+}$ for Photochemical CO_2RR.

We then turned our attention to $\mathbf{[Fe]^{2+}}$ as a catalyst for photochemical CO_2RR, anticipating that it would exhibit better activity, selectivity, and stability compared to $\mathbf{[Co]^{2+}}$ considering its two-electron reduction at more positive potentials and superior performance as an electrochemical CO_2RR catalyst. Optimization of photocatalysis in CH_3CN solution with 1 M phenol as a proton source led us to screen a range of organic and noble-metal photosensitizers compatible under these conditions. These photosensitizers include the mildly reducing organic dye Acriflavine (**Acr**, $E^0 = -1.53$ V vs $Fc^{+/0}$), whose reduction potential lies just 100 mV more negative than the catalytically relevant $\mathbf{[Fe]^{2+}}$ reduction, as well as **RuPS** and the highly reducing **IrPS-1** and **IrPS-2** sensitizers discussed previously (Figure 2.4a). In a typical experiment, 2 μM $\mathbf{[Fe]^{2+}}$ catalyst was added to a CO_2-saturated CH_3CN solution containing 200 μM photosensitizer, 100 mM BIH as a sacrificial electron donor, and 1 M phenol as a proton source. The reactions were irradiated in either 15- or 30-minute intervals using a blue LED light source. We first examined photocatalysis using the **RuPS**/BIH system; a TOF of 916 min^{-1} is reached within the first 15 minutes of the reaction, which to the best of our knowledge is the highest reported TOF value for CO_2RR driven by a molecular catalyst.[25] A plateau is reached after 30 minutes (Figure 2.4b), resulting in a total TON of 15,520 with 99% selectivity for CO product with negligible H_2 evolution. During this time, we observe bleaching of the photosensitizer from a bright orange to pale yellow color, indicating degradation of **RuPS**. This degradation has been reported to proceed by dissociation of bipyridine ligands from the Ru center during light irradiation.[65, 68] We confirmed that replenishing **RuPS** with BIH and phenol could partially recover activity of $\mathbf{[Fe]^{2+}}$ after the initial plateau, resulting in a maximum TON of 24,069 for CO production after a total of 75 min (Figure 2.4c). Photocatalytic activity could be further amplified by lowering the catalyst loading to 0.2 μM, achieving a TON of 30,349 within 45 minutes while still producing 30 μmols of CO with 97% product selectivity (Table 2.1, Entry 2). Control experiments performed confirm that the catalyst, photosensitizer, sacrificial electron donor, proton source, and CO_2 are all essential for the reaction to proceed (Table 2.1, Entries 4-7). Moreover, in contrast to the cobalt system, dynamic light scattering (DLS) measurements of the reaction mixture before and during peak catalytic activity at 0, 15, and 30 minutes confirm that the iron system is homogeneous, with no evidence of particle formation under photocatalytic conditions (Figure 2.12b).

We then employed Stern-Volmer analysis for the excited state quenching of **RuPS** using BIH and **[Fe]$^{2+}$** to probe the mechanism for photocatalysis (Figure 2.5). The bimolecular quenching rate constants (k_q) obtained for **[Fe]$^{2+}$** (2.7 x 10^9 $M^{-1}s^{-1}$) and BIH (2.2 x 10^9 $M^{-1}s^{-1}$) are comparable, indicating that oxidative and reductive quenching mechanisms are both accessible, but we reason that the large excess of BIH used relative to **[Fe]$^{2+}$** in the system will favor the reductive quenching pathway. [69] The quantum yield for CO production from the **RuPS** system with 2 μM **[Fe]$^{2+}$** was determined to be Φ= 11.1% by ferrioxalate actinometry.

As such, we turned our attention to the water-soluble organic dye **Acr**, which has a similar redox potential to Purpurin and has been reported for photocatalytic water splitting and CO_2 reduction at 400 μM concentrations in CH_3CN/H_2O mixtures.[57, 70] The maximum solubility of **Acr** in pure CH_3CN is approximately 125 μM. The use of a less reducing photosensitizer at lower concentrations led to slower photochemical CO_2RR catalysis, with a TON of 6,710 with 100% selectivity for CO product obtained after 2 hours of photolysis. We observe a gradual decrease in activity over time, likely due to the decomposition of the photosensitizer, as evidenced by bleaching observed much like with **RuPS**. These results establish a highly selective and active noble-metal free molecular system for catalytic photochemical CO_2RR using **Acr** and **[Fe]$^{2+}$** components.

Finally, we examined **[Fe]$^{2+}$**-catalyzed photochemical CO_2RR with the iridium-based photosensitizers **IrPS-1** and **IrPS-2** to provide a direct comparison with results obtained using **[Co]$^{2+}$**. In addition, Ir-C cyclometallation in these complexes provides longer photostability compared to **RuPS** and **Acr**,[71] providing an opportunity to probe contributions of photosensitizer stability to CO_2RR catalysis. Using **IrPS-1** as a photosensitizer with 2 μM **[Fe]$^{2+}$** as a CO_2RR catalyst results in a TON of 12,749 with 98% selectivity for CO (Table 2.1, Entry 8), representing a 20-fold improvement over **[Co]$^{2+}$**. Lowering the catalyst concentration to 0.2 μM gives a two-fold higher TON of 28,712 but with only 81% CO selectivity (Table 2.1, Entry 9). Using **IrPS-2** drives the highest TON of 18,502 at 2 μM **[Fe]$^{2+}$** catalyst loading conditions (Table 2.1, Entry 10). Interestingly, the plateau in catalytic activity observed using **IrPS-2** shows distinct behavior compared with the one observed with **RuPS**, since the former photosensitizer is cyclometalated and should not be the source of system deactivation. Indeed, we found that for the **IrPS-2** system, introduction of additional **[Fe]$^{2+}$**, but not BIH and phenol, can enable recovery of activity (Figure 2.13), in contrast to the **RuPS** system where replenishing with **RuPS**/BIH/phenol can restore catalysis (Figure 2.4c). These results suggest that using the more reducing iridium photosensitizers can drive rapid photochemical CO_2RR with high selectivity for CO production but also accelerate catalyst deactivation. Key results obtained for use of **[Fe]$^{2+}$** as a photocatalyst with all four photosensitizers and control experiments using are summarized in Table 1.

2.5. Electronic Structure Calculations for Reduced Iron, Cobalt, and Nickel tpyPY2Me Complexes Show Key Differences in Metal-Ligand Exchange Coupling that Correlate with Observed Redox and Catalytic Stability.

Computational predictions for the first and second reduction potentials of the $[\text{Co}]^{2+}$ complex, modeled as $[\text{Co(tpyPY2Me)(CH}_3\text{CN)}]^{2+}$, were obtained using DFT calculations employing ωB97X-V functionals and CH_3CN solvent. DFT analysis shows the first reduction of $[\text{Co}]^{2+}$ to $[\text{Co}]^{+}$ is a metal-centered process (Figure **2.**6, left), resulting in a singlet ground state (S = 0) and a predicted redox potential ($E^0 = -0.887$ V vs $\text{Fc}^{+/0}$) that is consistent with the experimental value (–0.81 V). Additional computational results from localized orbital bonding analysis (LOBA) confirm that the $[\text{Co}]^{+}$ complex can be described as a formal Co^{+} center bound to a neutral tpyPY2Me ligand. The first reduction is accompanied by the loss of the axial solvent ligand, resulting in a 5-coordinate $[\text{Co}]^{+}$ complex. DFT analysis of the doubly reduced $[\text{Co}]^{0}$ complex is consistent with the population of a ligand-based π* orbital belonging to the terpyridine fragment of the ligand (Figure **2.**6, right). The calculated redox potential ($E_0 = -2.22$ V vs $\text{Fc}^{+/0}$) matches the experimentally determined value ($E_{1/2} = -2.34$ V) and has a calculated spin state of S = 1/2. Interestingly, the spin density plot for $[\text{Co}]^{0}$ (Figure **2.**6c, right) suggests that this second reduction is accompanied by significant rearrangement of electrons occupying the metal d orbitals, leading to the population of a low-lying metal-ligand ($\pi^* + d_{z^2}$) orbital with concomitant reordering of Co-based electrons into a high-spin configuration. The computational results suggest that the $[\text{Co}]^{0}$ species exists as a formal Co^{2+} center bound to $(\text{tpyPY2Me}^{\bullet\bullet})^{2-}$. Taken together, these results highlight an intriguing outcome of formal oxidation of the metal center through reduction of the overall complex, made possible via delocalized reduction events as a result of metal-ligand exchange coupling. Coordinates of the optimized structures for $[\text{Co}]^{+}$ and $[\text{Co}]^{0}$ obtained using the ωB97X-D functional are shown in tables (Table 2.7, 2.8).

The reduction pathway of $[\text{Co}]^{2+}$ contrasts with computational studies of the analogous $[\text{Ni}]^{2+}$ and $[\text{Fe}]^{2+}$ complexes.[44, 53] Figure **2.**7 highlights how slight changes in the central metal orbitals lead to substantive changes in the metal-ligand orbital interactions and on the overall outcome of reduction events. Apart from affecting coordination number via loss of the axial solvent ligand, the molecular orbitals shown in Figure **2.**7 show distinct differences in the type of reduction event taking place within the complexes. Indeed, in contrast to the metal-centered one-electron reduction of $[\text{Co}]^{2+}$ to $[\text{Co}]^{+}$ to generate a complex with a formally reduced Co^{+} center bound to a neutral tpyPY2Me ligand, one-electron reductions of $[\text{Fe}]^{2+}$ and $[\text{Ni}]^{2+}$ involve a primarily ligand-centered event, resulting in $[\text{Fe}]^{+}$ and $[\text{Ni}]^{+}$ complexes with formal Fe^{2+} and Ni^{2+} centers bound to a reduced $(\text{tpyPY2Me}^{\bullet})^{-}$ ligand. It is noteworthy that a comparison of the first reduction events for the iron, cobalt, and nickel analogs exhibit a continuum of all three primary outcomes for reducing a transition metal complex bound to a redox-active ligand: (1) a pure ligand-based reduction (Fe), (2) a pure metal-based reduction (Co), and (3) a ligand-based reduction with a large character of coupling between a metal d orbital and ligand π* orbital, resulting in a broken symmetry configuration (Ni).

Despite the marked differences in electronic structure for the singly-reduced forms of the iron, cobalt, and nickel tpyPY2Me complexes, all three metals share similar electronic character upon introduction of a second reduction event. Comparing DFT results obtained for $[\text{Co}]^{0}$ (Figure **2.**6, right) to those of $[\text{Fe}]^{0}$[44] and $[\text{Ni}]^{0}$,[53] we observe that each first-row transition complex adopts a high-spin, unreduced formal M^{2+} center bound to a doubly-reduced $(tpyPY2Me^{\bullet\bullet})^{2-}$ ligand. Thus, in the case of the second reduction event, the complexes differ only in the extent of d /π* orbital coupling between the metal atom and surrounding terpyridine ligand fragment.

3. Concluding Remarks

In summary, we have presented a comparative study of redox behavior for first-row transition metal complexes bearing the redox-active ligand tpyPY2Me and applications of iron and cobalt congeners for photochemical CO_2RR. In particular, we established that the $[Fe(tpyPY2Me)]^{2+}$ (**$[Fe]^{2+}$**) complex is an extremely active and selective catalyst for photochemical reduction of CO_2 to CO, achieving up to 99% CO product selectivity with total TON and initial TOF exceeding 30,000 and 900 min^{-1}, respectively. Electrochemical analysis shows that the **$[Co]^{2+}$** complex has a markedly higher thermodynamic barrier for reduction by two electrons compared to the **$[Fe]^{2+}$** analog, with a negative potential shift of 770 mV due to a large separation of the first and second reductions in the cobalt derivative. This difference in redox behavior is manifested in **$[Co]^{2+}$** showing lower activity, selectivity, and stability for electrochemical CO_2RR relative to **$[Fe]^{2+}$**, with electrode deposition and low faradaic efficiency observed during electrolysis for the former. These reactivity trends are mirrored in photochemical CO_2RR, where the **$[Fe]^{2+}$** system is 20-fold more active than the **$[Co]^{2+}$** congener under similar conditions. DLS analysis shows that photolysis of the cobalt system leads to formation of nanoparticles with loss of CO_2RR activity, whereas the iron system remains homogeneous, consistent with trends in electrochemical stability. Electronic structure calculations predict that the origin of the disparate redox behavior and catalysis observed for the **$[Fe]^{2+}$** and **$[Co]^{2+}$** complexes is the electronic configuration of the reduced species. Going from **$[Co]^{2+}$** to **$[Co]^{+}$**, a metal-centered reduction is predicted, which supports the observed loss in selectivity for CO_2RR and increased HER from a formal Co^{+} species. Subsequent reduction of **$[Co]^{+}$** to **$[Co]^{0}$** is accompanied by a significant rearrangement of electrons to a metal-ligand coupling interaction in the form of an open-shell doublet with a formal Co^{2+} center bound to a doubly-reduced $(tpyPY2Me^{\bullet\bullet})^{2-}$ ligand. Indeed, bulk electrolysis and photocatalysis experiments suggest that this open-shell doublet **$[Co]^{0}$** species is catalytically competent for reduction of CO_2 to CO but is not a stable species, leading to inactive film or nanoparticle formation. In contrast, two-electron reduction to **$[Fe]^{0}$**, which bears an open-shell singlet electronic configuration driven by metal-ligand exchange coupling, proceeds at potentials that are nearly 800 mV more positive compared to the cobalt analog and shows high activity for both electrochemical and photochemical CO_2RR. This work highlights the value of metal-ligand exchange coupling as a design principle for tuning multielectron reactivity, presaging the use of this concept for advancing a broader array of catalytic transformations.

4. Experimental Section

4.1 Electrochemical Measurements

All electrochemical measurements were performed using a Bioanalytical Systems, Inc. (BASi) Epsilon potentiostat. Cyclic voltammetry (CV) data were measured in a three-electrode cell equipped with a glassy carbon disk (3.0 mm diameter) working electrode, platinum wire counter electrode, and a silver wire in a porous Vycor tip glass tube filled with electrolyte as a pseudo-reference electrode. The final concentration of **$[Co]^{2+}$** or **$[Fe]^{2+}$** catalyst was 1 mM. The working electrode was polished prior to each experiment with 0.05-micron alumina powder on a felt pad. The electrolyte was 0.1 M tetrabutylammonium hexafluorophosphate (NBu_4PF_6) in dry CH_3CN and sparged with either Ar or CO_2 as indicated. At the conclusion of each experiment, the pseudo-reference potentials were referenced against ferrocenium/ferrocene ($Fc^{+/0}$) used as an external standard. The scan rates for all cyclic voltammograms were 100 mV/s unless otherwise noted. All voltammograms were obtained with iR compensation. Controlled potential electrolysis experiments were performed in a gastight PEEK electrolysis cell with a working compartment (12 mL liquid volume) and counter compartment (4 mL liquid volume) separated by an ultrafine glass frit. Either a 1 cm^2 glassy carbon plate (Tokai Carbon; Kanagawa, Japan) or a ~ 1 x 1 x 0.6 cm piece of 100 ppi (pores per linear inch) reticulated vitreous carbon foam (ERG Duocel; Oakland, CA) was used as the working electrode. A 2.5 cm diameter graphite planchet (Ted Pella; Redding, CA) was used as the auxiliary electrode, and an Ag wire in a Vycor tipped glass tube filled with electrolyte was used as a pseudo-reference electrode. The working compartment was filled with 12 mL of a 1 mM solution of catalyst dissolved in electrolyte (0.1 M NBu_4PF_6/CH_3CN) containing either 0.1 M or 1 M phenol as a proton source. The counter electrode chamber was filled with 4 mL of a 20 mM solution of tetrabutylammonium acetate dissolved in electrolyte. This soluble source of acetate was sacrificially oxidized to generate CO_2 and ethane, thereby preventing GC detection of solvent oxidation byproducts. Both compartments were sealed to be gastight. The working compartment was sparged with CO_2 for 10 min, then sealed and injected with 0.50 mL of ethane as a gaseous internal standard. A CV scan was collected prior to the CPE measurement to calibrate the potential. The electrolyte solution was constantly stirred during the CPE experiment with a 1 cm stir bar. At the conclusion of the experiment, the headspace was injected directly into an SRI-GC (model #8610C) equipped with 6' Hayesep D and 13X molecular sieve chromatographic columns. Two in-line detectors were used: a TCD for H_2 detection and an FID with a methanizer for $CO/CO_2/C_2H_6$ detection. Analytes of interest were quantified by comparing a ratios of analyte/internal stand peak integrals to a calibration curve with known amounts of analyte.

4.2 Photocatalytic CO_2 Reduction

Experiments were conducted inside a 25 mL borosilicate culture tube equipped with a stir bar, rubber septum, and aluminum crimped top. These reaction vessels contained 5 mL CH_3CN, 2 μM catalyst, 200 μM photosensitizer, 100 mM BIH (112 mg), and 1 M phenol (470 mg). The reaction tubes were sparged with CO_2 for 10 minutes, followed by injection of a gaseous internal standard (0.1 mL of C_2H_6). Reactions were placed on a stir plate 13 cm from two Kessil blue LED lamps (440 nm) for 15 or 30 minutes at a time and kept at ambient temperature with a fan. Analysis of the headspace by GC was conducted for product detection as described for above for CPE. Samples were then re-sparged with CO_2, and the process was repeated for the following timepoint of an experiment.

4.3 Computational Details

Density functional theory (DFT) calculations for free energies, reduction potentials and localized orbital bonding analysis (LOBA) oxidation state analysis were performed with the Q-Chem electronic structure package.[72] Geometry optimizations and frequency analysis were obtained using the ωB97X-D and a mixed basis set (def2-TZVP for metal Co center, def2-SVP for ligand main group elements). Solvation energies with CH_3CN solvent used to compute reduction potentials were approximated with single point calculations employing a C-PCM solvent model and the ωB97M- V functional with the def2-TZVP basis set for all atoms. For all reductions of **[Co]$^{2+}$**, the minimum energy spin configuration was identified through an exhaustive search of viable spin states at each reduction level. The differences in adiabatic free energy for higher lying spin states are reported with respect to the minimum energy configurations in Table 2.9. Additional density functionals were probed, including similar range-separated hybrid functionals such as ωB97X-D and CAM-B3LYP, but all yielded substantially less agreement with experimental values (Table 2.6). The ferrocenium/ferrocene couple (Fc$^{+/0}$) was used as an internal standard for our reported reduction potentials. The Fc$^{+/0}$ couple was calculated with each reported density functional before standardizing to optimize potential error cancellation.

4.4 Materials

Acriflavine (Sigma 95%), Ir(ppy)$_3$ (Sigma 99%), [Ir(dFCF$_3$ppy)$_2$(dtbbpy)]$^+$ (Strem 99%), triethylamine (Sigma 99.5%), phenol (Sigma 99%), NBu$_4$PF$_6$ (Sigma 99%), K$_3$[Fe(C$_2$O$_4$)$_3$] (Strem), and acetonitrile (Fisher), were purchased from commercial vendors and used as received. [Ru(bpy)$_3$]PF$_6$ was prepared via salt metathesis of [Ru(bpy)$_3$]Cl$_2$ (Sigma 99%) with NH$_4$PF$_6$ in water. 1,3-dimethyl-2-phenyl-2,3-dihydro-1H-benzo[d]imidazole (BIH) and tpyPY2Me were synthesized according to previously reported methods.

4.5 Fluorescence Quenching

The fluorescence of a CO$_2$-saturated CH$_3$CN solution of [Ru(bpy)$_3$]$^{2+}$ (λ_{abs}= 450 nm, λ_{em}= 601 nm) was measured using a Photon Technology International Quanta Master 4 L-format scan spectrofluorometer equipped with an LPS-220B 75-W xenon lamp and power supply, A-1010B lamp housing with integrated igniter, switchable 814 photocounting/analog photomultiplier detection unit, and MD5020 motor driver. Excited state quenching experiments were carried out by adding either BIH or **[Fe]$^{2+}$** in 100 μM increments. The relative emission lifetime of the photosensitizer in the presence of quencher was used to calculate the Stern-Volmer quenching constant (k$_q$) using the following equation:

$$I_0/I_Q = 1+ \tau_f k_q [Q]$$

where I_0/I_Q is the emission intensity in the absence (I_0) or presence (I_Q) of quencher, τ_f is the emission lifetime of [Ru(bpy)$_3$]$^{2+}$ (890 ns), and [Q] is the concentration of the quencher.

4.6 Quantum Yield Determination

The quantum yield (Φ) of photocatalytic CO$_2$ reduction to CO was calculated for a 90-minute experiment using 2 μM **[Fe]$^{2+}$**, 200 μM **RuPS**, 100 mM BIH, and 1 M Phenol in CO$_2$-saturated CH$_3$CN according to the equation:

where the number of photons per unit time (photon flux) emitted by the blue LED light source used during photocatalytic experiments was measured via chemical actinometry.

$$\Phi = \frac{2 \text{ (number of CO molecules)}}{\text{number of photons absorbed}} \text{ x } 100\ \%$$

We used ferrioxalate ($K_3[Fe(C_2O_4)_3]$) for the actinometry experiment. The photochemical decomposition of ferrioxalate (Fe^{3+}) to Fe^{2+} can be monitored spectrophotometrically via the detection of free Fe^{2+} by chelation with phenanthroline according to the simplified reactions:

First, a 3 mL (V_1) solution of ferrioxalate (0.012 M in 0.05M H_2SO_4) was irradiated for 10, 20, and 30 seconds while another solution of the same volume was kept in the dark. A 0.5 mL (V_2) aliquot of the irradiated solution was then added to a 2 mL solution of buffered phenanthroline (0.1% phenanthroline in 1.6 M NaOAc/0.5 M H_2SO_4) and then diluted with deionized water in a 25 mL (V_3) volumetric flask. This final solution was used for absorption measurement at 510 nm using an l=1 cm quartz cuvette.

$$Fe^{3+} \xrightarrow{\Delta} Fe^{2+}$$

$$Fe^{2+} + 3\ \text{phen} \longrightarrow \underset{\lambda_{max} = 510\ \text{nm}}{[Fe(phen)_3]^{2+}}$$

The moles of Fe^{2+} formed in an irradiated solution can be calculated by:

$$\text{moles } Fe^{2+} = \frac{V_1 \times V_3 \times \Delta A_{510}}{10^3 \times V_2 \times l \times \varepsilon_{510}}$$

Where ΔA_{510nm} is the difference in absorption between the solution kept in the dark and the irradiated solution, and ε_{510nm} is the molar absorptivity of $[Fe(phen)_3]^{2+}$ at 510 nm (11100 L mol^{-1} cm^{-1}). The average photon flux was then calculated following equation:

$$\#\ \text{photons/sec} = \frac{6.022 \times 10^{23} \times \text{moles } Fe^{2+}}{\Phi_\lambda \times t}$$

where Φ_λ is excitation wavelength dependent quantum yield of ferrioxalate.

4.7 Dynamic Light Scattering

Dynamic light scattering (DLS) measurements were performed using a Zetasizer Nano instrument (ZEN3600 Malvern Instrument) with a scattering angle of 173°, at 23 °C. Photocatalytic CO_2 reduction experiments using either **[Co]**$^{2+}$ or **[Fe]**$^{2+}$ as a catalyst were monitored by DLS after 0, 15, and 30 minutes of irradiation.

5. Figures

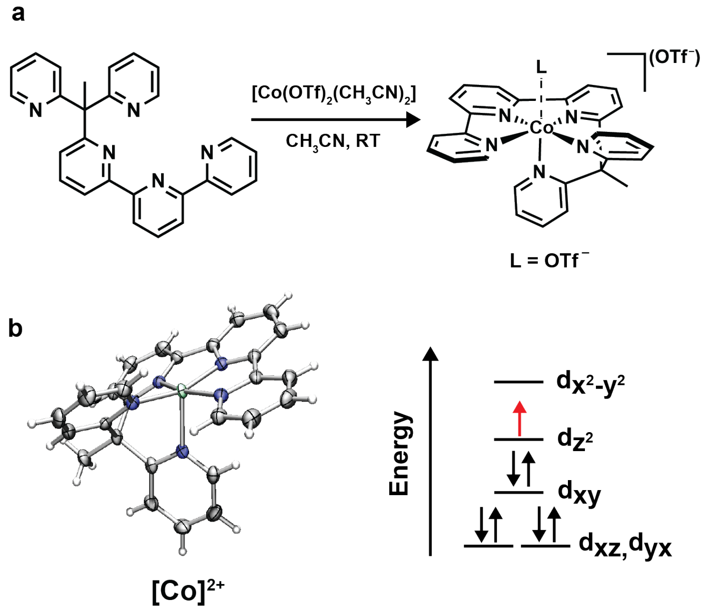

Figure 2.1. a) Synthetic scheme and (b) X-ray crystal structure for the [Co(tpyPY2Me)]$^{2+}$ (**[Co]$^{2+}$**) complex, with its simplified crystal field splitting diagram. Thermal ellipsoids are plotted at 80% probability.

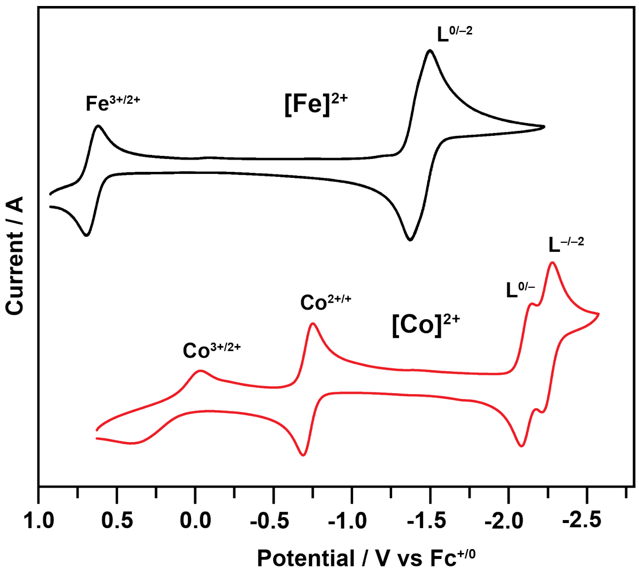

Figure 2.2. Cyclic voltammograms of **[Fe]$^{2+}$** (black) and **[Co]$^{2+}$** (red). Conditions: 1 mM [M(tpyPY2Me)]$^{2+}$ complex, 0.1 M NBu_4PF_6 in CH_3CN under Ar atmosphere using a glassy carbon electrode.

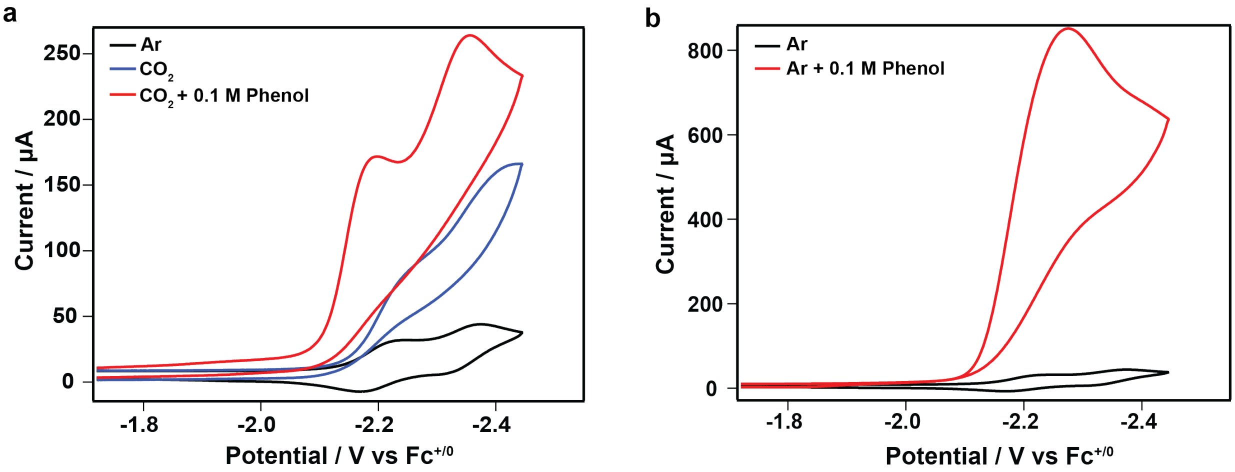

Figure 2.3. Cyclic voltammograms showing catalytic responses upon addition of 0.1 M phenol to **[Co]**$^{2+}$ (a) under CO_2 or (b) Ar atmosphere. Conditions: 1 mM **[Co]**$^{2+}$ in 0.1 M NBu_4PF_6/CH_3CN using a glassy carbon electrode.

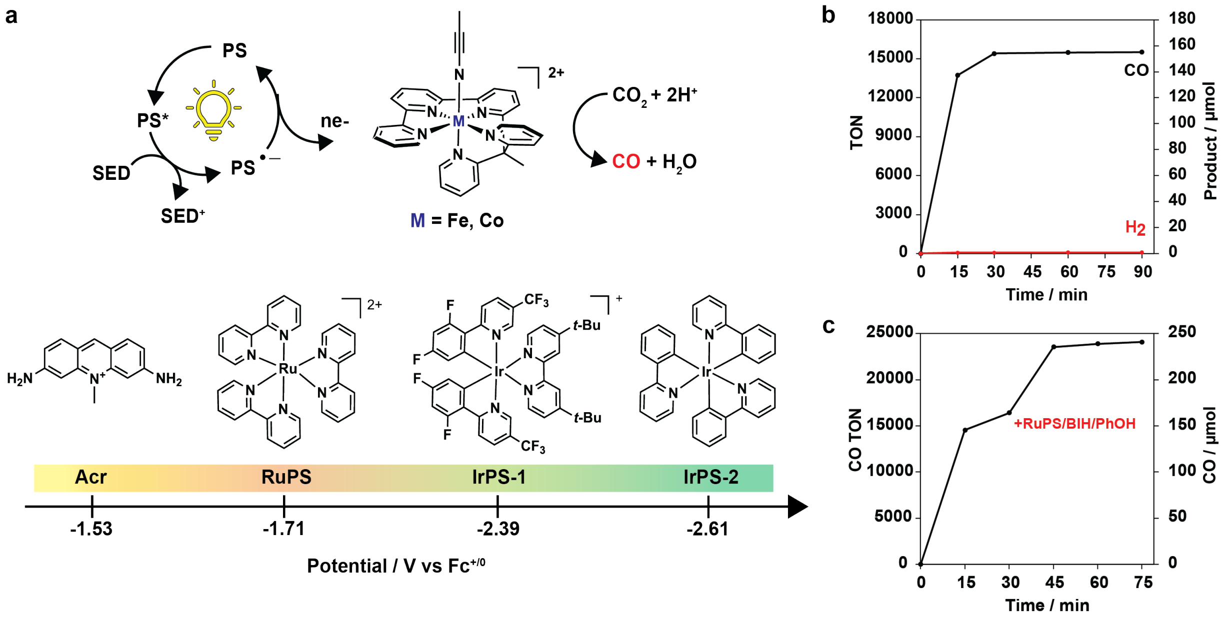

Figure 2.4. (a) Photochemical CO_2 reduction reactions catalyzed by iron and cobalt tpyPy2Me complexes, **[Fe]**$^{2+}$ and **[Co]**$^{2+}$, using **Acr**, **RuPS**, **IrPS-1**, and **IrPS-2** as photosensitizers with increasing driving forces for reduction. (b) Photocatalytic activity of **[Fe]**$^{2+}$ over 90 minutes and (c) with replenishing the photosensitizer, sacrificial electron donor, and proton source every 30 minutes. Conditions: 2 µM [**Fe]**$^{2+}$, 200 μM **RuPS**, 100 mM BIH, 1 M Phenol in CO_2-saturated CH_3CN solution.

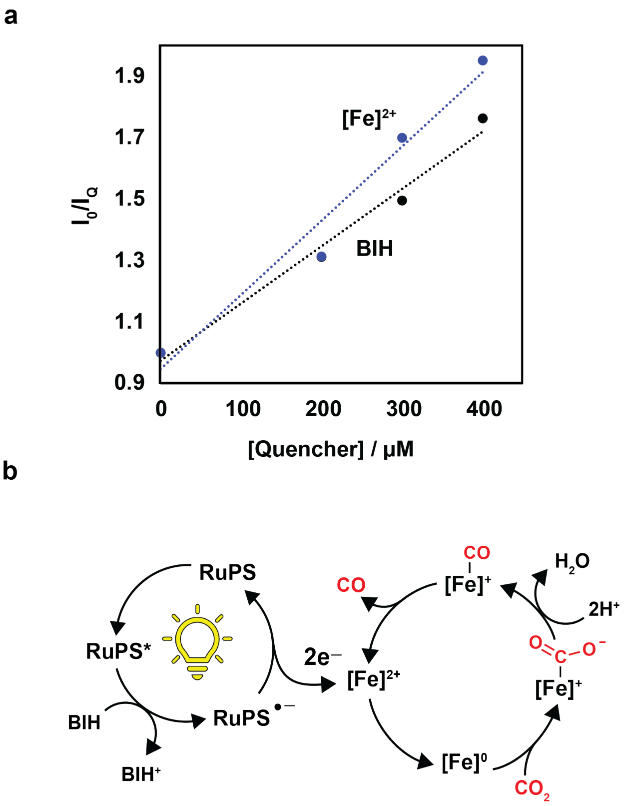

Figure 2.5. (a) Stern-Volmer plots for **RuPS** quenching with $[Fe1]^{2+}$ and BIH. Conditions: 50 µM **RuPS** with BIH in a CO_2 saturated CH_3CN solution. (b) Predicted reductive quenching mechanism for photocatalytic CO_2 Reduction using **$[Fe]^{2+}$** as the catalyst, BIH as the sacrificial electron donor, and RuPS as the photosensitizer.

Table 2.1. Photocatalytic activity of **[Fe]**$^{2+}$ under various conditions.

	TON		**Product (µmol)**		**Selectivity (%)**
Entry	**CO**	**H$_2$**	**CO**	**H$_2$**	**CO**
1	15520	86	155	0.86	99
2[a]	30349	1013	30	1	97
3[b]	43	52	0.4	0.5	52
4[c]	112	0	1.1	0	100
5[d]	150	0	1.5	0	100
6[e]	6	0	0	0	100
7[f]	0	222	0	2.2	0
8[g]	12749	163	127	1.6	98
9[h]	28712	6527	28	6.5	81
10[i]	18502	141	185	1.4	99
11[j]	6710	0	67	0	100

Reaction conditions: Standard conditions using 2 µM **[Fe]**$^{2+}$ catalyst, 200 µM **RuPS** photosensitizer, 100 mM BIH quencher, and 1 M phenol as a proton source in 5 mL of CO_2-saturated CH_3CN solution, irradiated for 90-120 minutes unless otherwise noted. [a] Using 0.2 µM catalyst. [b] Without catalyst. [c] Without **RuPS**. [d] Without BIH. [e] Without phenol. [f] Under Ar atmosphere. [g] Using 200 µM **IrPS-1** at 2 µM and [h] 0.2 µM catalyst loading. [i] Using 200 µM **IrPS-2**. [j] Using 125 µM Acriflavine (**Acr**).

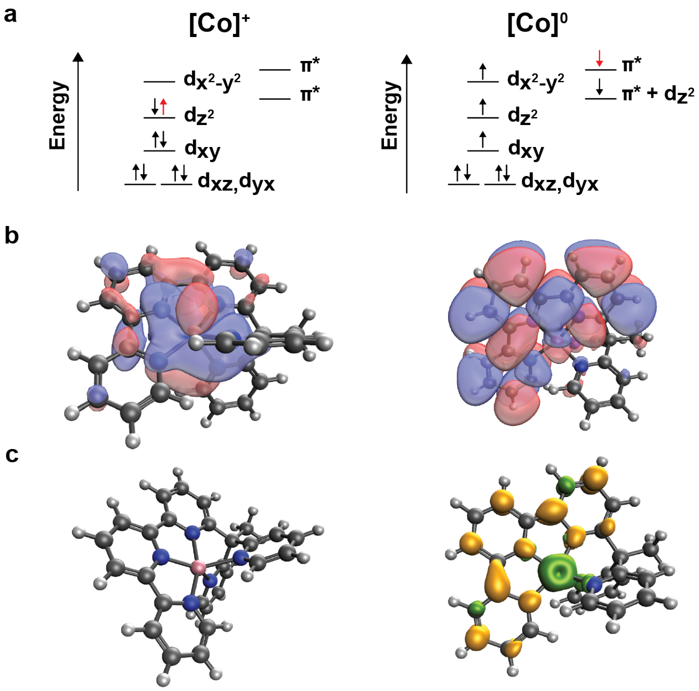

Figure 2.6. DFT analysis of electrochemically accessible reduced species, **[Co]**$^{+}$ and **[Co]**$^{\mathbf{0}}$. For each reduced species, the following are shown: (a) qualitative molecular orbital diagram consistent with DFT calculations, with newly added electrons highlighted in red; (b) relevant computed MO and (c) the computed spin density plot. The DFT results show that the first reduction is cobalt-centered to generate a formal Co^{+} species, whereas the second reduction is ligand-centered, leading to a substantial rearrangement of electron density resulting in restoration of a formal Co^{2+} complex with a doubly-reduced tpyPY2Me ligand.

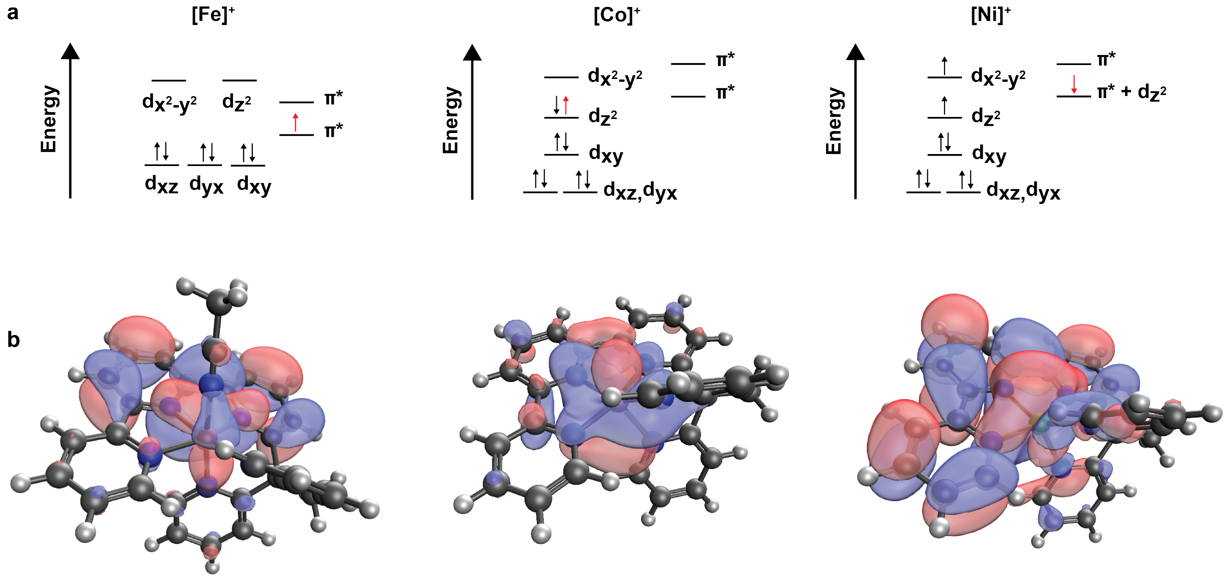

Figure 2.7. DFT analysis comparing varying metal-ligand redox behavior of iron, cobalt, and nickel metal centers bound to a redox-active tpyPY2Me ligand framework upon one-electron reduction. For each complex the resulting first reduction of **[M]**$^{2+}$ to **[M]**$^{+}$ is shown with: (a) qualitative molecular orbital diagram consistent with DFT calculations, with newly added electrons highlighted in red; (b) relevant computed molecular orbitals. The results show that the one-electron reduction of **[Co]**$^{2+}$ is primarily metal-centered while the **[Fe]**$^{2+}$ and **[Ni]**$^{2+}$ analogs are ligand-centered.

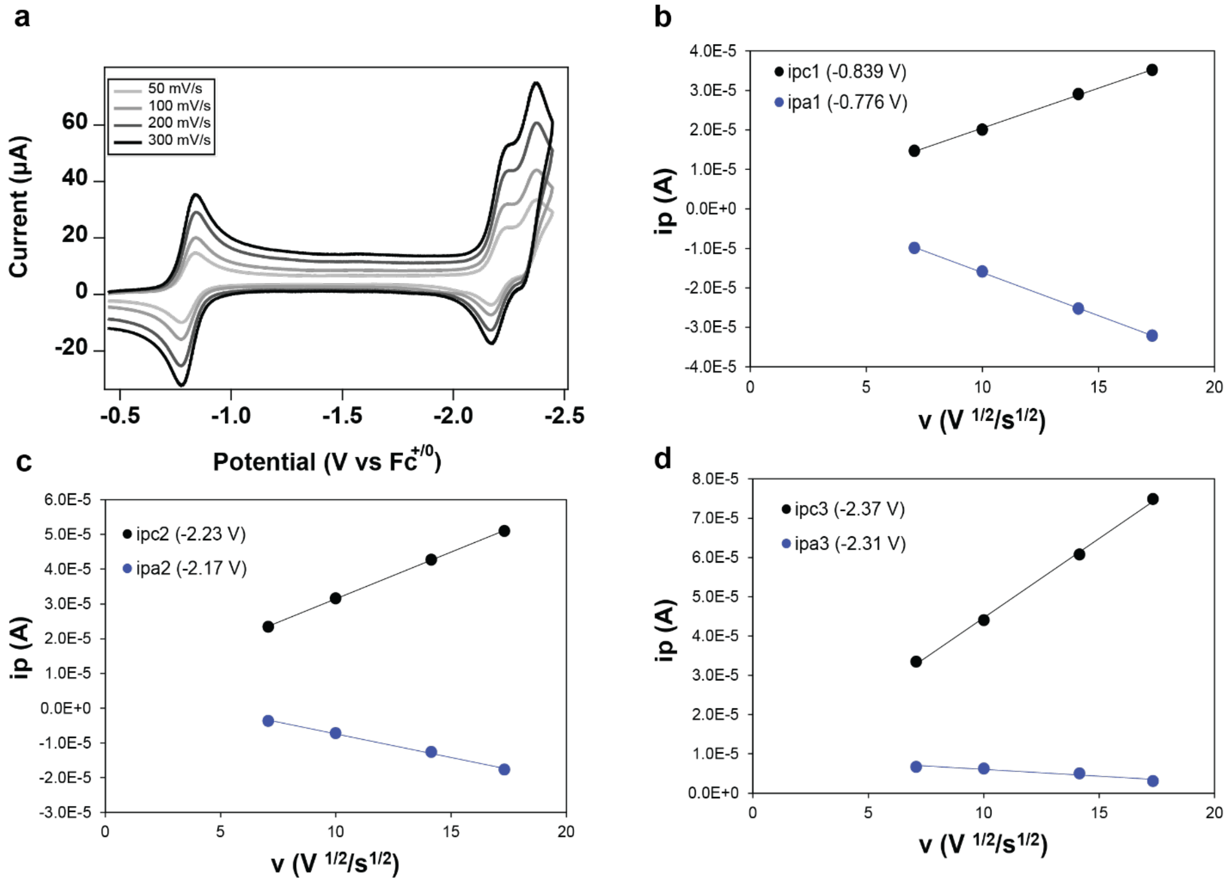

Figure 2.8. Scan rate dependent cyclic voltammograms (CVs) of **[Co]**$^{2+}$. (a) CVs recorded at scan rates ranging from 50 to 300 mV/s. (b) Peak current (ip) vs square root of the scan rate (ν) for Co$^{2+/+}$ centered at −0.81 V vs Fc$^{+/0}$, (c) L$^{0/-}$ at −2.2 V vs Fc$^{+/0}$ and (d) L$^{-/-2}$ at −2.34 V vs Fc$^{+/0}$. Conditions: 1 mM **[Co]**$^{2+}$ in 0.1 M NBu_4PF_6/CH_3CN under Ar atmosphere using a glassy carbon electrode.

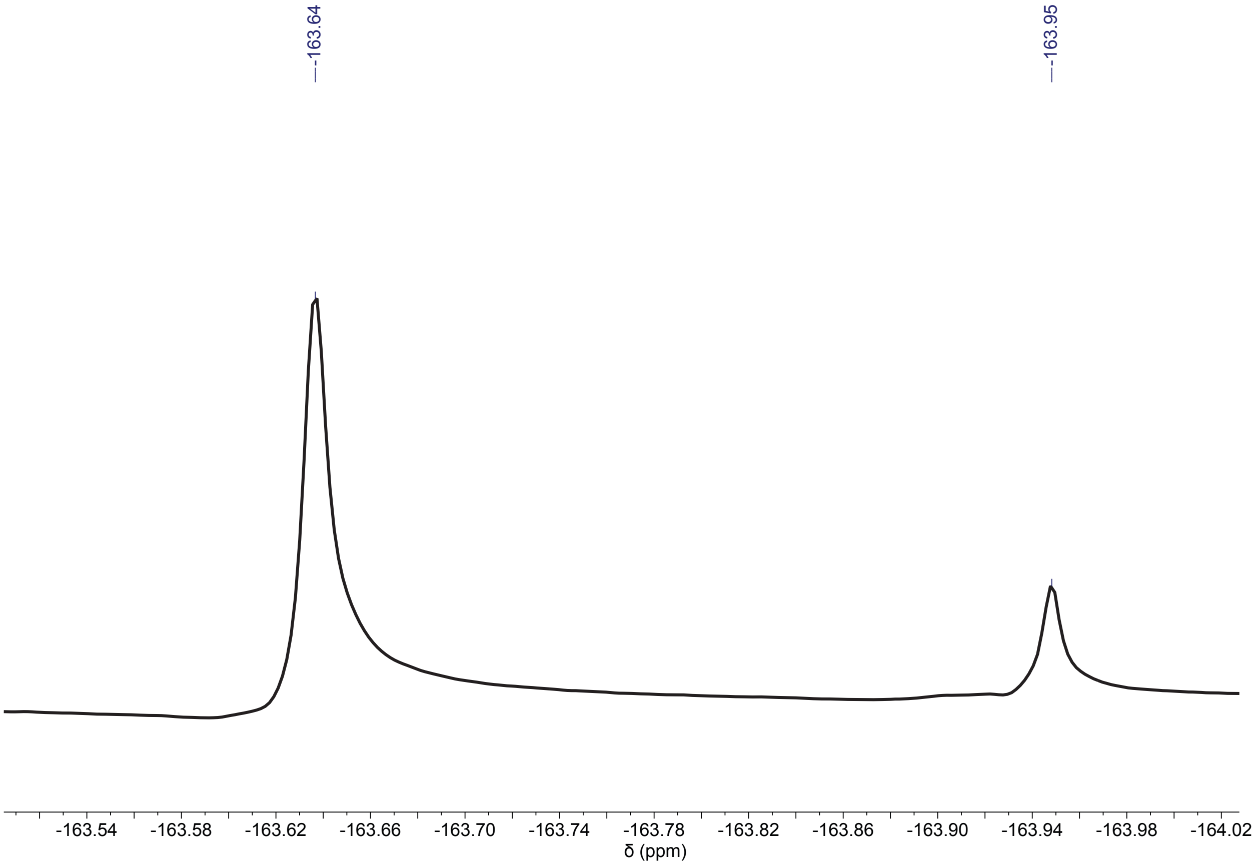

Figure 2.9. Evans' method analysis of **[Co]$^{2+}$** measured in CD_3CN by ^{19}F NMR at 293 K. Hexafluorobenzene was used as an internal standard.

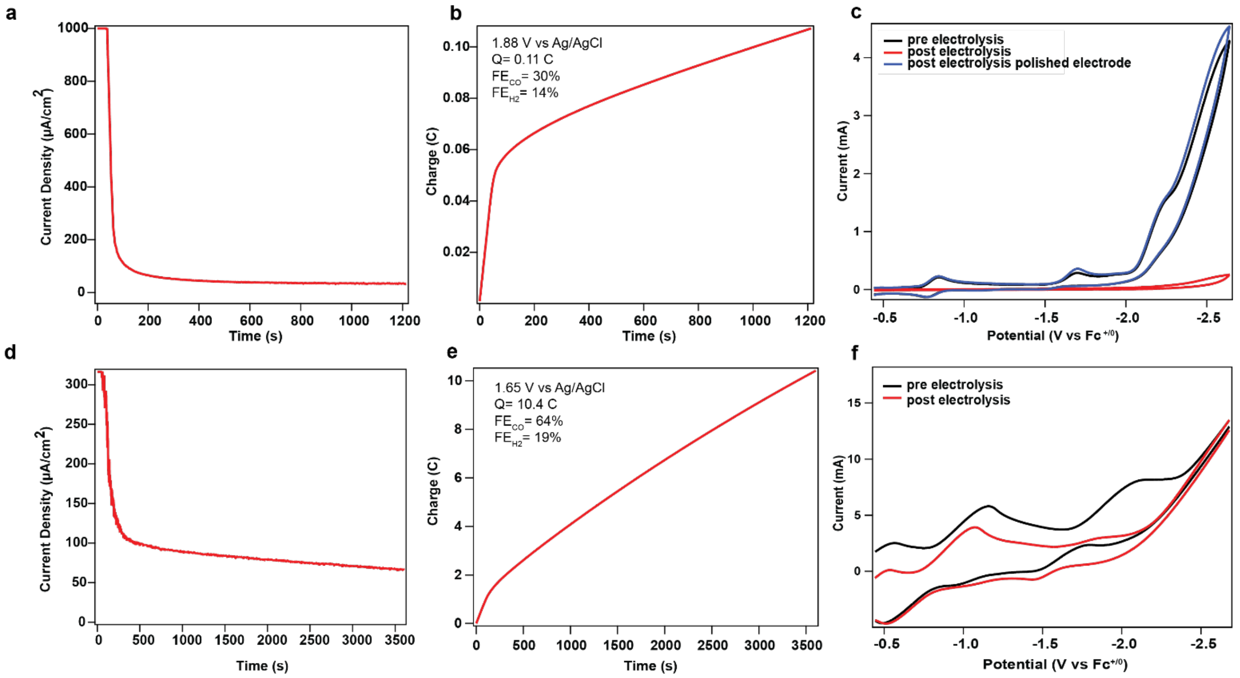

Figure 2.10. Controlled potential electrolysis (CPE) experiments using **$[Co]^{2+}$**. (a) Glassy carbon (GC) working electrode current density plot, (b) total charge passed and (c) pre- and post-electrolysis cyclic voltammograms (CVs) for a 30-minute experiment with an applied potential of –2.24 V vs $Fc^{+/0}$. (d) Reticulated vitreous carbon (RVC) working electrode current density plot, (e) total charge passed and (f) pre- and post-electrolysis CVs with an applied potential of –2.09 V vs $Fc^{+/0}$.

Table 2.2. Summary of CPE data obtained for **[Co]**$^{2+}$.

Working Electrode	**[Phenol]**	**Applied Potential (V vs Fc$^{+/0}$)**	**Charge Passed (C)**	**FE$_{CO}$ %**	**FE$_{H2}$%**	**CO Selectivity %**
1 cm^2 glassy carbon plate	0.1 M	–2.32	0.68	25.1	0.66	95
1 cm^2 glassy carbon plate	1 M	–2.24	0.11	30	14	52
31.6 cm^2 RVC foam	1 M	–2.09	10.4	63.76	18.40	63
39 cm^2 RVC foam	0.1 M	–2.42	8.6	13.25	11.88	36
35.1 cm^2 RVC foam	0.1 M	–2.32	15	8.93	11.47	28

Conditions: 1 mM **[Co]**$^{2+}$, 0.1 M NBu_4PF_6/CH_3CN saturated with CO_2.

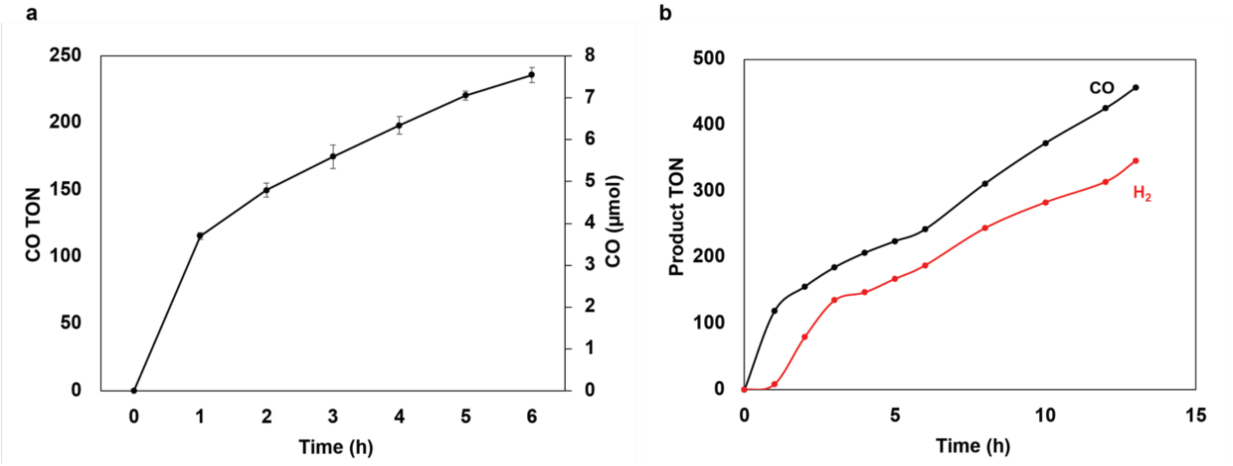

Figure 2.11. Photocatalytic activity of **[Co]**$^{2+}$ (a) on average over a 6-hour period and (b) over a 15-hour period showing both CO and H_2 production. Conditions: 2 µM **[Co]**$^{2+}$, 200 µM **IrPS-1**, 50 mM TEA, and 1 M phenol in CO_2-saturated CH_3CN solution.

Table 2.3. Summary of Photocatalytic activity of **$[Co]^{2+}$**

Photosensitizer (200 µM)	**Sacrificial Electron Donor**	**[Acid]**	**CO TON/h**	**H_2 TON/h**	**CO Selectivity (%)**
RuPS	100 mM BIH	1 M PhOH	170	464	27
IrPS-1	100 mM BIH	1 M PhOH	122	512	19
IrPS-2	50 mM BIH	1 M PhOH	256	655	28
IrPS-1	50 mM BIH	1 M PhOH	647	132	83
RuPS	50 mM BIH	1 M PhOH	376	189	67
IrPS-1	50 mM TEA	1 M PhOH	120	8	94
IrPS-1	50 mM TEA	0.5 M PhOH	13	58	18
IrPS-1	50 mM TEA	0.1 M 4-Cl-PhOH	14	72	17
IrPS-1	50 mM TEA	100 mM TFE	18	29	38

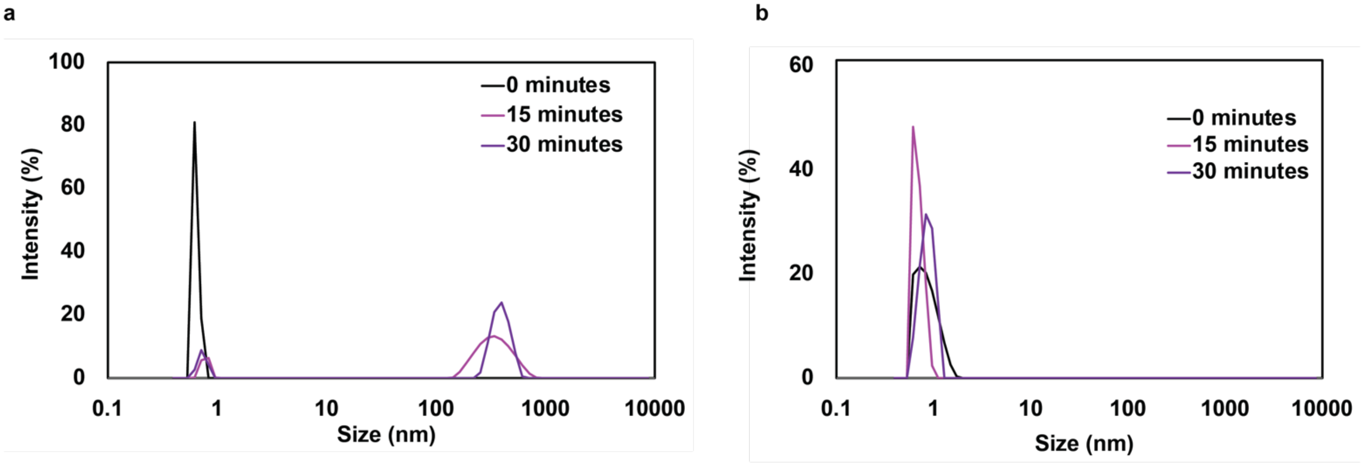

Figure 2.12. Dynamic light scattering measurements for 0, 15 and 30 minutes of photocatalytic activity from (a) 2 μM **[Co]**$^{2+}$, 200 μM **IrPS-1**, 100 mM BIH, and 1 M phenol and (b) 2 μM **[Fe]**$^{2+}$, 200 μM **RuPS**, 100 mM BIH, and 1 M phenol.

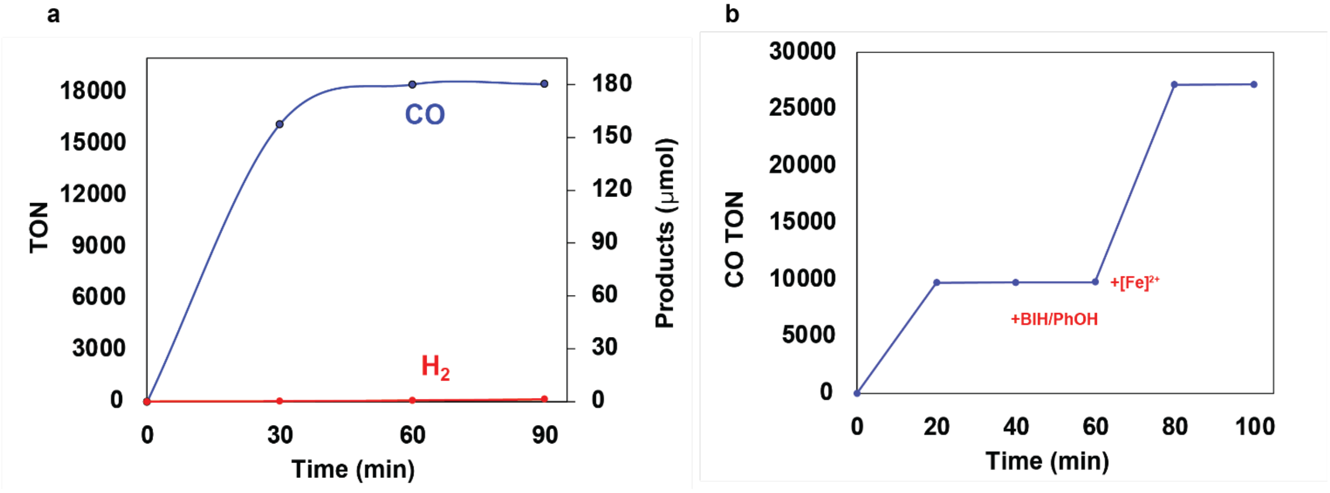

Figure 2.13. Photocatalytic activity of (a) 2 µM **[Fe]**$^{2+}$ using 200 µM **IrPS-2**, 100 mM BIH, and 1 M phenol for 90 minutes. (b) Photocatalytic activity of **[Fe]**$^{2+}$ using **IrPS-2** for 40 minutes, followed by addition of 100 mM BIH and 1 M phenol. After seeing no recovery in catalytic activity after 60 minutes, additional **[Fe]**$^{2+}$ was added.

Table 2.4. Crystallographic data for **[Co]$^{2+}$**.

	[Co(tpyPY2Me)] (OTf)$_2$
Empirical formula	$C_{29}H_{21}CoF_6N_5O_6S_2$
Formula weight	772.56
Crystal system, space group	Orthorhombic, Pbca
Temperature/K	100(2)
a (Å)	15.2899(4)
b (Å)	16.6026(4)
c (Å)	23.1604(6)
V (Å^3)	5879.3(3)
Z	8
μ (mm^{-1})	0.819
F(000)	3128.0
Crystal size (mm^3)	0.24 × 0.2 × 0.12
θ range for data collection (°)	2.927 to 26.37
Radiation	MoKα (λ = 0.71073)
No. of reflections for cell measurement	16238
Index ranges	$-16 \leq h \leq 19$ $-20 \leq k \leq 20$ $-28 \leq l \leq 24$
Reflections collected/ unique	38669 / 6007
$R_{int} = 0.0589$	$R_{int} = 0.0589$
Data/restraints/parameters	6007 / 0 /443
Goodness-of-fit on F^2	1.038
Final R indexes [I>=2σ (I)]	$R_1 = 0.0352$, $wR_2 = 0.0796$
Largest diff. peak/hole (e Å^{-3})	0.47/-0.47

[a] Obtained with a rotating-anode X-ray tube, Rigaku Mo Kα ($\lambda = 0.71073$ Å) X-ray source. [b] $R1 = \sum||F0| - FC||/\sum|F0|$,$R2 = (\sum[w(F0\ 2 - F0\ 2\ )\ 2\ ]/\sum[\ w(F0\ 2\ )\ 2\ ])1/2$.

Table 2.5. Selected bond lengths (Å) and angles (°) for **[Co]$^{2+}$**.

Atoms	**Distance**	**Atoms**	**Distance**
Co1—N1	1.8975(17)	C4—C5	1.379(3)
Co1—N2	1.8658(18)	C5—C6	1.465(3)
Co1—N3	1.9610(18)	C6—C7	1.396(3)
Co1—N4	1.9564(17)	C7—C8	1.387(3)
Co1—N5	2.0647(18)	C8—C9	1.389(3)
Co1—O5	2.5958(15)	C9—C10	1.382(3)
N1—C15	1.340(3)	C10—C11	1.476(3)
N1—C11	1.364(3)	C11—C12	1.377(3)
N2—C6	1.340(3)	C12—C13	1.387(3)
N2—C10	1.351(3)	C13—C14	1.381(3)
N3—C1	1.340(3)	C14—C15	1.388(3)
N3—C5	1.369(3)	C15—C16	1.536(3)
N4—C23	1.351(3)	C16—C17	1.537(3)
N4—C27	1.344(3)	C16—C18	1.549(3)
N5—C18	1.354(3)	C18—C19	1.387(3)
N5—C22	1.339(3)	C19—C20	1.385(3)
O5—S2	1.4523(16)	C20—C21	1.378(3)
C1—C2	1.387(3)	C21—C22	1.378(3)
C2—C3	1.385(3)	C23—C24	1.383(3)
C3—C4	1.383(3)	C24—C25	1.383(3)

Atoms	**Angle**	**Atoms**	**Angle**
N1—Co1—N3	163.58(7)	N3—Co1—N5	96.73(7)
N1—Co1—N4	92.88(7)	N3—Co1—O5	84.25(6)
N1—Co1—N5	85.85 (7)	N4—Co1—N3	103.46(7)
N1—Co1—O5	95.53(6)	N4—Co1—N5	95.53 (6)
N2—Co1—N1	81.75(7)	N4—Co1—O5	85.66 (6)
N2—Co1—N3	82.15(8)	N5—Co1—O5	171.75(6)
N2—Co1—N4	162.20(8)	N2—Co1—O5	78.03(6)
N2—Co1—N5	110.22(7)		

Table 2.6. Predicted redox potentials of **[Co]**$^{2+}$ (vs Fc$^{+/0}$) using various DFT functionals.

Functional	1st Reduction	2nd Reduction
wB97M-V	-0.88	-2.22
wB97X-D	-0.57	-2.30
CAM-B3LYP	-0.57	-2.24
MN15	-0.36	-3.08
PBE0	-0.45	-2.84
SCAN	-0.73	-1.57
B97-D	-1.02	-1.26

Table 2.7. DFT optimized structure of **[Co]**$^+$ from calculations using ωB97X-D functionals and CH_3CN solvent.

Atom	**x**	**y**	**z**
H	0.23008	9.41986	-6.27122
C	0.13593	9.55785	-5.19251
H	-0.52895	11.62251	-5.30539
C	-0.28507	10.77368	-4.66626
C	-0.38259	10.88537	-3.28653
H	-0.69966	11.8178	-2.81337
N	-0.09596	9.87501	-2.4603
C	0.3152	8.69544	-2.94859
C	0.44086	8.51068	-4.32792
H	0.77389	7.56173	-4.74101
C	0.6273	7.57435	-1.92501
C	1.06011	6.29827	-2.65044
H	0.27391	5.93618	-3.32494
H	1.28531	5.49717	-1.9353
Co	-0.1416	10.11391	-0.41331
C	-0.65246	7.31591	-1.09455
C	-1.27111	6.06495	-1.04521
H	-0.86711	5.21691	-1.5925
C	-2.42443	5.8963	-0.28407
C	-2.93758	6.98038	0.41692
H	-3.8331	6.89615	1.03287
C	-2.27106	8.19476	0.32568
H	-2.61526	9.07033	0.88184
N	-1.58836	11.41001	-0.22468
C	-2.80175	11.3431	-0.79287
H	-2.9806	10.48196	-1.44116
C	-3.77902	12.29984	-0.58057
H	-4.75192	12.20102	-1.0621
C	-3.48664	13.37979	0.2582
C	-2.23458	13.45939	0.84663
H	-1.98143	14.28861	1.50745
C	-1.29389	12.4578	0.59348
C	0.05684	12.3943	1.15182
C	0.68661	13.27926	2.00206
H	0.17757	14.17898	2.34912
C	2.01011	13.00792	2.4175
C	2.65953	11.85983	1.97059
H	3.68418	11.65088	2.28236
C	1.989	10.9839	1.11494
C	2.44452	9.7506	0.51971
C	3.69469	9.13484	0.68489

H	4.44359	9.58132	1.33972
C	3.95322	7.96596	-0.00057
H	4.91683	7.46625	0.11029
C	2.98173	7.41819	-0.85727
H	3.2096	6.50676	-1.40401
C	1.75785	8.05692	-0.98849
N	1.50508	9.17923	-0.2932
N	0.70381	11.26889	0.72617
N	-1.16469	8.3529	-0.41183
H	2.52397	13.70522	3.07938
H	1.96322	6.47336	-3.24827
H	-2.91257	4.92086	-0.24049
H	-4.23455	14.15138	0.44933

Table 2.8. DFT optimized structure of **[Co]^{0}** from calculations using ωB97X-D functionals and CH_3CN solvent.

Atom	**x**	**y**	**z**
H	0.10751	9.05497	-6.40233
C	-0.00275	9.2678	-5.33697
H	-0.82087	11.26392	-5.60613
C	-0.51431	10.48703	-4.905
C	-0.62458	10.69254	-3.53731
H	-1.01493	11.62815	-3.12653
N	-0.26397	9.77247	-2.63852
C	0.22879	8.58745	-3.03013
C	0.37041	8.31346	-4.39621
H	0.77083	7.36299	-4.73987
C	0.63419	7.56825	-1.93482
C	1.08201	6.25693	-2.58714
H	0.27898	5.80999	-3.18921
H	1.38657	5.52834	-1.82608
Co	-0.24634	10.24192	-0.59139
C	-0.58368	7.30537	-1.0126
C	-1.08017	6.01702	-0.77871
H	-0.62418	5.14678	-1.24426
C	-2.17255	5.83773	0.06361
C	-2.76007	6.94657	0.6636
H	-3.61849	6.85394	1.3297
C	-2.21491	8.19291	0.3903
H	-2.62256	9.10779	0.82992
N	-1.6795	11.65135	-0.27396
C	-2.94597	11.68975	-0.75527
H	-3.22599	10.84564	-1.3963
C	-3.84646	12.68945	-0.48729
H	-4.85081	12.65192	-0.91133
C	-3.43342	13.76577	0.35246
C	-2.15457	13.75468	0.85676
H	-1.81248	14.5659	1.50234
C	-1.26508	12.69901	0.55007
C	0.08876	12.60681	1.03535
C	0.7787	13.50452	1.87992
H	0.29559	14.40661	2.25661
C	2.09454	13.2139	2.22481
C	2.7375	12.06154	1.75535
H	3.76924	11.84635	2.03447
C	2.01331	11.19825	0.91914
C	2.46544	9.95407	0.31526
C	3.73599	9.38375	0.46169

H	4.48632	9.88288	1.07764
C	4.03054	8.19309	-0.17674
H	5.01501	7.73421	-0.07374
C	3.0352	7.56593	-0.97461
H	3.27374	6.63016	-1.47617
C	1.79675	8.16052	-1.09127
N	1.51185	9.32348	-0.46373
N	0.73603	11.49846	0.59498
N	-1.16509	8.35877	-0.41884
H	2.63936	13.90038	2.87746
H	1.94812	6.42375	-3.23895
H	-2.56038	4.83346	0.24658
H	-4.11862	14.5815	0.59031

Table 2.9. Free energy adiabatic spin gaps for the **[Co]$^{n+}$** (*n* = 2,1,0) complex; referenced against the minimum energy spin state for each reduction level. Reference spin states are reported as a quartet, singlet, and doublet for the unreduced (*n* = 2), singly reduced (*n* = 1), and doubly reduced (*n* = 0) complexes respectively. Values are reported in kcal/mol and obtained using the ωB97M-V functional.

[Co]$^{2+}$	**[Co]$^{+}$**	**[Co]^{0}**
+3.34 (quartet -> doublet)	+11.83 (singlet -> triplet)	+3.35 (doublet -> quartet)
	+14.85 (singlet -> quintet)	+5.71 (doublet -> sextet)

References:

(1) Sanz-Pérez, E. S.; Murdock, C. R.; Didas, S. A.; Jones, C. W. Direct Capture of CO_2 from Ambient Air. *Chem. Rev.* **2016**, *116* (19), 11840-11876.

(2) Hepburn, C.; Adlen, E.; Beddington, J.; Carter, E. A.; Fuss, S.; Mac Dowell, N.; Minx, J. C.; Smith, P.; Williams, C. K. The technological and economic prospects for CO_2 utilization and removal. *Nature* **2019**, *575* (7781), 87-97.

(3) Wang, Z. J.; Song, H.; Liu, H.; Ye, J. Coupling of Solar Energy and Thermal Energy for Carbon Dioxide Reduction: Status and Prospects. *Angew. Chem. Int. Ed.* **2020**, *59* (21), 8016-8035.

(4) Proppe, A. H.; Li, Y. C.; Aspuru-Guzik, A.; Berlinguette, C. P.; Chang, C. J.; Cogdell, R.; Doyle, A. G.; Flick, J.; Gabor, N. M.; van Grondelle, R.; et al. Bioinspiration in light harvesting and catalysis. *Nat. Rev. Mat.* **2020**, *5* (11), 828-846.

(5) Meyer, T. J. Chemical approaches to artificial photosynthesis. *Acc. Chem. Res.* **1989**, *22* (5), 163-170.

(6) Lewis, N. S.; Nocera, D. G. Powering the planet: Chemical challenges in solar energy utilization. *Proc. Natl. Acad. Sci.* **2006**, *103* (43), 15729-15735.

(7) Nocera, D. G. Chemistry of Personalized Solar Energy. *Inorg. Chem.* **2009**, *48* (21), 10001-10017.

(8) Gray, H. B. Powering the planet with solar fuel. *Nat. Chem.* **2009**, *1* (1), 7-7.

(9) Morris, A. J.; Meyer, G. J.; Fujita, E. Molecular Approaches to the Photocatalytic Reduction of Carbon Dioxide for Solar Fuels. *Acc. Chem. Res.* **2009**, *42* (12), 1983-1994.

(10) Nocera, D. G. The Artificial Leaf. *Acc. Chem. Res.* **2012**, *45* (5), 767-776.

(11) Takeda, H.; Cometto, C.; Ishitani, O.; Robert, M. Electrons, Photons, Protons and Earth-Abundant Metal Complexes for Molecular Catalysis of CO_2 Reduction. *ACS Catal.* **2016**, *7* (1), 70-88.

(12) Nocera, D. G. Solar Fuels and Solar Chemicals Industry. *Acc. Chem. Res.* **2017**, *50* (3), 616-619.

(13) Smith, P. T.; Nichols, E. M.; Cao, Z.; Chang, C. J. Hybrid Catalysts for Artificial Photosynthesis: Merging Approaches from Molecular, Materials, and Biological Catalysis. *Acc. Chem. Res.* **2020**, *53* (3), 575-587.

(14) Pannwitz, A.; Klein, D. M.; Rodríguez-Jiménez, S.; Casadevall, C.; Song, H.; Reisner, E.; Hammarström, L.; Bonnet, S. Roadmap towards solar fuel synthesis at the water interface of liposome membranes. *Chem. Soc. Rev.* **2021**, *50* (8), 4833-4855.

(15) Nocera, D. G. Proton-Coupled Electron Transfer: The Engine of Energy Conversion and Storage. *J. Am. Chem. Soc.* **2022**, *144* (3), 1069-1081.

(16) Benson, E. E.; Kubiak, C. P.; Sathrum, A. J.; Smieja, J. M. Electrocatalytic and homogeneous approaches to conversion of CO_2 to liquid fuels. *Chem. Soc. Rev.* **2009**, *38* (1), 89-99.

(17) Rao, H.; Schmidt, L. C.; Bonin, J.; Robert, M. Visible-light-driven methane formation from CO_2 with a molecular iron catalyst. *Nature* **2017**, *548* (7665), 74-77.

(18) Call, A.; Cibian, M.; Yamamoto, K.; Nakazono, T.; Yamauchi, K.; Sakai, K. Highly Efficient and Selective Photocatalytic CO_2 Reduction to CO in Water by a Cobalt Porphyrin Molecular Catalyst. *ACS Catal.* **2019**, *9* (6), 4867-4874.

(19) Wu, Y.; Kim, D.; Teets, T. S. Photophysical Properties and Redox Potentials of Photosensitizers for Organic Photoredox Transformations. *Synlett* (EFirst).

(20) Yuan, H.; Cheng, B.; Lei, J.; Jiang, L.; Han, Z. Promoting photocatalytic CO_2 reduction with a molecular copper purpurin chromophore. *Nat. Commun.* **2021**, *12* (1), 1835.

(21) Leung, C.-F.; Lau, T.-C. Organic Photosensitizers for Catalytic Solar Fuel Generation. *Energy & Fuels* **2021**, *35* (23), 18888-18899.

(22) Stanley, P. M.; Haimerl, J.; Thomas, C.; Urstoeger, A.; Schuster, M.; Shustova, N. B.; Casini, A.; Rieger, B.; Warnan, J.; Fischer, R. A. Host–Guest Interactions in a Metal–Organic Framework Isoreticular Series for Molecular Photocatalytic CO_2 Reduction. *Angew. Chem. Int. Ed.* **2021**, *60* (33), 17854-17860.

(23) Zhang, X.; Cibian, M.; Call, A.; Yamauchi, K.; Sakai, K. Photochemical CO_2 Reduction Driven by Water-Soluble Copper(I) Photosensitizer with the Catalysis Accelerated by Multi-Electron Chargeable Cobalt Porphyrin. *ACS Catal.* **2019**, *9* (12), 11263-11273.

(24) Cheung, P. L.; Kapper, S. C.; Zeng, T.; Thompson, M. E.; Kubiak, C. P. Improving Photocatalysis for the Reduction of CO_2 through Non-covalent Supramolecular Assembly. *J. Am. Chem. Soc.* **2019**, *141* (38), 14961-14965.

(25) Arcudi, F.; Đorđević, L.; Nagasing, B.; Stupp, S. I.; Weiss, E. A. Quantum Dot-Sensitized Photoreduction of CO_2 in Water with Turnover Number > 80,000. *J. Am. Chem. Soc.* **2021**, *143* (43), 18131-18138.

(26) Lian, S.; Kodaimati, M. S.; Weiss, E. A. Photocatalytically Active Superstructures of Quantum Dots and Iron Porphyrins for Reduction of CO_2 to CO in Water. *ACS Nano* **2018**, *12* (1), 568-575.

(27) Tamaki, Y.; Ishitani, O. Supramolecular Photocatalysts for the Reduction of CO_2. *ACS Catal.* **2017**, *7* (5), 3394-3409.

(28) Yang, Z.-Z.; He, L.-N.; Gao, J.; Liu, A.-H.; Yu, B. Carbon dioxide utilization with C–N bond formation: carbon dioxide capture and subsequent conversion. *Energy Environ. Sci.* **2012**, *5* (5), 6602-6639.

(29) Sampaio, R. N.; Grills, D. C.; Polyansky, D. E.; Szalda, D. J.; Fujita, E. Unexpected Roles of Triethanolamine in the Photochemical Reduction of CO_2 to Formate by Ruthenium Complexes. *J. Am. Chem. Soc.* **2020**, *142* (5), 2413-2428.

(30) Bhattacharya, M.; Sebghati, S.; VanderLinden, R. T.; Saouma, C. T. Toward Combined Carbon Capture and Recycling: Addition of an Amine Alters Product Selectivity from CO to Formic Acid in Manganese Catalyzed Reduction of CO_2. *J. Am. Chem. Soc.* **2020**, *142* (41), 17589-17597.

(31) Yamazaki, Y.; Miyaji, M.; Ishitani, O. Utilization of Low-Concentration CO_2 with Molecular Catalysts Assisted by CO_2-Capturing Ability of Catalysts, Additives, or Reaction Media. *J. Am. Chem. Soc.* **2022**, *144* (15), 6640-6660.

(32) Bhattacharya, M.; Sebghati, S.; Vercella, Y. M.; Saouma, C. T. Electrochemical Reduction of Carbamates and Carbamic Acids: Implications for Combined Carbon Capture and Electrochemical CO_2 Recycling. *J. Electrochem. Soc.* **2020**, *167* (8), 086507.

(33) Smieja, J. M.; Kubiak, C. P. Re(bipy-tBu)(CO)3Cl−improved Catalytic Activity for Reduction of Carbon Dioxide: IR-Spectroelectrochemical and Mechanistic Studies. *Inorg. Chem.* **2010**, *49* (20), 9283-9289.

(34) Thoi, V. S.; Chang, C. J. Nickel N-heterocyclic carbene–pyridine complexes that exhibit selectivity for electrocatalytic reduction of carbon dioxide over water. *Chem. Commun.* **2011**, *47* (23), 6578-6580.

(35) Bourrez, M.; Molton, F.; Chardon-Noblat, S.; Deronzier, A. [Mn(bipyridyl)(CO)3Br]: An Abundant Metal Carbonyl Complex as Efficient Electrocatalyst for CO_2 Reduction. *Angew. Chem. Int. Ed.* **2011**, *50* (42), 9903-9906.

(36) Thoi, V. S.; Kornienko, N.; Margarit, C. G.; Yang, P.; Chang, C. J. Visible-Light Photoredox Catalysis: Selective Reduction of Carbon Dioxide to Carbon Monoxide by a Nickel N-Heterocyclic Carbene–Isoquinoline Complex. *J. Am. Chem. Soc.* **2013**, *135* (38), 14413-14424.

(37) Smieja, J. M.; Sampson, M. D.; Grice, K. A.; Benson, E. E.; Froehlich, J. D.; Kubiak, C. P. Manganese as a Substitute for Rhenium in CO2 Reduction Catalysts: The Importance of Acids. *Inorg. Chem.* **2013**, *52* (5), 2484-2491.

(38) Machan, C. W.; Chabolla, S. A.; Kubiak, C. P. Reductive Disproportionation of Carbon Dioxide by an Alkyl-Functionalized Pyridine Monoimine Re(I) fac-Tricarbonyl Electrocatalyst. *Organometallics* **2015**, *34* (19), 4678-4683.

(39) Guo, Z.; Cheng, S.; Cometto, C.; Anxolabehere-Mallart, E.; Ng, S. M.; Ko, C. C.; Liu, G.; Chen, L.; Robert, M.; Lau, T. C. Highly Efficient and Selective Photocatalytic CO_2 Reduction by Iron and Cobalt Quaterpyridine Complexes. *J Am Chem Soc* **2016**, *138* (30), 9413-9416.

(40) Liyanage, N. P.; Dulaney, H. A.; Huckaba, A. J.; Jurss, J. W.; Delcamp, J. H. Electrocatalytic Reduction of CO_2 to CO With Re-Pyridyl-NHCs: Proton Source Influence on Rates and Product Selectivities. *Inorg. Chem.* **2016**, *55* (12), 6085-6094.

(41) Elgrishi, N.; Chambers, M. B.; Wang, X.; Fontecave, M. Molecular polypyridine-based metal complexes as catalysts for the reduction of CO_2. *Chem. Soc. Rev.* **2017**, *46* (3), 761-796.

(42) Sung, S.; Kumar, D.; Gil-Sepulcre, M.; Nippe, M. Electrocatalytic CO_2 Reduction by Imidazolium-Functionalized Molecular Catalysts. *J. Am. Chem. Soc.* **2017**, *139* (40), 13993-13996.

(43) Sung, S.; Li, X.; Wolf, L. M.; Meeder, J. R.; Bhuvanesh, N. S.; Grice, K. A.; Panetier, J. A.; Nippe, M. Synergistic Effects of Imidazolium-Functionalization on fac-$Mn(CO)_3$ Bipyridine Catalyst Platforms for Electrocatalytic Carbon Dioxide Reduction. *J. Am. Chem. Soc.* **2019**, *141* (16), 6569-6582.

(44) Derrick, J. S.; Loipersberger, M.; Chatterjee, R.; Iovan, D. A.; Smith, P. T.; Chakarawet, K.; Yano, J.; Long, J. R.; Head-Gordon, M.; Chang, C. J. Metal–Ligand Cooperativity via Exchange Coupling Promotes Iron- Catalyzed Electrochemical CO_2 Reduction at Low Overpotentials. *J. Am. Chem. Soc.* **2020**, *142* (48), 20489-20501.

(45) Qin, Y.; Chen, L.; Chen, G.; Guo, Z.; Wang, L.; Fan, H.; Robert, M.; Lau, T. C. A highly active and robust iron quinquepyridine complex for photocatalytic CO_2 reduction in aqueous acetonitrile solution. *Chem. Commun.* **2020**, *56* (46), 6249-6252.

(46) Boutin, E.; Merakeb, L.; Ma, B.; Boudy, B.; Wang, M.; Bonin, J.; Anxolabéhère-Mallart, E.; Robert, M. Molecular catalysis of CO_2 reduction: recent advances and perspectives in electrochemical and light-driven processes with selected Fe, Ni and Co aza macrocyclic and polypyridine complexes. *Chem. Soc. Rev.* **2020**, *49* (16), 5772-5809.

(47) Gonell, S.; Lloret-Fillol, J.; Miller, A. J. M. An Iron Pyridyl-Carbene Electrocatalyst for Low Overpotential CO_2 Reduction to CO. *ACS Catal.* **2021**, *11* (2), 615-626.

(48) Wang, X.-Z.; Meng, S.-L.; Chen, J.-Y.; Wang, H.-X.; Wang, Y.; Zhou, S.; Li, X.-B.; Liao, R.-Z.; Tung, C.-H.; Wu, L.-Z. Mechanistic Insights Into Iron(II) Bis(pyridyl)amine-Bipyridine Skeleton for Selective CO_2 Photoreduction. *Angew. Chem. Int. Ed.* **2021**, *60* (50), 26072-26079.

(49) Tsubonouchi, Y.; Takahashi, D.; Berber, M. R.; Mohamed, E. A.; Zahran, Z. N.; Alenad, A. M.; Althubiti, N. A.; Yagi, M. Highly selective electrocatalysis for carbon dioxide reduction to formic acid by a Co(II) complex with an equatorial N_4 ligand. *Electrochim. Acta* **2021**, *387*, 138545.

(50) Queyriaux, N. Redox-Active Ligands in Electroassisted Catalytic H^+ and CO_2 Reductions: Benefits and Risks. *ACS Catal.* **2021**, *11* (7), 4024-4035.

(51) Loipersberger, M.; Cabral, D. G. A.; Chu, D. B. K.; Head-Gordon, M. Mechanistic Insights into Co and Fe Quaterpyridine-Based CO_2 Reduction Catalysts: Metal–Ligand Orbital Interaction as the Key Driving Force for Distinct Pathways. *J. Am. Chem. Soc.* **2021**, *143* (2), 744-763.

(52) Nganga, J. K.; Wolf, L. M.; Mullick, K.; Reinheimer, E.; Saucedo, C.; Wilson, M. E.; Grice, K. A.; Ertem, M. Z.; Angeles-Boza, A. M. Methane Generation from CO2 with a Molecular Rhenium Catalyst. *Inorg. Chem.* **2021**, *60* (6), 3572-3584.

(53) Wuttig, A.; Derrick, J. S.; Loipersberger, M.; Snider, A.; Head-Gordon, M.; Chang, C. J.; Toste, F. D. Controlled Single-Electron Transfer via Metal–Ligand Cooperativity Drives Divergent Nickel-Electrocatalyzed Radical Pathways. *J. Am. Chem. Soc.* **2021**, *143* (18), 6990-7001.

(54) Chan, S. L.-F.; Lam, T. L.; Yang, C.; Yan, S.-C.; Cheng, N. M. A robust and efficient cobalt molecular catalyst for CO_2 reduction. *Chem. Commun.* **2015**, *51* (37), 7799-7801.

(55) Roy, S.; Sharma, B.; Pécaut, J.; Simon, P.; Fontecave, M.; Tran, P. D.; Derat, E.; Artero, V. Molecular Cobalt Complexes with Pendant Amines for Selective Electrocatalytic Reduction of Carbon Dioxide to Formic Acid. *J. Am. Chem. Soc.* **2017**, *139* (10), 3685-3696.

(56) Zhang, L.; Li, S.; Liu, H.; Cheng, Y.-S.; Wei, X.-W.; Chai, X.; Yuan, G. Highly Efficient and Selective Visible-Light Driven CO_2 Reduction by Two Co-Based Catalysts in Aqueous Solution. *Inorg. Chem.* **2020**, *59* (23), 17464-17472.

(57) Chen, X.; Wei, Y.; Sun, W.; Meng, X.; Hao, S.; Gao, Y. Turning off hydrogen evolution via an organic dye photosensitizer in aqueous acetonitrile solution during photocatalytic CO_2 reduction to CO. *Mol. Catal.* **2021**, *500*, 111299.

(58) Su, X.; McCardle, K. M.; Chen, L.; Panetier, J. A.; Jurss, J. W. Robust and Selective Cobalt Catalysts Bearing Redox-Active Bipyridyl-N-heterocyclic Carbene Frameworks for Electrochemical CO_2 Reduction in Aqueous Solutions. *ACS Catal.* **2019**, *9* (8), 7398-7408.

(59) Sun, Y.; Bigi, J. P.; Piro, N. A.; Tang, M. L.; Long, J. R.; Chang, C. J. Molecular Cobalt Pentapyridine Catalysts for Generating Hydrogen from Water. *J. Am. Chem. Soc.* **2011**, *133* (24), 9212-9215.

(60) Kilner, C. A.; Halcrow, M. A. An unusual discontinuity in the thermal spin transition in $[Co(terpy)_2][BF_4]_2$. *J. Chem. Soc., Dalton Trans.* **2010**, *39* (38), 9008-9012.

(61) England, J.; Bill, E.; Weyhermüller, T.; Neese, F.; Atanasov, M.; Wieghardt, K. Molecular and Electronic Structures of Homoleptic Six-Coordinate Cobalt(I) Complexes of 2,2′:6′,2″-Terpyridine, 2,2′-Bipyridine, and 1,10-Phenanthroline. An Experimental and Computational Study. *Inorg. Chem.* **2015**, *54* (24), 12002-12018.

(62) Hamann, T. W. The end of iodide? Cobalt complex redox shuttles in DSSCs. *J. Chem. Soc., Dalton Trans.* **2012**, *41* (11), 3111-3115.

(63) Kashif, M. K.; Axelson, J. C.; Duffy, N. W.; Forsyth, C. M.; Chang, C. J.; Long, J. R.; Spiccia, L.; Bach, U. A New Direction in Dye-Sensitized Solar Cells Redox Mediator Development: In Situ Fine-Tuning of the Cobalt(II)/(III) Redox Potential through Lewis Base Interactions. *J. Am. Chem. Soc.* **2012**, *134* (40), 16646-16653.

(64) Giribabu, L.; Bolligarla, R.; Panigrahi, M. Recent Advances of Cobalt(II/III) Redox Couples for Dye-Sensitized Solar Cell Applications. *Chem. Rec.* **2015**, *15* (4), 760-788.

(65) Nippe, M.; Khnayzer, R. S.; Panetier, J. A.; Zee, D. Z.; Olaiya, B. S.; Head-Gordon, M.; Chang, C. J.; Castellano, F. N.; Long, J. R. Catalytic proton reduction with transition metal complexes of the redox-active ligand bpy2PYMe. *Chem. Sci* **2013**, *4* (10), 3934-3945.

(66) Guo, Z.; Yu, F.; Yang, Y.; Leung, C.-F.; Ng, S.-M.; Ko, C.-C.; Cometto, C.; Lau, T.-C.; Robert, M. Photocatalytic Conversion of CO_2 to CO by a Copper(II) Quaterpyridine Complex. *ChemSusChem* **2017**, *10* (20), 4009-4013.

(67) Rao, H.; Lim, C.-H.; Bonin, J.; Miyake, G. M.; Robert, M. Visible-Light-Driven Conversion of CO_2 to CH_4 with an Organic Sensitizer and an Iron Porphyrin Catalyst. *J. Am. Chem. Soc.* **2018**, *140* (51), 17830-17834.

(68) Durham, B.; Caspar, J. V.; Nagle, J. K.; Meyer, T. J. Photochemistry of tris(2,2'-bipyridine)ruthenium(2+) ion. *J. Am. Chem. Soc.* **1982**, *104* (18), 4803-4810.

(69) Khnayzer, R. S.; Olaiya, B. S.; El Roz, K. A.; Castellano, F. N. Homogeneous Photocatalytic H_2 Production Using a RuII Bathophenanthroline Metal-to-Ligand Charge-Transfer Photosensitizer. *ChemPlusChem* **2016**, *81* (10), 1090-1097.

(70) Gong, L.; Wang, J.; Li, H.; Wang, L.; Zhao, J.; Zhu, Z. Acriflavine–cobaloxime–triethanolamine homogeneous photocatalytic system for water splitting and the multiple effects of cobaloxime and triethanolamine. *Catal. Commun.* **2011**, *12* (12), 1099-1103.

(71) Yuan, Y.-J.; Yu, Z.-T.; Chen, D.-Q.; Zou, Z.-G. Metal-complex chromophores for solar hydrogen generation. *Chem. Soc. Rev.* **2017**, *46* (3), 603-631.

(72) Epifanovsky, E.; Gilbert, A. T. B.; Feng, X.; Lee, J.; Mao, Y.; Mardirossian, N.; Pokhilko, P.; White, A. F.; Coons, M. P.; Dempwolff, A. L.; et al. Software for the frontiers of quantum chemistry: An overview of developments in the Q-Chem 5 package. *J. Chem. Phys.* **2021**, *155* (8), 084801.

Chapter 3: Synergistic Porosity and Charge Effects in a Supramolecular Porphyrin Cage Promote Efficient Photocatalytic CO_2 Reduction

This work was published in the following scientific journal:

Lun An, Patricia De La Torre, Peter T. Smith, Mina R. Narouz, and Christopher J. Chang, Synergistic Porosity and Charge Effects in a Supramolecular Porphyrin Cage Promote Efficient Photocatalytic CO_2 Reduction. *Angew. Chem. Int. Ed.* 2023, 62, e202209396; *Angew. Chem.* **2023**, *135*, e202209396.

Abstract:

We present a supramolecular approach to catalyzing photochemical CO_2 reduction through second-sphere porosity and charge effects. An iron porphyrin box (**PB**) bearing 24 cationic groups, **FePB-2(P)**, was made via post-synthetic modification of an alkyne-functionalized supramolecular synthon. **FePB-2(P)** promotes the photochemical CO_2 reduction reaction (CO_2RR) with 97% selectivity for CO product, achieving turnover numbers (TON) exceeding 7000 and initial turnover frequencies (TOF_{max}) reaching 1400 min^{-1}. The cooperativity between porosity and charge results in a 41-fold increase in activity relative to the parent Fe tetraphenylporphyrin (**FeTPP)** catalyst, which is far greater than analogs that augment catalysis through porosity (**FePB-3(N)**, 4-fold increase) or charge (Fe *p*-tetramethylanilinium porphyrin (**Fe-*p*-TMA)**, 6-fold increase) alone. This work establishes that synergistic pendants in the secondary coordination sphere can be leveraged as a design element to augment catalysis at primary active sites within confined spaces.

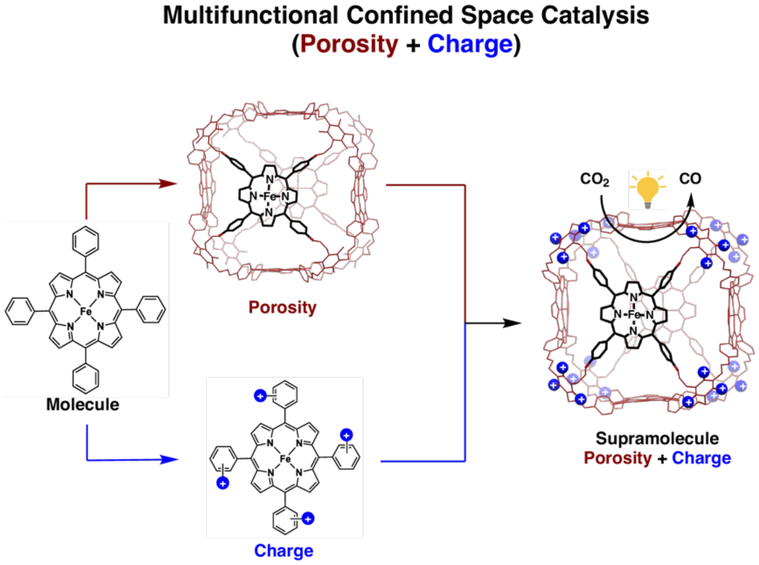

1. Introduction

Conversion of carbon dioxide (CO_2) into value-added chemical feedstocks using renewable energy inputs represents a sustainable solution to simultaneously mitigate growing global energy demands and reduce greenhouse gas concentrations.[1-4] These challenges continue to motivate widespread efforts in the development of new catalyst systems for the electrochemical and photochemical CO_2 reduction reaction (CO_2RR).[5-16] In this regard, homogeneous catalysts featuring well-defined metal active sites and ligand scaffolds are valuable in elucidating structure/activity relationships and mechanisms with molecular-level control.[6-8, 13-15] To date, two main strategies have been adopted to advance the field of molecular CO_2RR catalysis: (1) primary coordination sphere chemistry with ligand modifications to tune redox properties of metal centers,[17-23] and (2) secondary coordination sphere chemistry to introduce functionalities beyond the primary active site, including charged [24-31] or hydrogen-bonding groups,[31-47] to promote capture and transformation of CO_2 and its reduced intermediates. For the latter strategy, we have initiated a program to explore a supramolecular second-sphere approach to enhance CO_2RR[48] and related small-molecule activation reactions[49-51] by integrating planar molecular catalysts into three-dimensional confined space architectures. In particular, porous molecular cages, such as metal-organic coordination cages (MOCs) [52-60] and porous organic cages (POCs),[61-68] offer the ability to organize reaction substrates[69] and intermediates,[70] as well as tune reaction kinetics,[71] thus capturing the functional essence of enzyme-substrate binding processes.[72] As discrete molecular analogs of extended covalent organic framework (COF)[73-82] and metal organic framework (MOF)[83-94] materials used for CO_2RR, porous molecular cages offer comparable advantages of permanent porosity in confined spaces with higher solution processibility and homogeneous molecular control.[95]

However, despite early advances in the development of molecular cages for energy conversion reactions, these structures largely utilize only one second-sphere feature to augment catalysis – porosity. As such, we sought to incorporate additional second-sphere functionalities into such scaffolds, reasoning that synergy between multiple types of interactions could achieve higher cooperative gains in activity and/or selectivity compared to a single type of interaction. We now report the design, synthesis, and evaluation of a modular porphyrin-based organic cage platform that incorporates dual features of porosity and charge; these multiple second-sphere effects coordinate to amplify photochemical CO_2RR catalysis beyond incorporation of individual second-sphere elements alone (Scheme 3.1). An alkyne-functionalized iron porphyrin box (**FePB-1(A)**) synthon enables addition of 24 positively-charged ammonium groups via click chemistry to afford **FePB-2(P)**. CO_2RR activity comparisons across a systematic series of analogs that feature only porosity (**FePB-3(N)**) or charge (**Fe-*p*-TMA**) reveal that the dual-functionalized **FePB-2(P)** catalyst enhances CO_2RR catalysis by over 40-fold over the parent **FeTPP** compound. In contrast, porosity-only or charge-only interactions give more modest 4-fold or 6-fold increases, respectively. **FePB-2(P)** promotes efficient CO_2RR with 97% selectivity for CO product, achieving TON exceeding 1100 and initial TOF_{max} reaching 160 min^{-1} per Fe center. These results provide a starting point for the broader incorporation of multiple, synergistic second-sphere functionalities as a design element to enhance catalysis in confined molecular spaces.

2. Results and Discussion

2.1. Synthesis and Characterization of a Modular Porous Porphyrin Cage Platform Bearing Peripheral Positive Charges.

To start, motivated by broader interest in the development of methods for modular post-synthetic modifications of molecular cages,[96, 97] we designed and prepared the alkyne-containing clickable porphyrin box **PB-1(A)** starting from an alkyne functionalized triamine linker **1** (Synthetic Details 5.1). The reported procedure for the unfunctionalized **PB** linker 1,3,5-tris(aminomethyl)-2,4,6-trialkylbenzene features a bromomethylation/azidation/reduction sequence to introduce the three aminomethyl groups.[98] However, the harsh conditions required in the bromomethylation step (HOAc/HBr, 70 °C, 18 h) prevented us from introducing the alkynyl functionality in the early stage of the synthesis. Instead, three 1-chloro-hexyl groups were selectively introduced by substitution of phloroglucinol and 1-bromo-6-chlorohexane, which were well tolerated in the bromomethylation step and provided accessible chloric handles for late-stage alkynylation. The chloride groups were successfully converted to terminal aldehyde groups by a bromination/hydrolysis/oxidation sequence. However, neither the Seyferth-Gilbert homologation nor the Corey-Fuchs reaction was successful in transforming these aldehydes into terminal alkyne functionalities.[99, 100] After screening several reaction conditions, the alkynyl groups were introduced via an iron-catalyzed reductive etherification reaction of carbonyl with triethylsilane and trimethyl(pent-4-yn-1-yloxy)silane in 93% yield.[101] Upon deprotection with hydrazine, alkyl functionalized triamine linker (**1**) was obtained. The alkyne functionalized **PB-1(A)** was then assembled in 90% yield by condensing eight triamine linkers (**1**) and six tetraformylphenylporphyrin building blocks (**2**) in $CHCl_3$ solution with a catalytic amount of TFA.[98] **PB-1(A)** was thoroughly characterized by NMR, FT-IR, and UV-vis spectroscopies as well as MALDI mass spectrometry and elemental analysis; the presence of 24 terminal alkynes was confirmed by the observation of a triplet at 1.94 ppm in the ^{1}H-NMR spectrum (Figure 3.15) and a sharp peak at 3293 cm^{-1} corresponding to the C-H stretch of the terminal alkynes detected by FT-IR (Figure 3.19). Notably, this **PB-1(A)** cage serves as a versatile synthon for further functionalization by copper-catalyzed azide-alkyne cycloaddition (CuAAC) click chemistry, after its metalation with zinc acetate to prevent copper insertion into the porphyrin during the click reaction. Initial pilot screening reactions between **ZnPB-1(A)** and N_3-$(CH_2)_6$-$NMe_3^+PF_6^-$ using typical conditions[102]: $CuSO_4$ (1.0 eq., 4.2 mol% per alkyne) and sodium ascorbate (2.0 eq., 8.4 mol% per alkyne) in a *t*BuOH/H_2O solvent mixture at room temperature resulted in no product isolated after 24 hours (Table 3.1, entry 1). Further optimization attempts involving changes in catalyst loading, solvent, and reaction temperature failed to yield the desired product (Table 3.1, entries 2-4). To simplify the reaction system, we turned to Cu(I) as a catalyst in anhydrous DMF solution. Unfortunately, neither catalytic nor stoichiometric quantities of CuI or $Cu(PPh_3)_3Br$ were successful, even after raising the temperature to 60 °C (Table 3.1, entries 5-8). Finally, we were able to obtain the desired product using click-type polymerization conditions[103] consisting of Cu(I)Br (24.0 eq.) with pentamethyldiethylenetriamine (PMDETA) (24.0 eq.). The positively charged **ZnPB-2(P)** organic cage was prepared in 95% isolated yield as confirmed by ^{1}H- and ^{19}F-NMR, UV-vis, FT-IR, and elemental analysis (Scheme 3.2). ^{1}H-NMR analysis of **ZnPB-2(P)** in CD_3CN showed a new peak at 6.70 ppm with an integral of 24 protons (Figure 3.26), which was assigned as the triazole signal. Moreover, the singlet at 2.68 ppm corresponding to the trimethylammonium group and the multiple at 0.60 – 1.70 ppm assigned to alkyl chains further demonstrated the successful addition of N_3-$(CH_2)_6$-NMe_3^+ to **ZnPB-1(A)**. The presence of PF_6^- counter anions was confirmed by observation of a doublet at –72.6 ppm by ^{19}F-NMR (Figure 3.27).

Elemental analysis revealed a nitrogen percentage increase from 6.66% (6.72% calculated) to 10.89% (11.25% calculated) as a consequence of the formed triazole rings and added quaternary ammonium groups, while carbon percentage decreased from 74.53% (74.91% calculated) to 53.90% (56.27% calculated). Moreover, we were able to characterize **ZnPB-2(P)** using electrospray ionization mass spectrometry (ESI-MS). The multiply charged ions distribution from +13 to +20 were observed as **ZnPB-2(P)** losing the corresponding number of counterions (PF_6^-) ions (Table 3.2, Figures 3.30-3.38). Taken together, these data further confirm successful **PB** modification through a modular post-synthetic click chemistry method.

2.2. Synthesis, Redox Behavior, and Electrochemical CO_2 Reduction Activity of Porous Iron Porphyrin Cage Analogs With or Without Additional Charged Functionalities.

To systematically evaluate the effects of second-sphere porosity and charge within these confined space CO_2RR catalysts, we synthesized the Fe analogs of the alkyne-functionalized, neutral, and highly positively charged porphyrin boxes, **FePB-1(A)**, **FePB-3(N)**, and **FePB-2(P)**, respectively (Figure 3.1a). It is noteworthy that the charged **FePB-2(P)** organic cage is soluble in both DMF and CH_3CN solvents at up to 1 mM concentrations, which is uncommon in **PB** supramolecules.[104] The newly-synthesized FePB cages, as well as the mononuclear **FeTPP** and the tetracationic **Fe-*p*-TMA**, which provide control compounds for electrostatic effects in planar mononuclear catalysts, were first compared by cyclic voltammetry (CV) using a glassy carbon electrode. The CV of **FePB-1(A)** under an Ar atmosphere shows three redox waves at $E_{1/2} = -0.62$, -1.52, and -2.11 V vs. ferrocene/ferrocenium (Fc/Fc$^+$), which we assigned as the formal Fe^{III}/Fe^{II}, Fe^{II}/Fe^{I}, and Fe^{I}/Fe^{0} redox couples, respectively (Figure 3.1b). The slight positive shift of Fe^{I}/Fe^{0} couple in **FePB-1(A)** compared to **FeTPP** ($E_{1/2} = -2.15$ V) is likely the result of the electron-withdrawing effect of the imine linkages in the porphyrin box. However, these data show that supramolecular encapsulation has modest effects on intrinsic redox properties of molecular porphyrin building blocks. **FePB-3(N)** displays a similar Fe^{I}/Fe^{0} couple ($E_{1/2} = -2.10$ V) to **FePB-1(A)**, indicating the triazole formed after the click reaction also has little effect on the redox potential of the iron centers, while the broadening of the Fe^{III}/Fe^{II} and Fe^{II}/Fe^{I} redox couples may be due to increased molecular complexity or varied metal ligation by solvent or counteranion. Interestingly, a 150-mV positive shift of the Fe^{I}/Fe^{0} wave was observed in **FePB-2(P)** ($E_{1/2} = -1.95$ V) compared with **FePB-1(A)** (Figure 3.1b). The electrostatic effect of introducing twenty-four trimethylammonium groups onto the periphery of a porous porphyrin cage scaffold is similar to what was reported for the inductive effect of adding four trimethylanilinium groups to a planar **FeTPP** compound in **Fe-*p*-TMA** ($E_{1/2} = -2.00$ V).[105] This charge effect is also responsible for a significant shift of E_{cat0} toward positive potentials (*vide infra*). Upon the addition of CO_2 and 1.0 M of 2,2,2-trifluoroethanol (TFE) as a proton source, a large current increase is observed for **FePB-2(P),** indicating fast CO_2 reduction catalysis (Figure 3.1c). The peak catalytic current under CO_2 for **FePB-2(P)** is substantially higher than that for each of the non-porous or non-cationic catalysts studied. In order to quantify product selectivity and evaluate the electrochemical stability of **FePB-2(P)**, controlled potential electrolysis (CPE) experiments at various applied potentials were conducted in CO_2-saturated acetonitrile solutions with 1.0 M TFE as the proton source and 1.67 μM of catalyst (10 μM Fe). Carbon monoxide (CO) was detected as the major product with a Faradaic efficiency (FE) of ca. 80%. The low catalyst loading demonstrated the high activity of **FePB-2(P)** for electrochemical CO_2RR, which gave a high total TON of 2656 within one hour (Figure 3.55).

2.3. Photochemical CO_2 Reduction Activity of Porous Iron Porphyrin Cage Analogs With or Without Additional Charged Functionalities.

Encouraged that **FePB-2(P)** is capable of electrochemical CO_2RR activity, we turned our attention to light-driven CO_2 reduction catalysis. In a typical experiment, 2 µM **FePB-2(P)** catalyst was added to a CO_2-saturated CH_3CN solution containing 200 µM Tris[2-phenylpyridinato-C^2,*N*]iridium(III) (Ir(ppy)$_3$) as a photosensitizer, 100 mM 1,3-dimethyl-2-phenyl-2,3-dihydro-1*H*-benzo[*d*]imidazole (BIH) as a sacrificial electron donor, and 1.0 M TFE as a proton source; the reactions were irradiated using a 440 nm blue LED light source. Figure 2a shows the catalytic activity of **FePB-2(P)** over a 1-hour period. Within the first two minutes of the reaction, a TOF_{max} of 1429 min^{-1} is reached; rates of this magnitude are unprecedented for homogeneous Fe porphyrin photocatalysts.[106-110] After a 1-hour photolysis period, we obtained a TON of 7,006 per box (1,168 per Fe center) with 97% selectivity for CO. Control experiments performed show that the catalyst, CO_2, proton source, sacrificial electron donor, light, and photosensitizer, are all required for activity (Table 3.3, Entries 6-11). Stern-Volmer analysis of the Ir(ppy)$_3$ excited state was used in order to determine a photocatalytic mechanism. We measured a bimolecular quenching rate constant (k_q) of 1.79 x10^{11} M^{-1} s^{-1} in CH_3CN between Ir(ppy)$_3$ and **FePB-2(P)** with no emission quenching observed using BIH (Figure 3.56), indicative of an oxidative quenching mechanism. All other catalysts gave similar quenching rate constants when measured in DMF (Figure 3.57). The quantum yield for CO production was determined to be Φ = 5.75% by ferrioxalate actinometry.

To disentangle contributions of second-sphere porosity and charge in **FePB-2(P)**, we evaluated the photocatalytic activity of **FeTPP**, **Fe-*p*-TMA**, and **FePB-3(N)**. To achieve a fair comparison and to ensure homogeneous conditions for all the catalysts, we used DMF as the solvent, increased catalyst concentration to 12 µM for mononuclear Fe porphyrins and corrected turnover number per iron center ($TON_{[Fe]}$) to reflect activity per Fe center, assuming there are 6 active iron centers per molecule of **FePB** catalyst. Figure 2b shows the photocatalytic activity of **FeTPP**, **Fe-*p*-TMA**, **FePB-3(N)**, and **FePB-2(P)** after 1-hour irradiation in CO_2-saturated DMF using the same standard conditions. We observe that the neutral porous cage catalyst **FePB-3(N)** outperforms **FeTPP**, which we attribute to enhanced substrate confinement effects in porous catalyst structures,[48] giving **FePB-3(N)** a 4-fold higher $TON_{[Fe]}$ and superior CO selectivity of 88% (Figure 3.2b). The previously reported[107, 108] incorporation of four trimethylanilinium groups into an **FeTPP** framework is reproduced under these conditions, showing higher selectivity and 6-fold higher TON value for CO_2RR with **Fe-*p*-TMA** (FE_{CO} = 88%, $TON_{[Fe]}$ = 70) compared to **FeTPP** (FE_{CO} = 70%, $TON_{[Fe]}$ = 12).

Interestingly, the data reveal that **FePB-2(P)**, which is endowed with both electrostatic and porosity functionalities, achieves a $TON_{[Fe]}$ of 496 after 1 h irradiation, representing a 41-fold increase in CO_2RR activity over the parent **FeTPP** catalyst. This enhancement is larger than what is observed for porosity-only **FePB-(N)** (4-fold) and charge-only **Fe-p-TMA** (6-fold) congeners, suggesting that integrating dual porosity and electrostatic interactions onto a single platform can work together to enhance photocatalytic CO_2RR activity in synergistic manner (Figure 3.2b, Table 3.3, Entries 1-5). Moreover, the high activity of **FePB-2(P)** enables photochemical CO_2RR to proceed under low CO_2 concentrations.[111-113] Indeed, Figure 3.2c shows **FePB-2(P)** achieves a CO

TON of 5476 with as little as 2% CO_2 in CH_3CN, maintaining 78% of its activity compared to saturated CO_2 conditions. We speculate that the ability of **FePB-2(P)** to maintain high relative CO_2RR rates even at low CO_2 concentrations may be attributed to the propensity of the porous organic cage to promote both carbon capture and conversion.[48, 98] We then compared the CO_2RR activity per [Fe] of **FePB-2(P)** with **FeTPP** and **FePB-3(N)** in DMF (Figure 3.2d). Going from the planar **FeTPP** catalyst to three-dimensional porous **FePB-3(N)** cage results in an 18-fold increase in TOF under 50% CO_2 concentrations, suggesting that porosity can play a critical role in facilitating substrate capture and conversion. Moreover, combining second-sphere porosity and charge in **FePB-2(P)** further augments the system, resulting in a 15-fold increase in TOF compared to **FePB-3(N)** at 2% CO_2 levels.

3. Concluding Remarks

To close, we have presented a supramolecular approach to enhancing photochemical CO_2RR in confined spaces through synergistic second-sphere porosity and charge effects. We enabled this strategy through the modular post-synthetic modification of porous porphyrin organic cages, where the incorporation of 24 alkyne groups provides a versatile platform for further functionalization via click chemistry. Using this synthon, addition of neutral carbon chain and cationic trimethylammonium groups onto the periphery of the cage scaffold affords **FePB-3(N)** and **FePB-2(P)** supramolecules featuring porosity-only and dual porosity/charge effects, respectively. Comparison of these catalysts with a planar **Fe-*p*-TMA** catalyst with charge-only effects establishes that dual second-sphere porosity and charge interactions can augment CO_2RR activity in a cooperative manner, exceeding the additive performance of introducing porosity or charge alone. **FePB-2(P)** achieves efficient CO_2RR with 97% selectivity for CO, TON of 7,006, and initial TOF rate of 1,429 min^{-1}. Moreover, these combined effects enable retention of efficient photochemical CO_2RR activity at concentrations of CO_2 down to 2%. This work highlights the use of multiple synergistic second-sphere interactions as an effective design strategy to enhance CO_2 capture and conversion activity, a concept that can be applied to a broader array of small-molecule activation reactions.

4. Experimental Section

4.1 General Methods

All reagents and solvents were purchased from commercial sources and used without further purification unless specified. Carbon dioxide (99.99%), carbon monoxide (99.5%), hydrogen (99.999%), ethane (99.9%), and argon (99.999%) were purchased from Praxair. *meso*-Tetraphenylporphyrin iron(III) chloride (FeTPP, >97%) and iron(III) *meso*-tetra(4-*N,N,N,N*-trimethylanilinium) porphine pentachloride (Fe-*p*-TMA, >95%) were purchased from Frontier Specialty Chemicals. $FeBr_2$ was purchased from Strem Chemicals and stored in the glovebox. Tris[2-phenylpyridinato-C^2,*N*]iridium(III) ($Ir(ppy)_3$, 99%), 2,2,2-trifluoroethanol (TFE, ≥99%), electrochemical grade tetrabutylammonium hexafluorophosphate ($TBAPF_6$, 99%), and 2,6-lutidine (99%) were purchased from Sigma-Aldrich. 1,3-Dimethyl-2-phenyl-2,3-dihydro-1H-benzo[d]imidazole (BIH) was synthesized according to the previously reported method.[114] HPLC grade *N,N*-dimethylformamide (DMF) and acetonitrile (CH_3CN) for photochemistry were purchased from Fisher and used as received. Tetrahydrofuran (THF) was dried using a JC Meyer solvent purification system. Deionized water was obtained from a Millipore Autopure system. FT-IR spectra were collected using a Bruker Vertex80 spectrometer. UV/Vis spectra were collected using an Agilent Cary 60 spectrophotometer at room temperature. Electrospray ionization (ESI) mass spectrometry was collected on a PerkinElmer AxION 2 TOF MS. Matrix-assisted laser desorption ionization (MALDI) mass spectrometry spectra were obtained using a Shimadzu AXIMA Performance. ESI mass spectra for **ZnPB-2(P)** were recorded using an LTQ FT-ICR mass spectrometer equipped with an electrospray ionization source (Finnigan LTQ FT, Thermo Fisher Scientific, Waltham, MA) operated in positive ion mode in the UC Berkeley's QB3/Chemistry mass spectrometry facility. Nuclear magnetic resonance (NMR) spectra were obtained on a Bruker AV-600 instrument at UC Berkeley's College of Chemistry NMR Facility. The chemical shifts (δ) are given in parts per million (ppm) relative to $CDCl_3$ (7.26 ppm for ^1H) or TMS (0 ppm for ^1H) and $CDCl_3$ (77.0 ppm for ^{13}C), and coupling constants (J) are reported in Hertz (Hz). The following abbreviations were used to explain the multiplicities: s = singlet, d = doublet, t = triplet, m = multiplet, br = broad, td = triplet of doublets, app. t = apparent triplet.

4.2 Electrochemical Measurements

Cyclic Voltammetry Methods. Cyclic voltammetry experiments were performed using a Bioanalytical Systems, Inc. (BASi) Epsilon potentiostat. A 10 mL 2-neck pear-shaped flask was equipped with a glassy carbon disk (3.0 mm diameter, BASi) working electrode, a platinum wire counter electrode, and an Ag wire contained in a porous Vycor tipped glass tube filled with electrolyte as a pseudo-reference electrode. Before use, the working electrode was thoroughly polished with 0.05 μm alumina powder on a felt pad. The electrolyte was 0.1 M $TBAPF_6$ in DMF or CH_3CN freshly prepared with anhydrous solvent and saturated with either CO_2 or Ar by sparging for 10 minutes. Gas flow was continued throughout the experiment with sparging in between scans and blanketing the solvent during scans. Cyclic voltammograms were obtained with internal resistance compensation measured immediately prior to each scan. The scan rates for all cyclic voltammograms were 100 mV/s unless otherwise noted. At the conclusion of the experiment, potentials were referenced against the ferrocene/ferrocenium redox couple of added ferrocene.

4.3 Controlled Potential Electrolysis Methods

Controlled potential electrolysis experiments were performed using a Bioanalytical Systems, Inc. (BASi) Epsilon potentiostat. Experiments were performed in a custom-made, gas-tight PEEK cell that is a miniaturized version of one previously reported by our laboratory.[41] The working chamber (25 mL liquid volume) and counter chamber (5 mL liquid volume) were separated by an ultra-fine glass frit (Ace Glass). A 1 cm × 1 cm × 0.6 cm Duocel® RVC foam (ERG Aerospace Corp.) attached to a stainless steel rod was used as the working electrode. A platinum gauze of about 1 cm^2 area (Sigma-Aldrich) connected to a platinum wire was used as the counter electrode, and an Ag wire in a Vycor tipped glass tube filled with electrolyte was used as a pseudo-reference electrode. The working compartment was filled with 12 mL of a 1.67 μM solution of **FePB-2(P)** dissolved in 0.1 M $TBAPF_6$ in CH_3CN containing 1.0 M TFE as a proton source. The counter electrode chamber was filled with 4 mL of a 20 mM solution of tetrabutylammonium acetate dissolved in 0.1 M $TBAPF_6$ in CH_3CN. This soluble source of acetate was sacrificially oxidized to generate CO_2 and ethane, thereby avoiding GC detection of solvent or anode oxidation byproducts. Both compartments were sealed to be gas-tight. The working compartment was sparged with CO_2 for 15 min, then sealed and injected with 0.5 mL of ethane as a gaseous internal standard. The electrolyte solution was constantly stirred during the electrolysis with a 1 cm stir bar. At the conclusion of the experiment, the headspace was injected directly into an SRI gas chromatography instrument (model #8610C) equipped with a Haysep D column (1/8"

× 6’) and a 13X Mol Sieve column (1/8” × 6’). Carbon monoxide and ethane were quantified using an in-line flame ionization detector (FID) equipped with a methanizer, and hydrogen and ethane were quantified using a thermal conductivity detector (TCD). Analytes of interest were quantified by comparing ratios of analyte/internal stand peak integrals to a calibration curve with known amounts of analyte.

4.4 Photocatalytic CO2 Reduction

Experiments were conducted inside a 25 mL borosilicate culture tube equipped with a stir bar, rubber septum, and aluminum crimped top. These reaction vessels contained either 5 mL CH_3CN or DMF, 2 µM catalyst, 200 µM photosensitizer, 100 mM BIH (112 mg), and 1.0 M TFE (360 µL). The reaction tubes were sparged with CO_2 for 10 minutes, followed by injection of a gaseous internal standard (0.1 mL of C_2H_6). For low concentration setup: CO_2 gas was diluted with Ar (2%, 10%, 25%, 50%, 75%, and 100% CO_2 gas) using a Miller 299-006-1C Argon/CO_2 Gas Mixer. Reactions were placed on a stir plate 13 cm from two Kessil blue LED lamps (440 nm) for the specified time in each experiment and kept at ambient temperature with a fan. Analysis of the headspace by GC was conducted for product detection as described above for CPE. Samples were then re-sparged with CO_2, and the process was repeated for the following timepoint of an experiment.

4.5 Fluorescence Quenching

The fluorescence of a CO_2-saturated CH_3CN solution of $Ir(ppy)_3$ (λ_{abs}= 380 nm, λ_{em}= 515 nm) was measured using a Photon Technology International Quanta Master 4 L-format scan spectrofluorometer equipped with an LPS-220B 75-W xenon lamp and power supply, A-1010B lamp housing with the integrated igniter, switchable 814 photocounting/analog photomultiplier detection unit, and MD5020 motor driver. Excited-state quenching experiments were carried out by adding either BIH or **FePB-2(P)**. The relative emission lifetime of the photosensitizer in the presence of quencher was used to calculate the Stern-Volmer quenching constant (k_q) using the following equation:

$$I_0/I_Q = 1 + \tau_f k_q [Q]$$

Where I_0/I_Q is the emission intensity in the absence (I_0) or presence (I_Q) of quencher, τ_f is the emission lifetime of $Ir(ppy)_3$ (2 µs), and [Q] is the concentration of the quencher.

A plausible reaction pathway for the photochemically CO_2 reduction to CO was proposed based on the fluorescence quenching results:

$$\mathrm{Ir(ppy)_3} \xrightarrow{hv} \mathrm{Ir(ppy)_3}^*$$

$$[\mathrm{Fe}]^n + n\ {}^*\mathrm{Ir(ppy)_3} \longrightarrow [\mathrm{Fe}]^0 + n\ \mathrm{Ir(ppy)_3}^+$$

$$[\mathrm{Fe}]^0 + \mathrm{CO_2} \longrightarrow [\mathrm{Fe}]^{II}\mathrm{CO_2}^{2-}$$

$$[\mathrm{Fe}]^{II}\mathrm{CO_2}^{2-} + 2\mathrm{H}^+ \longrightarrow [\mathrm{Fe}]^{II}\mathrm{CO} + \mathrm{H_2O}$$

$$[\mathrm{Fe}]^{II}\mathrm{CO} + e^- \longrightarrow [\mathrm{Fe}]^{I} + \mathrm{CO}$$

$$\mathrm{Ir(ppy)_3}^+ + \mathrm{BIH} \longrightarrow \mathrm{Ir(ppy)_3} + [\mathrm{BIH}]^{\cdot +}$$

4.6 Quantum Yield Determination

The quantum yield (Φ) of photocatalytic CO_2 reduction to CO was calculated for a 90-minute experiment using 2 µM **FePB-2(P)**, 200 µM Ir(ppy)$_3$, 100 mM BIH, and 1 M TFE in CO_2-saturated CH_3CN according to the equation:

$$\Phi = \frac{2\text{ (number of CO molecules)}}{\text{number of photons absorbed}} \text{ x } 100\ \%$$

Where the number of photons per unit time (photon flux) emitted by the blue LED light source used during photocatalytic experiments was measured via chemical actinometry.

$$Fe^{3+} \xrightarrow{\Delta} Fe^{2+}$$

$$Fe^{2+} + 3\text{ phen} \longrightarrow \underset{\lambda_{max} = 510\text{ nm}}{[Fe(phen)_3]^{2+}}$$

We used ferrioxalate ($K_3[Fe(C_2O_4)_3]$) for the actinometry experiment. The photochemical decomposition of ferrioxalate (Fe^{3+}) to Fe^{2+} can be monitored spectrophotometrically via the detection of free Fe^{2+} by chelation with phenanthroline according to the simplified reactions: First, a 3 mL (V_1) solution of ferrioxalate (0.012 M in 0.05M H_2SO_4) was irradiated for 10, 20, and 30 seconds while another solution of the same volume was kept in the dark. A 0.5 mL (V_2) aliquot of the irradiated solution was then added to a 2 mL solution of buffered phenanthroline (0.1% phenanthroline in 1.6 M NaOAc/0.5 M H_2SO_4) and then diluted with deionized water in a 25 mL (V_3) volumetric flask. This final solution was used for absorption measurement at 510 nm using an l=1 cm quartz cuvette.

The moles of Fe^{2+} formed in an irradiated solution can be calculated by:

$$\text{moles } Fe^{2+} = \frac{V_1 \text{ x } V_3 \text{ x } \Delta A_{510}}{10^3 \text{ x } V_2 \text{ x } l \text{ x } \varepsilon_{510}}$$

Where ΔA_{510nm} is the difference in absorption between the solution kept in the dark and the irradiated solution, and ε_{510nm} is the molar absorptivity of $[Fe(phen)_3]^{2+}$ at 510 nm (11100 L mol^{-1} cm^{-1}).

The average photon flux was then calculated using the following equation:

$$\#\text{ photons/sec} = \frac{6.022 \text{ x} 10^{23} \text{ x moles } Fe^{2+}}{\Phi_\lambda \text{ x } t}$$

Where Φ_λ is the excitation wavelength dependent quantum yield of ferrioxalate.

5. Synthetic Details

5.1 Synthesis of Triamine Linker 1

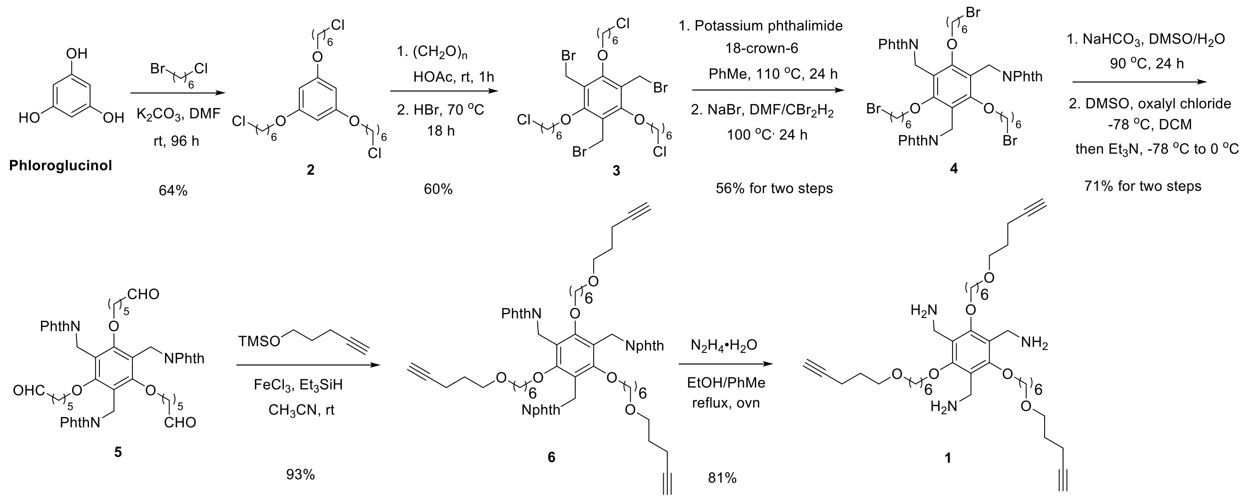

1,3,5-Tris((6-chlorohexyl)oxy)benzene (2). To a suspension of 1-Bromo-6-chlorohexane (500 g, 2.5 mol, 5.0 eq.) and anhydrous K_2CO_3 (414.7 g, 3.0 mol, 6.0 eq.) in DMF (1.0 L) was added a solution of phloroglucinol (63.1 g, 0.5 mol, 1.0 eq.) in DMF (0.5 L) over a period of 2 h at room temperature. Upon completion of addition, the reaction mixture was stirred at room temperature for another 96 h. The reaction mixture was then filtered through a pad of Celite, and the filtrate was concentrated under reduced pressure. The residue was redissolved in dichloromethane (DCM, 300 mL). The organic layer was washed successively with water (3 × 100 mL) and brine (100 mL), dried over anhydrous $MgSO_4$, and concentrated under reduced pressure. The crude product was purified by silica gel column chromatography (Hexane/DCM = 2:1) to give compound **2** as a colorless oil. Yield: 61.6 g (64 %). It should be noted that the purified product contains some bromine-functionalized product as indicated by ^{1}H NMR. ^{1}H NMR (600 MHz, $CDCl_3$) δ 6.05 (s, 3 H), 3.91 (t, *J* = 6.4 Hz, 6 H), 3.55 (CH_2Cl, t, *J* = 6.7 Hz, 5.3 H), 3.42 (CH_2Br, t, *J* = 6.8 Hz, 0.7 H), 1.92 – 1.87 (CH_2CH_2Br, m, 0.7 H), 1.84 – 1.74 (CH_2CH_2Cl, m, 11.3 H), 1.54 – 1.45 (m, 12 H). ^{13}C NMR (151 MHz, $CDCl_3$) δ 160.9, 93.8, 67.7, 45.0, 33.7, 32.7, 32.5, 29.0, 27.9, 26.6, 25.4, 25.3. MS (MALDI-TOF): calculated for $C_{24}H_{40}Cl_3O_3$ $[M+H]^+$: 481.20, found: 481.21.

1,3,5-Tris(bromomethyl)-2,4,6-tris((6-chlorohexyl)oxy)benzene (3). 1,3,5-Tris((6-chlorohexyl)oxy)benzene **2** (61.1 g, 126.0 mmol) and paraformaldehyde (17.5, 583 mmol) were suspended in glacial acetic acid (105 mL) in a pressure flask. After stirring at room temperature for 1 h, HBr (33% in acetic acid, 130 mL) was added, and the reaction mixture was stirred at 70 °C for 18 h. After cooling down to rt, the reaction mixture was poured into ice-cold water (300 mL) and extracted with DCM (3×150 mL). The combined organic layers were washed successively with water (3×100 mL), saturated aqueous $KHCO_3$ solution (100 mL), and brine (100 mL). The organic layer was dried over $MgSO_4$ and concentrated under reduced pressure. The residue was further by silica gel column chromatography (Hexane/DCM = 2:1) to give compound **3** as a colorless oil. Yield: 57 g (60%). ^{1}H NMR (600 MHz, $CDCl_3$) δ 4.57 (s, 6 H), 4.27 (t, *J* = 6.5 Hz, 6 H), 3.58 (CH_2Cl, t, *J* = 6.7 Hz, 5.3 H), 3.45 (CH_2Br, t, *J* = 6.8 Hz, 0 .7 H), 1.99 – 1.92 (m, 6.7 H), 1.90 – 1.82 (m, 5.3 H), 1.65 – 1.55 (m, 12 H). ^{13}C NMR (151 MHz, $CDCl_3$) δ 159.4, 123.2, 74.7, 45.0, 32.5, 30.1, 26.7, 25.1, 23.0. MS (ESI): calculated for $C_{27}H_{42}Br_3Cl_3O_3Na$ $[M+Na]^+$: 778.96, found: 779.02.

2,2',2''-((2,4,6-Tris((6-bromohexyl)oxy)benzene-1,3,5-triyl)tris(methylene))tris(isoindoline-1,3-dione) (4).To a solution of 1,3,5-tris(bromomethyl)-2,4,6-tris((6-chlorohexyl)oxy)benzene **3**

(57 g, 74.9 mmol, 1.0 eq.) and 18-crown-6 (5.94 g, 22.47 mmol, 0.3 eq.) in toluene (800 mL) was added potassium phthalimide (41.64 g, 224.7 mmol, 3.0 eq.). The reaction mixture was heated at 110 °C under N_2 for 24 h before being concentrated under reduced pressure. The resulting residue was redissolved in DCM (300 mL). The organic phase was washed successively with water (3 × 100 mL) and brine (100 mL), dried over $MgSO_4$, and concentrated to give the crude product as a pale-yellow oil. A mixture of the above crude product and sodium bromide (46.3 g, 449.6 mmol, 6.0 eq.) in DMF (300 mL) and dibromomethane (150 mL) was stirred at 100 ºC for 24 h. After cooling to room temperature, the reaction mixture was concentrated, and the resulting residue was redissolved in DCM (300 mL). The organic layer was washed with water (3 x 150 mL) and brine (100 mL), dried over anhydrous $MgSO_4$, and concentrated under reduced pressure. The residue was purified by silica gel column chromatography (DCM/EA = 30:1) to give compound **4** as a white solid. Yield: 45.8 g (56% yield for two steps). ^{1}H NMR (600 MHz, $CDCl_3$) δ 7.69 (dd, J = 5.5, 3.0 Hz, 6H), 7.62 (dd, J = 5.4, 3.0 Hz, 6H), 4.85 (s, 6H), 3.97 (t, J = 7.1 Hz, 6H), 3.35 (t, J = 6.9 Hz, 6H), 1.82 – 1.76 (m, 6H), 1.69 – 1.63 (m, 6H), 1.44 – 1.35 (m, 6H), 1.34 – 1.25 (m, 6H). ^{13}C NMR (151 MHz, $CDCl_3$) δ 167.7, 157.9, 133.6, 132.1, 122.9, 118.7, 74.3, 33.8, 33.4, 32.7, 29.7, 28.0, 24.9. MS (MALDI-TOF): calculated for $C_{51}H_{54}Br_3N_3O_9Na$ $[M+Na]^+$: 1112.13, found: 1112.14.

6,6',6''-((2,4,6-Tris((1,3-dioxoisoindolin-2-yl)methyl)benzene-1,3,5-triyl)tris(oxy))trihexanal (5). To a stirred solution of compound **4** (3.7 g, 3.3 mmol, 1.0 eq.) in a mixture of DMSO (24) and water (6 mL) was added $NaHCO_3$ (2.5 g, 29.7 mmol, 9.0 eq.), and the resulting suspension was stirred at 95 ºC for 24 h. After cooling to room temperature, water (100 mL) was added, and the aqueous phase was extracted with DCM (3 x 50 mL). The combined organic extracts were washed with water, dried over $MgSO_4$, and concentrated under reduced pressure. The crude product was used in the next step without further purification. A solution of DMSO (3.1 g, 39.6 mmol, 12.0 eq.) in anhydrous DCM (20 mL) was added dropwise over 30 min to a stirred solution of oxalyl chloride (2.5 g, 19.8 mmol, 6.0 eq.) in anhydrous DCM (60 mL) at -78 °C under N_2. Upon completion of the addition, the mixture was stirred at -78 °C for 5 min, followed by adding a solution of the above crude product in anhydrous DCM (20 mL) over 30 min at -78 °C. The reaction mixture was stirred at -78 °C for 40 min, then Et_3N (6.0 g, 59.4 mmol, 18.0 eq.) was added dropwise over 10 min. The resulting mixture was allowed to warm to 0 °C and stirred at 0 °C for 1 h. Water (50 mL) was added to quench the reaction, and the organic layer was separated and further washed with water (3 x 30mL) and brine. The organic layer was dried over anhydrous $MgSO_4$ and concentrated under reduced pressure. The residue was purified by silica gel column chromatography (DCM/EA = 5:1) to give compound **5** as a white solid. Yield: 2.10 g (71% over two steps) ^{1}H NMR (600 MHz, $CDCl_3$) δ 9.72 (t, J = 1.8 Hz, 3H), 7.67 (dd, J = 5.5, 3.0 Hz, 6H), 7.61 (dd, J = 5.4, 3.2 Hz, 6H), 4.84 (s, 6H), 3.98 (t, J = 7.1 Hz, 6H), 2.37 (td, J = 7.4, 1.8 Hz, 6H), 1.71 – 1.65 (m, 6H), 1.64 – 1.57 (m, 6H), 1.37 – 1.29 (m, 6H). ^{13}C NMR (151 MHz, $CDCl_3$) δ 202.5, 167.7, 157.9, 133.6, 132.0, 122.9, 118.8, 74.2, 43.7, 33.4, 29.6, 25.3, 21.9. MS (MALDI-TOF): calculated for $C_{51}H_{51}N_3O_{12}Na$ $[M+Na]^+$: 920.33, found: 920.34.

2,2',2''-((2,4,6-Tris((6-(pent-4-yn-1-yloxy)hexyl)oxy)benzene-1,3,5-triyl)tris(methylene))tris(isoindoline-1,3-dione) (6). To a solution of anhydrous iron(III) chloride (146 mg, 0.9 mmol, 0.3 eq.) and compound **5** (2.7 g, 3.0 mmol, 1.0 eq.) in anhydrous CH_3CN (45 mL) were added trimethyl(pent-4-yn-1-yloxy)silane **6** (1.7 g, 10.8 mmol, 3.6 eq.) and triethylsilane (1.3 g, 10.8 mmol, 3.6 eq.) successively at 0 °C under N_2 atmosphere. After stirring at r.t. for 8 h, the reaction mixture was diluted with DCM (50 mL). The organic layer was washed with brine, dried over $MgSO_4$, filtered, and concentrated. The residue was purified by silica gel column chromatography (DCM/EA = 5:1) to yield compound 6 as a colorless oil (3.1 g, 93%). ^1H NMR (600 MHz, $CDCl_3$) δ 7.68 (dd, J = 5.5, 3.0 Hz, 6H), 7.61 (dd, J = 5.5, 3.1 Hz, 6H), 4.85 (s, 6H), 3.95 (t, J = 7.2 Hz, 6H), 3.46 (t, J = 6.2 Hz, 6H), 3.35 (t, J = 6.7 Hz, 6H), 2.26 (td, J = 7.1, 2.7 Hz, 6H), 1.93 (t, J = 2.7 Hz, 3H), 1.76 (appt. p, J = 6.6 Hz, 6H), 1.68 – 1.61 (m, 6H), 1.50 (appt. p, J = 6.7 Hz, 6H), 1.35 – 1.21 (m, 12H). ^{13}C NMR (151 MHz, $CDCl_3$) δ 167.7, 157.9, 133.5, 132.1, 122.9, 118.7, 84.1, 74.5, 70.9, 69.0, 68.3, 33.4, 29.9, 29.6, 28.6, 26.0, 25.6, 15.2. MS (MALDI-TOF): calculated for $C_{66}H_{75}O_{12}Na$ $[M+Na]^+$: 1124.52, found: 1124.49.

(2,4,6-Tris((6-(pent-4-yn-1-yloxy)hexyl)oxy)benzene-1,3,5-triyl)trimethanamine (1). To a stirred solution of **6** (3.1 g, 2.8 mmol, 1.0 eq.) in a mixture of EtOH/PhMe (10 mL/5 mL) was added $N_2H_4 \cdot H_2O$ (4.3 g, 30.0 eq.), the reaction mixture was stirred at 90 °C overnight. After cooling to room temperature, the reaction mixture was diluted with DCM (100 mL) and filtered through a pad of Celite to remove the white precipitation. The filtrate was washed with H_2O (3 × 50 mL) and brine (50 mL), dried over $MgSO_4$, filtered, and concentrated. Compound **1** was obtained as a colorless oil. ^1H NMR (600 MHz, $CDCl_3$) δ 3.82 (t, J = 6.6 Hz, 6H), 3.79 (s, 6H), 3.50 (t, J = 6.2 Hz, 6H), 3.43 (t, J = 6.5 Hz, 6H), 2.29 (td, J = 7.1, 2.7 Hz, 6H), 1.94 (t, J = 2.7 Hz, 3H), 1.88 – 1.76 (m, 12H), 1.66 – 1.57 (m, 6H), 1.56 – 1.48 (m, 6H), 1.48 – 1.40 (m, 6H). ^{13}C NMR (151 MHz, $CDCl_3$) δ 155.9, 127.2, 84.0, 75.3, 70.8, 69.0, 68.3, 36.6, 30.4, 29.6, 28.6, 26.1, 25.9, 15.2. MS (ESI): calculated for $C_{42}H_{70}N_3O_6$ $[M+H]^+$: 712.53, found: 712.54.

5.2 Synthesis of Free Base Porphyrin Box PB-1(A).

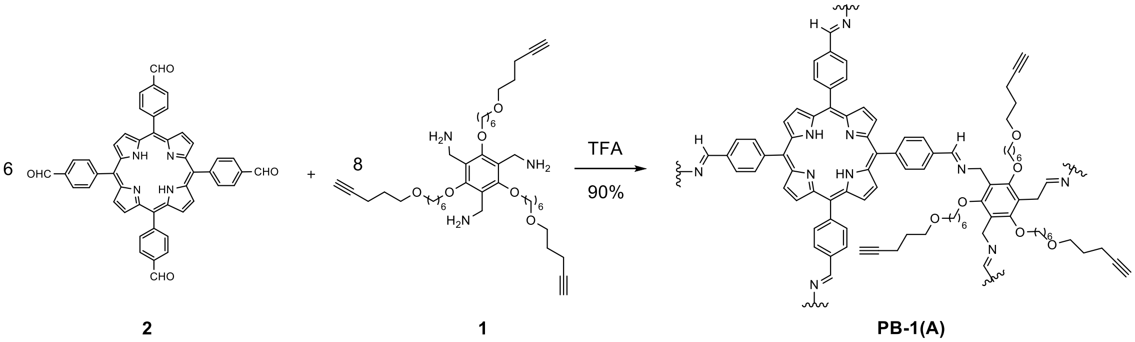

PB-1(A) was synthesized according to the literature with a slightly modified procedure.[104] To a solution of *meso*-tetra(*p*-formylphenyl)porphyrin **2** (176 mg, 0.242 mmol) and triamine **1** (860 mg, 1.21 mmol, 5.0 eq.) in $CHCl_3$ (17.6 mL) was added a catalytic amount of trifluoroacetic acid (1.76 μL), the reaction mixture was allowed to stir at 55 °C for 24 h in a sealed 50 mL round bottom flask. After cooling down to room temperature, the solvent was removed under reduced pressure. Methanol (20 mL) was added, and after sonication for 1 minute to suspend the product, the precipitated purple solid was collected by filtration and washed with methanol (3 × 20 mL). The collected purple solid was suspended in chloroform and sonicated for 1 minute, the suspension was filtered to remove any insoluble solid, and the chloroform filtrate was concentrated to give a purple solid. This washing cycle with methanol was repeated another two times. **PB-1(A)** (349 mg, 90%) was obtained as a purple powder. ^1H NMR (600 MHz, $CDCl_3$) δ 8.89 (s, 24H), 8.73 (s, 48H), 8.30 (d, J = 7.8 Hz, 24H), 8.20 (d, J = 7.8 Hz, 24H), 8.09 (d, J = 7.8 Hz, 24H), 7.96 (d, J = 7.8 Hz, 24H), 5.11 (s, 48H), 4.25 (s, 48H), 3.48 (t, J = 6.6 Hz, 48H), 3.43 (t, J = 6.2 Hz, 48H), 2.13 (td, *J* = 7.1, 2.7 Hz, 48H), 1.94 (t, *J* = 7.3 Hz, 24H), 1.72 (app. t, *J* = 6.7 Hz, 48H), 1.69 – 1.49 (m, 192H), -3.05 (s, 12H). ^{13}C NMR (151 MHz, CDCl$_3$) δ 160.5, 159.0, 144.3, 135.9, 134.8, 128.0, 124.6, 122.8, 119.7, 83.8, 71.0, 69.0, 68.4, 30.1, 29.9, 28.6, 26.2, 26.0, 15.2. FT-IR (solid): ν = 3293 (-C≡C-H), 2932, 2854, 1639 (C=N), 1580, 1430, 1100, 964, 798, 626 cm^{-1}; MS (MALDI-TOF): calculated. for $C_{624}H_{685}N_{48}O_{48}$ [M+H]$^+$: 9625.6, found: 9625.6; Elemental analysis data: Anal. Calcd. for $C_{624}H_{684}N_{48}O_{48}$: C, 77.87; H, 7.16; N, 6.99. Found: C, 77.89; H, 7.30; N, 6.89. UV/Vis (DCM) λ_{abs} 420, 518, 553, 592, 649 nm.

5.3 Synthesis of Zinc Porphyrin Box ZnPB-1(A).

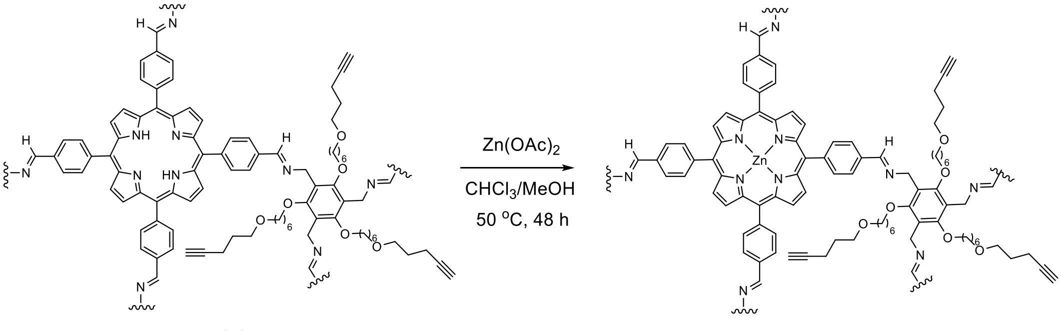

PB-1(A) **ZnPB-1(A)**

ZnPB-1(A) was synthesized according to the reported procedure.[115] To a chloroform solution (5 mL) of **PB-1(A)** (49.5 mg, 5.1 µmol, 1.0 eq.) was added a methanol solution (2.5 mL) of Zn(OAc)$_2$ (28 mg, 0.15 mmol, 30 eq.) at room temperature. After stirring at 50 °C for 48 h, the reaction mixture was concentrated. Methanol (15 mL) was added, and the violet precipitate was filtered and washed with methanol (3 x 15 mL). Yield: 51 mg (quant.). ^{1}H NMR (600 MHz, CDCl$_3$) δ 8.90 (s, 24H), 8.84 (s, 48H), 8.29 (d, *J* = 7.8 Hz, 24H), 8.21 (d, *J* = 7.8Hz, 24H), 8.07 (d, *J* = 7.8Hz, 24H), 7.96 (d, *J* = 7.8Hz, 24H), 5.11 (s, 48H), 4.24 (s, 48H), 3.47 (t, *J* = 6.6 Hz, 48H), 3.41 (t, *J* = 6.2 Hz, 48H), 2.09 (td, *J* = 7.1, 2.7 Hz, 48H), 1.94 (t, *J* = 7.4 Hz, 24H), 1.71 (app. t, *J* = 6.7 Hz, 48H), 1.67 – 1.47 (m, 192H). MS (MALDI-TOF): m/z calcd. for $C_{624}H_{672}N_{48}O_{48}Zn_6$ [M]$^+$: 9999.7, found: 9999.1; FT-IR (neat): ν = 3285 (-C≡C-H), 2932, 2854, 1639 (C=N), 1580, 1433, 1099, 993, 793, 527 cm^{-1}. Elemental analysis data: Anal. calcd. for $C_{624}H_{672}N_{48}O_{48}Zn_6$: C, 74.91; H, 6.77; N, 6.72. Found: C, 74.53; H, 7.00; N, 6.66. UV/Vis (DCM) λ_{abs} 425, 550, 595 nm.

5.4 Optimization of Reaction Conditions for Positively Charge Zinc Porphyrin Box ZnPB-2(P).

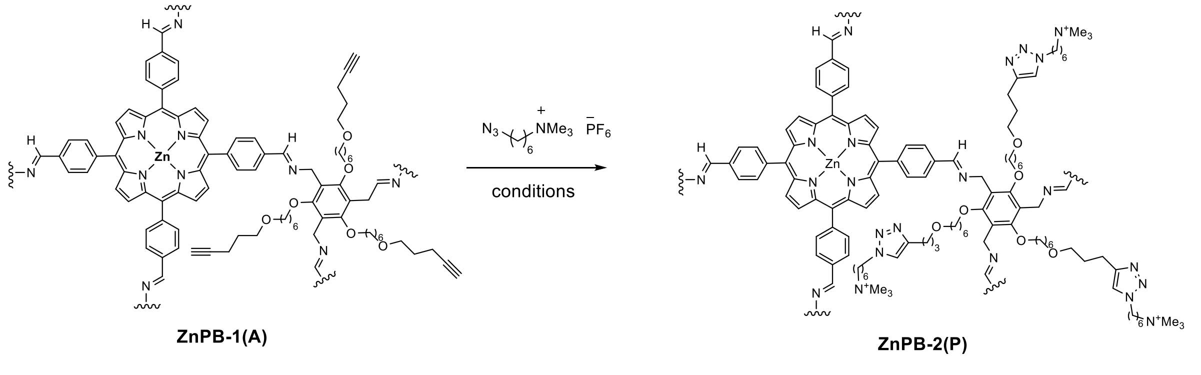

ZnPB-1(A) **ZnPB-2(P)**

Table 3.1. Optimization of Reaction Conditions.

Entry	Catalyst(eq.)	Ligand	Reductant(eq.)	Solvents	Temp(°C)	Yield
1	$CuSO_4$ (1.0)	None	SA (2.0)	*t*BuOH/H_2O	25	NR
2	$CuSO_4$ (1.0)	None	SA (2.0)	THF/H_2O	25	NR
3	$CuSO_4$ (24.0)	None	SA (48.0)	*t*BuOH/H_2O	25	NR
4	$CuSO_4$ (24.0)	None	SA (48.0)	THF/H_2O	60	NR
5	CuI (1.0)	None	None	DMF	60	NR
6	CuI (24.0)	None	None	DMF	60	NR
7	$Cu(PPh_3)_3Br$ (1.0)	None	None	DMF	60	NR
8	$Cu(PPh_3)_3Br$ (24.0)	None	None	DMF	60	NR
9	CuBr (24.0)	PMDETA (24.0)	None	DMF	25	95%
10	CuBr (24.0)	None	None	DMF	25	NR

Reaction conditions (unless otherwise specified): **ZnPB-1(A)** (5.0 mg, 0.5 µmol, 1.0 eq.), N_3-$(CH_2)_6$-$NMe_3^+PF_6^-$ (10.0 mg, 30 µmol, 60.0 eq.), anhydrous DMF (1 mL) for 18 h. SA = Sodium Ascorbate. PMDETA = *N*,*N*,*N′*,*N″*,*N″*-Pentamethyldiethylenetriamine. NR = no reaction.

$CuSO_4$/SA Catalysis System: $CuSO_4 \cdot 5H_2O$ (0.13 mg, 0.5 µmol, 1.0 eq. or 1.5 mg, 12 µmol, 24.0 eq.), sodium ascorbate (0.2 mg, 0.5 µmol, 2.0 eq. or 2.4 mg, 12 µmol, 48.0 eq.), 6-azido-*N*,*N*,*N*-trimethylhexan-1-aminium hexafluorophosphate (10 mg, 30 µmol, 60.0 eq.), and **ZnPB-1(A)** (5 mg, 0.5 µmol, 1.0 eq.) were suspended in *t*BuOH/H_2O (1 mL/ 1mL) or THF/H_2O (1 mL/ 1mL). The reaction mixture was stirred at the indicated temperature for 18 h. The reaction mixture was then diluted with CH_2Cl_2 (20 mL), washed with H_2O (5 × 20 mL) and brine (20 mL), dried over $MgSO_4$, filtered, and evaporated to give a purple solid. ^{1}H-NMR in CD_3CN indicated no product formation.

CuI or $Cu(PPh_3)_3Br$ Catalysis System:

Under a nitrogen atmosphere, CuI (0.1 mg, 0.5 µmol, 1.0 eq. or 2.3 mg, 12 µmol, 24.0 eq.) or $Cu(PPh_3)_3Br$ (0.47 mg, 0.5 µmol, 1.0 eq. or 11.2 mg, 12 µmol, 24.0 eq.), 6-azido-*N*,*N*,*N*-trimethylhexan-1-aminium hexafluorophosphate (10 mg, 30 µmol, 60.0 eq.), and **ZnPB-1(A)** (5 mg, 0.5 µmol, 1.0 eq.) were dissolved in anhydrous DMF (1 mL). The reaction mixture was stirred at the indicated temperature for 18 h. Subsequently, the solvent was removed under reduced pressure. Then, methanol (25 mL) was added, and after sonication for 30 s to suspend the product, the suspension was transferred to a conical tube and centrifuged. The supernatant was decanted, and the solid was collected. This washing cycle with methanol was repeated ten times. ^{1}H-NMR in CD_3CN indicated no product formation.

CuBr/PMDETA Catalysis System:
Under a nitrogen atmosphere, CuBr (1.7 mg, 12 µmol, 24.0 eq.), 6-azido-*N*,*N*,*N*-trimethylhexan-1-aminium hexafluorophosphate (10 mg, 30 µmol, 60.0 eq.), and **ZnPB-1(A)** (5 mg, 0.5 µmol, 1.0 eq.) were dissolved in anhydrous DMF (1 mL). Subsequently, PMDETA (2.1 mg, 12 µmol, 24.0 eq.) was added, and the reaction mixture was stirred at room temperature for 18 h. DMF was removed under reduced pressure, and the resulting residue was suspended in methanol (25 mL) and sonicated for 30 s. The suspension was transferred to a conical tube and centrifuged. The supernatant was decanted, and the solid was collected. After repeating this washing cycle with methanol ten times, **ZnPB-2(P)** was obtained as a purple powder in quantitative yield. Analytical data for **ZnPB-2(P)**: ^{1}H NMR (600 MHz, CD_3CN) δ 8.98 (s, 24H), 8.71 (s, 48H), 8.24 (d, *J* = 7.9 Hz, 24H), 8.10 (d, *J* = 8.0 Hz, 24H), 8.04 (d, *J* = 7.4 Hz, 24H), 7.98 (d, *J* = 7.8 Hz, 24H), 6.73 (br, 24H), 5.03 (br, 48H), 4.17 (br, 48H), 3.71 – 3.14 (m, 144H), 3.10 (br, 48H), 2.80 (br, 48H), 2.68 (s, 216H), 1.79 – 0.43 (m, 432H). ^{19}F NMR (565 MHz, CD_3CN) δ -72.59 (d, *J* = 707.1 Hz). FT-IR (solid) v= 2934, 2855, 1638, 1484, 1104, 992, 834, 556 cm^{-1}. UV/Vis (CH_3CN) λ_{abs} 431, 568, 609 nm. Elemental analysis data: Anal. calcd. for $C_{840}H_{1176}N_{144}O_{48}Zn_6F_{144}P_{24}$: C, 56.27; H, 6.61; N, 11.25. Found: C, 53.90; H, 6.56; N, 10.89. For ESI-MS data, see Table 2.

Table 3.2: Electrospray-ionization mass spectrometry analysis of **ZnPB-2(P)**.

Symbol	Formula	Charge (z)	m/z calculated monoisotopic mass	m/z calculated average mass	Found
$[M-20(PF_6)]^{20+}$	$C_{840}H_{1176}N_{144}O_{48}Zn_6P_4F_{24}$	20	750.6411	751.5759	751.5920
$[M-19(PF_6)]^{19+}$	$C_{840}H_{1176}N_{144}O_{48}Zn_6P_5F_{30}$	19	797.7782	798.7623	798.7264
$[M-18(PF_6)]^{18+}$	$C_{840}H_{1176}N_{144}O_{48}Zn_6P_6F_{36}$	18	850.1528	851.1915	851.0988
$[M-17(PF_6)]^{17+}$	$C_{840}H_{1176}N_{144}O_{48}Zn_6P_7F_{42}$	17	908.6892	909.7890	909.8081
$[M-16(PF_6)]^{16+}$	$C_{840}H_{1176}N_{144}O_{48}Zn_6P_8F_{48}$	16	974.5425	975.7111	975.6692
$[M-15(PF_6)]^{15+}$	$C_{840}H_{1176}N_{144}O_{48}Zn_6P_9F_{54}$	15	1049.1763	1050.4228	1050.3782
$[M-14(PF_6)]^{14+}$	$C_{840}H_{1176}N_{144}O_{48}Zn_6P_{10}F_{60}$	14	1134.4721	1135.8076	1135.8302
$[M-13(PF_6)]^{13+}$	$C_{840}H_{1176}N_{144}O_{48}Zn_6P_{11}F_{66}$	13	1232.8903	1234.3286	1234.2761

5.5 Synthesis of Neutral Zinc Porphyrin Box ZnPB-3(N).

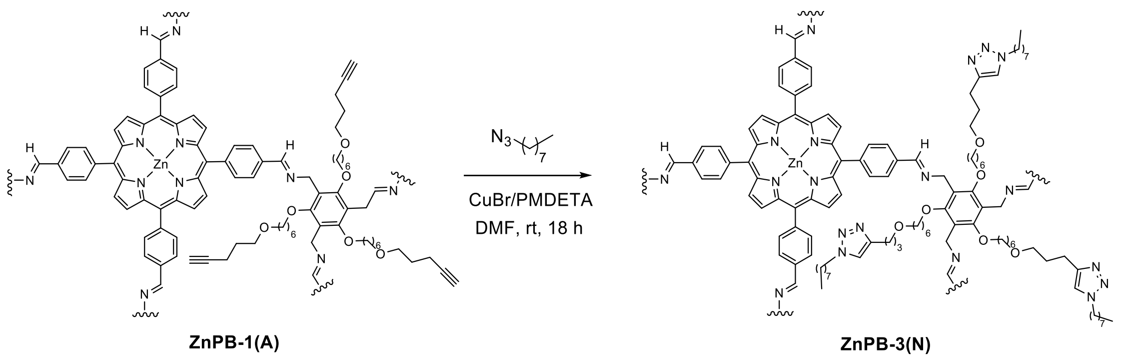

Under a nitrogen atmosphere, CuBr (3.5 mg, 24 µmol, 24.0 eq.), 1-azidooctane (10 mg, 30 µmol, 60.0 eq.), and **ZnPB-1(A)** (10 mg, 1 µmol, 1.0 eq.) were dissolved in anhydrous DMF (2 mL). Subsequently, PMDETA (4.2 mg, 24 µmol, 24.0 eq.) was added, and the reaction mixture was stirred at room temperature for 18 h. DMF was removed under reduced pressure, and the resulting residue was suspended in methanol (25 mL) and sonicated for 30 s. The suspension was transferred to a conical tube and centrifuged. The supernatant was decanted, and the solid was collected. After repeating this washing cycle with methanol ten times, **ZnPB-3(N)** was obtained in 97% yield. ^{1}H NMR (600 MHz, DMF-*d*$_7$) δ 9.10 (s, 24H), 8.79 (s, 24H), 8.41 – 8.20 (m, 48H), 8.12 (br, 48H), 7.21 (br, 24H), 5.09 (s, 48H), 4.28 (s, 48H), 3.79 (s, 48H), 3.44 (br, 96H), 3.28 (s, 48H), 2.22 (br, 48H), 1.97 (br, 48H), 1.71 (br, 48H), 1.65 – 1.25 (m, 192H), 1.04 (br, 48H), 0.95 (br, 96H), 0.65 (br, 72H). FT-IR (solid) ν = 3134 (triazole ring), 2924, 2852, 1638, 1582, 1433, 1103, 992, 793, 716 cm^{-1}. UV/Vis (CH$_2$Cl$_2$) λ_{abs} 430, 565, 605 nm. Elemental analysis data: Anal. calcd. for $C_{816}H_{1080}N_{120}O_{48}Zn_6(CH_2Cl_2)_8$: C, 68.68; H, 7.67; N, 11.66. Found: C, 67.44; H, 7.61; N, 11.45.

5.6 Synthesis of Iron Porphyrin Box FePB-1(A).

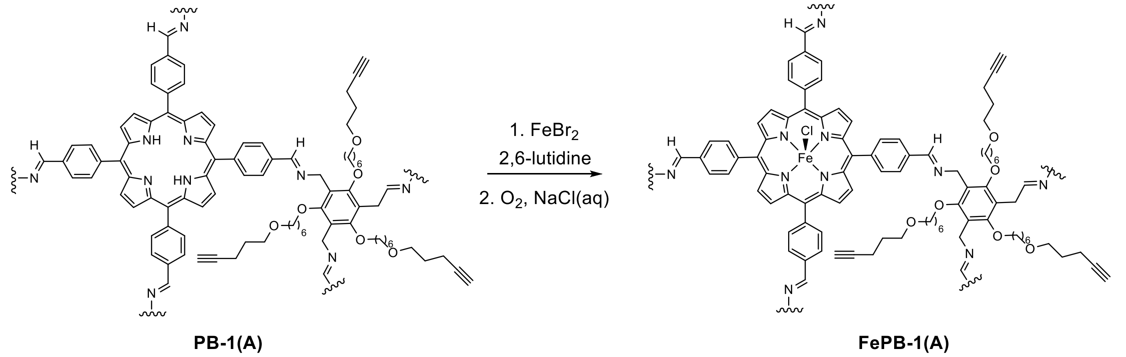

FePB-1(A) was synthesized according to the literature.[48] To a 150 mL pressure flask was added free-base **PB-1(A)** (72.2 mg, 7.5 µmol), FeBr$_2$ (162 mg, 0.75 mmol, 100 eq.), 2,6-lutidine (27 µL, 0.225 mmol, 30 eq.) and THF (100 mL) under N$_2$ atmosphere. The mixture was heated at 70 ºC for 12 h. After cooling to room temperature, the reaction was opened to air, and the solvent was removed under reduced pressure. The brown residue was taken up in CH$_2$Cl$_2$ (100 mL), washed with water (4 x 50 mL), and then with saturated aqueous NaCl solution (2 x 50 mL). The organic layer was separated, additional saturated aqueous NaCl solution (100 mL) was added, and the mixture was vigorously stirred for 30 min. The organic layer was decanted, dried over anhydrous MgSO$_4$, and filtered. The solvent was evaporated to give **FePB-1(A)** as a dark brown solid (68 mg, 92% yield). MS (MALDI-TOF): m/z calcd. for $C_{624}H_{672}N_{48}O_{48}Fe_6Cl_6$ [M]$^+$: 10157.6, found: 10157.7. FT-IR (neat): ν = 3287 (-C≡C-H), 2930, 2854, 1639 (C=N), 1580, 1432, 1102, 997, 801, 628 cm^{-1}. Elemental analysis calcd for $C_{624}H_{672}N_{48}O_{48}Fe_6Cl_6$: C, 73.77; H, 6.67; N, 6.62. Found: C, 71.18; H, 6.71; N, 6.29. UV/Vis (CH_2Cl_2) λ_{abs} 380, 419, 512, 586 nm.

5.7 Synthesis of Positively Charged Iron Porphyrin Box FePB-2(P).

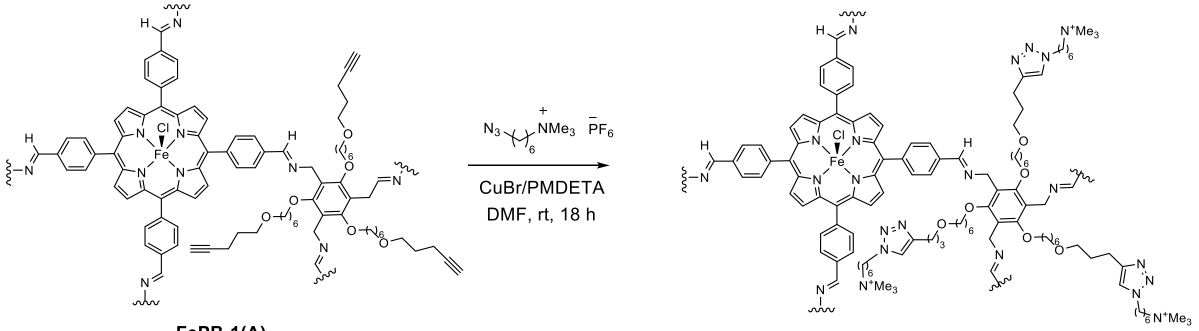

FePB-1(A) **FePB-2(P)**

Under a nitrogen atmosphere, CuBr (31.5 mg, 216 µmol, 24.0 eq.), 6-azido-*N*,*N*,*N*-trimethylhexan-1-aminium hexafluorophosphate (180 mg, 540 µmol, 60.0 eq.), and **FePB-1(A)** (90 mg, 9 µmol, 1.0 eq.) were dissolved in anhydrous DMF (18 mL). Subsequently, PMDETA (38 mg, 216 µmol, 24.0 eq.) was added, and the reaction mixture was stirred at room temperature for 18 h. DMF was removed under reduced pressure, and the resulting residue was suspended in methanol (25 mL) and sonicated for 30 s. The suspension was transferred to a conical tube and centrifuged. The supernatant was decanted, and the solid was collected. After repeating this washing cycle with methanol ten times, **FePB-2(P)** was obtained in 96% yield. ^{19}F NMR (565 MHz, CD_3CN) δ -72.45 (d, *J* = 715.3 Hz). FT-IR (solid) *v* = 2939, 2857, 1635, 1482, 1106, 997, 832, 556 cm^{-1}. UV/Vis (CH_3CN) λ_{abs} 416, 573, 615 nm.

5.8 Synthesis of Neutral Porphyrin Box FePB-3(N).

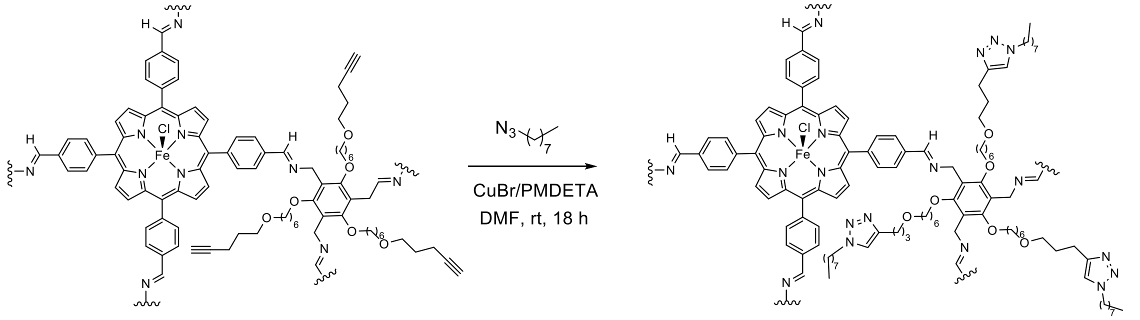

FePB-1(A) **FePB-3(N)**

Under a nitrogen atmosphere, CuBr (10.5 mg, 72 µmol, 24.0 eq.), 1-azidooctane (30 mg, 180 µmol, 60.0 eq.), and **FePB-1(A)** (30.5 mg, 3 µmol, 1.0 eq.) were dissolved in anhydrous DMF (6 mL). Subsequently, PMDETA (12.5 mg, 72 µmol, 24.0 eq.) was added, and the reaction mixture was stirred at room temperature for 18 h. DMF was removed under reduced pressure, and the resulting residue was suspended in methanol (25 mL) and sonicated for 30 s. The suspension was transferred to a conical tube and centrifuged. The supernatant was decanted, and the solid was collected. After repeating this washing cycle with methanol ten times, **FePB-3(N)** was obtained in 93% yield. FT-IR (solid) v = 3130 (triazole ring), 2923, 2851, 1641, 1580, 1432, 1100, 997, 799, 718 cm^{-1}. UV/Vis (CH_2Cl_2) λ_{abs} 418, 578, 623 nm.

6. Figures

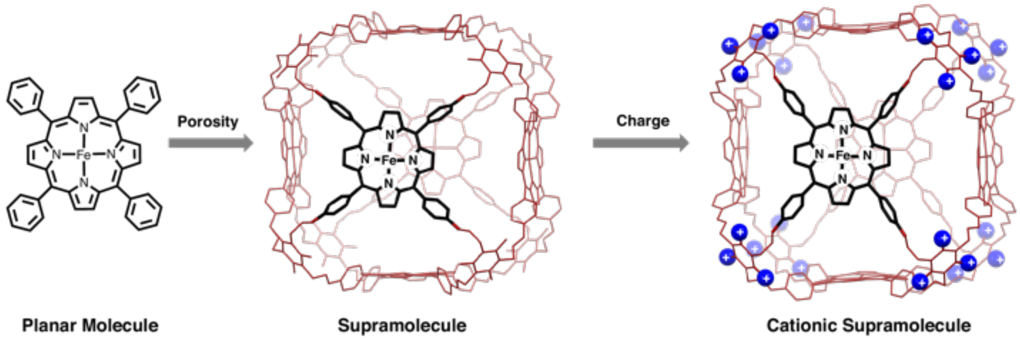

Scheme 3.1. The design of supramolecular CO_2 reduction reaction (CO_2RR) catalysts based on iron porphyrin organic cages that incorporate cooperative second-sphere porosity and charge effects.

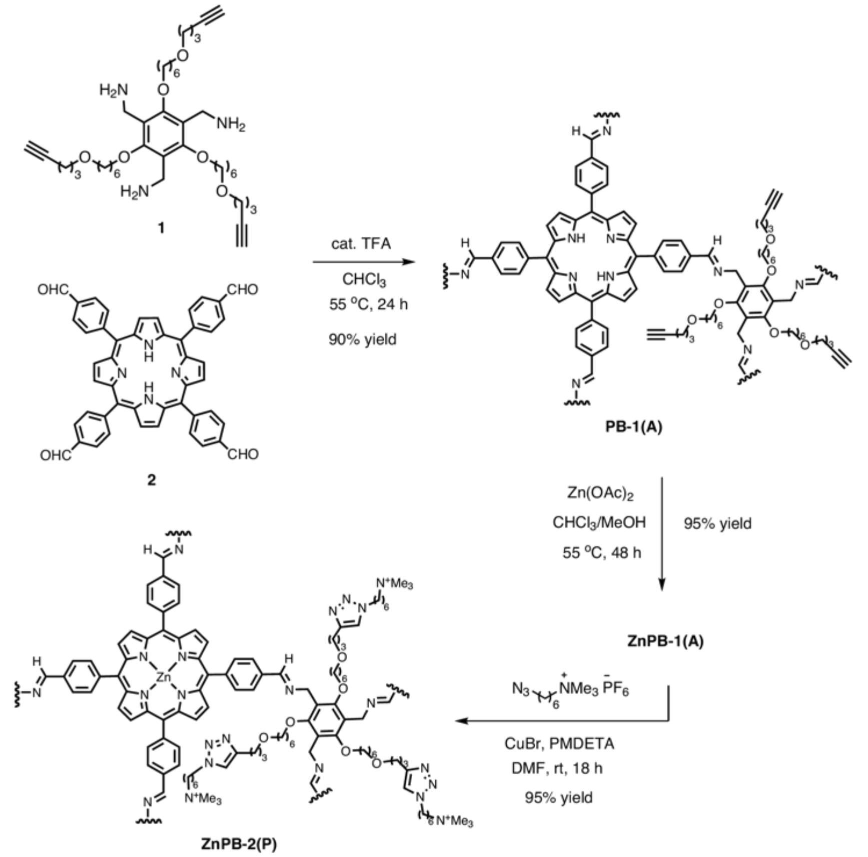

Scheme 3.2. Synthesis of the alkyne-functionalized porphyrin cage **PB-1(A)** and the Zn-metalated, charged porphyrin cage **ZnPB-2(P)**.

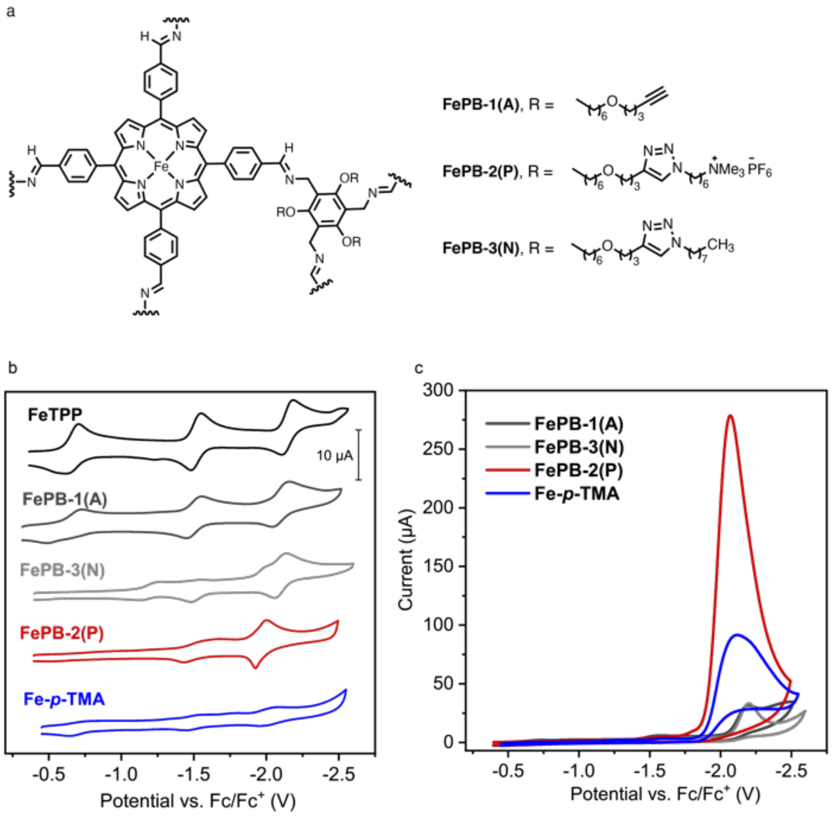

Figure 3.1. (a) Structures of the alkyne porous cage synthon **FePB-1(A)**, the neutral porous cage **FePB-3(N)**, and the charged porous cage **FePB-2(P)**. Electrochemical characterization in 0.1 M Bu_4NPF_6/DMF of 0.1 mM **FePB-1(A)** (dark grey), **-2(P)** (red) **-3(N)** (light grey), 0.6 mM **FeTPP** (black) and **Fe-*p*-TMA** (blue) under (b) Argon atmosphere and (c) CO_2 atmosphere with 1.0 M TFE as a proton source.

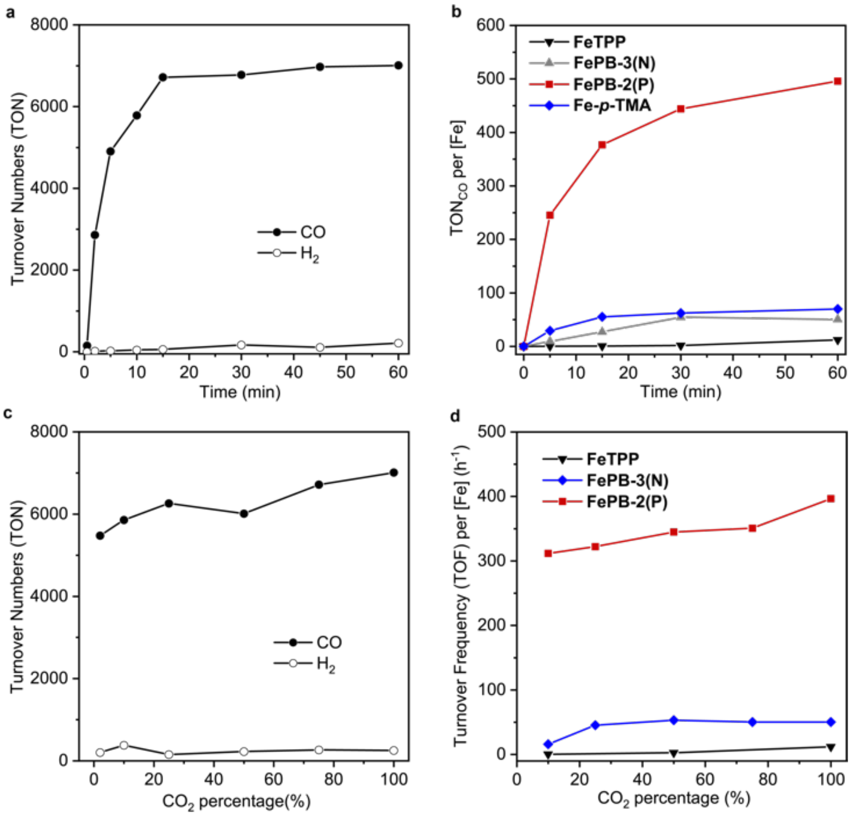

Figure 3.2. (a) Photocatalytic CO_2RR activity of **FePB-2(P)** in CO_2-saturated CH_3CN. (b) Photocatalytic CO_2RR activity of **FePB-2(P)** in CO_2-saturated DMF, comparing TON per [Fe] to **FePB-3(N)**, **FeTPP**, and **Fe-p-TMA**. (c) Photochemical CO_2RR reduction activity of **FePB-2(P)** in CH_3CN under varying CO_2 concentrations, showing activity down to 2% CO_2. (d) Photochemical CO_2RR activity of **FePB-2(P)** in DMF under varying CO_2 concentrations, showing a comparison per [Fe] between **FePB-2(P)**, **FePB-3(N)**, and **FeTPP**. **FePB-2(P)** is active down to 5% CO_2 concentrations. Conditions: 2 μM **PB** or 12 μM mononuclear catalyst, 200 μM Ir(ppy)$_3$, 100 mM BIH, and 1.0 M TFE.

Table 3.3. Photocatalytic activity of [Fe] under various conditions

Entry	Catalyst	TON Per [Fe]		$TOF^{max}_{[Fe]}$ (min^{-1}) [h]	Selectivity CO (%)
		CO	H_2		
1[a]	**FePB-2(P)**	1,168	42	164	97
2	**FePB-2(P)**	496	7	49	98
3	**FePB-3(N)**	50	7	1.9	88
4	**FeTPP**	12	5	0.08	70
5	**Fe-*p*-TMA**	70	10	5.8	88
6[b]	None	0	1	-	-
7[c]	**FePB-2(P)**	0	182	-	-
8[d]	**FePB-2(P)**	40	143	-	22
9[e]	**FePB-2(P)**	0	0	-	-
10[f]	**FePB-2(P)**	0	0	-	-
11[g]	**FePB-2(P)**	33	0	-	100

Reaction Conditions: 200 μM Ir(ppy)$_3$, 100 mM BIH, 1.0 M TFE after 1 hour irradiation in a CO_2 saturated DMF solution unless otherwise noted; control experiment data collected after 30-minute irradiation in entries 6-11. [a]In CH_3CN. [b]Without **FePB-2(P)** catalyst. [c]Under Ar atmosphere. [d]Without TFE. [e]Without BIH. [f]Without light irradiation. [g]Without Ir(ppy)$_3$. [h] Within the first 5 minutes of the reaction, per [Fe].

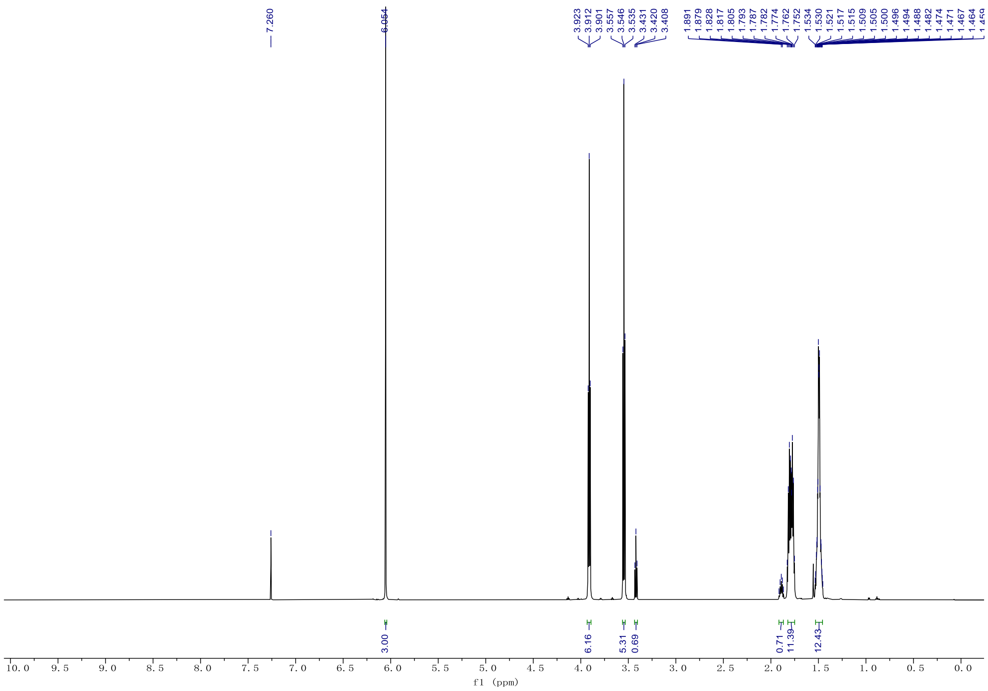

Figure 3.3. ^{1}H NMR (600 MHz) spectrum of compound **2** in $CDCl_3$.

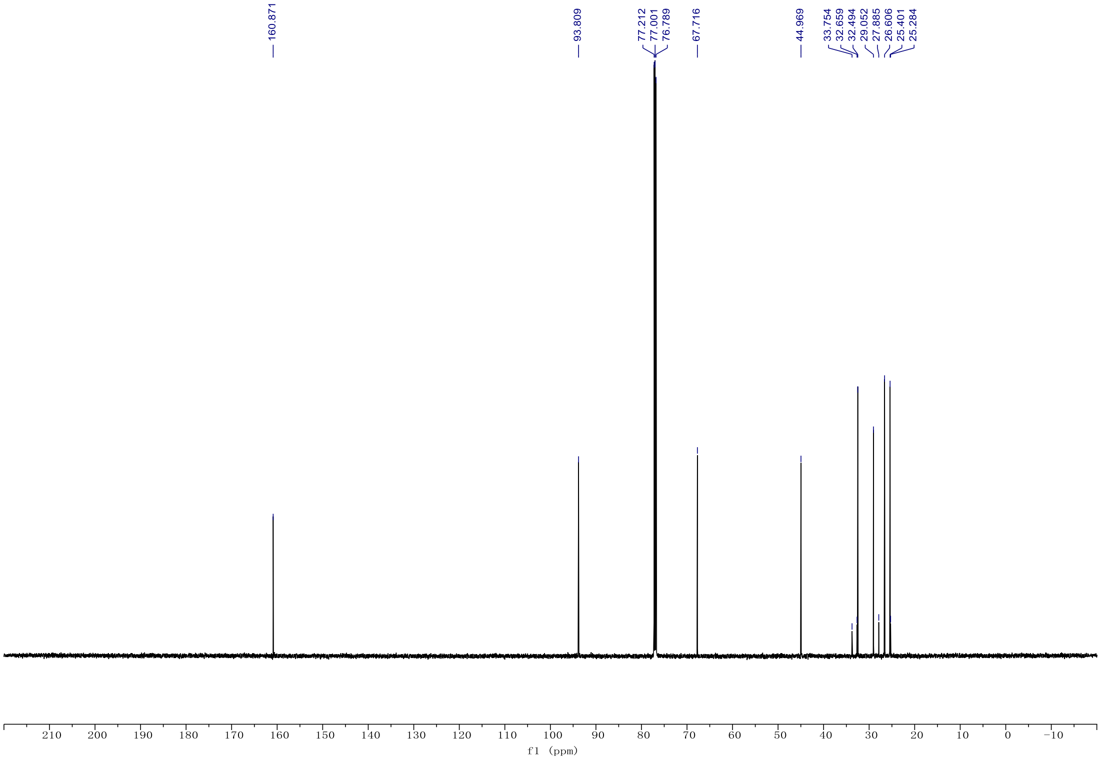

Figure 3.4. ^{13}C NMR (151 MHz) spectrum of compound **2** in $CDCl_3$.

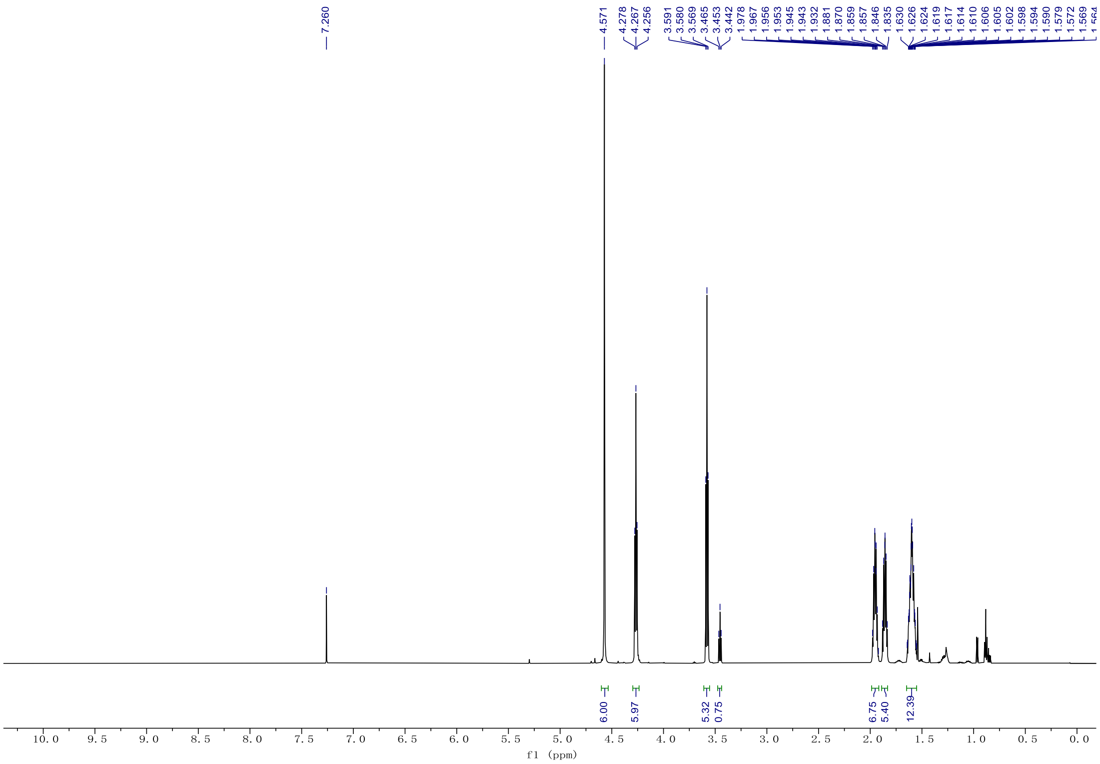

Figure 3.5. ^{1}H NMR (600 MHz) spectrum of compound **3** in $CDCl_3$.

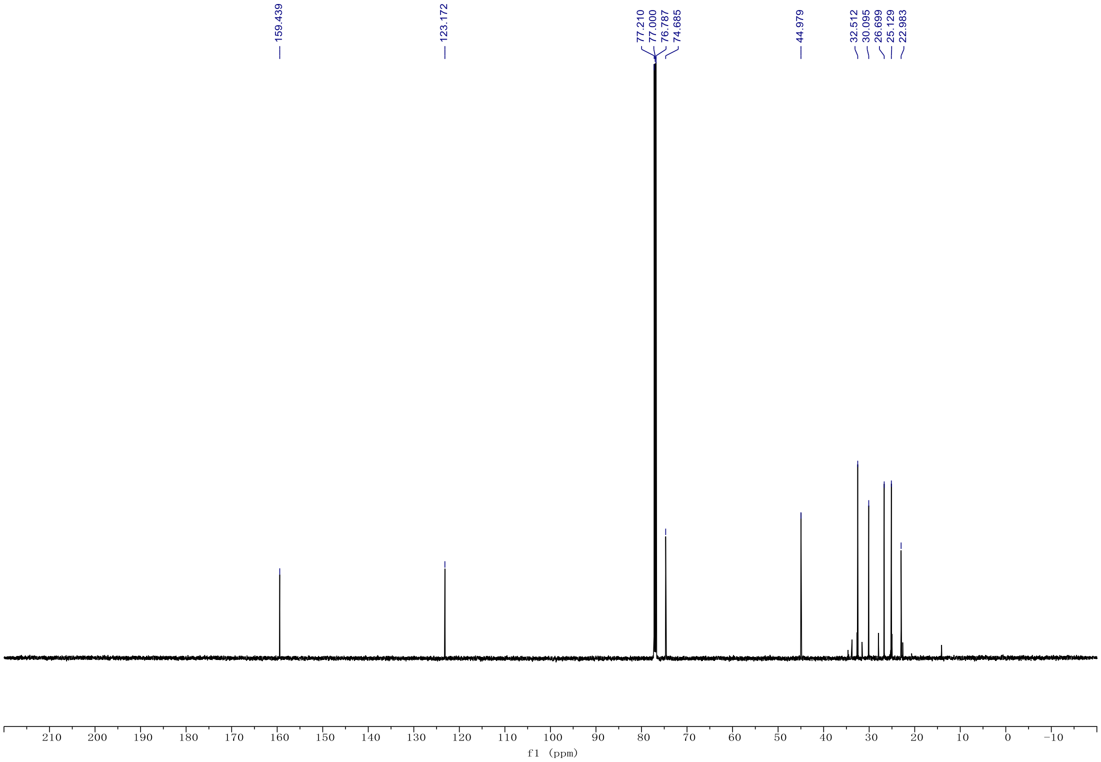

Figure 3.6. ^{13}C NMR (151 MHz) spectrum of compound **3** in $CDCl_3$.

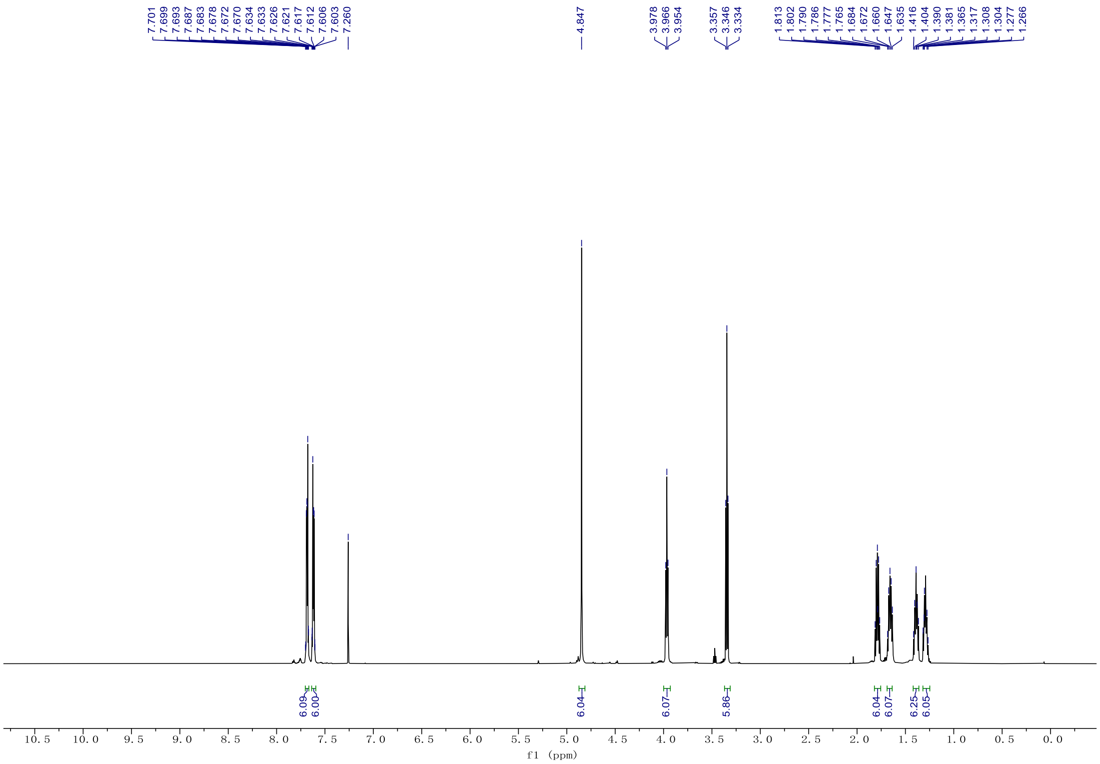

Figure 3.7. ^{1}H NMR (600 MHz) spectrum of compound **4** in $CDCl_3$.

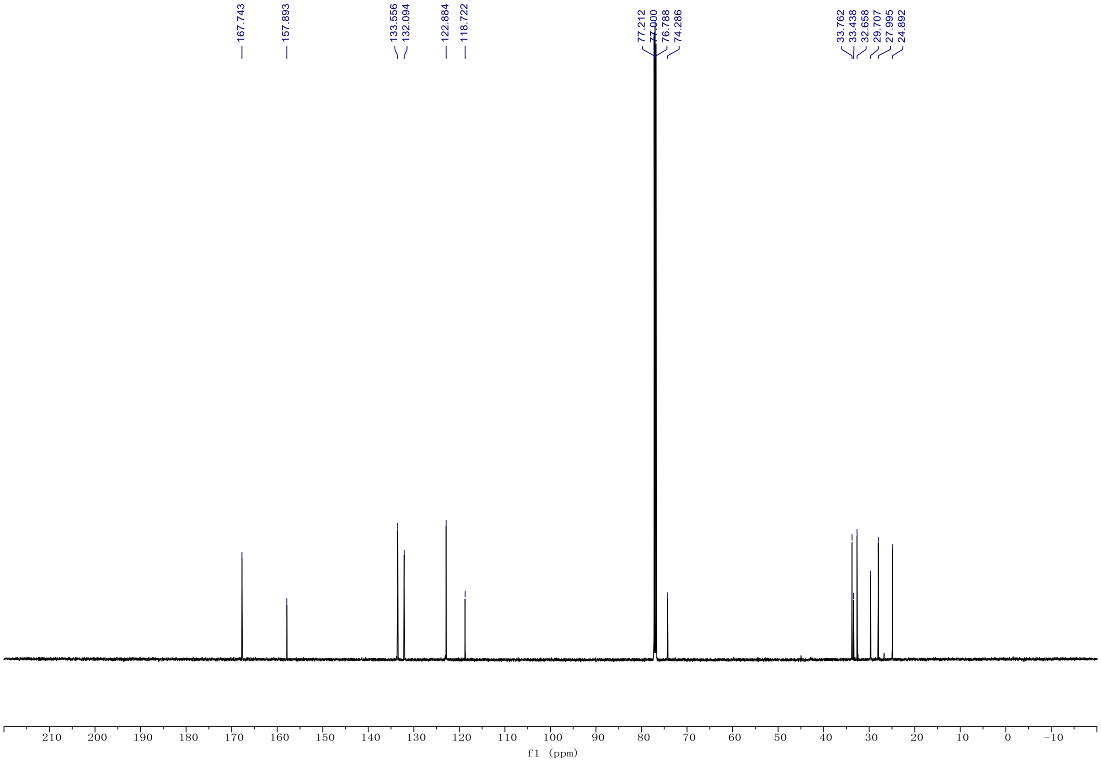

Figure 3.8. ^{13}C NMR (151 MHz) spectrum of compound **4** in CDCl$_3$.

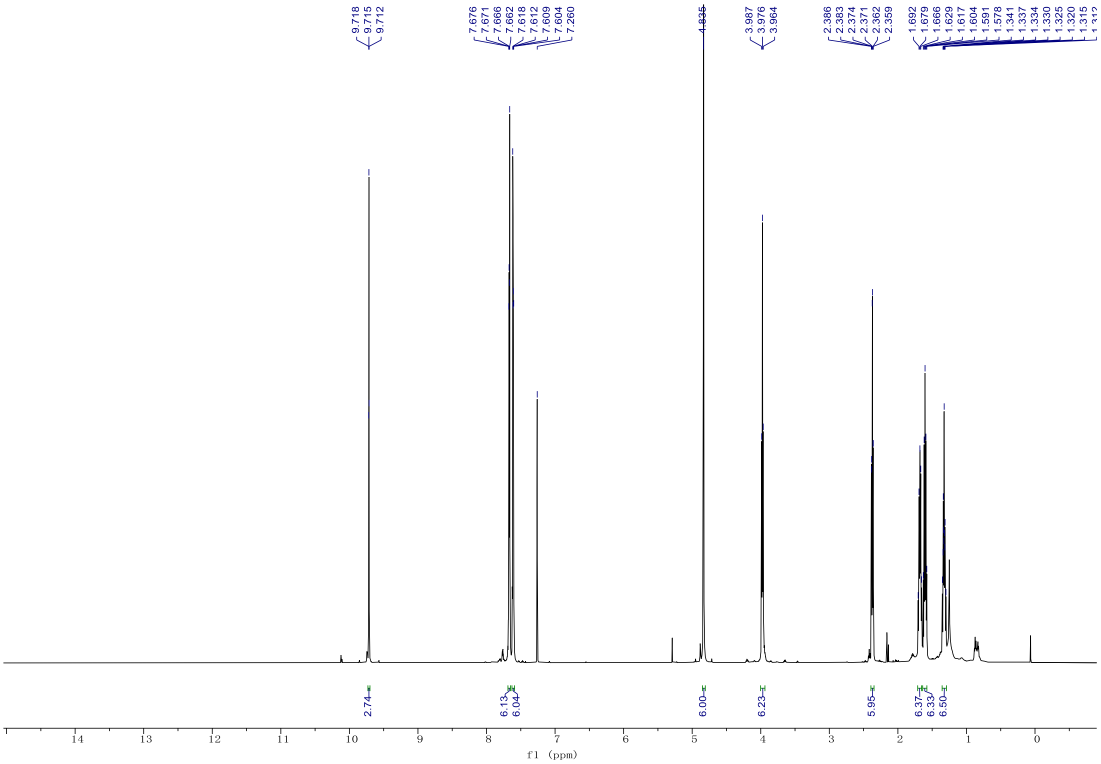

Figure 3.9. ^{1}H NMR (600 MHz) spectrum of compound **5** in $CDCl_3$.

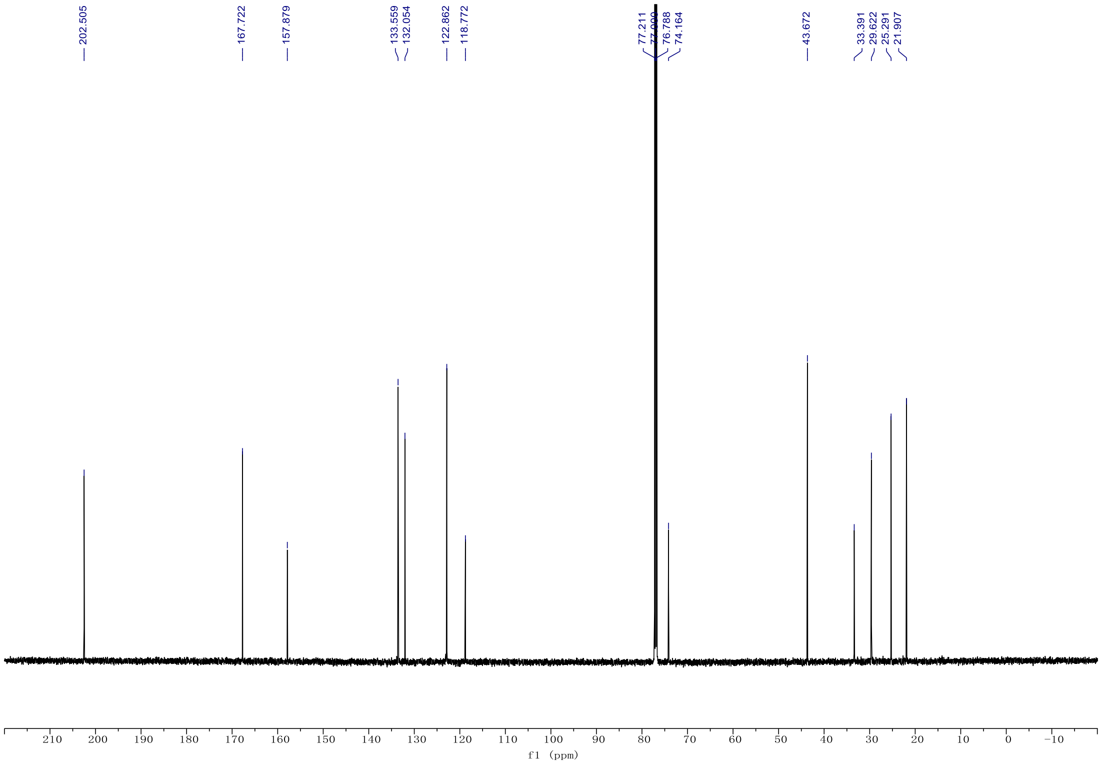

Figure 3.10. ^{13}C NMR (151 MHz) spectrum of compound **5** in $CDCl_3$.

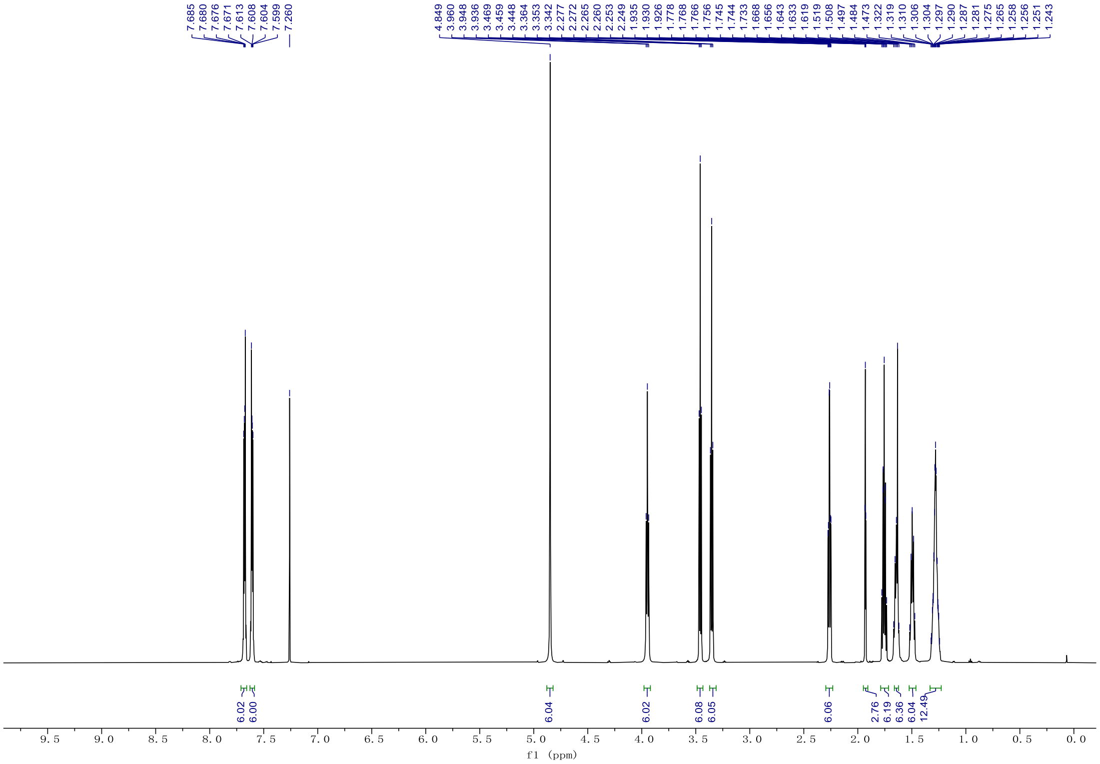

Figure 3.11. ^{1}H NMR (600 MHz) spectrum of compound **6** in $CDCl_3$.

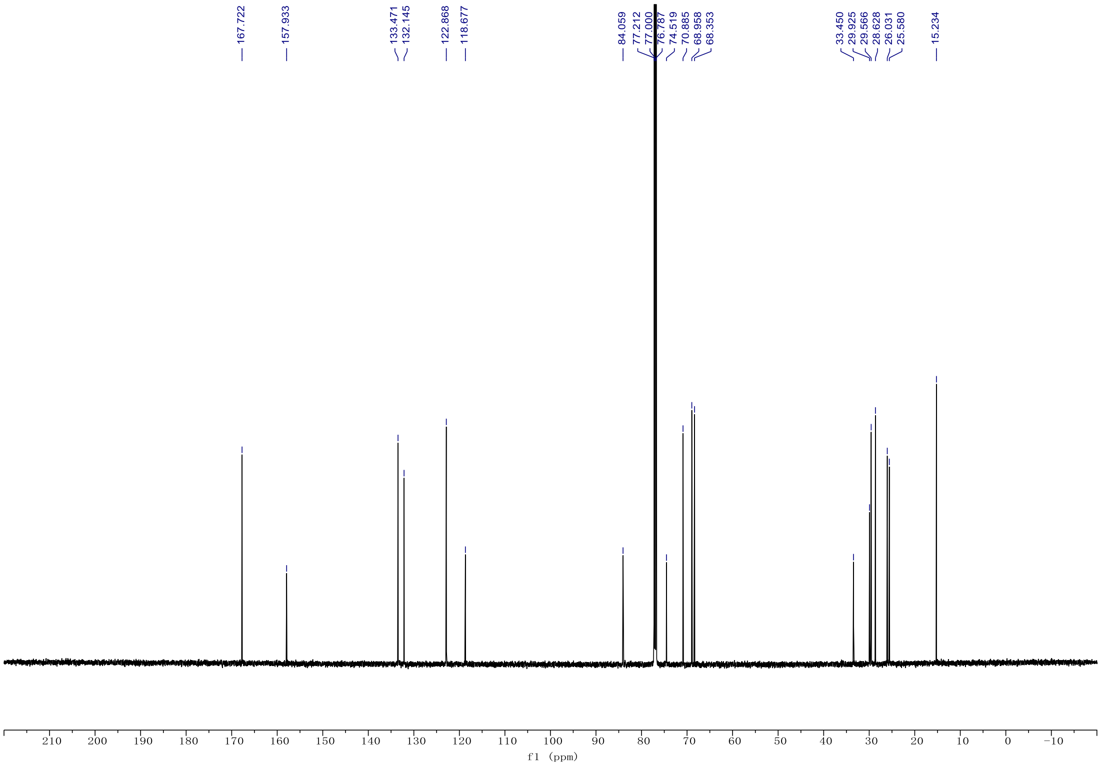

Figure 3.12. ^{13}C NMR (151 MHz) spectrum of compound **6** in $CDCl_3$.

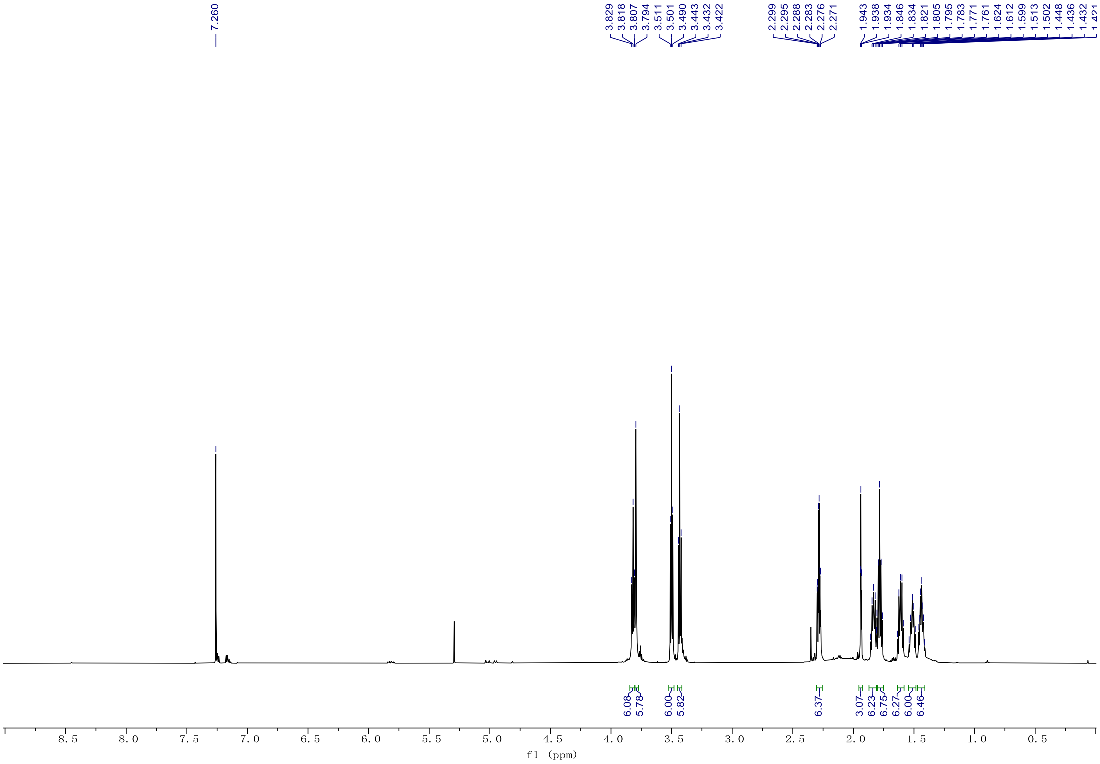

Figure 3.13. ^{1}H NMR (600 MHz) spectrum of compound **1** in $CDCl_3$.

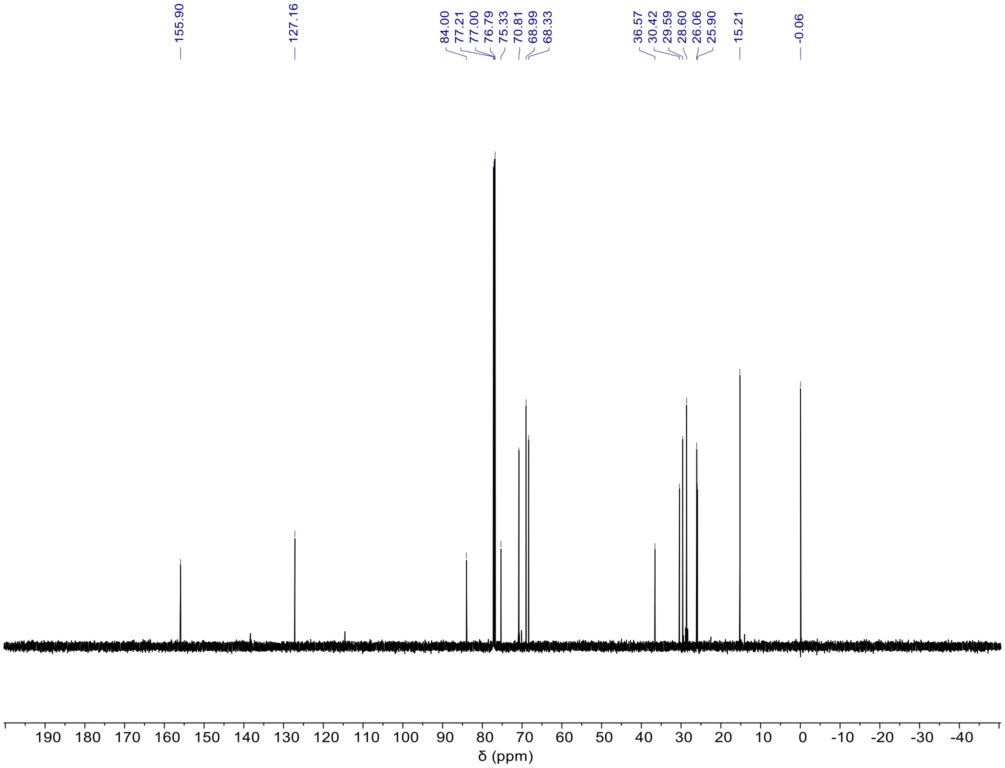

Figure 3.14. ^{1}H NMR (151 MHz) spectrum of compound **1** in CDCl$_3$.

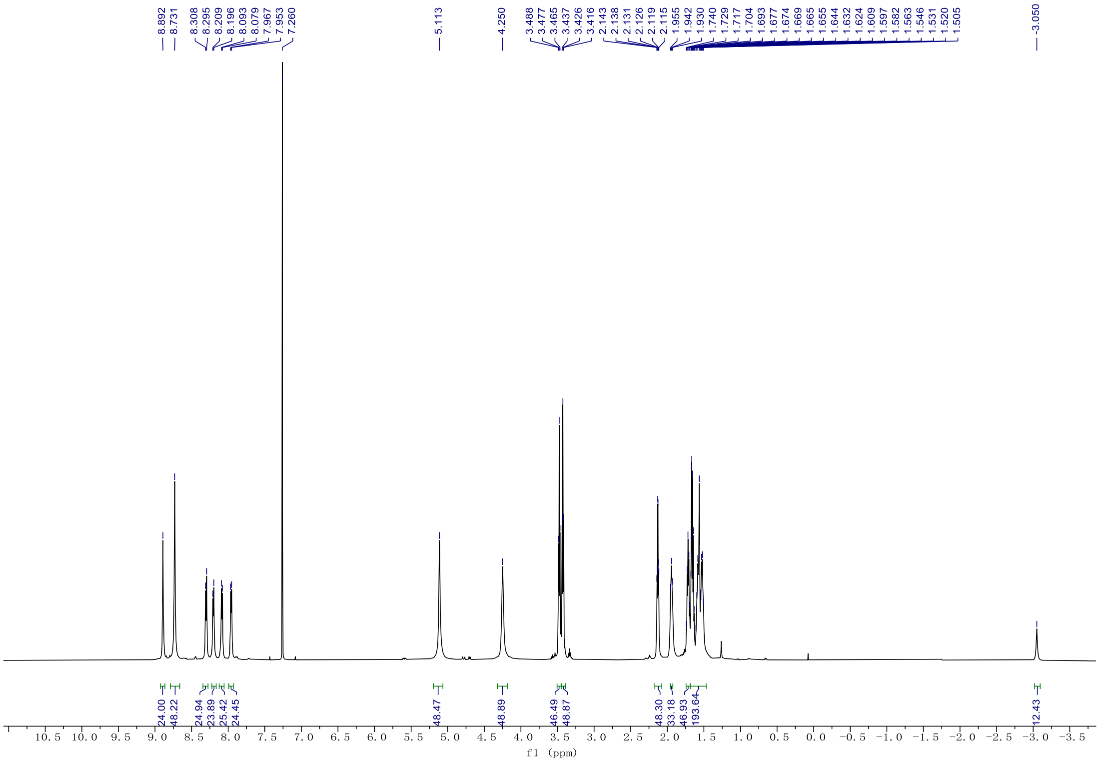

Figure 3.15. ^{1}H NMR (600 MHz) spectrum of compound **PB-1(A)** in $CDCl_3$.

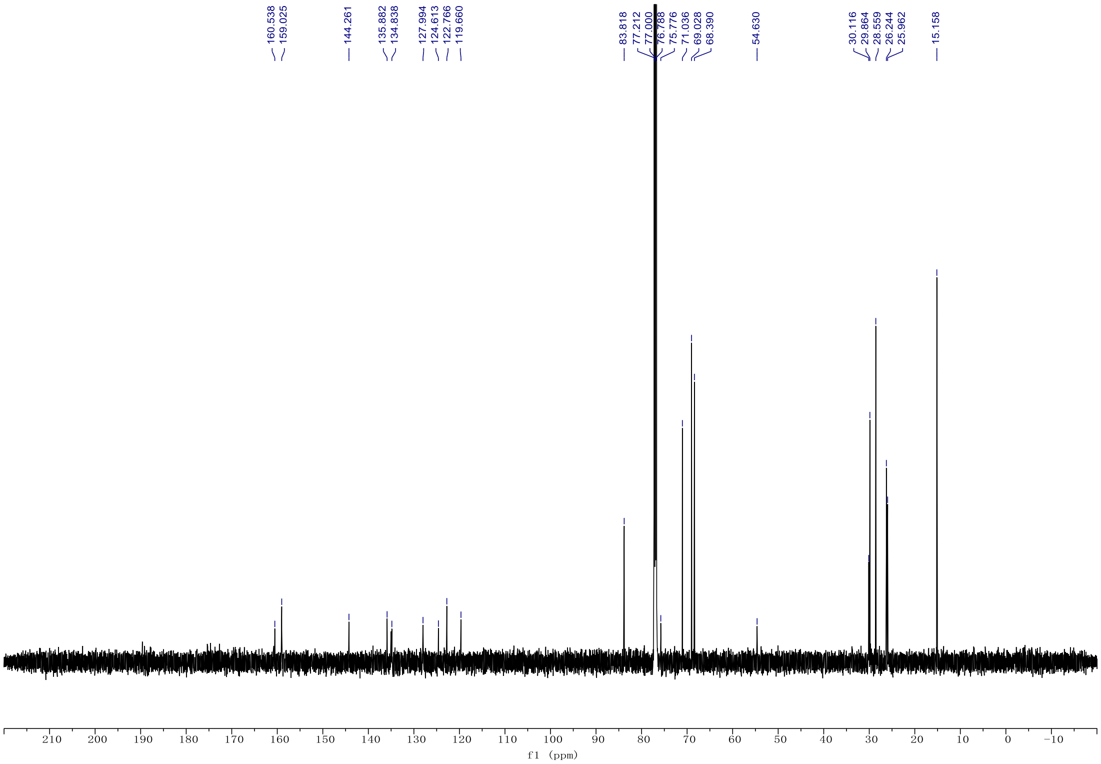

Figure 3.16. ^{1}H NMR (151 MHz) spectrum of compound **PB-1(A)** in CDCl$_3$.

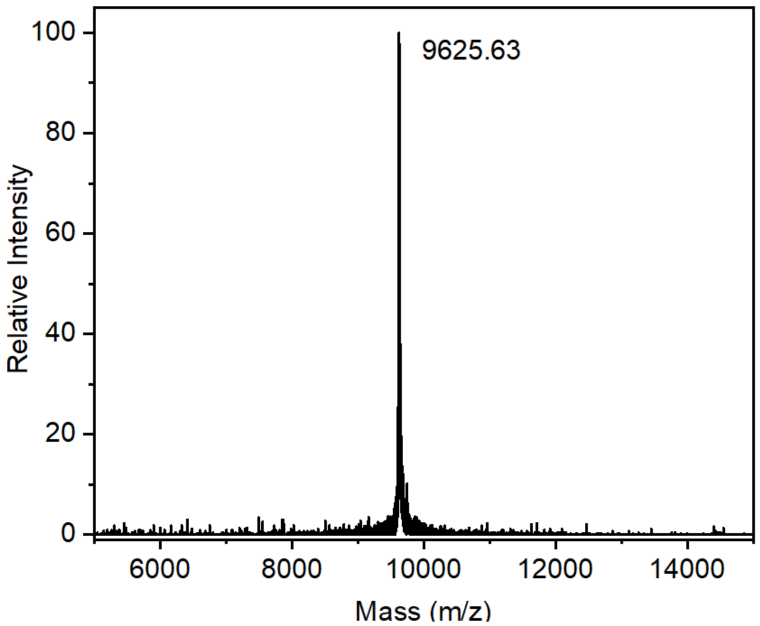

Figure 3.17. MALDI-MS spectrum with DCTB matrix of **PB-1(A)**. *m*/*z* calculated. for $C_{624}H_{685}N_{48}O_{48}$ $[M+H]^+$: 9625.6, found: 9625.6.

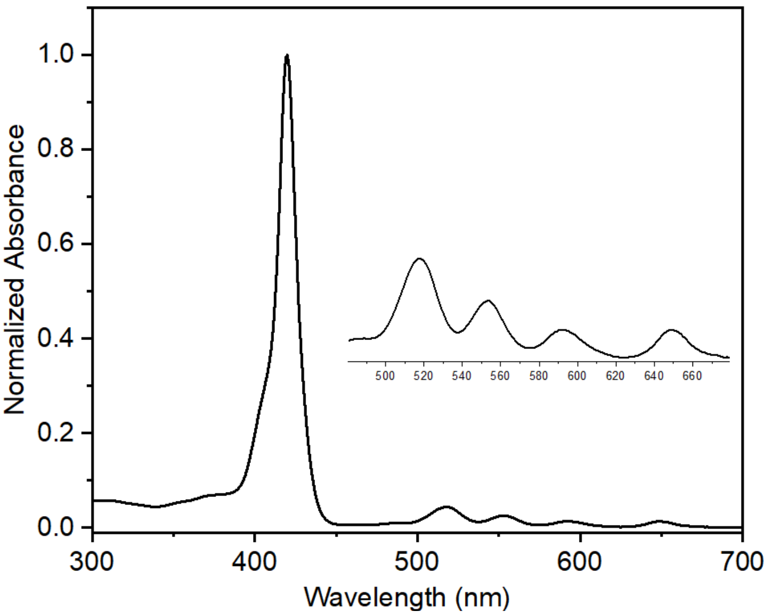

Figure 3.18. UV/Vis spectrum of **PB-1(A)** in DCM. λ_{abs} 420, 518, 553, 592, 649 nm.

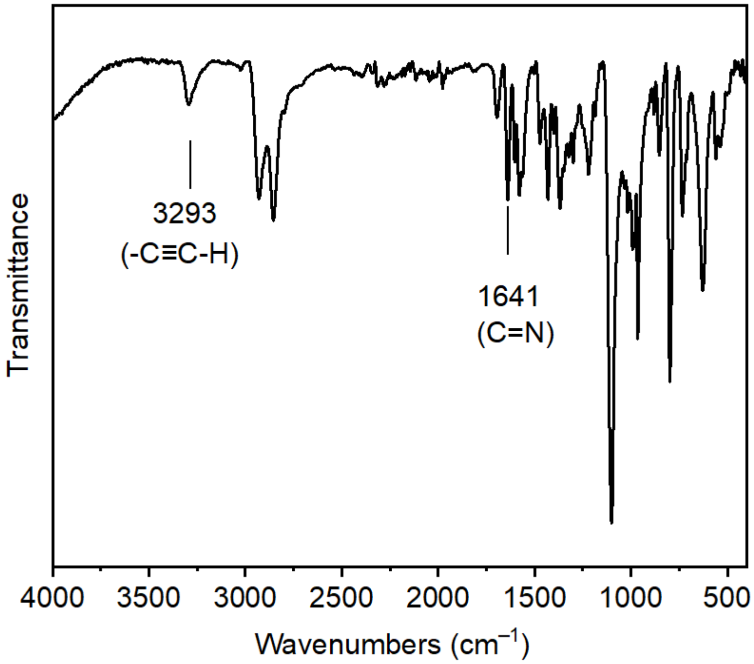

Figure 3.19. FT-IR spectrum of **PB-1(A)**. Terminal alkyne C-H stretching at 3293 cm^{-1}and imine stretching peak observed at 1641 cm^{-1}.

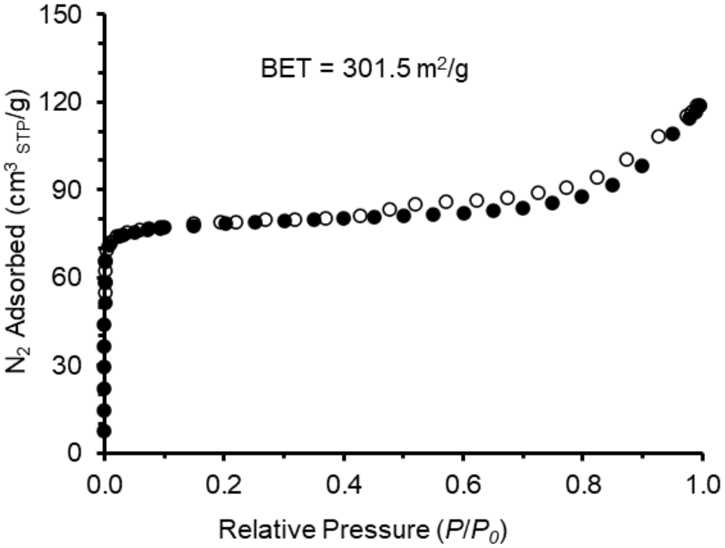

Figure 3.20. N_2 sorption isotherm at 77 K for **PB-1(A)**. Filled symbols indicate adsorption and unfilled symbols indicate desorption. Before the measurement, residual solvents were gradually exchanged with *n*-pentane and further evacuated by heating to 80 ºC under vacuum for 12 h.

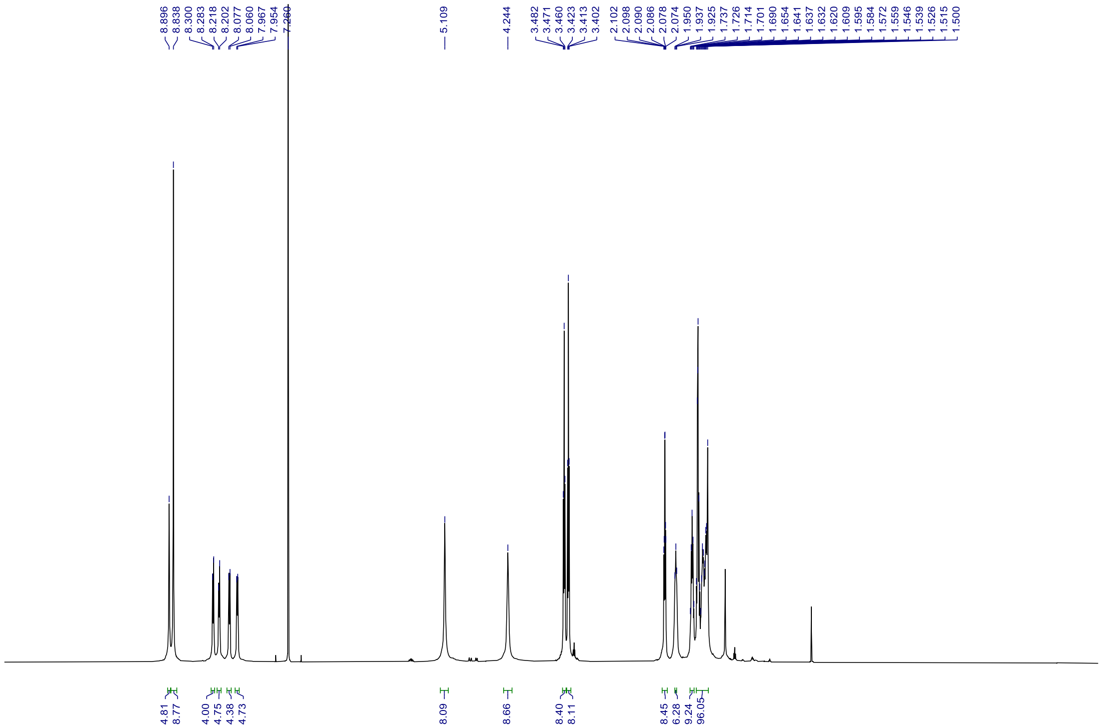

Figure 3.21. ^{1}H NMR (600 MHz) spectrum of compound **ZnPB-1(A)** in $CDCl_3$.

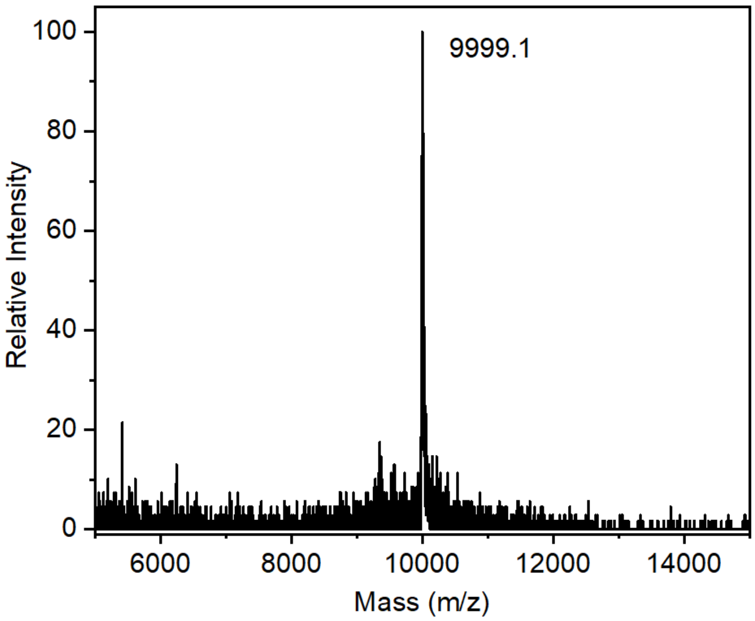

Figure 3.22. MALDI-MS spectrum with DCTB matrix of **ZnPB-1(A)**. *m/z* calculated. for $C_{624}H_{672}N_{48}O_{48}Zn_6$ $[M]^+$: 9999.7, found: 9999.1.

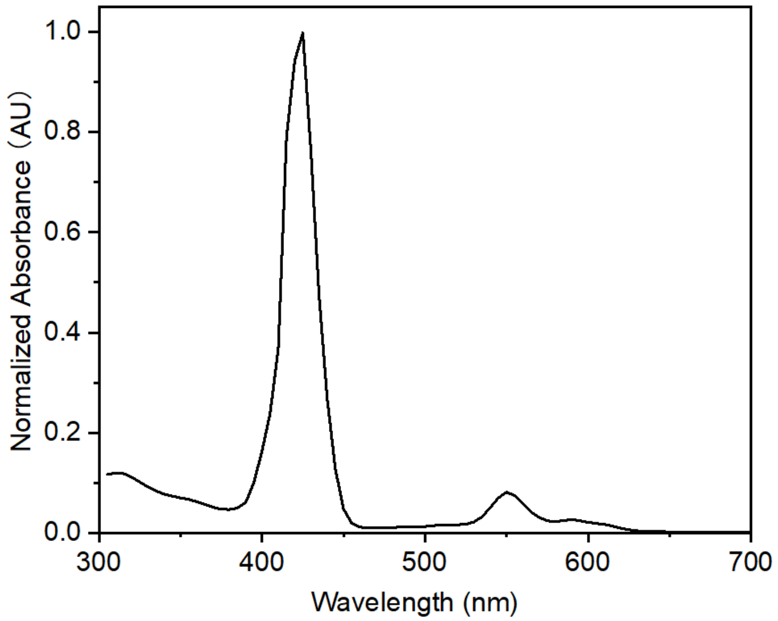

Figure 3.23. UV/Vis spectrum of **ZnPB-1(A)** in DCM. λ_{abs} 425, 550, 595 nm.

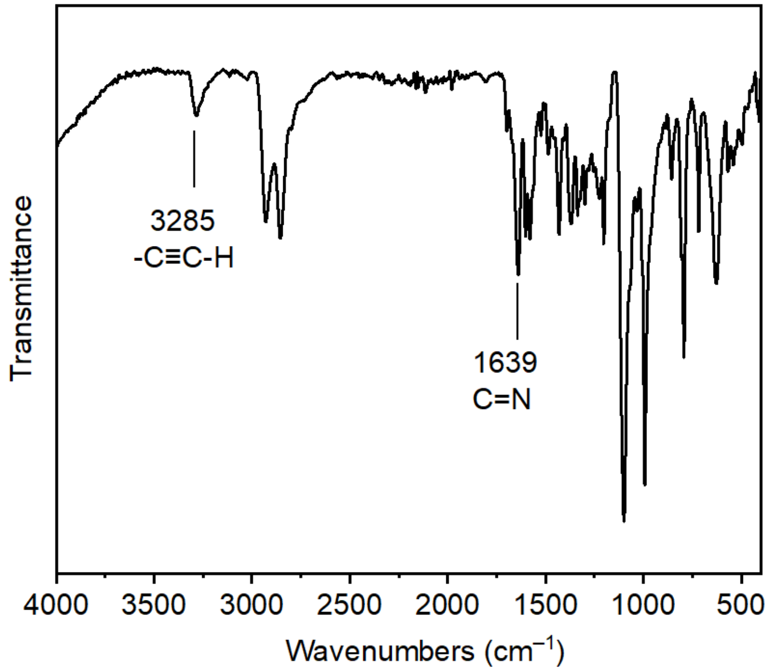

Figure 3.24. FT-IR spectrum of **ZnPB-1(A)**. Terminal alkyne C-H stretching at 3285 cm^{-1}and imine stretching peak observed at 1639 cm^{-1}.

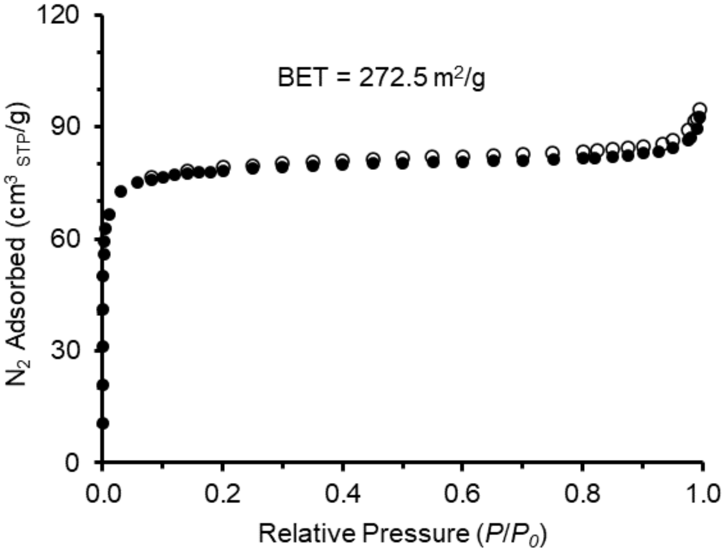

Figure 3.25. N_2 sorption isotherm at 77 K for **ZnPB-1(A)**. Filled symbols indicate adsorption and unfilled symbols indicate desorption. Before the measurement, residual solvents were gradually exchanged with *n*-pentane and further evacuated by heating to 80 ºC under vacuum for 12 h.

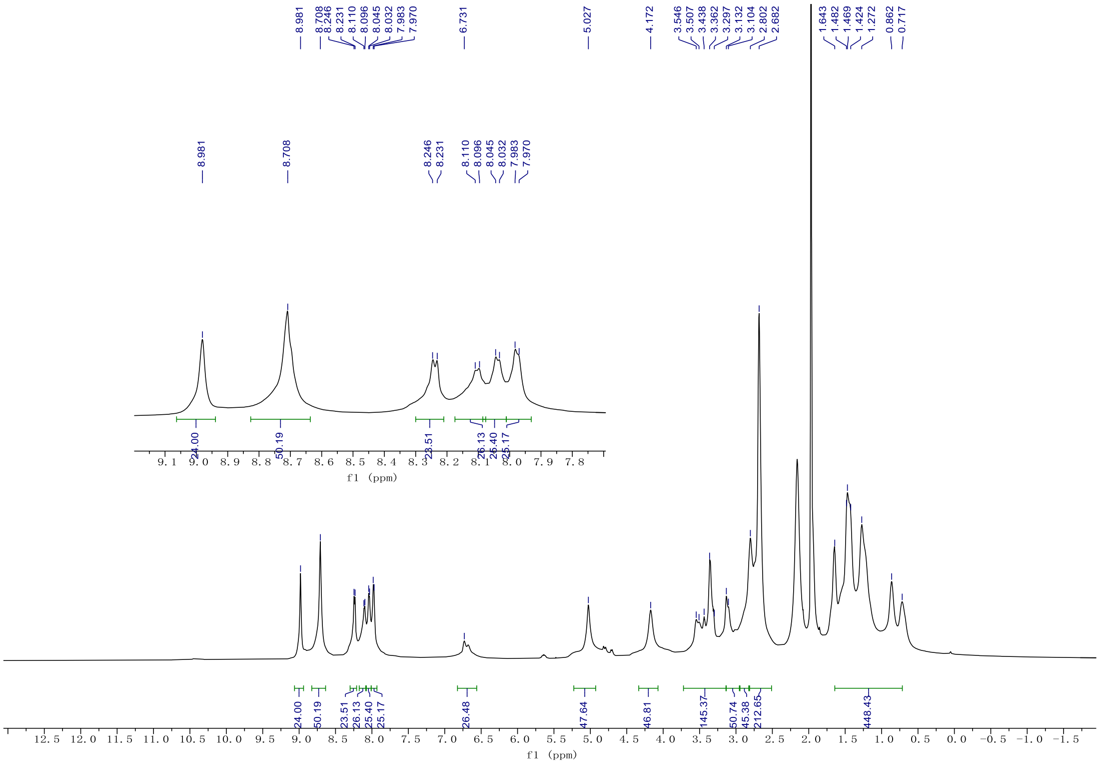

Figure 3.26. ^{1}H NMR (600 MHz) spectrum of compound **ZnPB-2(P)** in CD_3CN.

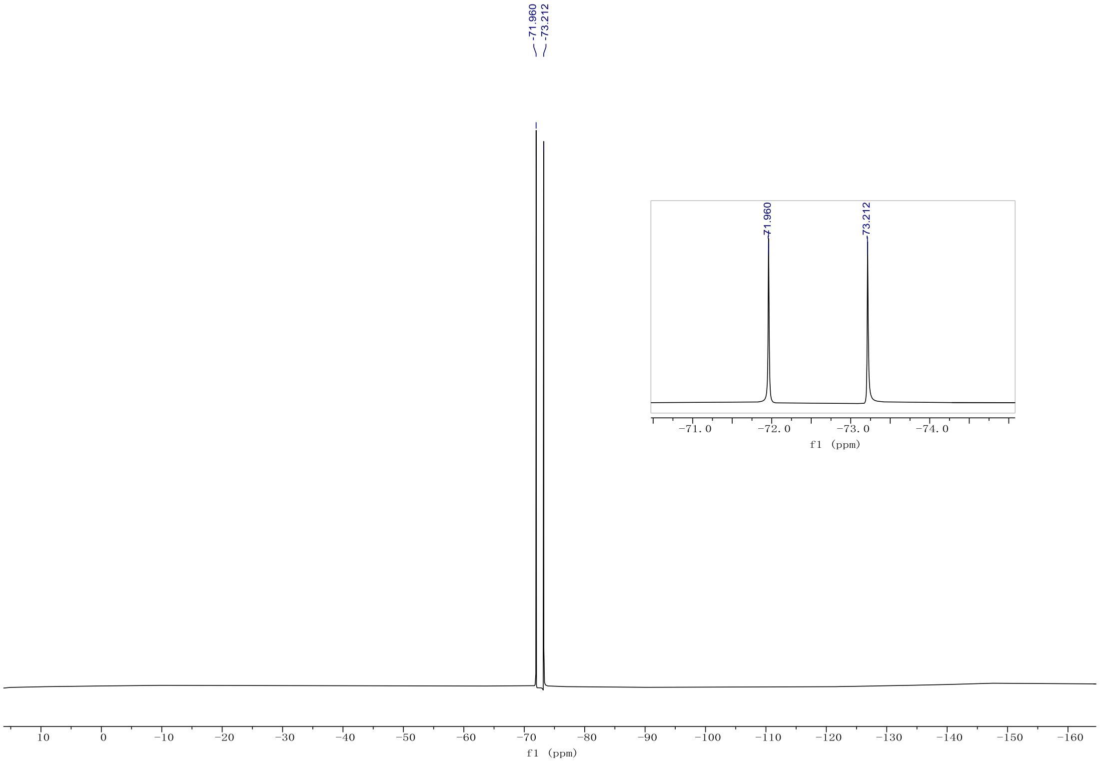

Figure 3.27. ^{19}F NMR (565 MHz) spectrum of compound **ZnPB-2(P)** in CD_3CN.

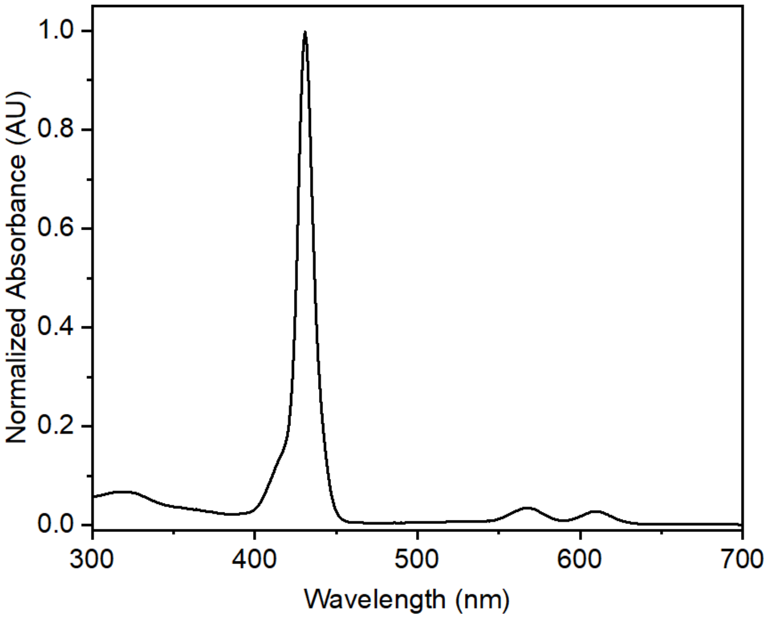

Figure 3.28. UV/Vis spectrum of **ZnPB-2(P)** in CH_3CN. λ_{abs} 431, 568, 609 nm.

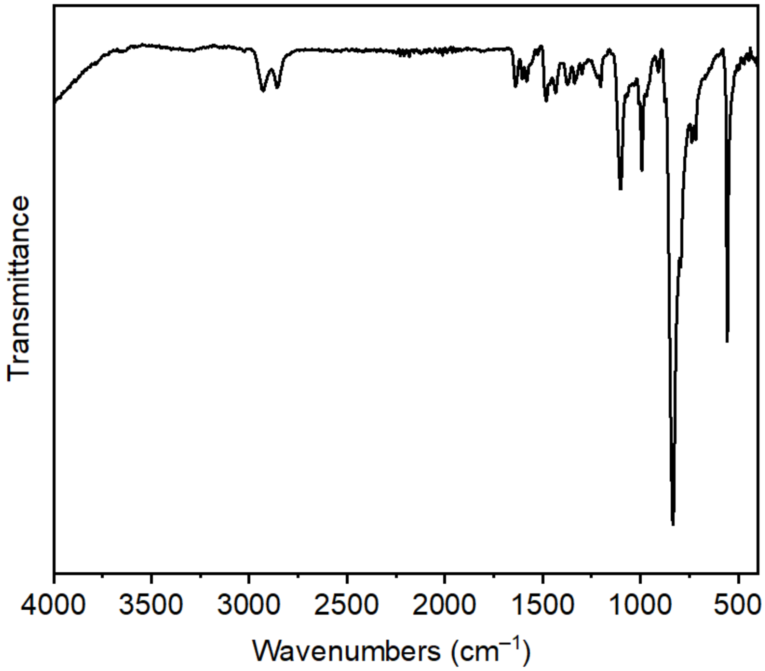

Figure 3.29. FT-IR spectrum of **ZnPB-2(P)**.

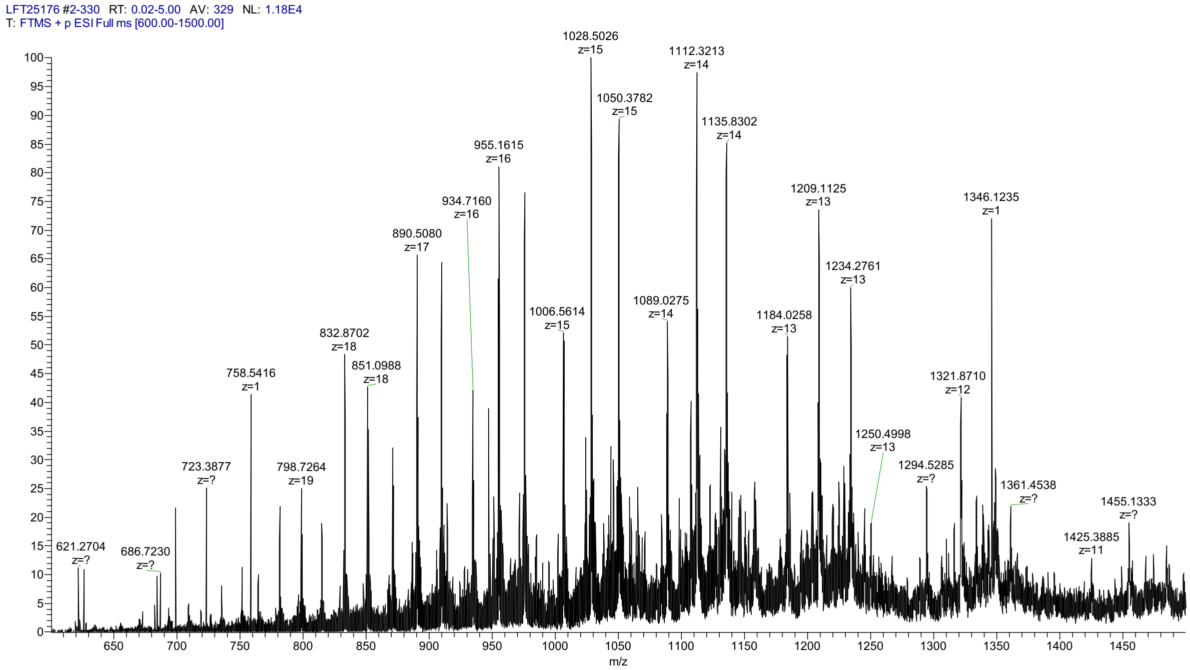

Figure 3.30. ESI-MS for a DMF solution of **ZnPB-2(P)** [$C_{840}H_{1176}N_{144}O_{48}Zn_6(PF_6)_{24}$]

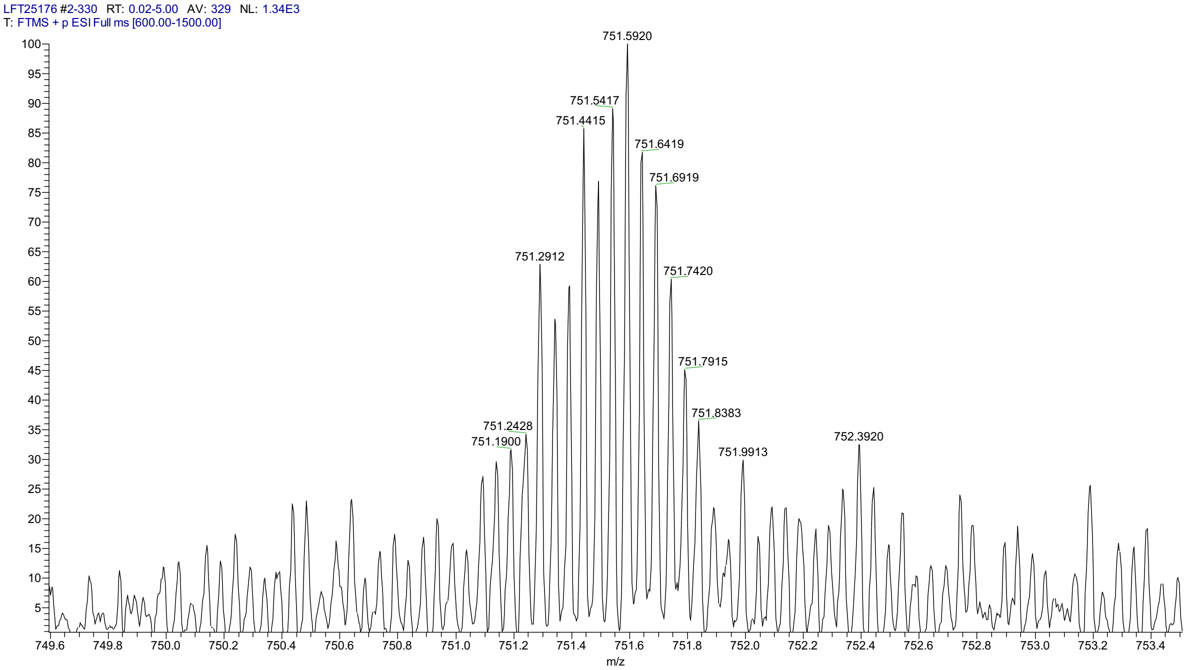

Figure 3.31. Expansion of ESI-MS (m/z =20) for **ZnPB-2(P)** showing the $C_{840}H_{1176}N_{144}O_{48}Zn_6P_4F_{24}$ $[M-20(PF_6)]^{20+}$ with a calculated average mass: 751.5759 and found mass: 751.5920.

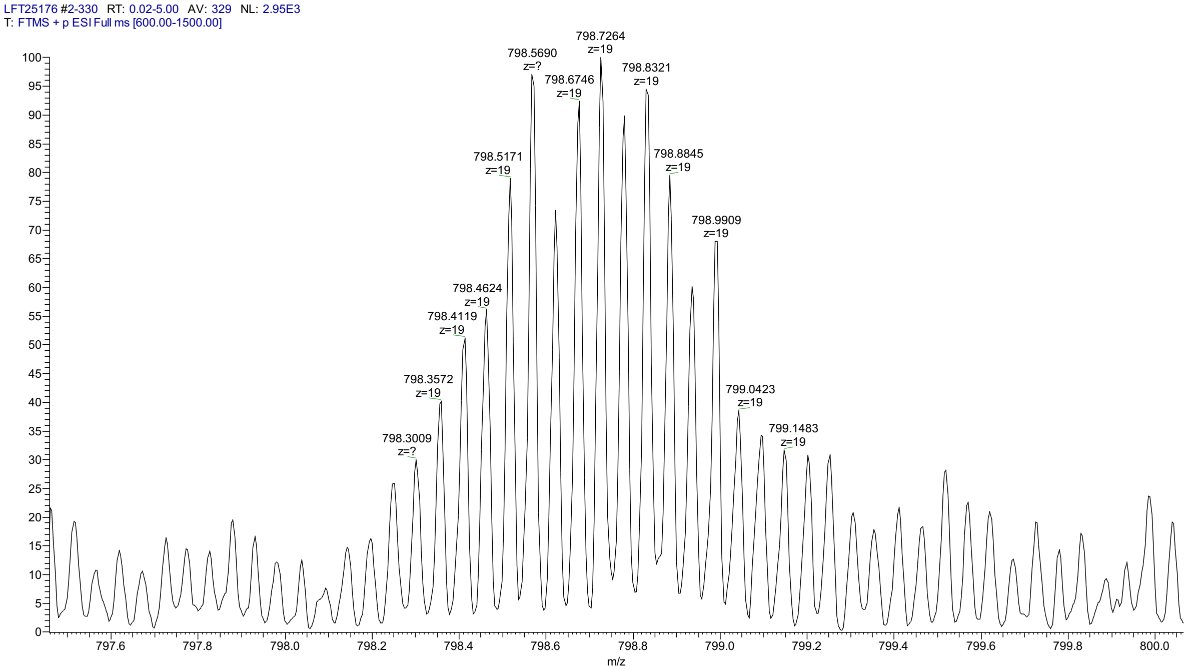

Figure 3.32. Expansion of ESI-MS (m/z =19) for **ZnPB-2(P)** showing the $C_{840}H_{1176}N_{144}O_{48}Zn_6P_5F_{30}[M-19(PF_6)]^{19+}$ with a calculated average mass: 798.7623 and found mass: 798.7264.

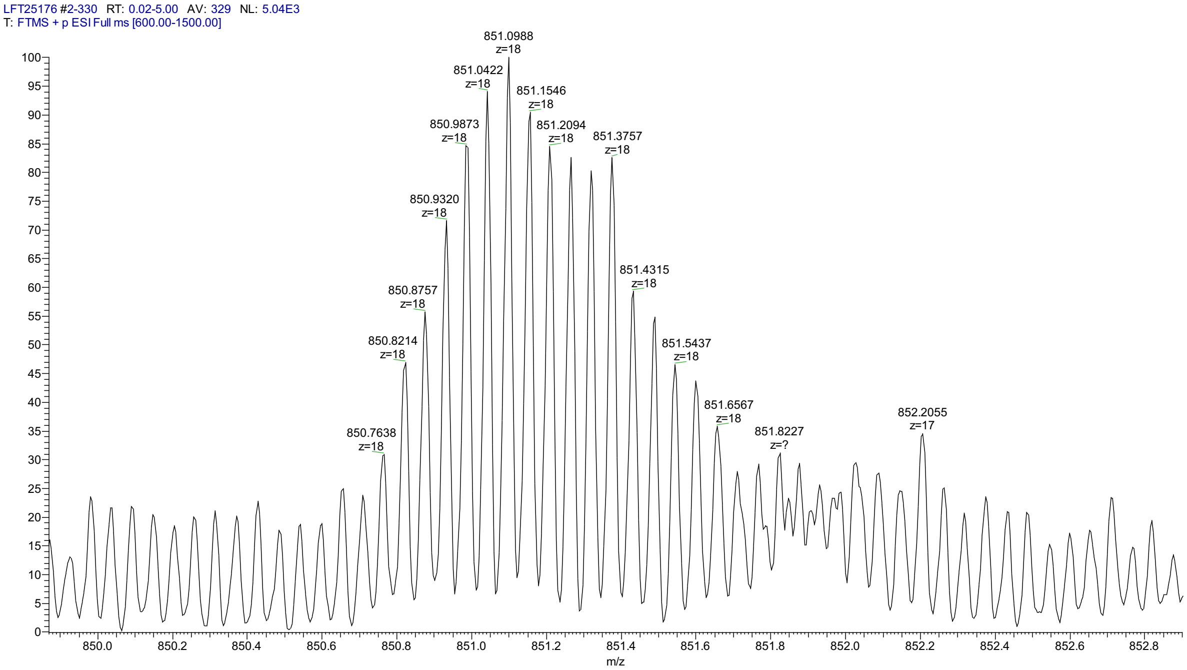

Figure 3.33. Expansion of ESI-MS (m/z =18) for **ZnPB-2(P)** showing the $C_{840}H_{1176}N_{144}O_{48}Zn_6P_6F_{36}[M-18(PF_6)]^{18+}$ with a calculated average mass: 851.1915 and found mass: 851.0988.

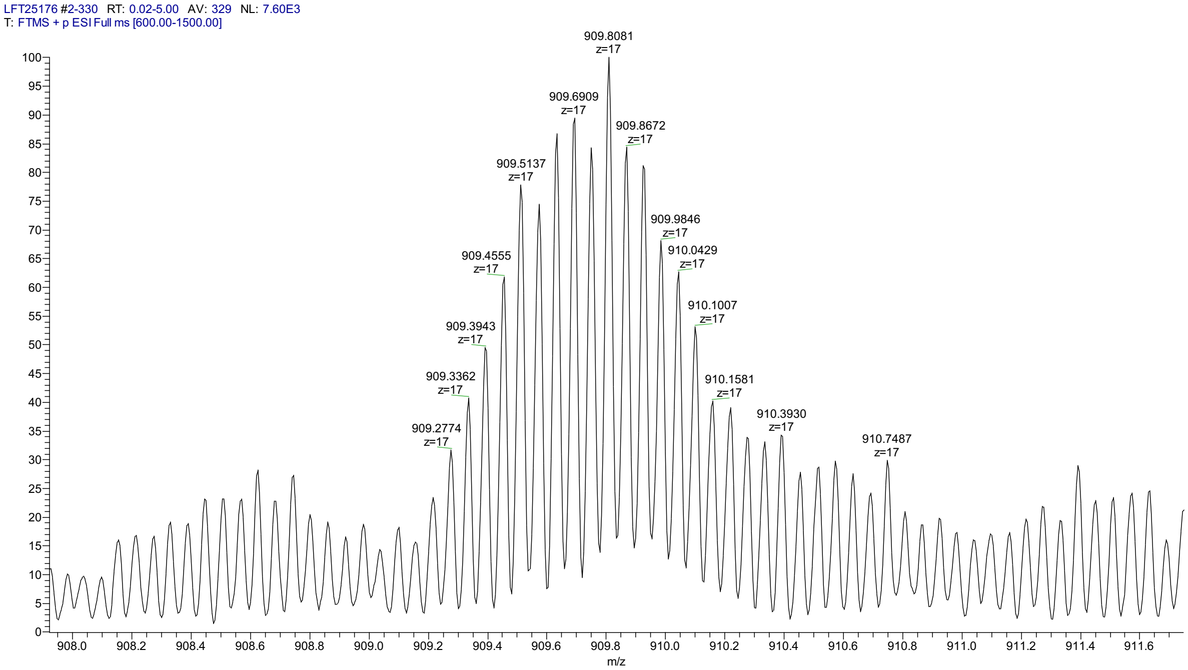

Figure 3.34. Expansion of ESI-MS (m/z =17) for **ZnPB-2(P)** showing the $C_{840}H_{1176}N_{144}O_{48}Zn_6P_7F_{42}[M-17(PF_6)]^{17+}$ with a calculated average mass: 909.7890 and found mass: 909.8081.

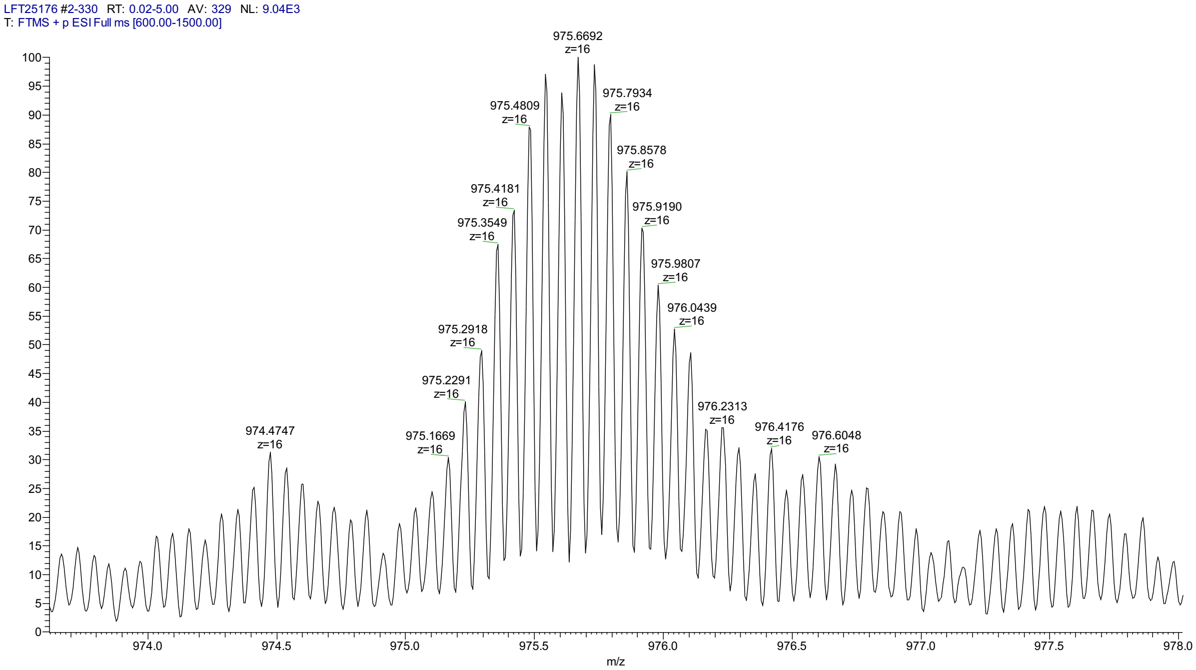

Figure 3.35. Expansion of ESI-MS (m/z =16) for **ZnPB-2(P)** showing the $C_{840}H_{1176}N_{144}O_{48}Zn_6P_8F_{48}[M-16(PF_6)]^{16+}$ with a calculated average mass: 975.7111 and found mass: 975.6692.

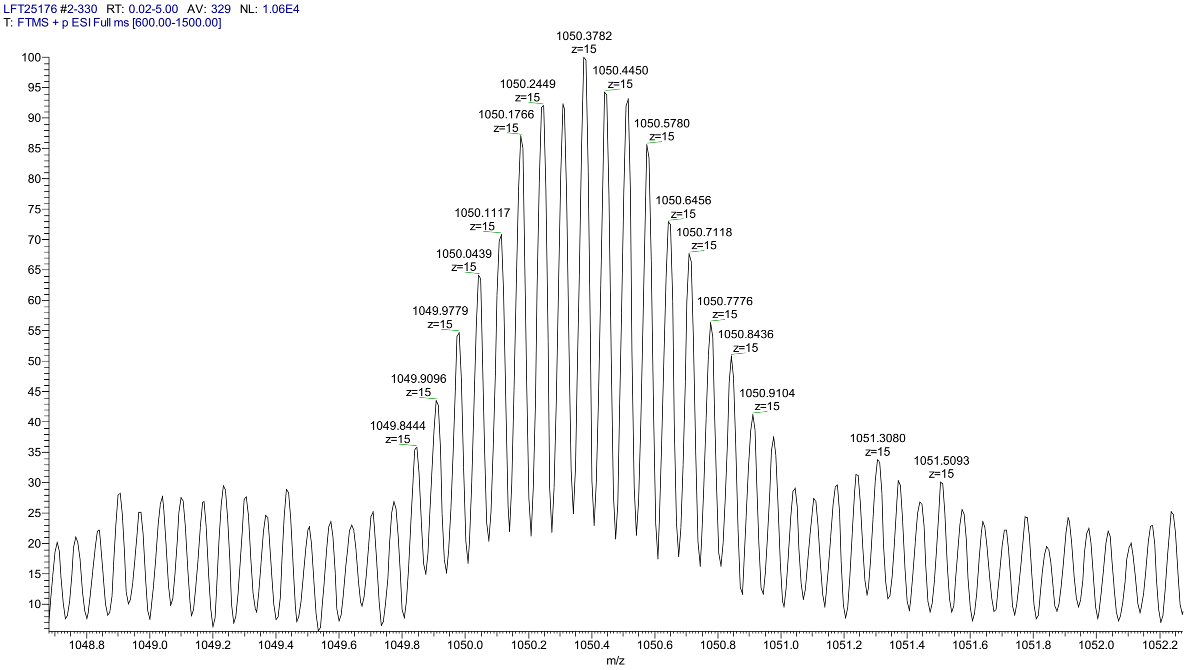

Figure 3.36. Expansion of ESI-MS (m/z =15) for **ZnPB-2(P)** showing the $C_{840}H_{1176}N_{144}O_{48}Zn_6P_9F_{54}[M-15(PF_6)]^{15+}$ with a calculated average mass: 1050.4228 and found mass: 1050.3782.

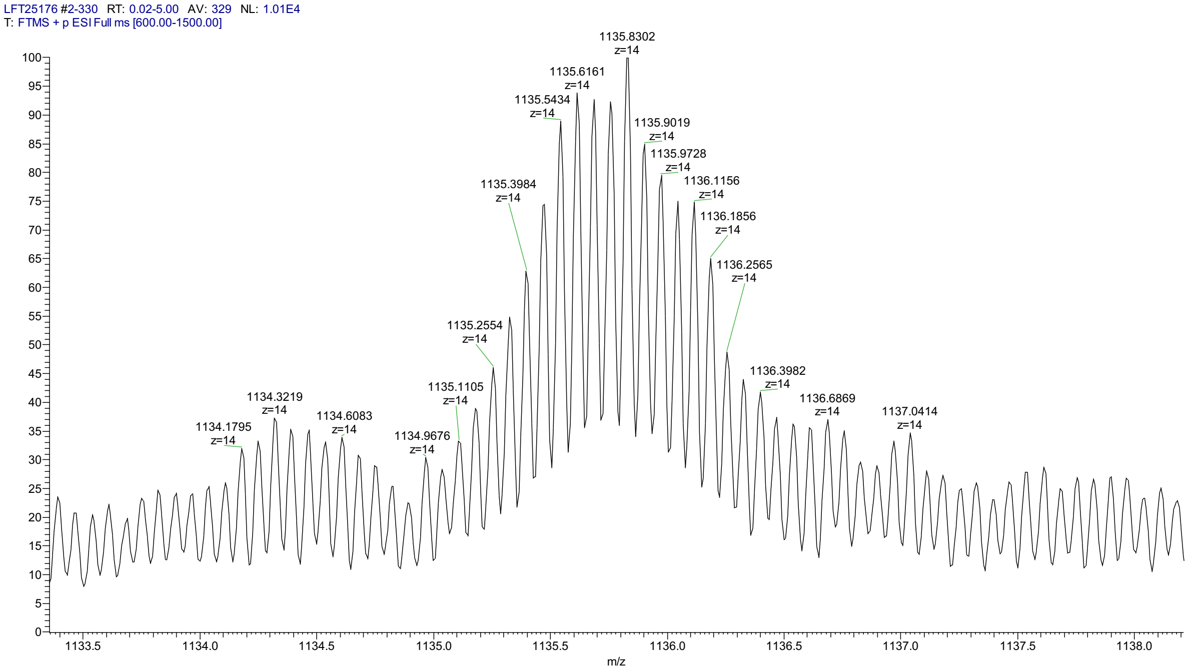

Figure 3.37. Expansion of ESI-MS (m/z =14) for **ZnPB-2(P)** showing the $C_{840}H_{1176}N_{144}O_{48}Zn_6P_9F_{54}[M-14(PF_6)]^{14+}$ with a calculated average mass: 1135.8076 and found mass: 1135.8302.

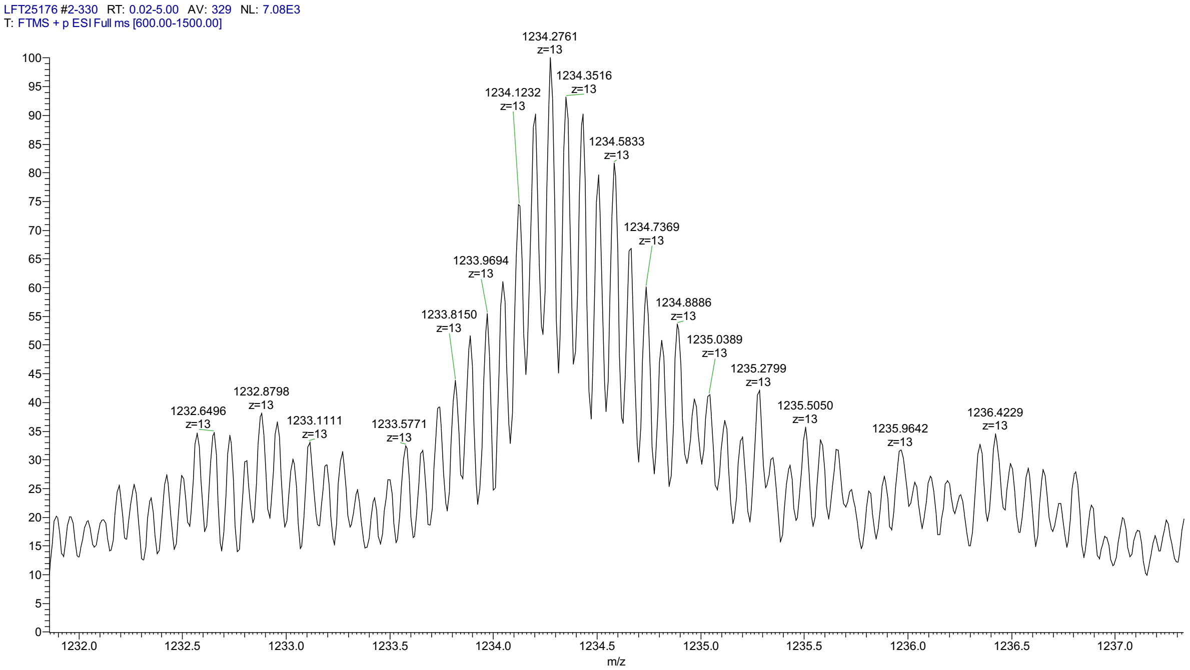

Figure 3.38. Expansion of ESI-MS (m/z =13) for **ZnPB-2(P)** showing the $C_{840}H_{1176}N_{144}O_{48}Zn_6P_{11}F_{66}[M-14(PF_6)]^{13+}$ with a calculated average mass: 1234.3286 and found mass: 1234.2761.

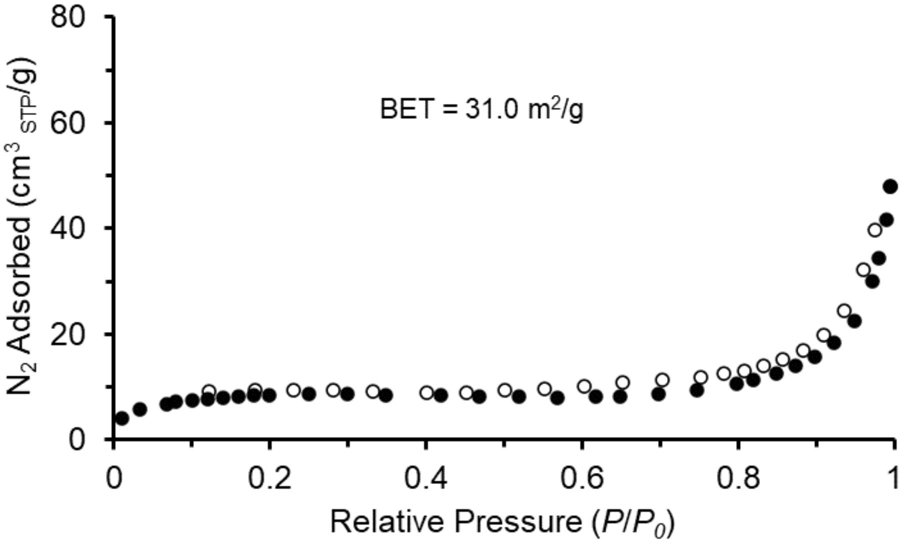

Figure 3.39. N$_2$ sorption isotherm at 77 K for **ZnPB-2(P)**. Filled symbols indicate adsorption and unfilled symbols indicate desorption. Before the measurement, residual solvents were gradually exchanged with *n*-pentane and further evacuated by heating to 80 ºC under vacuum for 12 h.

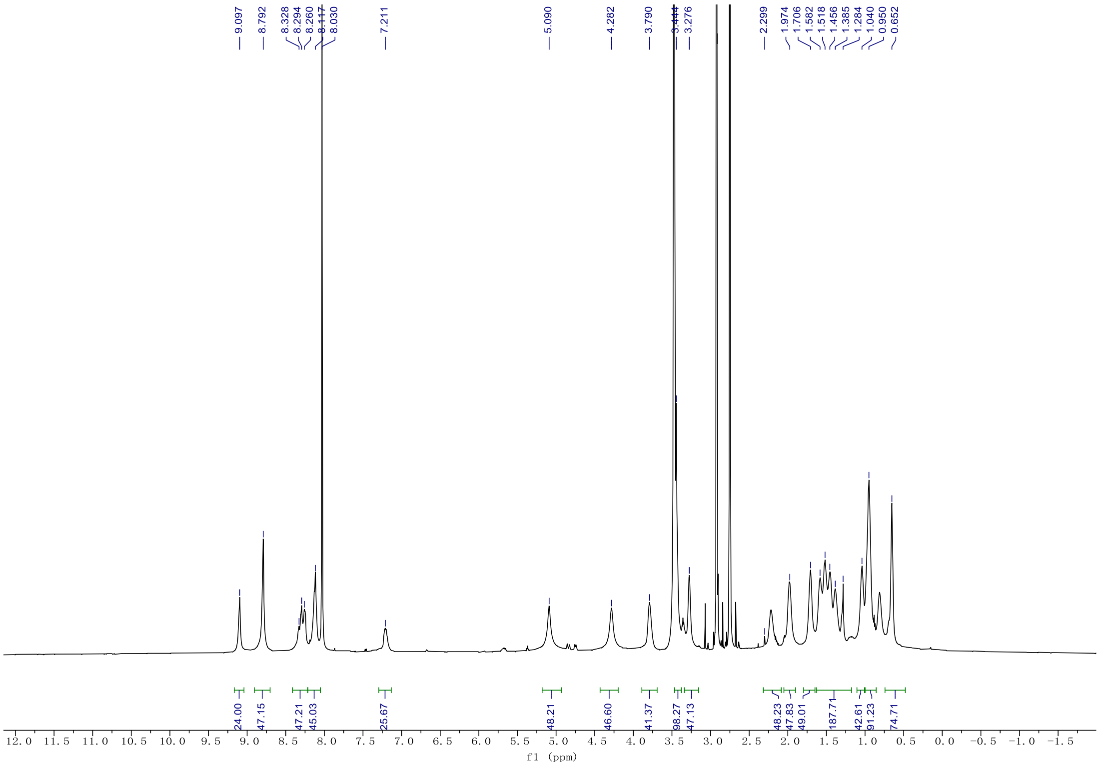

Figure 3.40. ^{1}H NMR (600 MHz) spectrum of compound **ZnPB-3(N)** in DMF-d_7.

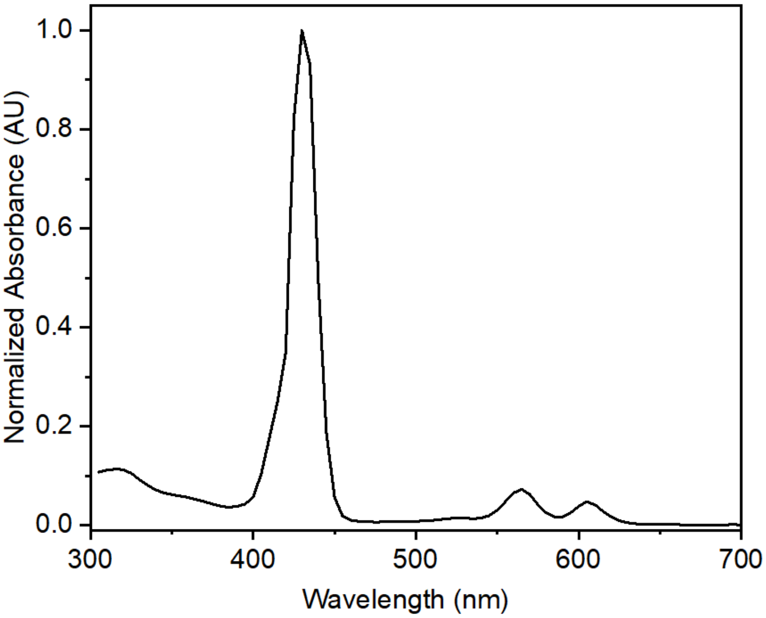

Figure 3.41. UV/Vis spectrum of **ZnPB-3(N)** in DCM. λ_{abs} 430, 565, 605 nm.

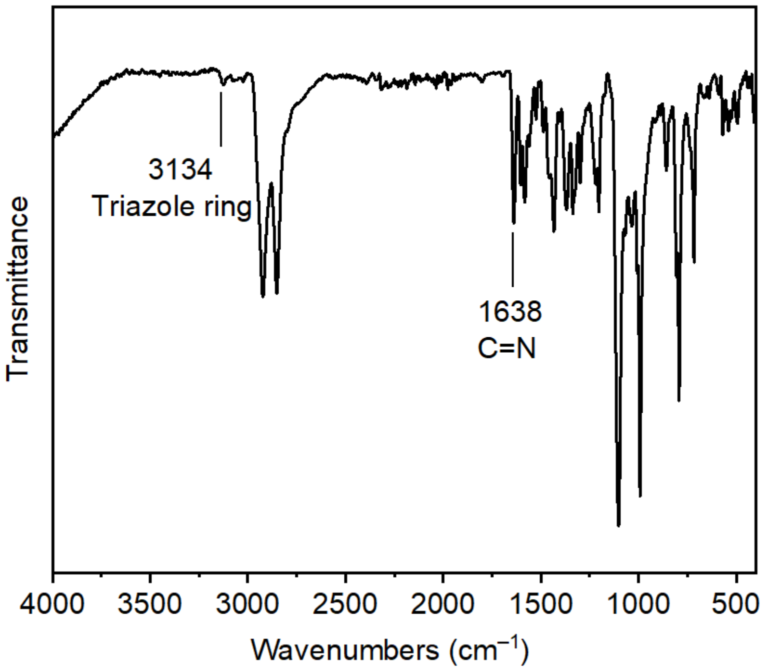

Figure 3.42. FT-IR spectrum of **ZnPB-3(N)**. Triazole ring observed at 3285 cm^{-1}and imine stretching peak observed at 1639 cm^{-1}.

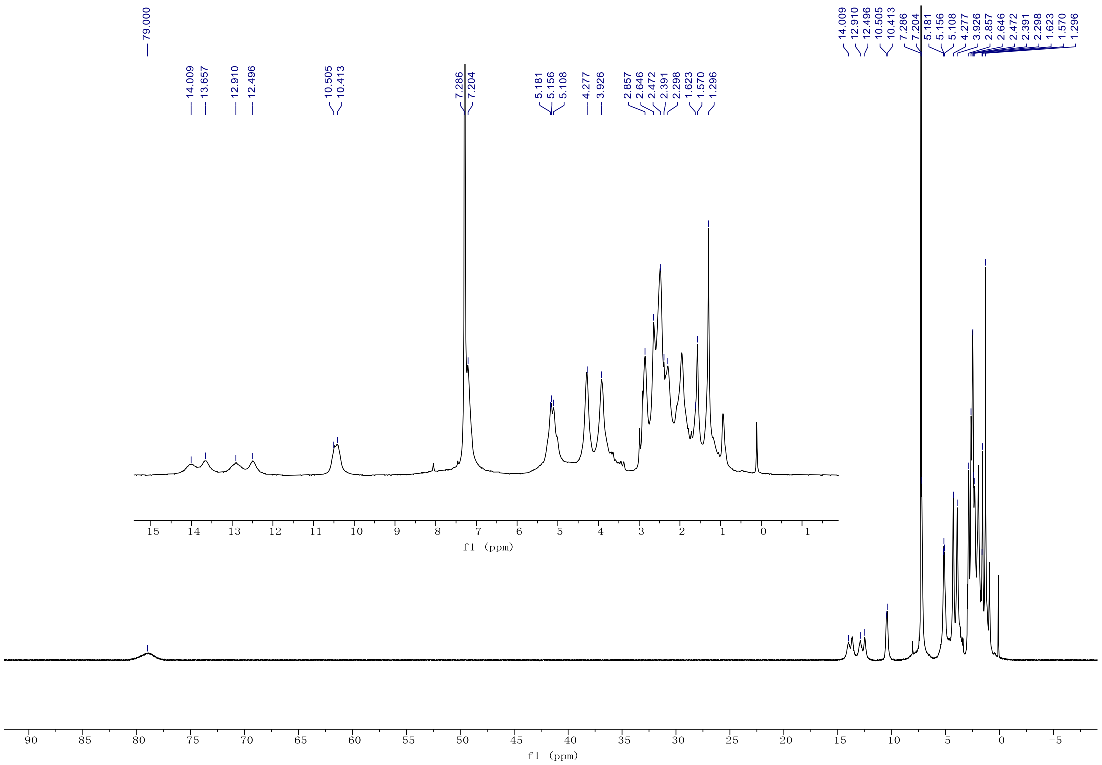

Figure 3.43. ^{1}H NMR (600 MHz) spectrum of compound **FePB-1(A)** in $CDCl_3$. The paramagnetic **FePB-1(A)** maintains the high symmetry of the rhombicuboctahedral structure.

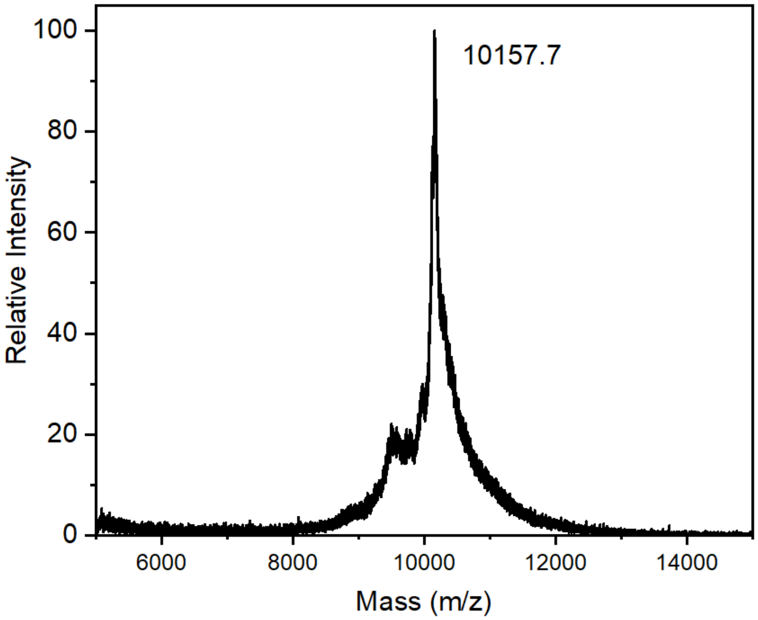

Figure 3.44. MALDI-MS spectrum with DCTB matrix of **FePB-1(A)**. *m*/*z* calculated for $C_{624}H_{672}N_{48}O_{48}Fe_6Cl_6$ $[M]^+$: 10157.6, found: 10157.7.

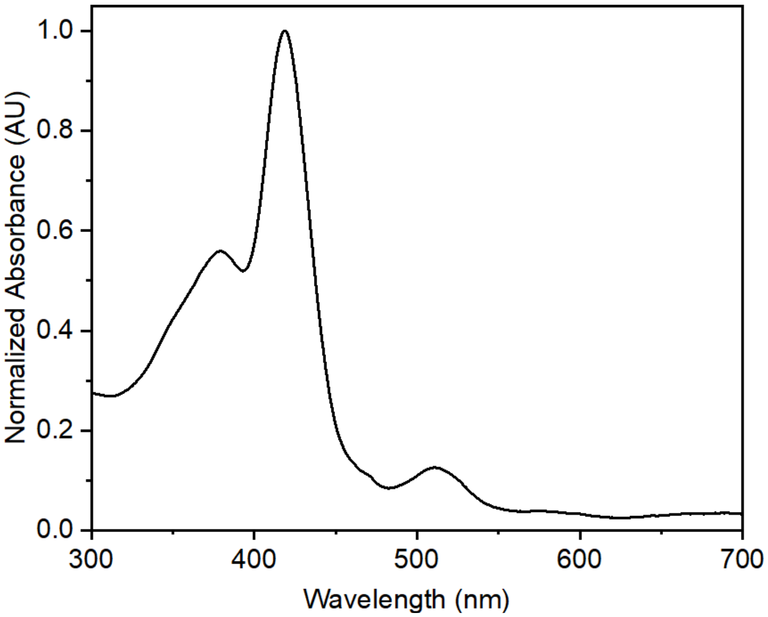

Figure 3.45. UV/Vis spectrum of **FePB-1(A)** in CH_2Cl_2. λ_{abs} 380, 419, 512, 586 nm.

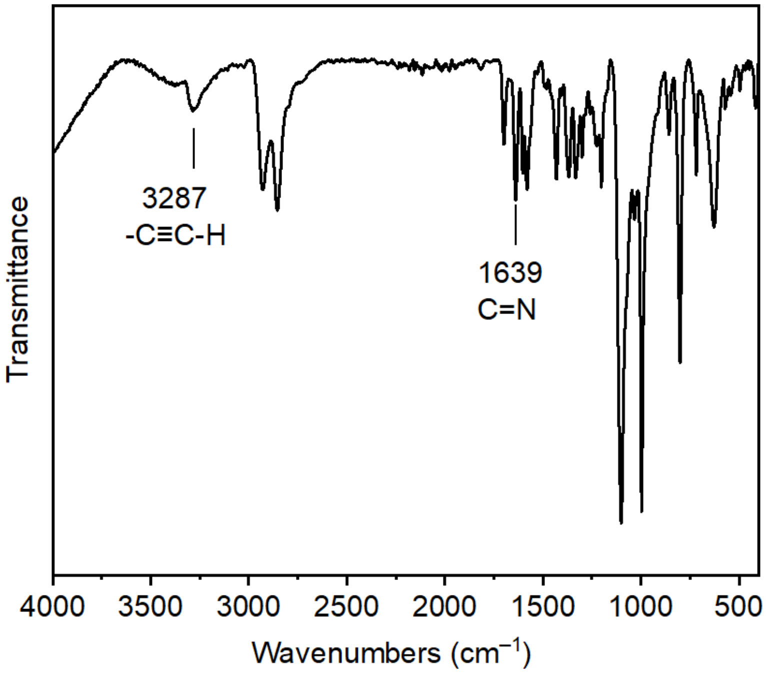

Figure 3.46. FT-IR spectrum of **FePB-1(A)**. Terminal alkyne C-H stretching at 3287 cm^{-1}and imine stretching peak observed at 1639 cm^{-1}.

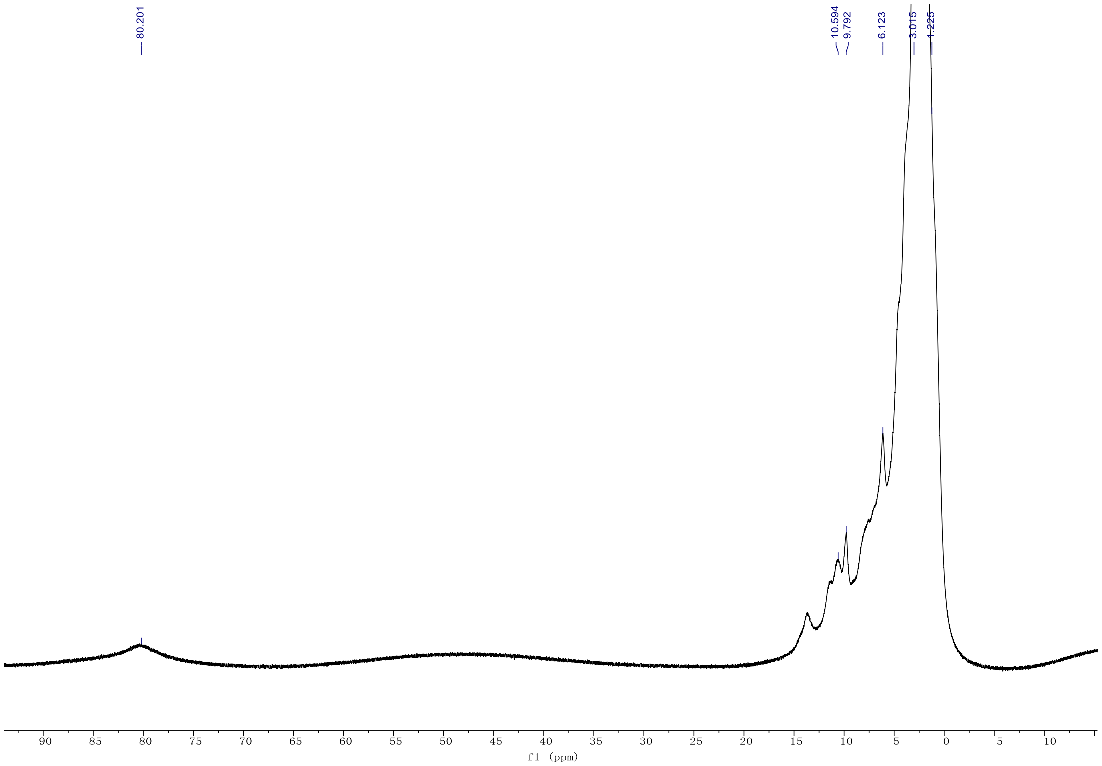

Figure 3.47. ^{1}H NMR (600 MHz) spectrum of compound **FePB-2(P)** in CD_3CN.

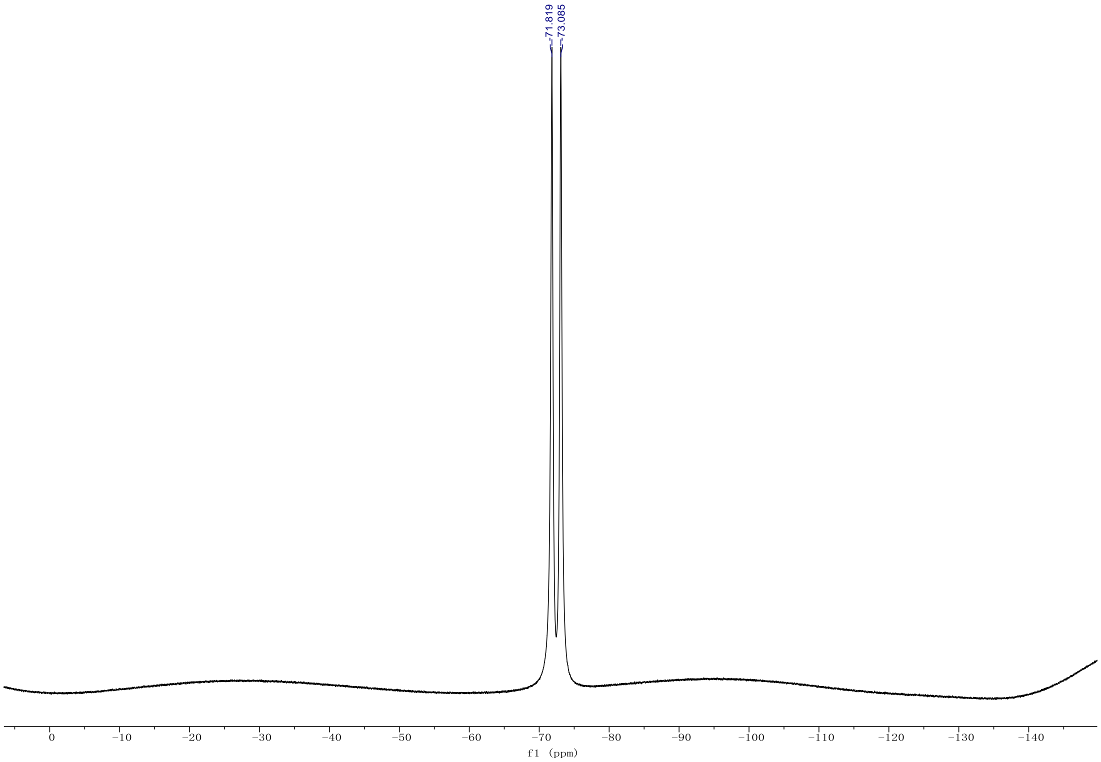

Figure 3.48. ^{19}F NMR (565 MHz) spectrum of compound **FePB-2(P)** in CD_3CN.

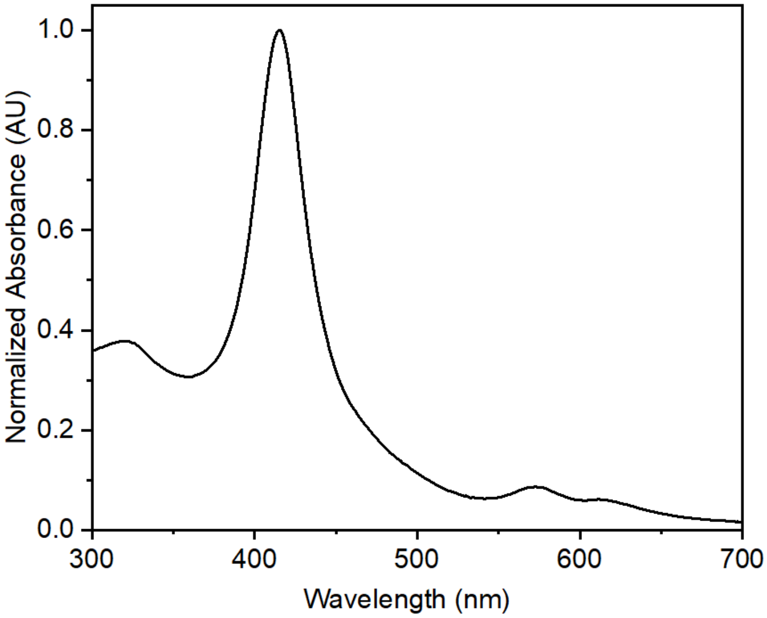

Figure 3.49. UV/Vis spectrum of **FePB-2(P)** in CH_3CN. λ_{abs} 416, 573, 615 nm.

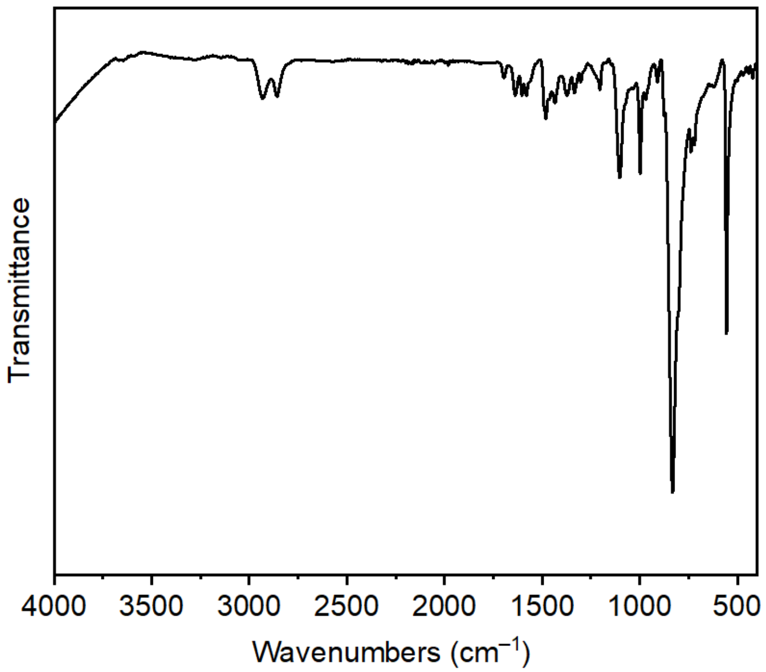

Figure 3.50. FT-IR spectrum of **FePB-2(P)**.

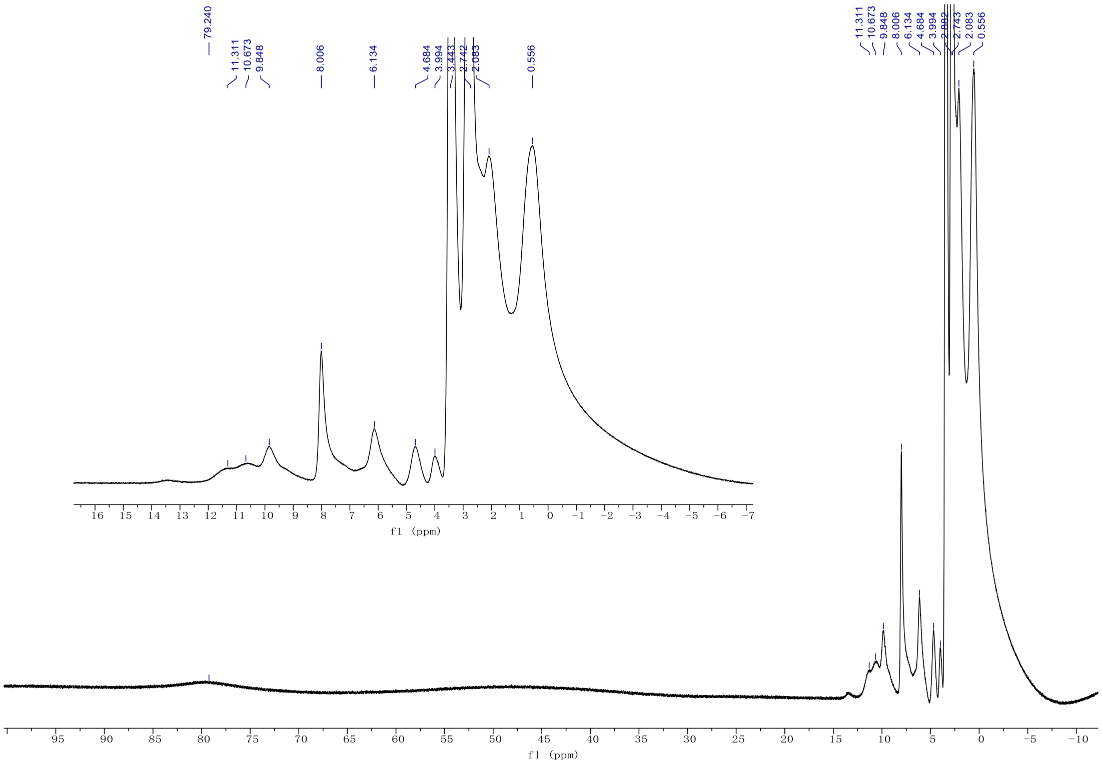

Figure 3.51. ^{1}H NMR (600 MHz) spectrum of compound **FePB-3(N)** in DMF-*d*$_7$.

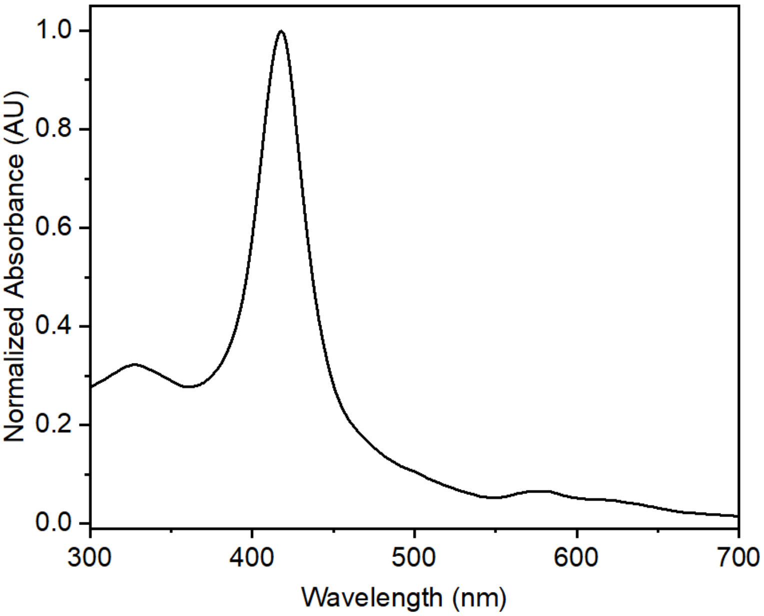

Figure 3.52. UV/Vis spectrum of **FePB-3(N)** in DCM. λ_{abs} 418, 578, 623 nm.

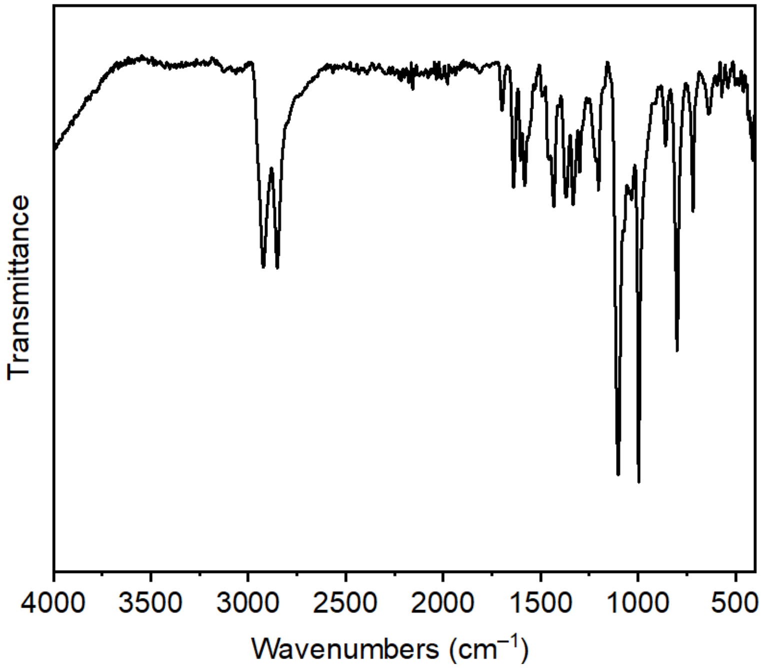

Figure 3.53. FT-IR spectrum of **FePB-3(N)**.

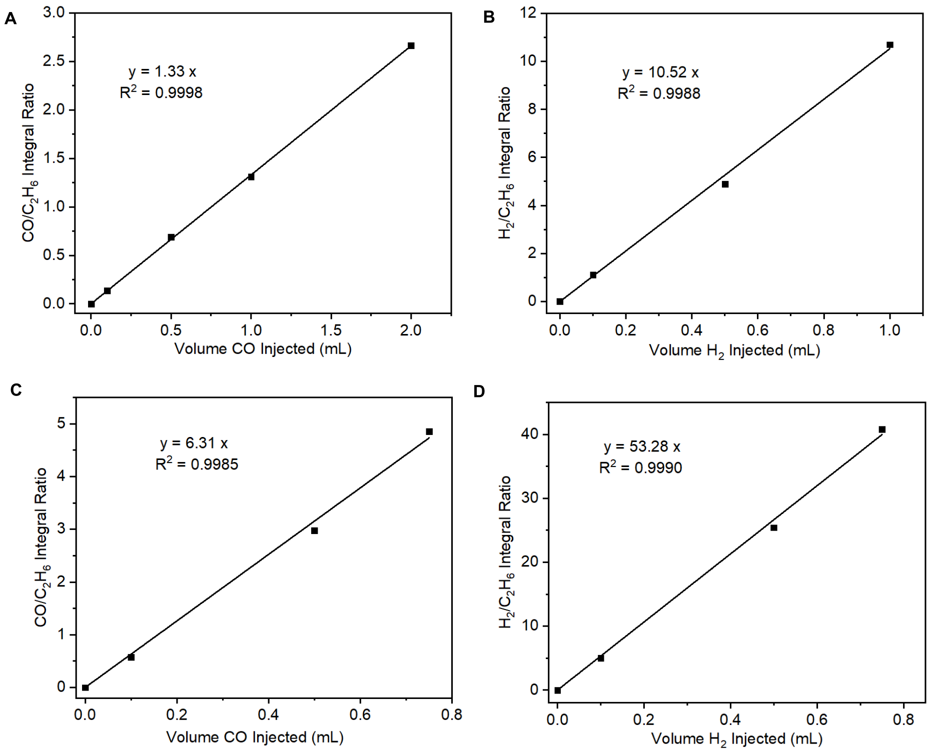

Figure 3.54. Gas chromatography calibration curves for CO and H_2 with C_2H_6 as an internal standard. (A) CO detection for electrolysis setup with medium gain FID, (B) H_2 detection for electrolysis setup with low gain TCD, (C) CO detection for photolysis setup with medium gain FID, and (D) H_2 detection for photolysis setup with low gain TCD.

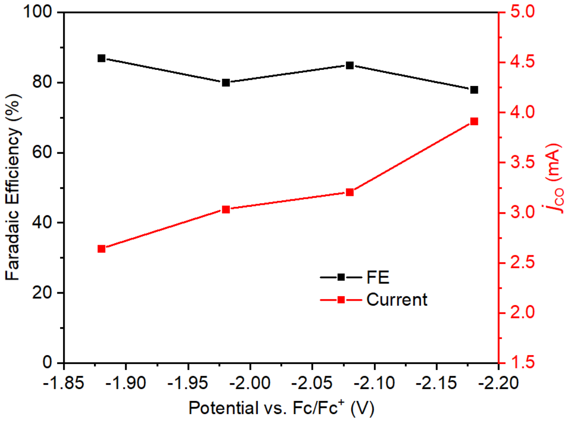

Figure 3.55. Controlled potential electrolysis of 0.1 mM **FePB-2(P)** in 0.1 M NBu_4PF_6/CH_3CN with 1 M TFE.

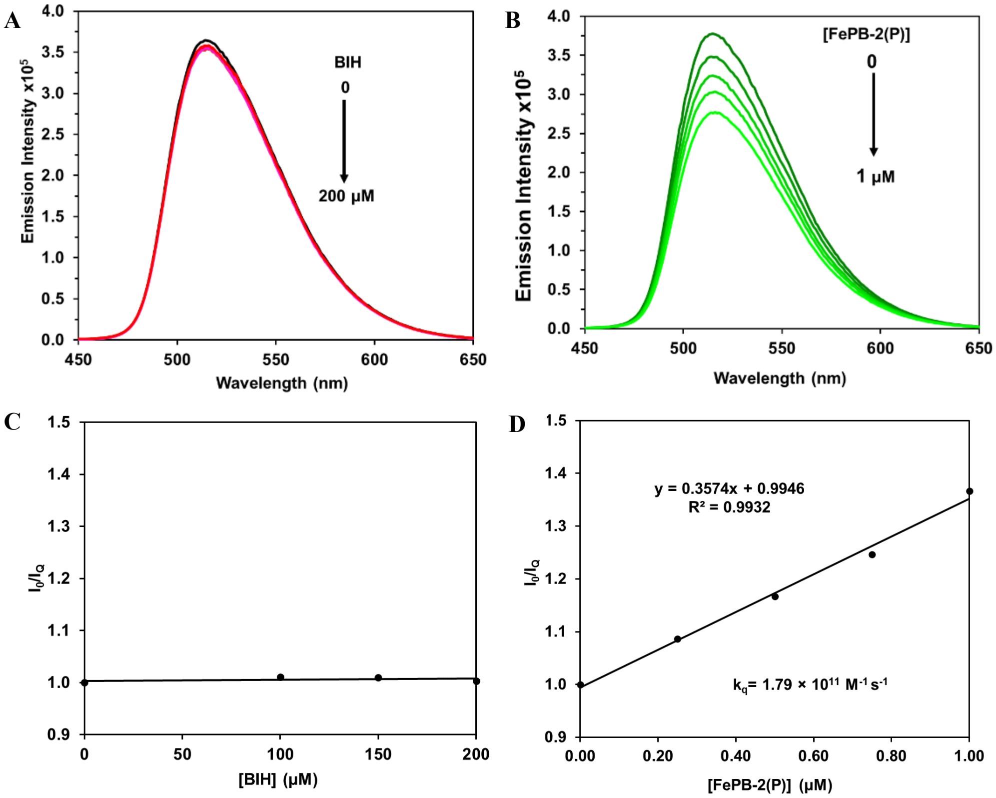

Figure 3.56. Emission decay (top) and Stern-Volmer quenching kinetic plots (bottom) of 50 µM Ir(ppy)$_3$ quenched using BIH (A, C) or **FePB-2(P)** (B, D) in CH_3CN.

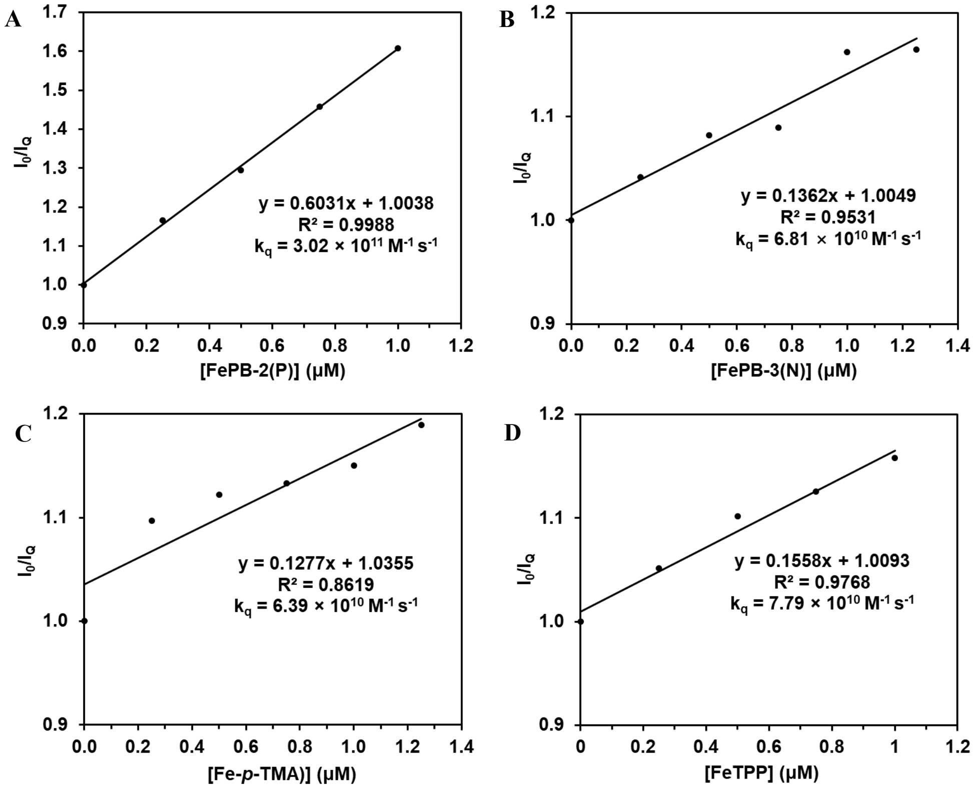

Figure 3.57. Quenching rate constants for the quenching of Ir(ppy)$_3$ emission for **FePB-2(P)** (A), **FePB-3(N)** (B), **Fe-p-TMA** (C), and **FeTPP** (D) in DMF.

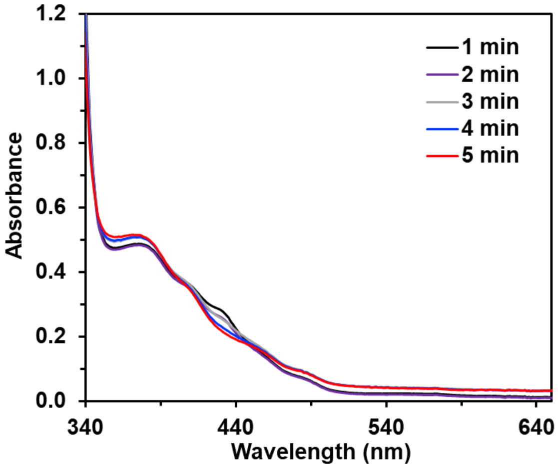

Figure 3.58. Pre- and post-experiment UV-VIS spectra of a typical photocatalytic reaction of Ir(ppy)$_3$, **FePB-2(P)**, BIH, and TFE under CO$_2$.

References:

(1) Lewis, N. S.; Nocera, D. G. Powering the planet: Chemical challenges in solar energy utilization. *Proc. Natl. Acad. Sci.* **2006**, *103* (43), 15729-15735.

(2) De Luna, P.; Hahn, C.; Higgins, D.; Jaffer Shaffiq, A.; Jaramillo Thomas, F.; Sargent Edward, H. What would it take for renewably powered electrosynthesis to displace petrochemical processes? *Science* **2019**, *364* (6438), eaav3506.

(3) Proppe, A. H.; Li, Y. C.; Aspuru-Guzik, A.; Berlinguette, C. P.; Chang, C. J.; Cogdell, R.; Doyle, A. G.; Flick, J.; Gabor, N. M.; van Grondelle, R.; et al. Bioinspiration in light harvesting and catalysis. *Nat. Rev. Mat.* **2020**, *5* (11), 828-846.

(4) Appel, A. M.; Bercaw, J. E.; Bocarsly, A. B.; Dobbek, H.; DuBois, D. L.; Dupuis, M.; Ferry, J. G.; Fujita, E.; Hille, R.; Kenis, P. J. A.; et al. Frontiers, Opportunities, and Challenges in Biochemical and Chemical Catalysis of CO_2 Fixation. *Chem. Rev.* **2013**, *113* (8), 6621-6658.

(5) Hori, Y. Electrochemical CO_2 Reduction on Metal Electrodes. In *Modern Aspects of Electrochemistry*, Vayenas, C. G., White, R. E., Gamboa-Aldeco, M. E. Eds.; Springer New York, 2008; pp 89-189.

(6) Benson, E. E.; Kubiak, C. P.; Sathrum, A. J.; Smieja, J. M. Electrocatalytic and homogeneous approaches to conversion of CO_2 to liquid fuels. *Chem. Soc. Rev.* **2009**, *38* (1), 89-99.

(7) Costentin, C.; Robert, M.; Savéant, J.-M. Catalysis of the electrochemical reduction of carbon dioxide. *Chem. Soc. Rev.* **2013**, *42* (6), 2423-2436.

(8) Francke, R.; Schille, B.; Roemelt, M. Homogeneously Catalyzed Electroreduction of Carbon Dioxide—Methods, Mechanisms, and Catalysts. *Chem. Rev.* **2018**, *118* (9), 4631-4701.

(9) Nitopi, S.; Bertheussen, E.; Scott, S. B.; Liu, X.; Engstfeld, A. K.; Horch, S.; Seger, B.; Stephens, I. E. L.; Chan, K.; Hahn, C.; et al. Progress and Perspectives of Electrochemical CO_2 Reduction on Copper in Aqueous Electrolyte. *Chem. Rev.* **2019**, *119* (12), 7610-7672.

(10) Zhang, S.; Fan, Q.; Xia, R.; Meyer, T. J. CO_2 Reduction: From Homogeneous to Heterogeneous Electrocatalysis. *Acc. Chem. Res.* **2020**, *53* (1), 255-264.

(11) Smith, P. T.; Nichols, E. M.; Cao, Z.; Chang, C. J. Hybrid Catalysts for Artificial Photosynthesis: Merging Approaches from Molecular, Materials, and Biological Catalysis. *Acc. Chem. Res.* **2020**, *53* (3), 575-587.

(12) Saha, P.; Amanullah, S.; Dey, A. Selectivity in Electrochemical CO_2 Reduction. *Acc. Chem. Res.* **2022**, *55* (2), 134-144.

(13) Boutin, E.; Merakeb, L.; Ma, B.; Boudy, B.; Wang, M.; Bonin, J.; Anxolabéhère-Mallart, E.; Robert, M. Molecular catalysis of CO_2 reduction: recent advances and perspectives in electrochemical and light-driven processes with selected Fe, Ni and Co aza macrocyclic and polypyridine complexes. *Chem. Soc. Rev.* **2020**, *49* (16), 5772-5809.

(14) Wagner, A.; Sahm, C. D.; Reisner, E. Towards molecular understanding of local chemical environment effects in electro- and photocatalytic CO_2 reduction. *Nat. Catal.* **2020**, *3* (10), 775-786.

(15) Nichols, A. W.; Machan, C. W. Secondary-Sphere Effects in Molecular Electrocatalytic CO_2 Reduction. *Front. Chem.* **2019**, *7:397* (397).

(16) Shafaat, H. S.; Yang, J. Y. Uniting biological and chemical strategies for selective CO_2 reduction. *Nat. Catal.* **2021**, *4* (11), 928-933.

(17) Azcarate, I.; Costentin, C.; Robert, M.; Savéant, J.-M. Dissection of Electronic Substituent Effects in Multielectron–Multistep Molecular Catalysis. Electrochemical CO_2-to-CO Conversion Catalyzed by Iron Porphyrins. *J. Phys. Chem. C* **2016**, *120* (51), 28951-28960.

(18) Johnson, B. A.; Maji, S.; Agarwala, H.; White, T. A.; Mijangos, E.; Ott, S. Activating a Low Overpotential CO_2 Reduction Mechanism by a Strategic Ligand Modification on a Ruthenium Polypyridyl Catalyst. *Angew. Chem. Int. Ed.* **2016**, *55* (5), 1825-1829.

(19) Gonell, S.; Lloret-Fillol, J.; Miller, A. J. M. An Iron Pyridyl-Carbene Electrocatalyst for Low Overpotential CO_2 Reduction to CO. *ACS Catal.* **2021**, *11* (2), 615-626.

(20) Kosugi, K.; Kondo, M.; Masaoka, S. Quick and Easy Method to Dramatically Improve the Electrochemical CO_2 Reduction Activity of an Iron Porphyrin Complex. *Angew. Chem. Int. Ed.* **2021**, *60* (40), 22070-22074.

(21) Nie, W.; Tarnopol, D. E.; McCrory, C. C. L. Enhancing a Molecular Electrocatalyst's Activity for CO_2 Reduction by Simultaneously Modulating Three Substituent Effects. *J. Am. Chem. Soc.* **2021**, *143* (10), 3764-3778.

(22) Derrick, J. S.; Loipersberger, M.; Chatterjee, R.; Iovan, D. A.; Smith, P. T.; Chakarawet, K.; Yano, J.; Long, J. R.; Head-Gordon, M.; Chang, C. J. Metal–Ligand Cooperativity via Exchange Coupling Promotes Iron- Catalyzed Electrochemical CO_2 Reduction at Low Overpotentials. *J. Am. Chem. Soc.* **2020**, *142* (48), 20489-20501.

(23) De La Torre, P.; Derrick, J. S.; Snider, A.; Smith, P. T.; Loipersberger, M.; Head-Gordon, M.; Chang, C. J. Exchange Coupling Determines Metal-Dependent Efficiency for Iron- and Cobalt-Catalyzed Photochemical CO2 Reduction. *ACS Catal.* **2022**, *12* (14), 8484-8493.

(24) Azcarate, I.; Costentin, C.; Robert, M.; Savéant, J.-M. Through-Space Charge Interaction Substituent Effects in Molecular Catalysis Leading to the Design of the Most Efficient Catalyst of CO_2-to-CO Electrochemical Conversion. *J. Am. Chem. Soc.* **2016**, *138* (51), 16639-16644.

(25) Zhang, R.; Warren, J. J. Controlling the Oxygen Reduction Selectivity of Asymmetric Cobalt Porphyrins by Using Local Electrostatic Interactions. *J. Am. Chem. Soc.* **2020**, *142* (31), 13426-13434.

(26) Erickson, J. D.; Preston, A. Z.; Linehan, J. C.; Wiedner, E. S. Enhanced Hydrogenation of Carbon Dioxide to Methanol by a Ruthenium Complex with a Charged Outer-Coordination Sphere. *ACS Catal.* **2020**, *10* (13), 7419-7423.

(27) Barlow, J. M.; Ziller, J. W.; Yang, J. Y. Inhibiting the Hydrogen Evolution Reaction (HER) with Proximal Cations: A Strategy for Promoting Selective Electrocatalytic Reduction. *ACS Catal.* **2021**, *11* (13), 8155-8164.

(28) Martin, D. J.; Mayer, J. M. Oriented Electrostatic Effects on O_2 and CO_2 Reduction by a Polycationic Iron Porphyrin. *J. Am. Chem. Soc.* **2021**, *143* (30), 11423-11434.

(29) Mao, Y.; Loipersberger, M.; Kron, K. J.; Derrick, J. S.; Chang, C. J.; Sharada, S. M.; Head-Gordon, M. Consistent inclusion of continuum solvation in energy decomposition analysis: theory and application to molecular CO_2 reduction catalysts. *Chem. Sci* **2021**, *12* (4), 1398-1414.

(30) Hooe, S. L.; Moreno, J. J.; Reid, A. G.; Cook, E. N.; Machan, C. W. Mediated Inner-Sphere Electron Transfer Induces Homogeneous Reduction of CO_2 via Through-Space Electronic Conjugation. *Angew. Chem. Int. Ed.* **2022**, *61* (1), e202109645.

(31) Narouz, M. R.; De La Torre, P.; An, L.; Chang, C. J. Multifunctional Charge and Hydrogen-Bond Effects of Second-Sphere Imidazolium Pendants Promote Capture and Electrochemical Reduction of CO_2 in Water Catalyzed by Iron Porphyrins**. *Angew. Chem. Int. Ed.* **2022**, *61* (37), e202207666.

(32) Drover, M. W. A guide to secondary coordination sphere editing. *Chem. Soc. Rev.* **2022**, *51* (6), 1861-1880.

(33) Costentin, C.; Drouet, S.; Robert, M.; Savéant, J.-M. A Local Proton Source Enhances CO_2 Electroreduction to CO by a Molecular Fe Catalyst. *Science* **2012**, *338* (6103), 90-94.

(34) Costentin, C.; Passard, G.; Robert, M.; Savéant, J.-M. Ultraefficient homogeneous catalyst for the CO_2-to-CO electrochemical conversion. *Proc. Natl. Acad. Sci.* **2014**, *111* (42), 14990-14994.

(35) Haviv, E.; Azaiza-Dabbah, D.; Carmieli, R.; Avram, L.; Martin, J. M. L.; Neumann, R. A Thiourea Tether in the Second Coordination Sphere as a Binding Site for CO_2 and a Proton Donor Promotes the Electrochemical Reduction of CO_2 to CO Catalyzed by a Rhenium Bipyridine-Type Complex. *J. Am. Chem. Soc.* **2018**, *140* (39), 12451-12456.

(36) Chapovetsky, A.; Welborn, M.; Luna, J. M.; Haiges, R.; Miller, T. F.; Marinescu, S. C. Pendant Hydrogen-Bond Donors in Cobalt Catalysts Independently Enhance CO_2 Reduction. *ACS Cent. Sci* **2018**, *4* (3), 397-404.

(37) Sung, S.; Li, X.; Wolf, L. M.; Meeder, J. R.; Bhuvanesh, N. S.; Grice, K. A.; Panetier, J. A.; Nippe, M. Synergistic Effects of Imidazolium-Functionalization on fac-$Mn(CO)_3$ Bipyridine Catalyst Platforms for Electrocatalytic Carbon Dioxide Reduction. *J. Am. Chem. Soc.* **2019**, *141* (16), 6569-6582.

(38) Gotico, P.; Boitrel, B.; Guillot, R.; Sircoglou, M.; Quaranta, A.; Halime, Z.; Leibl, W.; Aukauloo, A. Second-Sphere Biomimetic Multipoint Hydrogen-Bonding Patterns to Boost CO_2 Reduction of Iron Porphyrins. *Angew. Chem. Int. Ed.* **2019**, *58* (14), 4504-4509.

(39) Gotico, P.; Roupnel, L.; Guillot, R.; Sircoglou, M.; Leibl, W.; Halime, Z.; Aukauloo, A. Atropisomeric Hydrogen Bonding Control for CO_2 Binding and Enhancement of Electrocatalytic Reduction at Iron Porphyrins. *Angew. Chem. Int. Ed.* **2020**, *59* (50), 22451-22455.

(40) Amanullah, S.; Saha, P.; Dey, A. Activating the Fe(I) State of Iron Porphyrinoid with Second-Sphere Proton Transfer Residues for Selective Reduction of CO_2 to HCOOH via Fe(III/II)–COOH Intermediate(s). *J. Am. Chem. Soc.* **2021**, *143* (34), 13579-13592.

(41) Nichols, E. M.; Derrick, J. S.; Nistanaki, S. K.; Smith, P. T.; Chang, C. J. Positional effects of second-sphere amide pendants on electrochemical CO_2 reduction catalyzed by iron porphyrins. *Chem. Sci* **2018**, *9* (11), 2952-2960.

(42) Nichols, E. M.; Chang, C. J. Urea-Based Multipoint Hydrogen-Bond Donor Additive Promotes Electrochemical CO_2 Reduction Catalyzed by Nickel Cyclam. *Organometallics* **2019**, *38* (6), 1213-1218.

(43) Smith, P. T.; Weng, S.; Chang, C. J. An NADH-Inspired Redox Mediator Strategy to Promote Second-Sphere Electron and Proton Transfer for Cooperative Electrochemical CO_2 Reduction Catalyzed by Iron Porphyrin. *Inorg. Chem.* **2020**, *59* (13), 9270-9278.

(44) Zee, D. Z.; Nippe, M.; King, A. E.; Chang, C. J.; Long, J. R. Tuning Second Coordination Sphere Interactions in Polypyridyl–Iron Complexes to Achieve Selective Electrocatalytic Reduction of Carbon Dioxide to Carbon Monoxide. *Inorg. Chem.* **2020**, *59* (7), 5206-5217.

(45) Loipersberger, M.; Zee, D. Z.; Panetier, J. A.; Chang, C. J.; Long, J. R.; Head-Gordon, M. Computational Study of an Iron(II) Polypyridine Electrocatalyst for CO_2 Reduction: Key Roles for Intramolecular Interactions in CO_2 Binding and Proton Transfer. *Inorg. Chem.* **2020**, *59* (12), 8146-8160.

(46) Nichols, A. W.; Hooe, S. L.; Kuehner, J. S.; Dickie, D. A.; Machan, C. W. Electrocatalytic CO_2 Reduction to Formate with Molecular Fe(III) Complexes Containing Pendent Proton Relays. *Inorg. Chem.* **2020**, *59* (9), 5854-5864.

(47) Derrick, J. S.; Loipersberger, M.; Nistanaki, S. K.; Rothweiler, A. V.; Head-Gordon, M.; Nichols, E. M.; Chang, C. J. Templating Bicarbonate in the Second Coordination Sphere Enhances Electrochemical CO_2 Reduction Catalyzed by Iron Porphyrins. *J. Am. Chem. Soc.* **2022**, *144* (26), 11656-11663.

(48) Smith, P. T.; Benke, B. P.; Cao, Z.; Kim, Y.; Nichols, E. M.; Kim, K.; Chang, C. J. Iron Porphyrins Embedded into a Supramolecular Porous Organic Cage for Electrochemical CO_2 Reduction in Water. *Angew. Chem. Int. Ed.* **2018**, *57* (31), 9684-9688.

(49) Gong, M.; Cao, Z.; Liu, W.; Nichols, E. M.; Smith, P. T.; Derrick, J. S.; Liu, Y.-S.; Liu, J.; Wen, X.; Chang, C. J. Supramolecular Porphyrin Cages Assembled at Molecular–Materials Interfaces for Electrocatalytic CO Reduction. *ACS Cent. Sci* **2017**, *3* (9), 1032-1040.

(50) Smith, P. T.; Kim, Y.; Benke, B. P.; Kim, K.; Chang, C. J. Supramolecular Tuning Enables Selective Oxygen Reduction Catalyzed by Cobalt Porphyrins for Direct Electrosynthesis of Hydrogen Peroxide. *Angew. Chem. Int. Ed.* **2020**, *59* (12), 4902-4907.

(51) Smith, P. T.; Benke, B. P.; An, L.; Kim, Y.; Kim, K.; Chang, C. J. A Supramolecular Porous Organic Cage Platform Promotes Electrochemical Hydrogen Evolution from Water Catalyzed by Cobalt Porphyrins. *ChemElectroChem* **2021**, *8* (9), 1653-1657.

(52) Yoshizawa, M.; Klosterman, J. K.; Fujita, M. Functional Molecular Flasks: New Properties and Reactions within Discrete, Self-Assembled Hosts. *Angew. Chem. Int. Ed.* **2009**, *48* (19), 3418-3438.

(53) Tranchemontagne, D. J.; Ni, Z.; O'Keeffe, M.; Yaghi, O. M. Reticular Chemistry of Metal–Organic Polyhedra. *Angew. Chem. Int. Ed.* **2008**, *47* (28), 5136-5147.

(54) Cook, T. R.; Zheng, Y.-R.; Stang, P. J. Metal–Organic Frameworks and Self-Assembled Supramolecular Coordination Complexes: Comparing and Contrasting the Design, Synthesis, and Functionality of Metal–Organic Materials. *Chem. Rev.* **2013**, *113* (1), 734-777.

(55) Brown, C. J.; Toste, F. D.; Bergman, R. G.; Raymond, K. N. Supramolecular Catalysis in Metal–Ligand Cluster Hosts. *Chem. Rev.* **2015**, *115* (9), 3012-3035.

(56) Percástegui, E. G.; Ronson, T. K.; Nitschke, J. R. Design and Applications of Water-Soluble Coordination Cages. *Chem. Rev.* **2020**, *120* (24), 13480-13544.

(57) McTernan, C. T.; Davies, J. A.; Nitschke, J. R. Beyond Platonic: How to Build Metal–Organic Polyhedra Capable of Binding Low-Symmetry, Information-Rich Molecular Cargoes. *Chem. Rev.* **2022**, *122* (11), 10393-10437.

(58) Gosselin, A. J.; Rowland, C. A.; Bloch, E. D. Permanently Microporous Metal–Organic Polyhedra. *Chem. Rev.* **2020**, *120* (16), 8987-9014.

(59) Hauke, C. E.; Cook, T. R. 1.27 - Self-Assembly Processes for the Construction of Supramolecular Coordination Compounds. In *Comprehensive Coordination Chemistry III*, Constable, E. C., Parkin, G., Que Jr, L. Eds.; Elsevier, 2021; pp 1074-1085.

(60) McConnell, A. J. Metallosupramolecular cages: from design principles and characterisation techniques to applications. *Chem. Soc. Rev.* **2022**, *51* (8), 2957-2971.

(61) Evans, J. D.; Sumby, C. J.; Doonan, C. J. Synthesis and Applications of Porous Organic Cages. *Chem. Lett.* **2015**, *44* (5), 582-588.

(62) Ballester, P.; Fujita, M.; Rebek, J. Molecular containers. *Chem. Soc. Rev.* **2015**, *44* (2), 392-393.

(63) Zhang, G.; Mastalerz, M. Organic cage compounds – from shape-persistency to function. *Chem. Soc. Rev.* **2014**, *43* (6), 1934-1947.

(64) Leenders, S. H. A. M.; Gramage-Doria, R.; de Bruin, B.; Reek, J. N. H. Transition metal catalysis in confined spaces. *Chem. Soc. Rev.* **2015**, *44* (2), 433-448.

(65) Hasell, T.; Cooper, A. I. Porous organic cages: soluble, modular and molecular pores. *Nat. Rev. Mat.* **2016**, *1* (9), 16053.

(66) Cooper, A. I. Porous Molecular Solids and Liquids. *ACS Cent. Sci* **2017**, *3* (6), 544-553.

(67) Mastalerz, M. Porous Shape-Persistent Organic Cage Compounds of Different Size, Geometry, and Function. *Acc. Chem. Res.* **2018**, *51* (10), 2411-2422.

(68) Mukhopadhyay, R. D.; Kim, Y.; Koo, J.; Kim, K. Porphyrin Boxes. *Acc. Chem. Res.* **2018**, *51* (11), 2730-2738.

(69) Bender, T. A.; Bergman, R. G.; Raymond, K. N.; Toste, F. D. A Supramolecular Strategy for Selective Catalytic Hydrogenation Independent of Remote Chain Length. *J. Am. Chem. Soc.* **2019**, *141* (30), 11806-11810.

(70) Iwasawa, T.; Hooley, R. J.; Rebek, J. Stabilization of Labile Carbonyl Addition Intermediates by a Synthetic Receptor. *Science* **2007**, *317* (5837), 493-496.

(71) Yoshizawa, M.; Tamura, M.; Fujita, M. Diels-Alder in Aqueous Molecular Hosts: Unusual Regioselectivity and Efficient Catalysis. *Science* **2006**, *312* (5771), 251-254.

(72) Kuah, E.; Toh, S.; Yee, J.; Ma, Q.; Gao, Z. Enzyme Mimics: Advances and Applications. *Chemistry – A European Journal* **2016**, *22* (25), 8404-8430.

(73) Lin, S.; Diercks Christian, S.; Zhang, Y.-B.; Kornienko, N.; Nichols Eva, M.; Zhao, Y.; Paris Aubrey, R.; Kim, D.; Yang, P.; Yaghi Omar, M.; et al. Covalent organic frameworks comprising cobalt porphyrins for catalytic CO_2 reduction in water. *Science* **2015**, *349* (6253), 1208-1213.

(74) Diercks, C. S.; Lin, S.; Kornienko, N.; Kapustin, E. A.; Nichols, E. M.; Zhu, C.; Zhao, Y.; Chang, C. J.; Yaghi, O. M. Reticular Electronic Tuning of Porphyrin Active Sites in Covalent Organic Frameworks for Electrocatalytic Carbon Dioxide Reduction. *J. Am. Chem. Soc.* **2018**, *140* (3), 1116-1122.

(75) Yang, S.; Hu, W.; Zhang, X.; He, P.; Pattengale, B.; Liu, C.; Cendejas, M.; Hermans, I.; Zhang, X.; Zhang, J.; et al. 2D Covalent Organic Frameworks as Intrinsic Photocatalysts for Visible Light-Driven CO_2 Reduction. *J. Am. Chem. Soc.* **2018**, *140* (44), 14614-14618.

(76) Fu, Z.; Wang, X.; Gardner, A. M.; Wang, X.; Chong, S. Y.; Neri, G.; Cowan, A. J.; Liu, L.; Li, X.; Vogel, A.; et al. A stable covalent organic framework for photocatalytic carbon dioxide reduction. *Chem. Sci* **2020**, *11* (2), 543-550.

(77) Cheung, P. L.; Lee, S. K.; Kubiak, C. P. Facile Solvent-Free Synthesis of Thin Iron Porphyrin COFs on Carbon Cloth Electrodes for CO_2 Reduction. *Chem. Mater.* **2019**, *31* (6), 1908-1919.

(78) Huang, N.; Lee, K. H.; Yue, Y.; Xu, X.; Irle, S.; Jiang, Q.; Jiang, D. A Stable and Conductive Metallophthalocyanine Framework for Electrocatalytic Carbon Dioxide Reduction in Water. *Angew. Chem. Int. Ed.* **2020**, *59* (38), 16587-16593.

(79) Zhu, H.-J.; Lu, M.; Wang, Y.-R.; Yao, S.-J.; Zhang, M.; Kan, Y.-H.; Liu, J.; Chen, Y.; Li, S.-L.; Lan, Y.-Q. Efficient electron transmission in covalent organic framework nanosheets for highly active electrocatalytic carbon dioxide reduction. *Nat. Commun.* **2020**, *11* (1), 497.

(80) Gong, Y.-N.; Zhong, W.; Li, Y.; Qiu, Y.; Zheng, L.; Jiang, J.; Jiang, H.-L. Regulating Photocatalysis by Spin-State Manipulation of Cobalt in Covalent Organic Frameworks. *J. Am. Chem. Soc.* **2020**, *142* (39), 16723-16731.

(81) Han, B.; Jin, Y.; Chen, B.; Zhou, W.; Yu, B.; Wei, C.; Wang, H.; Wang, K.; Chen, Y.; Chen, B.; et al. Maximizing Electroactive Sites in a Three-Dimensional Covalent Organic Framework for Significantly Improved Carbon Dioxide Reduction Electrocatalysis. *Angew. Chem. Int. Ed.* **2022**, *61* (1), e202114244.

(82) Lu, M.; Zhang, M.; Liu, J.; Chen, Y.; Liao, J.-P.; Yang, M.-Y.; Cai, Y.-P.; Li, S.-L.; Lan, Y.-Q. Covalent Organic Framework Based Functional Materials: Important Catalysts for Efficient CO_2 Utilization. *Angew. Chem. Int. Ed.* **2022**, *61* (15), e202200003.

(83) Kornienko, N.; Zhao, Y.; Kley, C. S.; Zhu, C.; Kim, D.; Lin, S.; Chang, C. J.; Yaghi, O. M.; Yang, P. Metal–Organic Frameworks for Electrocatalytic Reduction of Carbon Dioxide. *J. Am. Chem. Soc.* **2015**, *137* (44), 14129-14135.

(84) Wang, Y.-R.; Huang, Q.; He, C.-T.; Chen, Y.; Liu, J.; Shen, F.-C.; Lan, Y.-Q. Oriented electron transmission in polyoxometalate-metalloporphyrin organic framework for highly selective electroreduction of CO_2. *Nat. Commun.* **2018**, *9* (1), 4466.

(85) Dou, S.; Song, J.; Xi, S.; Du, Y.; Wang, J.; Huang, Z.-F.; Xu, Z. J.; Wang, X. Boosting Electrochemical CO_2 Reduction on Metal–Organic Frameworks via Ligand Doping. *Angew. Chem. Int. Ed.* **2019**, *58* (12), 4041-4045.

(86) Huang, N.-Y.; Zhang, X.-W.; Xu, Y.-Z.; Liao, P.-Q.; Chen, X.-M. A local hydrophobic environment in a metal–organic framework for boosting photocatalytic CO_2 reduction in the presence of water. *Chem. Commun.* **2019**, *55* (98), 14781-14784.

(87) Kang, X.; Wang, B.; Hu, K.; Lyu, K.; Han, X.; Spencer, B. F.; Frogley, M. D.; Tuna, F.; McInnes, E. J. L.; Dryfe, R. A. W.; et al. Quantitative Electro-Reduction of CO_2 to Liquid Fuel over Electro-Synthesized Metal–Organic Frameworks. *J. Am. Chem. Soc.* **2020**, *142* (41), 17384-17392.

(88) Zhong, H.; Ghorbani-Asl, M.; Ly, K. H.; Zhang, J.; Ge, J.; Wang, M.; Liao, Z.; Makarov, D.; Zschech, E.; Brunner, E.; et al. Synergistic electroreduction of carbon dioxide to carbon monoxide on bimetallic layered conjugated metal-organic frameworks. *Nat. Commun.* **2020**, *11* (1), 1409.

(89) Qiu, X.-F.; Zhu, H.-L.; Huang, J.-R.; Liao, P.-Q.; Chen, X.-M. Highly Selective CO_2 Electroreduction to C2H4 Using a Metal–Organic Framework with Dual Active Sites. *J. Am. Chem. Soc.* **2021**, *143* (19), 7242-7246.

(90) He, H.; Perman, J. A.; Zhu, G.; Ma, S. Metal-Organic Frameworks for CO_2 Chemical Transformations. *Small* **2016**, *12* (46), 6309-6324.

(91) Trickett, C. A.; Helal, A.; Al-Maythalony, B. A.; Yamani, Z. H.; Cordova, K. E.; Yaghi, O. M. The chemistry of metal–organic frameworks for CO_2 capture, regeneration and conversion. *Nat. Rev. Mat.* **2017**, *2* (8), 17045.

(92) Majewski, M. B.; Peters, A. W.; Wasielewski, M. R.; Hupp, J. T.; Farha, O. K. Metal–Organic Frameworks as Platform Materials for Solar Fuels Catalysis. *ACS Energy Lett.* **2018**, *3* (3), 598-611.

(93) Liang, Z.; Qu, C.; Xia, D.; Zou, R.; Xu, Q. Atomically Dispersed Metal Sites in MOF-Based Materials for Electrocatalytic and Photocatalytic Energy Conversion. *Angew. Chem. Int. Ed.* **2018**, *57* (31), 9604-9633.

(94) Shah, S. S. A.; Najam, T.; Wen, M.; Zang, S.-Q.; Waseem, A.; Jiang, H.-L. Metal–Organic Framework-Based Electrocatalysts for CO_2 Reduction. *Small Structures* **2022**, *3* (5), 2100090.

(95) Huang, H. H.; Šolomek, T. Photochemistry Meets Porous Organic Cages. *Chimia (Aarau)* **2021**, *75* (4), 285-290.

(96) Wang, H.; Jin, Y.; Sun, N.; Zhang, W.; Jiang, J. Post-synthetic modification of porous organic cages. *Chem. Soc. Rev.* **2021**, *50* (16), 8874-8886.

(97) Liu, J.; Wang, Z.; Cheng, P.; Zaworotko, M. J.; Chen, Y.; Zhang, Z. Post-synthetic modifications of metal–organic cages. *Nat. Rev. Chem.* **2022**, *6* (5), 339-356.

(98) Hong, S.; Rohman, M. R.; Jia, J.; Kim, Y.; Moon, D.; Kim, Y.; Ko, Y. H.; Lee, E.; Kim, K. Porphyrin Boxes: Rationally Designed Porous Organic Cages. *Angew. Chem. Int. Ed.* **2015**, *54* (45), 13241-13244.

(99) Wang, Z. In *Comprehensive Organic Name Reactions and Reagents*, Wang, Z. Ed.; 2010; pp 2559-2562.

(100) Wang, Z. Corey-Fuchs Reaction. In *Comprehensive Organic Name Reactions and Reagents*, Wang, Z. Ed.; 2010; pp 717-721.

(101) Iwanami, K.; Seo, H.; Tobita, Y.; Oriyama, T. A Highly Efficient Method for the Reductive Etherification of Carbonyl Compounds with Triethylsilane and Alkoxytrimethylsilane Catalyzed by Iron(III) Chloride. *Synthesis* **2005**, *2005* (02), 183-186.

(102) Rostovtsev, V. V.; Green, L. G.; Fokin, V. V.; Sharpless, K. B. A Stepwise Huisgen Cycloaddition Process: Copper(I)-Catalyzed Regioselective "Ligation" of Azides and Terminal Alkynes. *Angew. Chem. Int. Ed.* **2002**, *41* (14), 2596-2599.

(103) Huang, D.; Qin, A.; Tang, B. Z. CHAPTER 2 Transition Metal-catalyzed Click Polymerization. In *Click Polymerization*, The Royal Society of Chemistry, 2018; pp 36-85.

(104) Benke, B. P.; Aich, P.; Kim, Y.; Kim, K. L.; Rohman, M. R.; Hong, S.; Hwang, I.-C.; Lee, E. H.; Roh, J. H.; Kim, K. Iodide-Selective Synthetic Ion Channels Based on Shape-Persistent Organic Cages. *J. Am. Chem. Soc.* **2017**, *139* (22), 7432-7435.

(105) Costentin, C.; Robert, M.; Savéant, J.-M.; Tatin, A. Efficient and selective molecular catalyst for the CO_2-to-CO electrochemical conversion in water. *Proc. Natl. Acad. Sci.* **2015**, *112* (22), 6882-6886.

(106) Bonin, J.; Robert, M.; Routier, M. Selective and Efficient Photocatalytic CO_2 Reduction to CO Using Visible Light and an Iron-Based Homogeneous Catalyst. *J. Am. Chem. Soc.* **2014**, *136* (48), 16768-16771.

(107) Rao, H.; Schmidt, L. C.; Bonin, J.; Robert, M. Visible-light-driven methane formation from CO_2 with a molecular iron catalyst. *Nature* **2017**, *548* (7665), 74-77.

(108) Rao, H.; Lim, C.-H.; Bonin, J.; Miyake, G. M.; Robert, M. Visible-Light-Driven Conversion of CO_2 to CH_4 with an Organic Sensitizer and an Iron Porphyrin Catalyst. *J. Am. Chem. Soc.* **2018**, *140* (51), 17830-17834.

(109) Pugliese, E.; Gotico, P.; Wehrung, I.; Boitrel, B.; Quaranta, A.; Ha-Thi, M.-H.; Pino, T.; Sircoglou, M.; Leibl, W.; Halime, Z.; et al. Dissection of Light-Induced Charge Accumulation at a Highly Active Iron Porphyrin: Insights in the Photocatalytic CO_2 Reduction. *Angew. Chem. Int. Ed.* **2022**, *61* (14), e202117530.

(110) Zhang, X.; Yamauchi, K.; Sakai, K. Earth-Abundant Photocatalytic CO_2 Reduction by Multielectron Chargeable Cobalt Porphyrin Catalysts: High CO/H_2 Selectivity in Water Based on Phase Mismatch in Frontier MO Association. *ACS Catal.* **2021**, *11* (16), 10436-10449.

(111) Nakajima, T.; Tamaki, Y.; Ueno, K.; Kato, E.; Nishikawa, T.; Ohkubo, K.; Yamazaki, Y.; Morimoto, T.; Ishitani, O. Photocatalytic Reduction of Low Concentration of CO2. *J. Am. Chem. Soc.* **2016**, *138* (42), 13818-13821.

(112) Kumagai, H.; Nishikawa, T.; Koizumi, H.; Yatsu, T.; Sahara, G.; Yamazaki, Y.; Tamaki, Y.; Ishitani, O. Electrocatalytic reduction of low concentration CO_2. *Chem. Sci* **2019**, *10* (6), 1597-1606.

(113) Yamazaki, Y.; Miyaji, M.; Ishitani, O. Utilization of Low-Concentration CO_2 with Molecular Catalysts Assisted by CO_2-Capturing Ability of Catalysts, Additives, or Reaction Media. *J. Am. Chem. Soc.* **2022**, *144* (15), 6640-6660.

(114) Hong, D.; Tsukakoshi, Y.; Kotani, H.; Ishizuka, T.; Kojima, T. Visible-Light-Driven Photocatalytic CO2 Reduction by a Ni(II) Complex Bearing a Bioinspired Tetradentate Ligand for Selective CO Production. *J. Am. Chem. Soc.* **2017**, *139* (19), 6538-6541.

(115) Kim, Y.; Koo, J.; Hwang, I.-C.; Mukhopadhyay, R. D.; Hong, S.; Yoo, J.; Dar, A. A.; Kim, I.; Moon, D.; Shin, T. J.; et al. Rational Design and Construction of Hierarchical Superstructures Using Shape-Persistent Organic Cages: Porphyrin Box-Based Metallosupramolecular Assemblies. *J. Am. Chem. Soc.* **2018**, *140* (44), 14547-14551.

Appendix A: A Ruthenium Polypyridyl Complex for CO_2 Reduction Beyond Two Electrons

Abstract:

In our studies of CO_2 reduction using metal polypyridyl catalysts, we have observed excellent stability and CO selectivity can be achieved with and Fe (II) metal center. We predict that the unique properties of the tpyPY2Me ligand platform can be further leveraged. Producing the two-electron reduced products CO or $HCOO^-$ is fairly ubiquitous in the literature for molecular electrocatalysts and photocatalysts. We propose that a tpyPY2Me complex bearing a Ru (II) metal center may be competent for CO_2 reduction beyond two electron products due to the predicted higher affinity of Ru-CO compared to Fe-CO intermediates. In this Appendix, we include a route for the metalation of tpyPY2Me with Ru and some preliminary characterization and electrochemical data.

Metalation of tpyPY2Me with Ru (II)

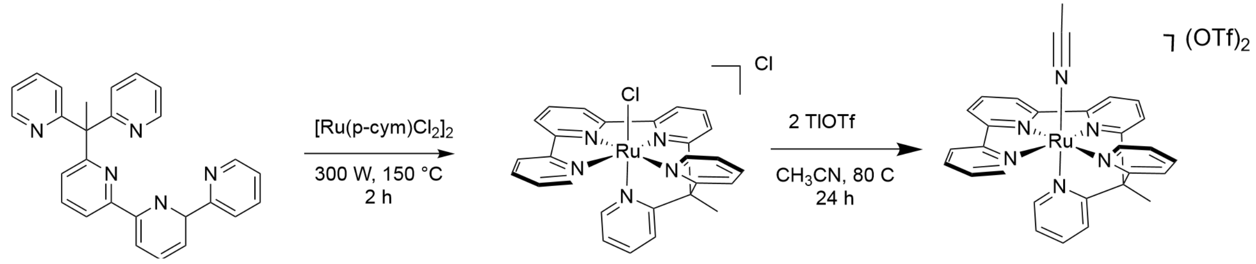

In a 10 mL microwave reactor tube, load 60 mg tpyPY2Me, 0.5 equivalents of the ruthenium dimer [Ru(*p*-cymene)Cl_2]$_2$, 5 mL of dry ethanol, and a stir bar. Place in the microwave reactor for two hours at 150 °C or 300 W. Transfer the reaction mixture to a round bottom flask and evaporate the ethanol, then dry on high vacuum line. Once dry, remove soluble impurities (yellow/orange; 416 m/Z free ligand and 686 m/Z Ru *p*-cymene side product) by washing with acetone. The product [RuCl(tpyPY2Me]Cl (552 m/Z) should be a dark red/brown solid, soluble in CH_3CN. Place 100 mg [RuCl(tpyPY2Me]Cl dissolved in a minimum volume of CH_3CN and two equivalents of TlOTf in a 20 mL scintillation vial loaded with a stir bar. Stir at 80 °C overnight. A white precipitate should form (TlCl) and the soluble product mixture [Ru(tpyPY2Me)CH_3CN](OTf)$_2$ will appear brownish/orange. Filter and dry. If impurity if evident by mass spec or NMR characterization (remaining 686 m/Z), purify by column chromatography using alumina with a methylene chloride mobile phase (up to 5% methanol if needed). Pure product is orange/red. Crystallization can be achieved by slow vapor diffusion of ether into a saturated CH_3CN solution of [Ru(tpyPY2Me)CH_3CN](OTf)$_2$.

Note: For the salt metathesis reaction, TlOTf is necessary due to ease of removing excess Tl compared to Ag (from AgOTf), which can produce stripping waves during electrochemical analysis. Thallium is toxic and should be handled with extreme care, using disposable glassware/pipet filters, and disposed of in a separate labeled waste container.

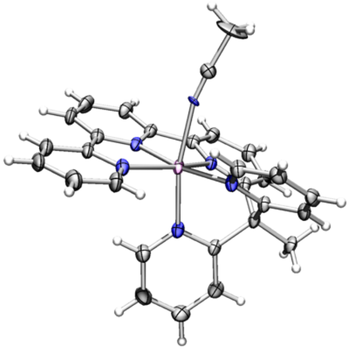

Figure A.1. Solid state structure of [Ru(tpyPY2Me)CH_3CN]$(OTf)_2$ with thermal ellipsoids plotted at the 50% probability level. Non-coordinated solvent molecules are omitted for clarity.

Table A.1 Crystallographic data[a] for **[Ru(tpyPY2Me)(MeCN)](OTf)$_2$**.

	[Ru(tpyPY2Me)(MeCN)](OTf)$_2$
Chemical formula	$C_{35}H_{25}RuN_5$•2(CF_3O_3S)•(C_2H_3N)
FW	910.64
Crystal system, space group	Triclinic, *P-1*
Temperature (K)	100(2)
a (Å)	10.4122(3)
b (Å)	13.4623(4)
c (Å)	15.3341(5)
a	115.758(3)
b	97.133(2)
γ	95.978(2)
V (Å^3)	1890.56(11)
Z	18
μ (mm^{-1})	4.082
F(000)	1638.0
Crystal size (mm)	0.15 × 0.24 × 0.26
2Θ range (°) for cell measurement	6.054–52.744
Radiation type	Mo *K*α
No. of reflections for cell measurement	40006
Index ranges	$-13 \leq h \leq 12$
	$-16 \leq k \leq 16$
	$-19 \leq l \leq 19$
Reflections collected / unique	40006 / 7719
R_{int}	0.0405
Data / restraints / parameters	7719 / 30 / 528
Goodness-of-fit on F^2	1.058
Final R indices[b]	$R_1 = 0.0861$, $wR_2 = 0.2452$
Largest diff. peak and hole, eÅ^{-3}	5.04 and –1.51

[a]Obtained with a rotating-anode X-ray tube, Rigaku Mo K_α ($\lambda = 0.71073$ Å) X-ray source. [b]$R_1 = \sum||F_0| - F_C||/\sum|F_0|$, $R_2 = \{\sum[w(F_0^2 - F_0^2)^2]/\sum[w(F_0^2)^2]\}^{1/2}$.

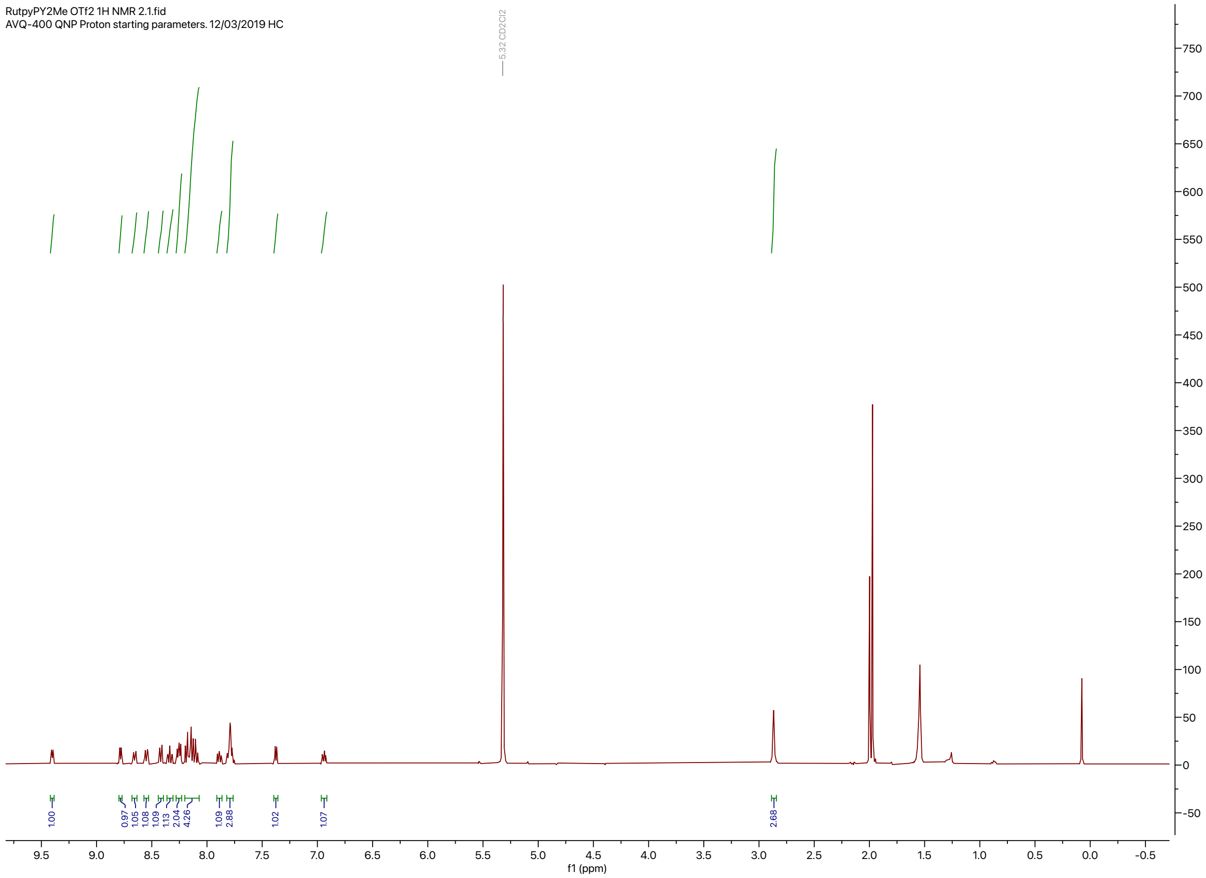

Figure A.2. 1H NMR Spectrum of [Ru(tpyPY2Me)CH_3CN]$(OTf)_2$ in CD_2Cl_2.

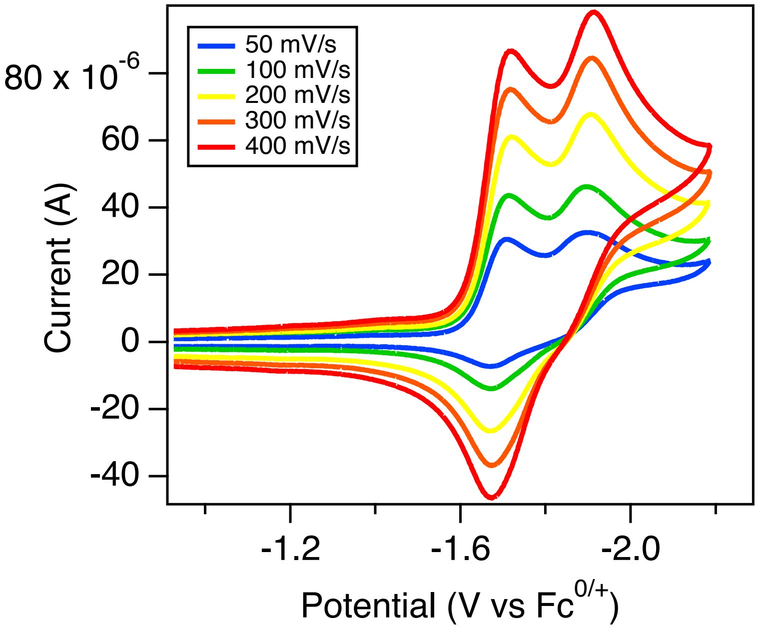

Figure A.3. Cyclic voltammetry of 1 mM [Ru(tpyPY2Me)OTf]OTf in 100 mM NBu_4PF_6/CH_3CN electrolyte using a glassy carbon electrode. Scans vary from 50 to 400 mV/s. Waves are centered at $E_{1/2} = -1.65$ and -1.83 V vs $Fc^{0/+}$.

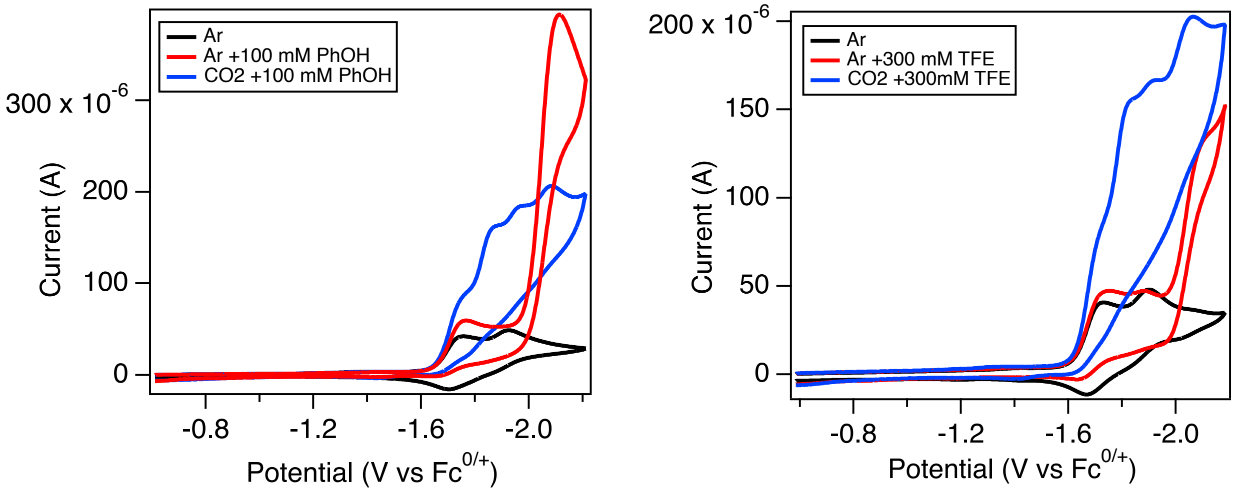

Figure A.4. Cyclic volammetry reactivity experiments. Left: CV of Ru complex under Ar (black), 100 mM of phenol under Ar (red), and 100mM phenol under CO_2 (blue). Right: CV of Ru complex under Ar (black), 100 mM of trifluoroethano(TFE) under Ar (red), and 300 mM TFE under CO_2 (blue).

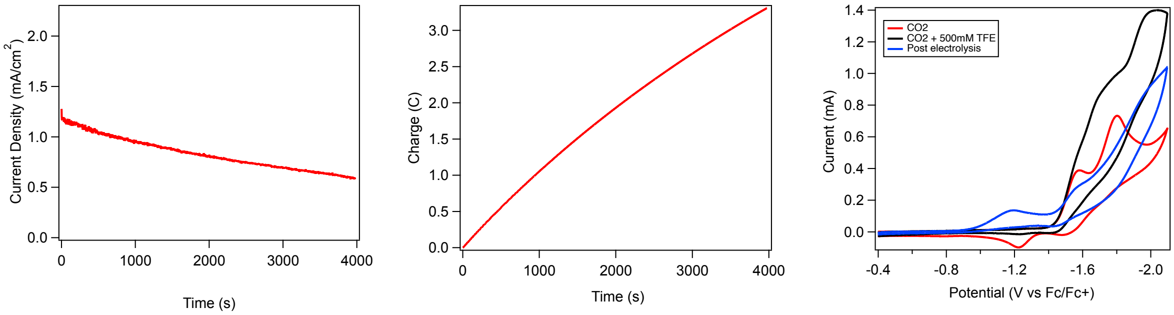

Figure A.5. Controlled potential electrolysis (CPE) experiment for 1 mM Ru complex under a CO_2 saturated solution of 100 mM NBu_4PF_6/CH_3CN and 500 mM TFE. Applied potential: −1.8 V vs Fc$^{0/+}$. Gas chromatography results showed no H_2, FE for CO = 6%. Liquid product detection should be prioritized in the future.

Appendix B: Experimental Procedures for the Evaluation of Homogeneous Photocatalysts

Abstract:

Photochemistry or photocatalysis involves the use of a light source to initiate electron (or energy) transfer via excitation of species in a reaction medium. This method can serve as a powerful tool for modeling artificial photosynthesis, in which bench-scale chemistry mirrors nature's use of light energy, CO_2, and a water to create value-added carbon species. In this appendix, we focus our attention on how we can understand and quantitatively evaluate the performance of homogeneous molecular catalysts in the context of photochemical carbon dioxide reduction (CO_2RR) using well established techniques such as redox potential matching, emission quenching, dynamic light scattering analysis, and quantum yield determination.

1. Components of a Photocatalytic CO_2RR System

A photocatalytic system for homogeneous CO_2RR is typically composed of the following:

Drivers
- Photosensitizer
- Catalyst
- Sacrificial Electron Donor
- Light

Substrates
- CO_2
- Acid Source
- Light

In this description, “drivers” are the parts of the system that perform the work related to electron transfer, while the “substrates” are the elements that will be transformed into the carbon-based product. Light is in both categories because it initiates electron transfer events, and the new bonds formed in the products (CO, $HCOO^-$, CH_3OH, etc) store light energy. A typical homogeneous photocatalytic system requires both a photosensitizer and a catalyst working together in solution. The photosensitizer (PS) is a molecule that can absorb a photon of discrete energy from the light source, promoting an electron to move into a higher energy excited state. This excited electron can terminate in release of energy as visible light (emission) or it can be transferred to the catalyst. In some cases, light absorption from a catalyst molecule can permit electron transfer to a neighboring catalyst molecule; a self-sensitized photocatalytic system will work without the addition of a PS. In CO_2-to-CO reduction, two cycles of light photosensitization will lead to two electrons transferred to the catalyst, which can then bind and reduce CO_2 with the help of the acid source. Whether or not we can expect productive electron transfer from the PS to the catalyst can be predicted by analyzing their redox potentials, this will be discussed further in section 2. The sacrificial electron donor (SED) or quencher is another small molecule in this reaction solution with the essential role of regenerating the PS. It is usually added in excess relative to the PS, and is the only driver that is not catalytic, hence “sacrificial”. Whether the SED transfers electrons to the PS before or after electron transfer to the catalyst defines the photocatalyst quenching mechanism, described in detail in section 3. All of these components exist in one solution, and are equipped with stirring, temperature regulation, and placed in front of a light source for reaction. Since we will attribute the reactivity observed to a specific homogeneous catalyst structure, it is important to verify that said catalyst is responsible for activity; this can be done through dynamic light scattering analysis, described in section 4. The light source in a typical bench-scale set up will be a lamp with a specific energy range (or a single wavelength). Knowing the power of this lamp is important in determining how many moles of CO are produced per mole of photons emitted, herein called the quantum yield (QY), described in detail in section 5. Finally, the reaction medium (solvent) in a homogeneous photocatalytic system, which is difficult to classify as a driver or substrate*, can play an essential role in the photocatalysis performance, therefore multiple solvents should be screened when finding optimal reaction conditions.

* In the case that protic solvents are used (e.g.,H_2O), they can also serve as your acid source.

2. How to Use Redox Potentials when Designing a Photocatalytic System

Matching a photosensitizer to a catalyst by analyzing tabulated redox potentials can inform experimental screening. It is most helpful if you first know the reduction potential of your catalyst, and assuming it is a novel catalyst, a cyclic voltammogram can help you obtain this. For example, in Chapter 2, the CV of catalyst **[Fe]$^{2+}$** helped inform the selection of PSs that should be capable of reducing it. Since the reductive chemistry occurs at the second wave, at a potential of –1.43 V vs Fc/Fc^{+}, we can proceed by choosing a PS whose reduction potential is more energetic. As seen in Chapter 2, Figure 2.4, all of the PS that are active for photochemical CO_2RR in conjunction with **[Fe]$^{2+}$** bear a reduction potential negative of –1.43 V. This is similar to choosing an applied potential for electrolysis, you want to be at or above the onset potential in order to generate enough of your reduced catalyst to perform CO_2RR. An excellent resource containing tabulated redox potentials for organic molecules and coordination complexes that have PS properties can be found in Chapter 2, reference 19. Technically, the value you want to know is the excited state reduction potential, since you are using the PS under light irradiation. This value is not something that can be measured by cyclic voltammetry, but rather is estimated via calculations described in Chapter 2, reference 19. An excited PS, though, will typically have higher oxidizing and reducing potential than it does in its ground state, so if an excited state redox potential value is not available, the ground state value will be a minimum estimate of the excited state value. To add a layer of complexity, electron transfer from an excited PS (PS*) to a catalyst does not always occur. Sometimes, the SED reduces PS*, then electron transfer from the one-electron reduced $PS^{\cdot-}$ to the catalyst follows. These quenching two mechanisms can be determined using spectroscopic methods (see section 3). Since the SED also participates in transferring electrons to either PS* or PS^{+} (depending on the quenching mechanism) it is another element in the photocatalytic system that can be carefully chosen based on redox potentials.

3. Emission Quenching and Stern-Volmer Analysis to Determine Photocatalyst Mechanism

As mentioned in previous sections, the photochemical quenching mechanism in your photocatalytic CO_2RR system can be predicted using spectroscopic techniques called emission quenching and Stern-Volmer analysis. In these experiments, we will separately determine the rate at which either the SED or the catalyst (CAT) can quench PS*, called the quenching rate constant (k_q). Once we know the rates of the two quenchers, we can deduce the following mechanisms:

SED has a larger k_q (reductive quenching)

1. PS + light = PS*
2. PS* + SED = $PS^{\cdot-}$ + $SED^{\cdot+}$
3. $PS^{\cdot-}$ + CAT = $CAT^{\cdot-}$ + PS

CAT has a larger k_q (oxidative quenching)

1. PS + light = PS*
2. PS* + CAT = $PS^{\cdot+}$ + $CAT^{\cdot-}$
3. $PS^{\cdot+}$ + SED = PS + $SED^{\cdot+}$

For a catalytic cycle depiction of these two mechanisms, please see Chapter 2, reference 11.

The first step in the experimental process is the emission quenching component. First, find out the excitation and emission wavelengths of your PS, as well as the associated excited state lifetime (τ_f). These values are listed in Chapter 2, reference 19 for many PSs. If you have synthesized a brand-new PS, then you will have to record all of its photophysical parameters from scratch in order to do this analysis. With the known excitation wavelength, you can record the fluorescence spectra of your PS in the range where you expect to see the emission wavelength (the fluorimeter software will ask you to input these values before recording spectra). After recording the first spectrum, add a known concentration of your quencher to the PS solution. The next spectrum you record will show a decrease in the emission intensity if it is capable of quenching PS*. Therefore, if increasing concentrations of the quencher causes no changes to the emission spectra of PS*, you likely have an oxidative quenching mechanism in your hands. For proper quantitative determination of this observation, add 4 aliquots of quencher in order to have 4 data points to plot for Stern-Volmer analysis. Repeat this experiment for the other quencher, so that you have two sets of data: emission quenching spectra for the addition of SED to PS, and addition of CAT to PS.

Note: It is important that the initial concentration of the PS is not too high, otherwise you will observe that upon addition of a quencher, the emission spectrum actually increases. This is because at high concentrations of PS, self-quenching can occur, so adding the external quencher will slow self-quenching- making the resulting emission intensity higher. For the PSs $[Ru(bpy)_3]^{2+}$ and $Ir(ppy)_3$, 50 μM worked well for these experiments and no self-quenching was observed (see Chapters 2 and 3).

Now that you have the data sets collected from the fluorimeter, you will analyze this data using Stern-Volmer quenching kinetics. Essentially, you will determine k_q for each quencher based off the linear regression following the Stern-Volmer equation:

$$I_0/I_Q = 1 + \tau_f k_q [Q]$$

where I_0/I_Q is the peak emission intensity (centered at the emission wavelength observed) in the absence (I_0) or presence (I_Q) of quencher, τ_f is the emission lifetime of PS* (in time units) and [Q] is the concentration of the quencher. Plot a line in which your X values are the incremental concentrations of the quencher (starting with 0) and the Y values are I_0/I_Q (from your fluorimeter data). With all of the values in SI units, solve for k_q.

4. Dynamic Light Scattering Analysis and Catalyst Stability

In the field of homogeneous CO_2RR catalysis, it is essential to provide data which supports the classification of your catalyst as homogeneous—evidence that shows that the active species under the reaction conditions is in fact a discrete molecular complex as reported, rather than a newly formed species such as nanoparticles. In electrochemical CO_2RR, rinse tests are used to corroborate that the catalyst is freely diffusing in solution, and that no heterogeneous species are forming on the electrode surface. In photochemical CO_2RR, a commonly used method is dynamic light scattering (DLS) analysis. DLS includes the use of a spectrophotometer to measure properties in your reaction mixture; incident light from the instrument shines through a solution, and the detector can assess the size of the particles in solution based off their Brownian motion and the resulting scattered light patterns over time. One approach to doing DLS experiments and analysis is to start with a sealable cuvette containing the entirety of your reaction components (possible structural decomposition of your catalyst should be modeled under precise conditions). The first measurement should be a zero timepoint with respect to irradiation, or a "dark" reaction. The DLS scan of this dark reaction mixture will be the baseline to compare the following experiments, in which you should irradiate the solution for a few time points. The resulting spectra you will get will show size distribution (0-10,000 nm) vs intensity (%). For a photocatalyst system in which the structural integrity does not change, the various timepoints with irradiation should show no deviation from the baseline dark timepoint, and the only peak (if any) should be on the lower size range. If a photocatalyst system starts to decompose into nanoparticles, the resulting spectra will show a size distribution away from the baseline, with peaks of increasing intensity at a higher size range.

5. Quantum Yield Determination via Chemical Actinometry

The quantum yield (Φ) of CO_2 reduction to CO using a photocatalytic system is defined by:

$$\Phi = \frac{\text{2 (number of CO molecules)}}{\text{number of photons absorbed}} \text{ x } 100\ \%$$

This parameter tells us what percentage of the light we shine at our reaction mixture results in the formation of one mole of CO. We multiply the numerator by 2 in the equation since we know that two electrons are required to reduce CO_2 to CO (and therefore, two photocatalytic cycles). It is analogous to faradaic efficiency, where we determine what percentage of the electrons of charge passed result in the formation of CO. With typical lamps, the quantum yield will be inherently inefficient, because the light emitted by the lamp is not concentrated at the sample. Most quantum yields reported in the literature are between 0.5 to 20 %. The number of photons per unit time (photon flux) emitted by the blue LED light source used during photocatalytic experiments can be measured via chemical actinometry. Note, fancy lamps have a feature that should tell you their power, so chemical actinometry is useful when this feature is not available. A chemical actinometry experiment uses a standard compound of well-known and tabulated photochemical properties. In chapter 2 and 3, we used ferrioxalate ($K_3[Fe(C_2O_4)_3]$) for the actinometry experiment. The photochemical decomposition of ferrioxalate (Fe^{3+}) to Fe^{2+} can be monitored spectrophotometrically via the detection of free Fe^{2+} by chelation with phenanthroline according to the simplified reactions:

$$Fe^{3+} \xrightarrow{\Delta} Fe^{2+}$$

$$Fe^{2+} + 3\text{ phen} \longrightarrow \underset{\lambda_{max} = 510\text{ nm}}{[Fe(phen)_3]^{2+}}$$

The moles of Fe^{2+} formed in an irradiated solution can be calculated by:

$$\text{moles } Fe^{2+} = \frac{V_1 \text{ x } V_3 \text{ x } \Delta A_{510}}{10^3 \text{ x } V_2 \text{ x } l \text{ x } \varepsilon_{510}}$$

Where ΔA_{510nm} is the difference in absorption between the solution kept in the dark and the irradiated solution, and ε_{510nm} is the molar absorptivity of $[Fe(phen)_3]^{2+}$ at 510 nm (11100 L mol^{-1} cm^{-1}). The average photon flux was then calculated following equation:

$$\text{\# photons/sec} = \frac{6.022 \text{ x} 10^{23} \text{ x moles } Fe^{2+}}{\Phi_\lambda \text{ x } t}$$

where Φ_λ is excitation wavelength dependent quantum yield of ferrioxalate. Experimental details for making and mixing the solutions of ferrioxalate and phenanthroline are in chapter 2. The final quantum yield should be calculated from an average of at least three photon flux measurements.